SQUID BASED CRYOGENIC CURRENT COMPARATOR FOR MEASURING LOW-INTENSITY ANTIPROTON BEAMS

Thesis submitted in accordance with the requirements of
the University of Liverpool for the degree of Doctor in Philosophy by

Miguel Filipe Abreu Fernandes

June 2018

Contents

Illustrations

List of Figures

List of Tables

Glossary

$\overline{p}$ antiproton.

AC Alternating Current.

AD Antiproton Decelerator.

ADC Analogue-to-Digital Converter.

APF Additional Positive Feedback.

BCS Bardeen Cooper Schrieffer.

BCT Beam Current Transformer.

CCC Cryogenic Current Comparator.

CERN European Organization for Nuclear Research.

DC Direct Current.

DCCT DC Current Transformer.

ELENA Extra Low ENergy Antiproton.

EMI Electro-Magnetic Interference.

FFT Fast Fourier Transform.

FLL Flux-Locked Loop.

HTS High-Temperature Superconductors.

HV Helium Vessel.

I-V Current-to-Voltage.

LINAC LINear ACcelerator.

LTS Low-Temperature Superconductors.

MLI Multi Layer Insulation.

PLC Programmable Logic Controller.

PS Proton Synchrotron.

QP Quasi-particle.

RadFET RADiation-sensitive Field-Effect Transistor.

RF Radio-Frequency.

RFQ Radio-Frequency Quadrupole.

RMS Root Mean Square.

RT Room Temperature.

SC Superconducting.

Schottky longitudinal-Schottky.

SNR Signal to Noise Ratio.

SQUID Superconducting QUantum Interference Device.

SR Slew Rate.

TS Thermal Shield.

V-Φ Voltage-to-Flux.

VV Vacuum Vessel.

Author's Contribution

Next are listed the contributions for the project developed by the author, indicating when this was accomplished with the help of other people, and which parts of the project where entirely developed by other people.

Magnetostatic simulations of the attenuation factor of the meander shaped superconducting shield structure are presented in Section 2.5.3 of Chapter 2. Starting from an existing shielding geometry different simulations were performed with varying dimensions in order to assess how these impact the resulting attenuation factor. The author of this thesis carried out these simulations.

In Chapter 3 standalone measurements of components of the Cryogenic Current Comparator (CCC) monitor are presented. The author performed the measurements of the selected Superconducting QUantum Interference Device (SQUID) sensor shown in Section 3.1. The measurement of the magnetic properties of the two samples of ferromagnetic cores at room and cryogenic temperatures presented in Section 3.2.2 were done by S. Aguilera, M. Krupa and the author of this thesis. The measurements of the ferromagnetic core that was used in the monitor had been previously performed by R. Geithner *et al.*

The analysis of the theoretical measurement sensitivity and resolution, and the derivation of the predicted frequency response taking into account the core frequency dependent magnetic permeability presented in Section 3.2.3 of Chapter 3 were performed by the author. In Section 3.3 is discussed the stability limits of the SQUID/Flux-Locked Loop (FLL) electronic readout scheme, these are related to the system bandwidth and the input signal slewrate based on a preexisting model. Several simulations of the SQUID/FLL system using Simulink/MATLAB software were performed by the author to illustrate and assess the stability of the system and the validity of the model.

Two different coupling circuits implementing a low-pass filtering aiming at reducing the Antiproton Decelerator (AD) beam signal slewrate are proposed and studied in Section 3.3.2. These were studied by the author in terms of their frequency response and additional induced noise. The previously implemented simulation of the SQUID/FLL system was used to verify the stability for the AD beam signal when using the proposed configuration for the coupling circuit.

The selected components and configuration of the coupling circuit was assembled and implemented by R. Neubert, as show in Section 3.4, using the magnetic shield and ferromagnetic core that had previously been developed by GSI and University Jena.

The architecture and assembly of the acquisition system described in Section 3.5 devised to enable the automatic control and operation of the CCC monitor, and enabling the integration with the AD operation system, was performed by the author. The respective software was implemented by M. Ludwig, E. Oponowicz and D. Alves after specification prepared by the author.

The simulations of the expected stray magnetic field in the CCC installation location due to the adjacent quadrupole magnets presented in Section 4.1 was performed by the author. The measurements of the stray magnetic field present in this same location were conducted by M. Buzio. The calculations of the transverse space occupied by the beam in the installation location were performed by the author with the help of P. Belochitskii.

The cryostat design shown in Section 4.3 was performed at CERN by the Cryogenic group, with the main participation T. Koettig and A. Lees, with requirements provided by the author. The cryostat fabrication was done by CERN's Mechanical and Engineering group with main participation of J.P. Brachet and D. Lombard.

Chapter 5 presents the measurements done with the developed monitor, these include the calibration curves, noise background, frequency transfer function, beam position dependency and response to a current like the one at AD injection. The characterization measurements of the CCC alone were done by the author with the help of R. Geithner and J. Golm at the University of Jena. The subsequent measurements of the CCC installed in the new cryostat were entirely performed by the author at CERN. The beam measurements presented in Section 5.2, as well as the comparison with the existing Schottky monitor and statistical analysis of the developed monitor were performed by the author.

Abstract

In the low-energy Antiproton Decelerator (AD) and the Extra Low ENergy Antiproton (ELENA) rings at CERN, an absolute measurement of the beam intensity is essential to commission and troubleshoot the different accelerator systems, to measure the operational efficiency, and to provide calibration information for the different experiments using the antiproton ($\overline{p}$) beam. Both the AD and ELENA are synchrotron decelerators, operating with both bunched and debunched - Direct Current (DC) - beams. The beam currents can be smaller than 100 nA, and the total number of circulating particles is of the order of 10^7 $\overline{p}$.

Non-intercepting measurements of low-intensity charged particle beams are particularly challenging due to the low amplitude of the induced electromagnetic fields. This is even more difficult for DC beams. The most common diagnostics that are able to measure DC beams are the DC Current Transformers (DCCTs), but these present considerable limitations when used to measure low-intensity beams, since these are limited in current resolution to 1 µA. In the AD a longitudinal-Schottky (Schottky) monitor is currently used for intensity measurements but this presents several limitations, including accuracy errors above 10 %.

Several laboratories have shown in the past the potential of Superconducting QUantum Interference Device (SQUID)-based Cryogenic Current Comparator (CCC), using Low-Temperature Superconductors (LTS) technology, to measure beam current intensities of slowly varying beams in the nano-ampere range. However, previous CCC beam monitors suffered from a strong susceptibility to mechanical vibrations, and Electro-Magnetic Interference (EMI) perturbations, and also presented limited availability which limited their operational use. Additionally, these were never able to cope with short bunched beams in a synchrotron accelerator.

In the present work a CCC system was developed for the AD machine. This monitor was optimised in terms of its current resolution, ability to cope with short bunched beams and overall system stability. Also, a dedicated cryostat was designed and fabricated to house the CCC, and to be installed in the AD beam line, aiming at decoupling external mechanical vibrations from the monitor, and to have a reduced heat in-leak, allowing for a standalone operation with an external liquid helium reliquefier.

The new monitor was characterized in laboratory and different measurements are presented. Measurements with real beam were also performed in the AD, and the resolution and accuracy of beam current and beam intensity measurements were assessed.

Optimal beam current resolutions of 2.5 nA, and beam intensity resolutions of $1.2 \times 10^4\,\overline{p}$ charges (at the highest beam energy) were obtained. However, the limiting factor in the obtained absolute measurement accuracy was the observed drift of the zero beam baseline, which could amount to 25 nA. These are the first CCC beam current and intensity measurements ever performed in a synchrotron machine with both coasting and short bunched beams.

Future improvements could be obtained by studying the origin and effect of the external perturbations causing the observed drift, leading to the implementation of mitigation and compensation techniques.

Acknowledgements

I would like to acklowdge my supervisor Prof. Dr. Carsten Welsch for giving me the opportunity of conducting this project as a PhD student at Univesity of Liverpool and member of the Quasar group. I would like to thank my CERN supervisor Dr. Jocelyn Tan for his guidance in the conduction of this work, and all his support for the project within CERN organisation. I am also grateful to CERN and the oPAC project Marie Curie European Grant for supporting me in this journey and providing an uniquely rich working and learning environments.

Many people from different groups and disciplines were involved in this project, and the obtained results would not have been possible without their contribution and hard work. Special thanks and acknowledgements go to:

- Dr. Torsten Koettig, Andrew Lees and Agostino Vacca from the Cryogenic group at CERN, which were involved in this project since its beginning, for their tireless work in designing, installing and testing the cryostat and cryogenic systems. I am grateful to have been able to work with them with whom I have learned a lot.

- Jean-Pierre Brachet, Giuseppe Foffano and Didier Lombard from the Materials Engineering group at CERN who were heavily involved in the detailed design, fabrication and assembly of the cryostat. This was acomplished in a very short time frame and required a strong effort from all involved people.

- Michael Ludwig, Ewa Oponowicz and Dr. Diogo Alves from the Software Section of the Beam Instrumentation group who implemented the software for the acquisition system that enabled the performed beam measurements.

- Dr. Marcus Schwickert and Dr. Febin Kurian from the beam instrumentation group at GSI for hosting me the at GSI for two weeks where I learned and I had my first hands-on experience with the CCC devices.

- Dr. René Geithner and Ralf Neubert for their work in the development of the superconducting magnetic shield and ferromagnetic core components use in this project. Also for receiving me at the University of Jena for 2 weeks of intensive laboratory measurements, and the many discussions and advices.

- My colleagues from the section Position and Intensity section in the Beam Instrumentation group at CERN for the support and camaraderie over the past 4 years.

In particular Patrick Odier for the many discussions about the functioning of beam intensity diagnostics.

- Dr. Henry Barthelmess from the Magnicon company for the extensive e-mail exchanges and precious help in clarifying the functioning of the SQUID sensors.

- Dr. Lee Devlin, Michal Krupa, Patrick Odier, Dr. David Belohrad, Dr. Torsten Koettig and and Andrew Lees for reviewing parts of this thesis.

I am also thankful to the friends I met over these years at CERN and in Geneva. And to my friends and office colleagues Thomas Silvia Aguilera and Michal Krupa, for their friendship and sharing of all the ups and downs of being a PhD student.

I would like to thank my parents and family for their love and for always having fostered my curiosity and making me believe and pursue my objectives. Without them I would not be the person I am. A final word of appreciation to Ana for all the motivation and support over these not so easy years.

Chapter 1

Introduction

The purpose of this chapter is to introduce the low-energy antiproton facilities at CERN, as well as the existing beam intensity diagnostics. Section 1.1 starts with a description of the antiproton production process and an explanation of why these need to be decelerated in the Antiproton Decelerator (AD) in order to be used by the low-energy experiments studying matter/antimatter asymmetries. An overview of the experiments and their objectives is also presented. Section 1.2 covers the need for beam intensity diagnostics in accelerator facilities, and describes the existing diagnostics in AD and their limitations in providing an accurate measurement of the beam intensity due to the reduced number of particles and their low-energy. The chapter continues by introducing the Cryogenic Current Comparator (CCC), in Section 1.3, as a beam current diagnostic capable of a superior current resolution and this is compared with the more common types of diagnostics. The chapter terminates by stating in Section 1.4 the objectives of the current project, the collaboration under which this was developed.

1.1 Low-Energy Antiproton Facilities at CERN

Particle physics and particle accelerator science are a rich and varied domain of science, addressing a wide range of scientific questions from the fundamental laws of the Universe to new techniques for cancer treatment. These areas have contributed to the development of a large number of cutting-edge technologies, many of which have found application in many other disciplines of science and engineering [1].

The European Organization for Nuclear Research (CERN) laboratory, located on the border between France and Switzerland, founded in 1954, pursues a wide range of research programs covering many areas in fundamental interactions physics and in the development of new technologies employed in its accelerator and detector facilities. In recent years CERN has been operating the world's largest and most powerful particle accelerator, the Large Hadron Collider (LHC). The LHC is 27 km long in circumference and accelerates protons and lead ions for head-on collision at a top energy per beam of 6.5 TeV and 1.38 TeV/nucleon, respectively. On the other end of the energy spectrum, CERN also develops a rich experimental program of low-energy antimatter research,

with the AD [2–4]. The AD is 188 m long in circumference and provides a beam of low-energy antiprotons ($\overline{p}$s) with 5.3 MeV kinetic energy to 5 experiments. These are ALPHA, AEgIS, ASACUSA, ATRAP and BASE [5]. The number of particles in the LHC and in the AD also differ by many orders of magnitude. When fully filled the LHC stores 3.2×10^{14} protons per beam while the AD usually operates with 3×10^{7} $\overline{p}$s. This results in a nominal LHC beam electric current of the order of 500 mA, and in the AD, at its lowest energy, it is only approximately 300 nA. Non-intercepting detection and measurement of the number of particles in these beams is crucial for the operation of these accelerators. Other fields and applications relying on low-intensity beams, besides low-energy antimatter studies with $\overline{p}$s [6, 7] are nuclear physics studies using rare isotope beams [8, 9], hadron cancer therapy [10], mass spectroscopy [11] or ion implantation in semiconductor fabrication [12]. All of these areas require or would profit from an improved non-intercepting beam intensity measurement.

The AD facility of CERN began its operation in 1999, and its function is to deliver low-energy antiprotons ($\overline{p}$s) to experiments studying the symmetries between normal matter and antimatter. Using techniques such as high-precision laser spectroscopy of antihydrogen and antiprotonic helium atoms, these experiments have measured the antiproton-to-electron mass ratio, and the magnetic moment of $\overline{p}$s. Other results concern the interaction of $\overline{p}$s with different types of target materials for which the energy loss and cross-sections have been measured. Also the biological effectiveness of $\overline{p}$ beams destroying cancer cells has been measured as a possible method for hadron therapy by the past experiment ACE [13]. New experiments, currently under the preparation and installation phases will attempt to measure the gravitational acceleration of antihydrogen. A review of the different experimental results can be found in [7].

Antimatter atoms can only be efficiently synthesised from component particles at electron-volt and lower energy scales, what is far below the production energy of $\overline{p}$s, in the GeV range. The AD is currently the only source of low energy $\overline{p}$s, but it can only decelerate the $\overline{p}$s down to 5.3 MeV which is higher than the experimental apparatus can trap. The new Extra Low ENergy Antiproton (ELENA) [14–16] synchrotron decelerator will receive the AD beam and further decelerate it to 100 keV. Figure 1.1 shows the layout of the building housing the AD and ELENA decelerators, as well as the different experimental areas and other equipment. Also the FAIR facility currently being built in Darmstadt, Germany has in its planning for a later phase, the construction of a low energy $\overline{p}$ facility under the FLAIR project.

The $\overline{p}$s are produced by colliding the CERN Proton Synchrotron (PS) beam containing $\approx 1.5 \times 10^{13}$ protons with kinetic energy $E_K = 26$ GeV on a 50 mm long solid iridium target. For a small fraction of the collisions, the following reaction will occur (or a similar one involving a target neutron),

$$p(\text{beam}) + p(\text{target}) \rightarrow p + p + p + \bar{p}. \tag{1.1}$$

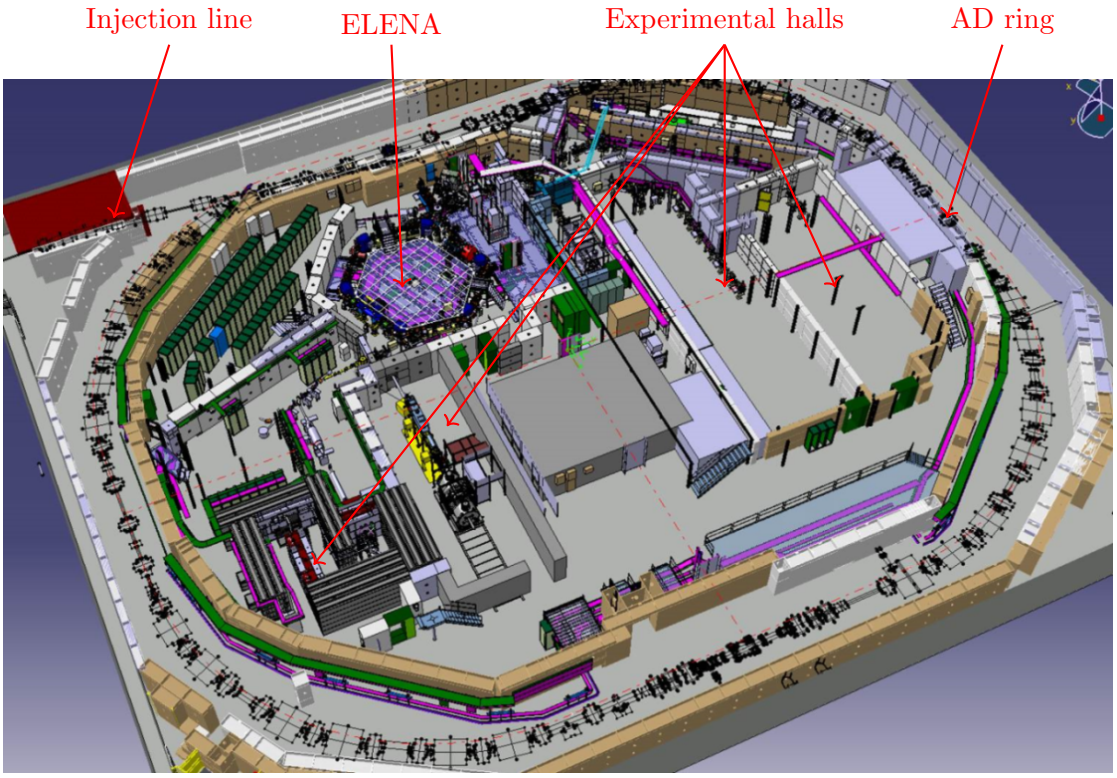

FIGURE 1.1: Organisation of the AD hall with the AD and ELENA synchrotron decelerators, as well as the different antimatter experimental halls. Image: CERN.

This reaction channel is open for incoming protons with $E_K \approx 6\,\text{GeV}$, but the higher energy of the PS beam provides for a higher production yield. At this energy, around 2.5×10^5 incoming protons are required for each produced $\overline{p}$. The $\overline{p}$ are produced with an energy distribution centred on $E_K \approx 2.75\,\text{GeV}$. Downstream of the production target, the shower of $\overline{p}$s is focused by a horn-type magnetic lens [17] into a parallel beam with transverse emittance[1] $\epsilon \approx 200\pi\,\text{mm mrad}$ and momentum spread $\Delta p/p \approx 6\,\%$. This beam containing $\approx 5 \times 10^7\,\overline{p}$ (nominal design value) is injected into the AD for deceleration.

Figure 1.2 shows the layout of the AD, the production target, transfer line, AD synchrotron ring, including the location of some of its relevant equipment: injection/ejection elements, Radio-Frequency (RF) cavities, stochastic and electron cooling. Additionally, the transfer lines for the different experiments are shown in red.

The kinetic energy of the injected $\overline{p}$s needs to be reduced to at least $\lesssim 10\,\text{keV}$ so that they can be trapped by the different experiments apparatus for further studies. This requires a reduction of the kinetic energy by almost 6 orders of magnitude, which is accomplished in part by the AD that reduces the energy while keeping a minimal spreading of the region occupied by the beam in position and momentum phase-space. At the end of the AD cycle, $\overline{p}$s with $E_K = 5.3\,\text{MeV}$ are ejected with a typical efficiency of $\approx 85\,\%$. In order to accomplish the beam deceleration with a high efficiency the AD

[1] Emittance is a measure of the average spread of the particle coordinates in position and momentum phase-space.

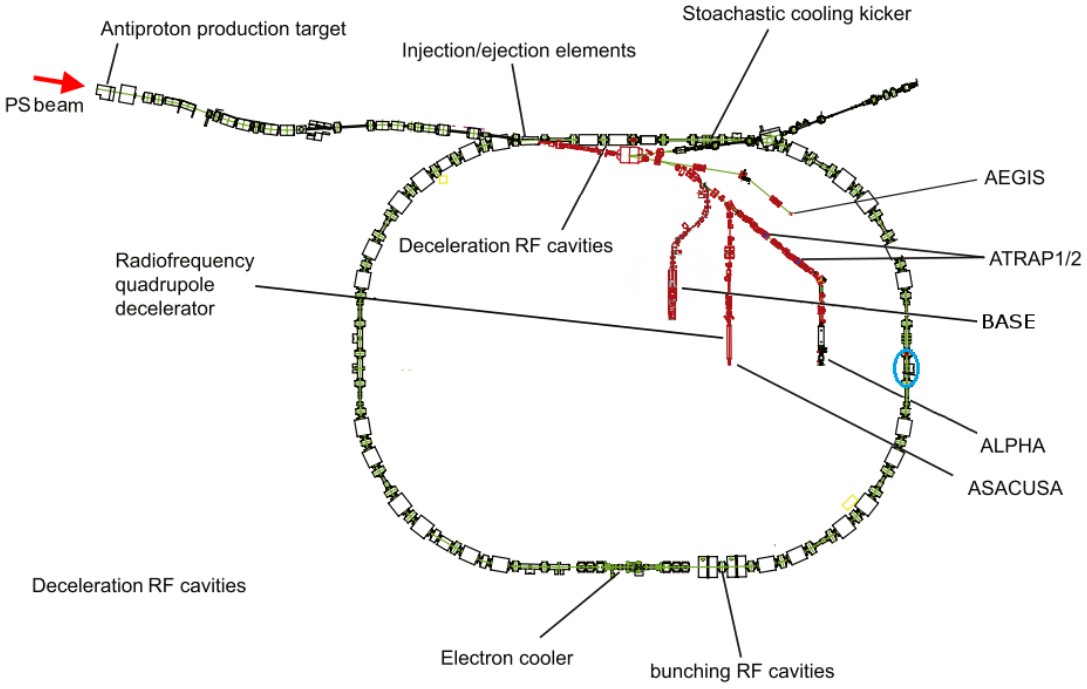

FIGURE 1.2: Layout of the AD hall including the AD ring, the production target, transfer lines and the experimental facilities locations. In blue is indicated the Section 15 in Sector 2, where the CCC monitor developed in this project was installed. Adapted from [7].

cycle comprises different phases that are shown in Figure 1.3. Right after injection, the RF cavities perform a bunch rotation to reduce the momentum spread of the beam from $\pm 3\,\%$ to $\pm 0.75\,\%$. Then, in order to reduce the emittance, stochastic beam cooling is applied. After this, the RF cavities are turned on to capture and bunch the beam, for the first deceleration ramp. The beam deceleration is accomplished by progressively reducing the RF frequency. At the end of the ramp the beam is debunched again by turning off the RF. The deceleration process causes the emittance growth due to adiabatic blow-up and betatron resonances [18]. In order to minimise the beam losses the emittance needs to be reduced again, which is done in a beam cooling phase after each deceleration ramp. This process continues as a sequence of four beam cooling plateaus, and three deceleration ramps. When the AD reaches its final energy, the beam is bunched again before being ejected to the experiment transfer lines.

Presently further deceleration of the $\overline{p}$s from 5.3 MeV down to (3-5) keV, the typical energy of captured particles in a trap, is carried out using a sequence of degrading foils (or gas filled cells), in which the particles lose energy by interacting with the electrons in the material as shown in Figure 1.4. This causes the particles to scatter, deviating from its trajectory and loosing kinetic energy. Each degrader will increase the energy spread resulting in a larger final energy spread. This is a very inefficient process, and the experiments are only able to trap (0.1-0.3) % of the particles. For a review of the early developments in $\overline{p}$s trapping and cooling techniques see [19].

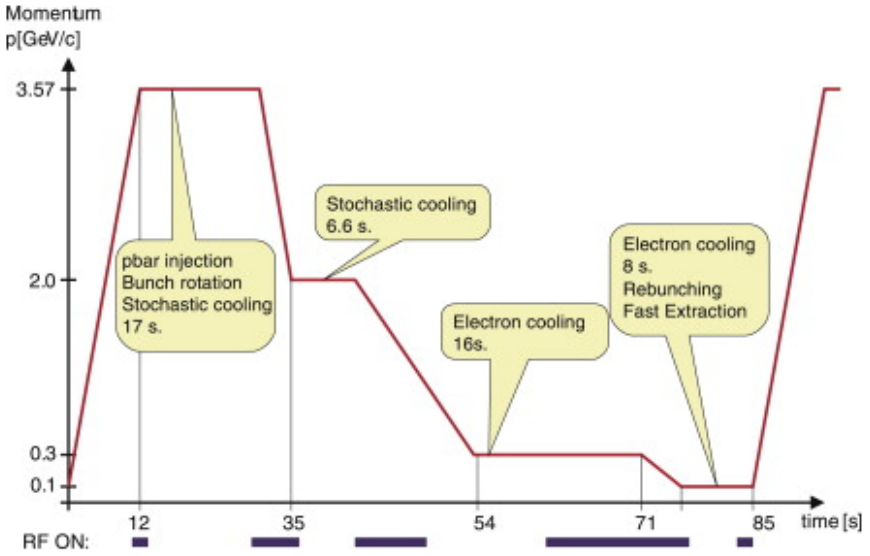

FIGURE 1.3: AD cycle with the succession of beam cooling plateaus and RF deceleration ramps. Adapted from [7].

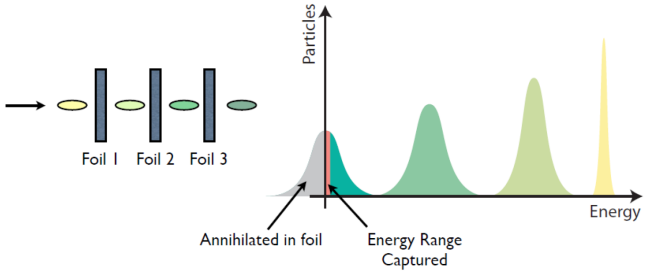

FIGURE 1.4: A schematic view of $\overline{p}$s deceleration in foils. Adapted from [14].

The ASACUSA experiment currently uses a Radio-Frequency Quadrupole (RFQ) for $\overline{p}$ deceleration down to around 100 keV [20]. The RFQ is an RF structure with four specially shaped electrodes that provide at the same time a decelerating and focusing quadrupolar field. It can be biased to different potentials to achieve the continuous adjustment of the output energy required by the ASACUSA experiment [21]. Despite the controlled deceleration, the RFQ also causes adiabatic blow up of the beam emittance (by a factor of 7 in each plane) which results in a significant reduction of the trapping efficiency [7]. Also the RFQ is very sensitive to trajectory and optics mismatch errors, making it difficult and time consuming to properly tune the transfer line from the AD. About 70 % of the beam is lost after passing through the RFQ, and since the transverse beam size is very big (more than 100 mm), only a short beam transport is possible after it (no more than few meters). The final $\overline{p}$ capturing efficiency of ASACUSA is about $(3-5)$ %.

The ELENA ring will improve the overall deceleration process efficiency by further decelerating the beam ejected from the AD down to $E_K = 100$ keV. This will represent

a 100× improvement in the number of $\overline{p}$s trapped by the experiments that currently use foil degraders.

An overview of the experiments using the AD beam is given in [7]. The first experiments to have synthesised antihydrogen at low energies were ATHENA and ATRAP in 2002. More recently, ALPHA and ATRAP have cooled clouds of $(10^3 - 10^6)\,\overline{p}$ to temperatures $T < 10\,\mathrm{K}$, allowing for the production of antihydrogen atoms with sufficiently low temperatures ($T < 1\,\mathrm{K}$) to be confined in a magnetic trap. The ASACUSA experiment, using a radiofrequency RFQ has managed to produce and trap $\bar{\mathrm{p}}\mathrm{He}^+$ atoms, where one of the atomic electrons is replaced by a $\overline{p}$.

The AEḡIS and GBAR experiments will probe the gravitational acceleration of antihydrogen. These will require $\overline{p}$s to be cooled down to mK temperature, to form a $\overline{p}$ beam with 100 m/s velocity in AEḡIS and 1 m/s in GBAR.

Figure 1.5 shows the wide range of energy scales that is covered by the CERN $\overline{p}$ facilities.

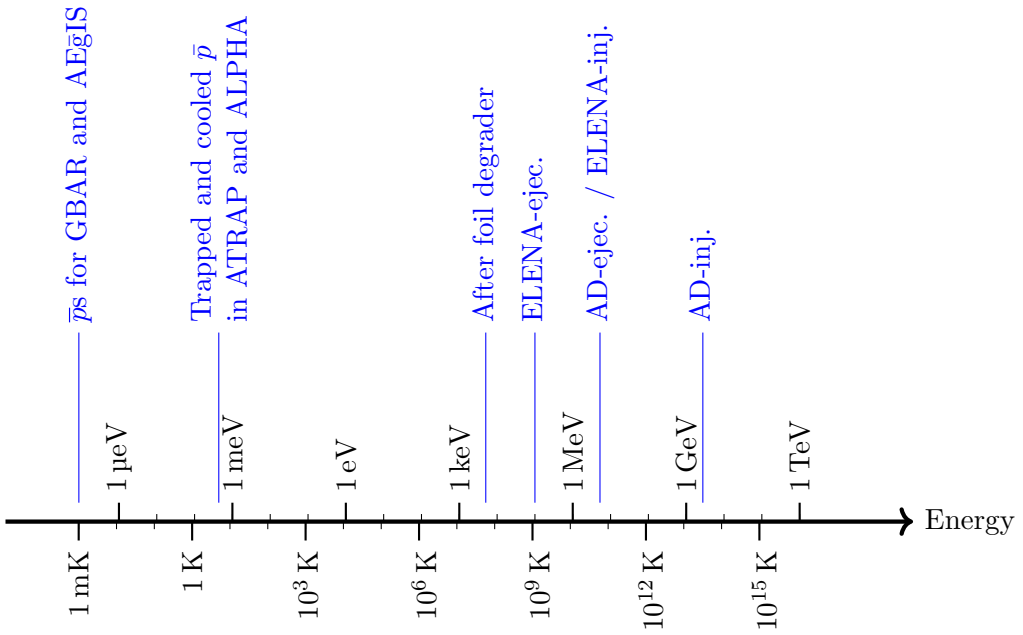

FIGURE 1.5: Energy and temperature scale of $\overline{p}$s, putting in evidence the required energy reduction, from production to trapping (inj. - injection; ejec - ejection;).

The deceleration cycle of the AD passes through different energy plateaus which are normally referred to by the corresponding $\overline{p}$ momentum. Table 1.1 shows the kinetic energy E_K and revolution frequency f_{rev} in the different plateaus, as well as the respective average beam current I_{avg} for the case of nominal injection of $N = 5 \times 10^7\,\overline{p}$, and the case of a low-intensity injection with $N = 1 \times 10^7\,\overline{p}$, assuming a 100 % efficiency. Currently, in a typical AD cycle, approximately $3.5 \times 10^7\,\overline{p}$ are injected and decelerated with an efficiency of $\approx 85\,\%$.

TABLE 1.1: AD beam parameters during the different phases in the deceleration cycle shown in Figure 1.3

Momemtum [GeV/c]	E_K [MeV]	f_{rev} [MHz]	$I_{\text{avg}}\left(5 \times 10^7\,\overline{p}\right)$ [µA]	$I_{\text{avg}}\left(1 \times 10^7\,\overline{p}\right)$ [µA]
3.57	2757	1.59	12.7	2.6
2.00	1271	1.49	11.9	2.4
0.30	46.8	0.500	4.0	0.8
0.10	5.3	0.174	1.4	0.3

1.2 Beam Instrumentation and Operations

The most important beam parameters in an accelerator are the beam energy, number of particles or total charge, which is closely related to the beam current, the beam temporal (or longitudinal) distribution, and the transverse position. Usually these parameters need to be monitored in an online and continuous way, making it important to have detection methods and instruments that do not intercept the beam, what would otherwise degrade it. These often rely on measuring the electromagnetic field of the beam.

The continuous measurement of beam intensity is important to ensure correct accelerator operation within its nominal parameters. In the AD and ELENA, the beam intensity is the main figure of merit to assess the machine operation performance, and a precise measurement of the number of accumulated $\overline{p}$s throughout the entire deceleration cycle is important to optimise the (de)accelerator settings and also to reduce the beam setup times.

Beam monitors can be designed to sense the beam electric field, magnetic field, or combination of both [22]. Devices that rely primarily on interaction with the beam's electric field are often called capacitive pickups, and pickups designed to interact with the magnetic field are called magnetic pickups or more commonly current monitors.

The beam is an assembly of electrically charged particles, creating an electric field with strength proportional to the total charge, and magnetic field proportional to the total charge and particle velocity. Beams are normally enclosed inside a vacuum chamber bounded by an electrically conducting metallic wall. The beam electric field will induce an image charge on the inner surface of the vacuum chamber wall travelling along with the beam, and no electric field Direct Current (DC) component from the beam will exist outside the conducting chamber. Conversely, the Alternating Current (AC) magnetic field components will be highly attenuated outside of the chamber wall, and only the DC component will not be attenuated.

In a circular synchrotron accelerator the beam is typically modulated longitudinally by using RF-cavities to create so called RF-buckets in the longitudinal phase-space that can be filled by bunches of particles. The frequency spectrum of the current of a bunched beam is composed of harmonics at the repetition rate with a DC component equal to the average current. If no RF-field is present the beam presents, to first approximation,

no longitudinal structure[2], and is said to be debunched or a coasting beam. Also, its spectrum energy is almost entirely located at the DC average component. The temporal structure of the beam will affect the frequency range of the electric and magnetic signals that are available to be measured by the detector pickups.

For a comprehensive reference on beam diagnostics see [23, 24]. For a reference specific to beam current and beam intensity monitors see [22].

The AD is operated with bunched beams during the deceleration phases and with a coasting beam during the stochastic and electron beam cooling phases [25]. Continuous measurement of the total beam intensity is important to monitor the efficiency of all these phases. A more detailed description of the AD operation cycle is presented in Section 3.3.1.

1.2.1 Beam Current and Intensity

The most general definition of beam intensity is the number of particles per unit of time, however in a storage ring the word intensity is sometimes also used to refer to the total number of stored particles N at any given moment. In this thesis, the latter definition is used. If the electrical charge Q of the particles is known and $Q \neq 0$, N can be related to the beam average electrical current I_{beam} and the revolution frequency by

$$N = \frac{I_{\text{beam}}}{Q \cdot e \cdot f_{\text{rev}}}. \tag{1.2}$$

Beams can be of low-intensity due to the reduced number of particles N, and/or due to their low velocity and consequently lower f_{rev}. Both these factors contribute to a low beam current which presents a considerable challenge for existing beam current diagnostics [26], due to the reduced amplitude of the induced electromagnetic fields.

Commonly used devices for measuring beam current and intensity are the Beam Current Transformer (BCT) and DC Current Transformer (DCCT), which measure the azimuthal beam-induced magnetic field. While the BCTs are insensitive to the DC average current but can exhibit a wide frequency bandwidth which enables them to probe beam temporal structure, the DCCT are able to measure the beam DC component but have a reduced bandwidth.

Assuming a DC beam current in a vacuum chamber with cylindrical symmetry, the beam's magnetic field will only have an azimuthal component as shown in Figure 1.6, given by the Biot-Savart law or the Maxwell-Ampère equation,

$$\boldsymbol{B} = \frac{\mu_0 \, I_{\text{beam}}}{2\pi \, r} \boldsymbol{e}_\phi, \tag{1.3}$$

where $\mu_0 = 4\pi \times 10^{-7}\,\text{V s/(A m)}$ is the vacuum permeability, and r is the distance to beam. For a beam current of 1 µA the field at $r = 100\,\text{mm}$ has a value of $B_\phi = 2\,\text{pT}$,

[2] Residual longitudinal modulation may be present even when RF power is off.

which is several orders of magnitude lower than the Earth's magnetic field $B_{\text{Earth}} \approx 50\,\mu\text{T}$.

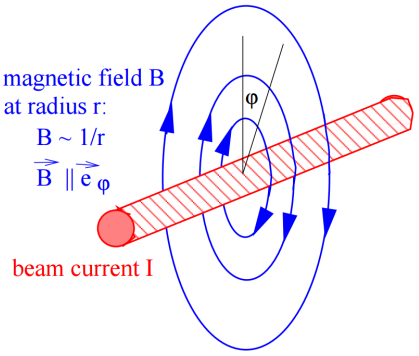

FIGURE 1.6: Azimuthal magnetic field induced by a linear beam current. Adapted from [24].

1.2.2 Beam Current Transformer Monitors

The BCT [27], shown in Figure 1.7, works much like an electrical transformer with a ferromagnetic core, where the primary winding is replaced by the particle beam. When the beam passes through the transformer it changes the magnetisation of the high-permeability core that induces an electromotive force in the secondary winding. According to the Maxwell-Faraday equation only a varying magnetic flux will induce an

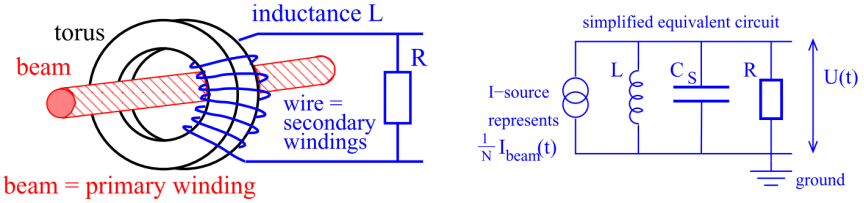

FIGURE 1.7: BCT and its equivalent circuit. Adapted from [24].

electromotive force in the secondary coil, hence BCTs are unable to measure the DC component of signals.

The signal induced in the secondary coil of the BCT can be read by a passive or an active electronic circuit, with equivalent circuit shown in Figure 1.7. The transfer function of the BCT has a passband shape, where the low-frequency cutoff is determined by the droop time constant τ_{droop}, and the high-frequency cutoff is related to the rise time constant τ_{rise}. Therefore, the BCT is unable to measure coasting (debunched) beams as the ones present in the AD during the beam cooling phases. A passive readout, usually using a $R = 50\,\Omega$ load resistor, is used to observe short beam bunches of less than a few micro seconds, when a small rise time τ_{rise} is required. For measuring long beam pulses, larger than several µs, the requirement for having a long τ_{droop} is normally implemented by having an active readout that reduces the load impedance seen by the secondary coil.

The BCT is used to perform bunch-by-bunch charge measurements. Active BCTs typically have a better current resolution, and are able to attain an accuracy at the $\approx 1\,\%$ level with a dynamic range that can go from $1\,\mu A$ to $100\,mA$ [3]. However, measurements of currents $< 10\,\mu A$ are difficult due to thermal and mechanical vibration noise. Additionally, they usually are sensitive to the beam position and bunch length, particularly at higher frequencies [28]. The calibration of BCTs is performed using a carefully shielded and terminated single wire paralleling the beam through the monitor core and driven by a precise current or charge source.

It is also worth noticing that for an ideal transformer connected to a low impedance load, the ratio between primary and secondary current is inversely proportional to the ratio of turns in the respective windings. So in the case of the BCT where the primary winding is always single-turn

$$I_{\text{sec}} = \frac{1}{N_{\text{sec}}} \cdot I_{\text{beam}}. \tag{1.4}$$

This means that the sensitivity to the beam current will be inversely proportional to the number of turns N in the BCT secondary coil. In the AD there are no BCTs installed in the ring for the purpose of intensity measurement, but there is one installed in the ejection line. Very wide-band BCT, so called Fast-BCT are used to probe the time structure of the bunched beam.

1.2.3 DC Current Transformer Monitors

To measure the average beam current of bunched and coasting beams, the DCCT was first introduced in the late 1960s [29, 30], inspired by the flux gate magnetic field sensors.

The DCCT is formed by two magnetic toroid cores, as shown in Figure 1.8, and uses the saturation effect of non-linear magnetisation curves of ferromagnetic materials. The magnetisation curve shows the dependence of the total magnetic induction field B inside a material as a function of the applied magnetic field H, and is also commonly referred to as the B-H curve). The two cores are periodically magnetised into saturation in opposite direction by a modulation current applied in series. The difference is detected by a common winding, and should equal zero when the cores are perfectly symmetric and no other magnetic field sources are present. A beam current traversing the two cores creates an additional magnetisation flux in each core in the same direction (common-mode), which adds up to the modulation flux. This breaks the magnetisation symmetry, and the difference flux is no longer zero. It is instead a periodic signal with twice the frequency of the modulation signal, and with the amplitude of the even harmonics proportional to the beam current. By demodulating one of these harmonics, it is possible to obtain a measure of the beam current. In reality a feedback scheme is used where the common-mode magnetisation is cancelled by a contrary feedback current which must be equal to the beam current.

[3] The maximum current can be higher, but not the dynamic range

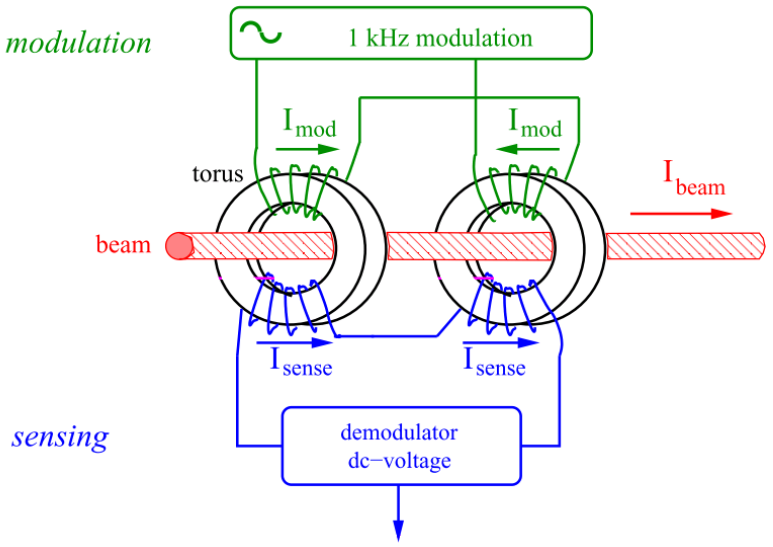

FIGURE 1.8: Schematic of the DCCT, with its two ferromagnetic cores, differential modulation winding and common-mode winding. Adapted from [24].

The absolute calibration of the DCCT is performed using a precision current source to inject a known current through a dedicated calibration winding parallel to the beam passing through the monitors cores. The bandwidth of the DCCT is limited to a maximum of half of the modulation frequency, which is typically in the range of (0.2-30) kHz [31, 32]. It is common to add an AC-coupled core together with the DCCT, in order to extend the measurement frequency range.

The DCCT current measurement resolution is limited by different factors [33]. Since these monitors modulate the magnetic cores with high magnetic fields to drive them into saturation, they are sensitive to the Barkhausen noise produced by the rearrangement of the magnetic domains in the material. Also, hysteresis in the B-H curve of the cores will affect measurement accuracy, as well as any remanent field present when the monitor is turned on. Temperature variations, usually due to high-frequency components in the beam, affect the magnetic properties of the core materials, and the influence of environmental factors like stray magnetic fields, Electro-Magnetic Interference (EMI) and mechanical vibrations (microphony) will also affect the measurement output. All these factors limit the current resolution of the DCCT to $> 1\mu$A, and require integration periods of the order of 1s [28, 33]. But the DCCTs are able to cover large dynamic ranges up to 140 dB.

In the first years of the AD operation it was possible to inject a higher intensity beam of $\approx 10^9$ protons, and a DCCT was installed to measure it. Together with this device an analogue module was used to normalise the beam current into beam intensity, using an amplifier with gain proportional to $1/\beta$, where β is the relativistic velocity, which changes with the AD magnetic cycle. The beam current resolution was typically 1.5 µA.

This corresponds to an intensity resolution of 5.9×10^6 charges at injection ($3.57\,\mathrm{GeV}/c$, $\beta = 0.967$), which deteriorates with the beam deceleration (due to the increase of the normalisation factor proportional to $1/\beta$), and at ejection ($100\,\mathrm{MeV}/c$, $\beta = 0.106$) the resolution was 5.4×10^7 charges [34]. This measurement performance was adequate to measure the proton beam but was insufficient to measure the operational beam with $10^7\,\overline{p}$, as is clearly visible in Figure 1.9.

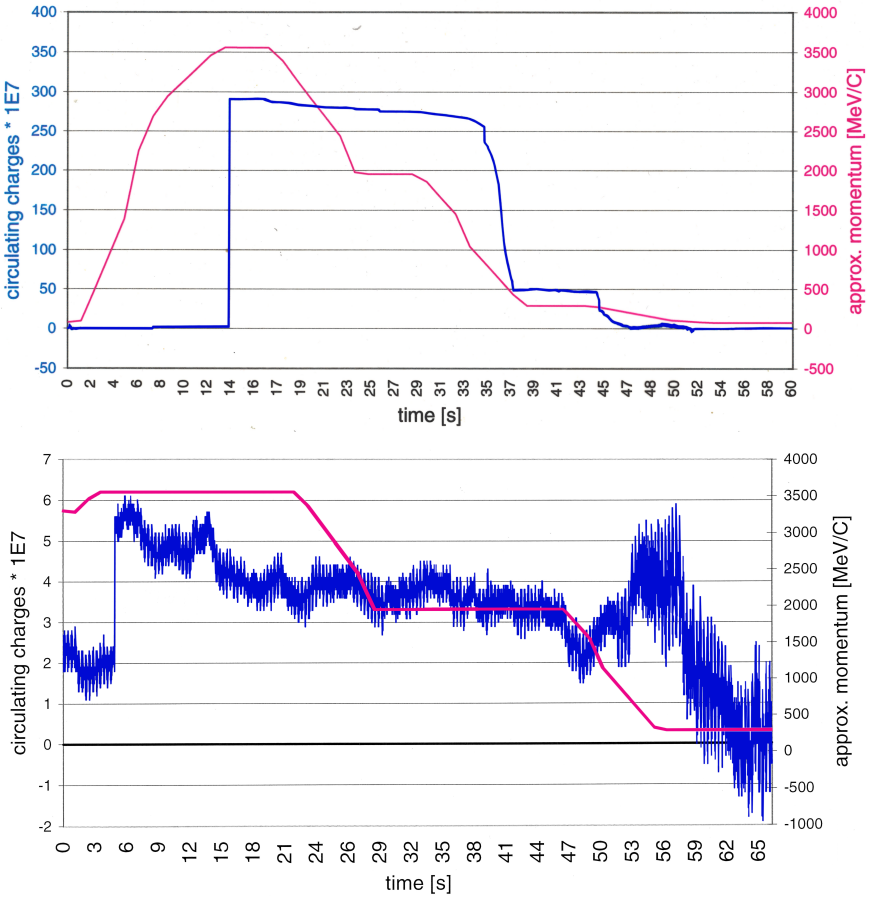

FIGURE 1.9: Measurement of the number of particles circulating in the AD obtained with the DCCT monitor. Top plot: cycle with proton beam; Bottom plot: cycle with $\overline{p}$ beam. Courtesy of P. Odier [35].

The DCCT measurement of the proton beam was used to cross-calibrate another beam intensity measurement provided by a Schottky noise monitor, which is discussed in the next Section. Nowadays, proton beams are no longer used to setup the AD and the DCCT has been uninstalled.

In both the BCT and the DCCT, almost always an insulating (ceramic) break is placed in the vacuum beam pipe around which the devices are located. This serves to break the beam mirror current that would otherwise shield the magnetic field seen by the monitors. It also avoids excitation of the monitors by stray currents that may circulate in the beam pipe. An electrical bypass is used to restore the electrical connectivity between the two sides of the beam pipe. In most cases this takes the form of an electrical casing well connected to the beam pipe, placed around the monitor, that also acts as an EMI

shield. Sometimes additional magnetic shielding is provided by using high-permeability materials such as mu-metal.

1.2.4 Longitudinal-Schottky Monitor

Any current created by a discrete ensemble of charge carriers presents random fluctuations which give rise to shot noise that can be detected in its frequency spectrum. This phenomenon was first investigated in electronic vacuum valves by W. Schottky in 1918 [36], and is usually referred to as Schottky noise. In a circular accelerator, this noise can be measured using a sensitive pickup and shows up as different frequency band structures centred around the harmonics of the revolution frequency. From the analysis of these frequency spectra it is possible to measure several beam parameters, like for example: the number of particles, the momentum distribution, tune, transverse emittance and chromaticity [37, 38]. This diagnostic techniques are mainly used in hadron storage rings, and it is not applicable in the case of LINear ACcelerators (LINACs) due to the non-repetitive circulation of the particles.

Different types of Schottky noise spectral structures may be measured depending on the pickup used and on the characteristics of the circulating beam [39]. There is the longitudinal-Schottky spectrum obtained from a pickup measuring the monopole moment, dependent on the current amplitude and independent of the transverse distribution. While the transverse-Schottky spectrum depends on the transverse position of the beam and is obtained from pickups measuring the beam dipole moment. A bunched or a debunched beam will also cause different spectral structures. The longitudinal-Schottky spectrum in the case of a coasting beam consists only of incoherent noise bands centred at harmonics of the revolution frequency. In the cased of bunched beams these bands are mixed with the synchrotron frequency originating multiple bands around each harmonic. Additionally, besides these incoherent bands, there will be a much stronger coherent peak component exactly at the harmonics of the revolution frequency.

Time resolution of Schottky beam measurements are typically limited, since in order to increase the frequency resolution and the Signal to Noise Ratio (SNR) of the measured spectrum, higher acquisition times are required. Since the integral of the power in each Schottky band stays constant, the required frequency resolution can be relaxed by looking at the band of a higher harmonic. However, since the integral is constant the amplitude of the Schottky bands decreases for higher harmonic, resulting also in a reduced SNR. Another important limitation of an intensity measurement using the Schottky noise is that this does not allow for an absolute calibration, what compromises the measurement accuracy.

The AD beam intensity is measured by a longitudinal-Schottky (Schottky) monitor, using a wide-band (20 kHz to 30 MHz) ultra-low-noise AC beam transformer pickup, but this presents some performance limitations due to the low intensity of the circulating beams [34, 40]. During the debunched beam phases the intensity is measured by integrating the total power in one of the Schottky noise bands, which is proportional to

N. This measurement can be considerably degraded, even by very small coherent contributions from residual longitudinal structure in the beam resulting for example from small signal that may be present in the RF cavities, what will distort the measurement by introducing baseline perturbations. During the bunched beam phases the intensity is obtained from analysing the coherent Fourier frequency components occurring at the revolution frequency harmonics. The amplitude of the coherent components will depend on the longitudinal bunch shape, hence this must be taken into account when estimating the beam intensity and this will also introduce significant errors in the measurement.

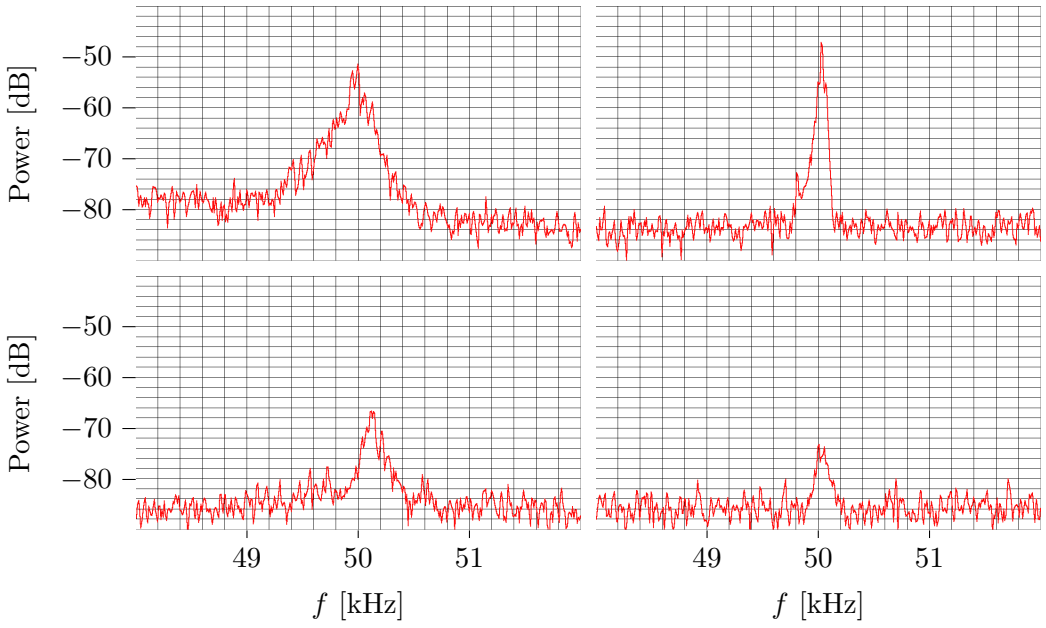

FIGURE 1.10: Examples of Schottky spectra during the four momentum plateaus in the AD cycle, after being down-mixed by a local oscillator of variable frequency such that the central frequency of the Schottky band is always at 50 kHz. Top-left: 3.5 GeV/c; Top-right: 2.0 GeV/c; Bottom-left: 300 MeV/c; Bottom-right: 100 MeV/c.

The measurement obtained with the Schottky monitor during a typical AD cycle is shown in Figure 1.11, in which the measurement points during the debunched phase are shown in red and the measurement points during the bunched phase are shown in black. The measurement during these two phases works in a fundamental different way.

Measurement of debunched beam:
During the debunched beam the Schottky noise is analysed using power spectral density of a Schottky band like the ones in Figure 1.10. Despite the optimisation and matching of the analysed Schottky band to the pickup sensitivity, the obtained Schottky noise spectrum presents a limited SNR, as shown in Figure 1.10 for different instants during each momentum plateau. The beam intensity measurement is proportional to the total power in the Schottky noise band, and is obtained by integrating measured power spectrum. To properly account only for the Schottky noise power the noise floor needs to be known. Any fluctuations and asymmetries in the noise baseline, due for example to a remaining RF longitudinal modulation of the beam, as can be observed in the

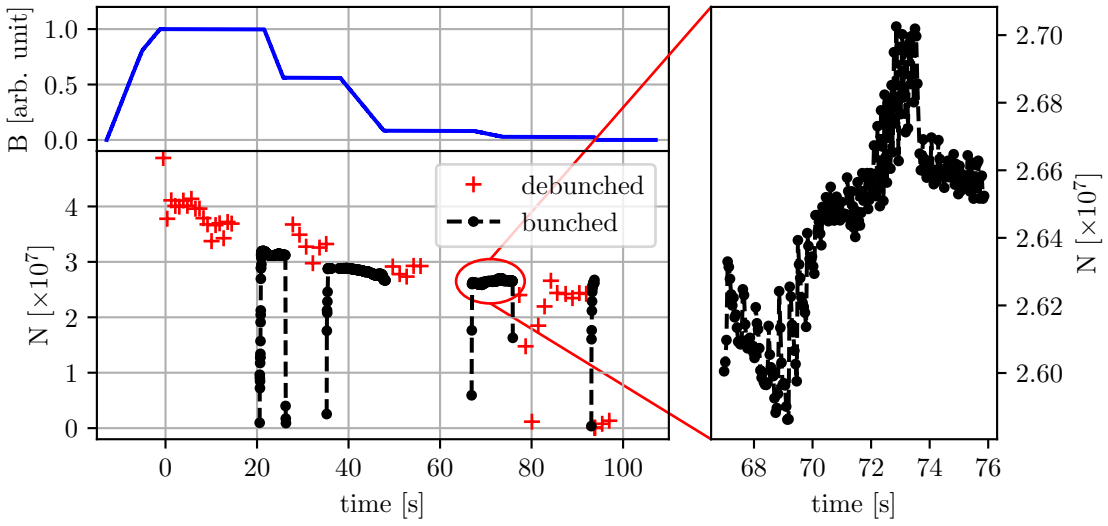

FIGURE 1.11: Measurement of the AD beam intensity from the analysis of Schottky spectrum during debunched phases (red crosses), and from the analysis of Fourier coefficients of the coherent components during the bunched phases (black dots). The top-left plot shows the magnetic cycle; the bottom-left plot shows the number of $\overline{p}$s throughout the entire cycle; and the right plot shows a zoom-in of the measurement during the third deceleration ramp.

top-left plot of Figure 1.10, will significantly perturb the intensity measurement. The obtained measurement resolution and accuracy is low with errors $\geq 10\,\%$, even with a low time resolution of $\approx 1.4\,\mathrm{s}$ [41]. An example of the intensity measurement during the debunched beam phases is shown by the red crosses in Figure 1.11. It is visible the high dispersion of the measurement points, and also that these are not entirely compatible with the intensity values measured during the bunched phases.

Measurement of bunched beam:

During the bunched beam phases, the measurement does not rely on the analysis of the Schottky noise, and hence is not a real Schottky measurement although it is processed through by the same hardware. In the present thesis both measurements will be referred to as being produced by the same Schottky monitor. The bunched beam intensity measurement relies on the analysis of the amplitude of the Fourier components at certain harmonics. It is assumed that the bunch current profile has the shape of a parabola, for which a template Fourier series is computed which has two free parameters: bunch amplitude and width. The coefficients of the truncated Fourier series for this signal are calculated and fitted with the observed amplitudes, and from this it is possible to derive the bunch length and current amplitude parameters. The total number of charges is then easily derived from these two values. The intensity resolution during the bunched phases is on the $\approx 1\,\%$ level, but there is a strong systematic error caused by deviations of the longitudinal bunch shape from the assumed parabolic shape. The error of this measurement can be of the order of $10\,\%$, and the time resolution is $1\,\mathrm{ms}$. In

the measurement in the left-hand side of Figure 1.11 it is clearly visible that during the initial bunching process the measurement is strongly dependent on the bunch length. The right-hand side of Figure 1.11 shows a zoom-in of the measurement in the third deceleration ramp, where an increase in the signal is measured. No new $\overline{p}$s (or other negatively charged particles) can be created during the cycle, and this increase in the signal is due to the changing of the bunch shape during the beam cooling process, deviating from the modelled parabolic bunch shape. The accuracy and time resolution of the debunched measurement is better than the one obtained during the debunched phases. However, the dependency on the longitudinal bunch shape introduces errors of $\approx 5\,\%$ [41].

The absence of absolute calibration procedure also limits the overall accuracy of the Schottky intensity measurement. Despite these limitations, this monitor has enabled routine operation of the AD over many years. The Schottky does not measure the beam current, but this can be derived from the number of particles. Assuming errors of $\approx 10\,\%$ in the intensity Schottky measurement at the last plateau of the AD cycle corresponds to a current error of $\gtrsim 100\,\mathrm{nA}$.

One possibility for improving the Schottky noise measurements is to increase the pickup sensitivity and SNR, therefore increasing the measurement resolution, with a resonant pickup cavity. Cavities with high quality factors have been used to measure beams with intensity as low as $10^1\,\overline{p}$ (beam current $50\,\mathrm{pA}$) [42], and more recently even measurement of single-ion beams have been demonstrated [43]. But in order to achieve these high sensitivities the pickup cavities need to be narrowly tuned to a very precise revolution frequency, while broad band pickups, required for tracking particles at different energies and de/acceleration phases, are much more limited in their SNR.

Besides the beam intensity measurement, transverse Schottky monitors are also used sometimes to measure beam emittance, tune and chromaticity [37, 38]. Schottky noise analysis is also an important measurement device to monitor action of the stochastic beam cooling technique [25].

1.3 Cryogenic Current Comparators

In order to improve the resolution of the beam current measurement obtained by probing the induced magnetic field, as in the case of the DCCT, one can consider using more sensitive magnetic sensors. The measurement of the low-intensity magnetic fields induced by the low-intensity $\overline{p}$ beams in the AD, which as seen in Section 1.2.1 can be $\leq 1\,\mathrm{pT}$, requires very sensitive magnetometers. The most sensitive magnetic measuring instruments available today are DC Superconducting QUantum Interference Devices (SQUIDs) made from Low-Temperature Superconductors (LTS) such as niobium [44].

Commercially available instruments have a noise floor of (1-10) $\mu\phi_0/\sqrt{\text{Hz}}$ [4] for the magnetic flux. Which for a sensing area of $1\,\text{mm}^2$ corresponds to (1-10) $\text{fT}/\sqrt{\text{Hz}}$ of the magnetic field. These numbers correspond to an energy resolution of $10^{-32}\,\text{J/Hz}$, or $\leq 10\,\hbar$ (where $\hbar$ is the reduced Planck constant) which is very close to the quantum limit [45, 46]. However, the resolution of a bare SQUID magnetic sensor does not provide with sufficient resolution to measure the lowest beam currents in the AD with a good resolution power. External perturbations which are always present in an accelerator environment, also contribute to additional performance degradation. Also, when measuring the magnetic field induced by an electric current, the spatial arrangement between the field sensor and the current path will affect the obtained measurement. In the design of a current and intensity monitor for a beam of particles, all of these aspects are of crucial importance. CCC measuring devices combine the resolution power of SQUID sensors with the magnetic shielding properties of Superconducting (SC) structures to overcome these problems.

The CCC was first developed by Harvey in 1972 [47] for the precise measurement of DC current ratios in metrology systems. Modern versions of this device are routinely used in electrical metrology laboratories for the precise comparison of electrical resistances with relative uncertainty of only $\sim 10^{-9}$, covering a resistance range from $100\,\mu\Omega$ to $1\,\text{G}\Omega$ [48]. These are also used for the amplification of extremely small electric currents.

A first proposal for utilising SQUID devices to measure beam current in a particle accelerator was made by Kuchnir at Fermilab [49]. Afterwards, the CCC was adapted and optimised for the measurement of particle beam currents by Peters *et al.* at GSI [50, 51] and Tanabe *et al.* at INS [52]. At DESY, Vodel *et al.* [53–56], have used a CCC to measure electron dark currents from SC RF accelerating cavities. Other groups, including Hao *et al.* [57] and Watanabe *et al.* [58], have developed CCC devices using High-Temperature Superconductors (HTS) superconductors. These projects have shown the principle ability of CCC devices and SQUID to measure beam currents with a nA resolution for the case of LTS CCCs, and 100 nA in the case of HTS devices. However, these implementations also suffered from issues concerning sensitivity to mechanical vibrations, EMI perturbations or limited availability. Furthermore, these early setups were only used to measure coasting beams or slowly extracted beams, usually from transfer lines of accelerators, where the induced beam signal presented a reduced slew rate, and were unable to measure short bunched beams presenting a high current slew rate.

The CCCs shown in Figure 1.12 work by measuring the magnetic flux induced by the beam current. This is contrary to the room temperature BCT which is only sensitive to the time-varying flux. The magnetic flux is concentrated in a high-permeability ferromagnetic pickup core, from which it is coupled into a SQUID by means of an SC coupling circuit. Both the coupling circuit and SQUID are placed inside a SC magnetic

[4] The quantity ϕ_0 is the magnetic flux quantum and its value is $2.067\,833\,83 \times 10^{-15}$ Wb.

shield cartridge. A SC magnetic shield structure around the pickup-core, as described in [51, 59, 60], renders the coupled magnetic field nearly independent of the beam position and attenuates external magnetic field perturbations. Figure 1.12 shows the general geometry of both the LTS and HTS prototypes that have been developed and used for measuring beam currents. The HTS materials available today are ceramics that are hard

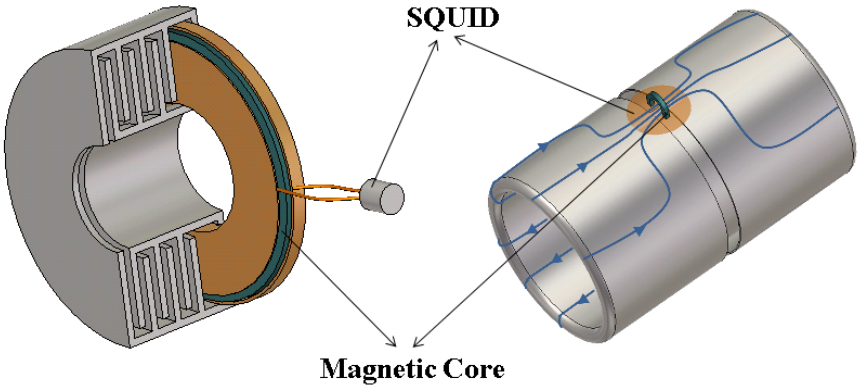

FIGURE 1.12: Schematic of two different CCC systems [61]. Left: a LTS version; Right: HTS version. The SC magnetic shields are shown in grey.

to manufacture into complex shapes, hence the much simpler shielding geometry shown in Figure 1.12. In addition it is difficult to form and connect HTS SC wires. Given these limitations the HTS CCC devices developed to date are based on a straight cylindrical tube of superconductor for shielding, with the SQUID sensor located directly on top of the cylinder as shown in Figure 1.12. To maximise the coupling of the magnetic field created by the mirror current to the sensor, a superconductor bridge pattern is created in order to concentrate the total current under the SQUID pickup coil. A small ferromagnetic core can also be used to increase the magnetic flux in the SQUID pickup coil. However, problems due to the finite length of the shielding tube, shielding from external sources and insufficient magnetic coupling to the SQUID detector, still limit the performance of these devices when compared with the LTS version [58, 62].

A comparison of the typical performance parameters of the previously discussed beam current and intensity monitors is presented in Table 1.2. The LTS CCC devices

Type	Resolution [µA]	Bandwidth
BCT	100	10 Hz to 1 GHz
DCCT	1	DC to 30 kHz
Schottky	0.1	DC to Hz
CCC (HTS)	0.1	DC to 10 Hz
CCC (LTS)	0.001	DC to 10 kHz

TABLE 1.2: Current resolution and bandwidth comparison of different beam current and intensity monitors [24, 33, 34, 50, 58, 63].

developed to date are the only non-perturbing intensity monitors which have achieved

the current resolution required to measure the AD beam with a high degree of accuracy. Hence this was the type of device that was selected to be used and further developed in the framework of this PhD project.

1.4 Requirements for a New Intensity Monitor in the AD

This project aimed at developing a low-intensity beam current and intensity monitor based on the CCC, optimised for the specific environment of the AD at CERN. This device should present considerable improvement over the existing Schottky detector, which should translate into an intensity measurement resolution at the 1 % level. Since the lowest expected number of $\overline{p}$s is 1×10^7 and considering the revolution frequency at ejection in Equation 1.2, results in a current resolution of at least 3 nA. Additionally, the measurement bandwidth should go from DC to at least 1 kHz. Below is a list of the requirements which guided the development of the project.

- Absolute measurement of bunched and debunched beams in AD
- Intensity resolution: $\leq 1 \times 10^5\,\overline{p}$
- Current resolution: $\leq 3\,\mathrm{nA}$
- Full range measurement: 300 nA to 12 µA
- Bandwidth: DC to 1 kHz
- Calibration with a precision current source
- Adapted to the AD environment and space constraints
- Stand-alone and continuous cryogenic operation

This project was developed in a collaboration between The University of Liverpool, CERN, the GSI Helmholtz Centre for Heavy Ion Research and the Friedrich Schiller University. The project was coordinated by the CERN Beam Instrumentation group and received extensive support from the Mechanical and Materials Engineering, and the Cryogenic groups.

1.5 Conclusion

This chapter introduced the low-energy antiproton experiments in the AD at CERN, which is currently the only antiproton synchrotron decelerator in the world. The ALPHA, AEgIS, ASACUSA, ATRAP and BASE experiments aim at studying the symmetry between antimatter and normal matter, in order to probe the fundamental physics of elementary particles. Most of these studies are based on synthesising antimatter atoms, such as anti-helium, to measure e.g. the $\overline{p}$ mass to charge ratio, or its coupling to the gravitational field. The $\overline{p}$s are produced with $E_K \approx 2.75\,\mathrm{GeV}$, but the experiments

can only trap particles with $E_K \lesssim 10\,\text{keV}$. The AD is used to decelerate the produced $\overline{p}$s down to 5.3 MeV, with further deceleration being done with metallic foils. In order to maximise the number of $\overline{p}$s delivered to the experiments, the AD needs to decelerate them with minimal losses. This is accomplished in a sequence of deceleration and beam cooling phases, to reduce the beam emittance, in a cycle with total duration of $\approx 100\,\text{s}$. A continuous measurement of the $\overline{p}$ beam during the AD cycle is essential to optimise the entire process. However, standard beam diagnostics are not able to provide an accurate measurement due to the low intensity of the circulating $\overline{p}$ beam, which can in some cases be smaller than 300 nA. Currently, the available intensity measurement is provided by Schottky monitor, but this presents strong accuracy limitations, and a low time resolution. Providing a continuous measurement of the $\overline{p}$ beam current and intensity throughout the entire AD cycle using an operations ready diagnostic is the objective of this project.

The SQUID-based CCC was developed for the precision measurement of electrical currents, and later adapted to measure particle beam currents. These are SC devices that measure the magnetic field proportional to the current amplitude, independently of the beam's spatial distribution. CCCs use a SC shield to isolate the azimuthal field component (proportional to the beam current) from all other field components (which are position dependent), including external magnetic perturbations. Both LTS and HTS prototypes have been developed, but only LTS ones have been able to achieve a resolution in the nano-ampere range, while HTS devices are until now limited to $\approx 100\,\text{nA}$. Based on this, it was decided to pursue the development of a LTS CCC for the AD, with the following requirements: Measurement of the full dynamic range of the AD average currents, from 300 nA to 12 µA, with a 1 % resolution, and a 1 kHz bandwidth. Measurement of the beam intensity with $1 \times 10^5\,\overline{p}$ resolution. Measurement of both the debunched and bunched beam, with shortest bunches with length $4\sigma_t = 30\,\text{ns}$, with equal performance. The reliability and high availability of the monitor was also needed in order to have an operational device. For this, a stand-alone cryogenic system with reduced maintenance was also required.

Chapter 2

Theoretical foundations of the CCC monitor

This chapter covers the basics of the elementary and macroscopic properties of superconductivity that are necessary to understand the different components of the CCC monitor. It starts with a description of the superconductivity phenomenology in Section 2.1. In Section 2.2 a brief mathematical overview of the fundamental superconductivity phenomena are laid out. The main superconductivity effects of interest are explained under this theoretical framework, including the Meissner-Ochsenfeld which is the basic principle behind the CCC magnetic shield, and the flux quantisation which is behind the SQUID sensor behaviour. Section 2.3 introduces the Josephson junctions, and analyses its dynamic behaviour culminating in voltage to current model, which is modulated by external magnetic fields. Josephson junctions are the building blocks of SQUID sensors, which are described in Section 2.4. The section proceeds to explain how can SQUIDs be used as magnetic sensors, and introduces the Flux-Locked Loop (FLL) electronic readout scheme as technique for linearising the SQUID transfer function. Section 2.5 provides an explanation of the functioning of the SC hollow cylinder as shielding structure, and continues with a concise overview of more elaborate geometries. The chapter concludes by presenting the performed magnetostatic simulations of the shielding geometry used in this project.

The following books and review article were used as references for this chapter [64–67].

2.1 Basics of superconductivity phenomenology

All SC materials observe the following properties: below a certain critical temperature and critical magnetic field their electrical resistance to DC vanishes, and magnetic fields are expelled from the interior of the material. It is known today that superconductivity is a widespread phenomenon, showing up at different critical temperature ranges, for many of the metals of the periodic table as well as more complex materials. Also, the SC state reveals itself through other phenomena besides perfect conductivity and perfect

diamagnetism. In general superconductors can be categorised according to the following criteria:

- Response to a magnetic field $\boldsymbol{B}$: Type-I (or soft) superconductors exhibit a single critical magnetic field $B < B_{c1}$ above which all superconductivity vanishes, while Type-II (or hard) superconductors show two critical temperatures. They behave exactly the same as Type-I for $B < B_{c1}$, and show a mixed state where a magnetic field is allowed to penetrate in the material while maintaining perfect conductivity for $B_{c1} < B < B_{c2}$.

- Critical temperature T_c: Depending on the temperature below which a material becomes SC they may be classified as LTS or HTS. The critical temperature LTS is below 30 K, while HTS have a critical temperature above 30 K. Other classifications consider the split temperature to be 77 K, since this is the boiling point for liquid nitrogen, enabling HTS to be cooled down with liquid nitrogen, which is more feasible than using liquid helium, as usually done for LTS. Usually LTS are Type-I superconductors (niobium is an important exception since it is both a LTS and Type-II), while all HTS are Type-II.

- Microscopic theory: "conventional" superconductor physics is successfully explained at the microscopic level through phonon-mediated interaction of the electrons by the Bardeen Cooper Schrieffer (BCS) and related theories, while at present there is no theoretical framework that fully describes the "unconventional" superconductors. Most "conventional" superconductors are Type-I.

- Type of material [68]: These may be pure elements, where metals are usually Type-I superconductors at ambient pressure, while non-metal elements become SC only at very high pressures. Many metal alloys are also superconductors and almost always of Type-II (only known exception is $TaSi_2$). Almost all known HTSs are ceramic materials from two families, cuprates and iron-based pnictide compounds. The simpler compound MgB_2 has also been found to be a HTS ($T_c = 39$ K), while at the same time behaving as a "conventional" superconductor.

For the rest of this thesis only LTS will be considered. Although superconductivity reveals many of its properties as a macroscopic collective phenomenon, it can only be explained in the frame of quantum mechanic interaction between electrons and ions in the crystal lattice of the material. The superconducting electrons are able to travel through the material without any resistance by occupying a quantum state that forbids the interaction ("collision") of these with the ions in the material.

The first well established theoretical model providing a phenomenological description was the London brothers' theory proposed in 1935 [69]. This purely classical theory assumed the existence of SC electrons that travel inside the superconductor materials as free electrons, without interacting with the crystal lattice, subject only to the effect

of the electric and magnetic fields. The London equations greatest success was the description of the Meissner-Ochsenfeld.

In 1950, Landau-Ginzburg proposed a more profound phenomenological theory that combined Landau's theory of second-order phase transitions with a Schrödinger wave-like equation, which was able to explain the difference between Type-I and Type-II superconductors [70].

2.1.1 Perfect conductivity

It was first observed by Kamerlingh Onnes [71, 72] that when mercury was cooled below a certain threshold temperature a phase transition occurred that led to an abrupt decrease of the electrical resistance by at least 14 orders of magnitude[1]. The plot in Figure 2.1, from Onnes original publication, shows his measurement of the electric resistance versus temperature for mercury, with the SC transition at 4.20 K. Precision measurements of

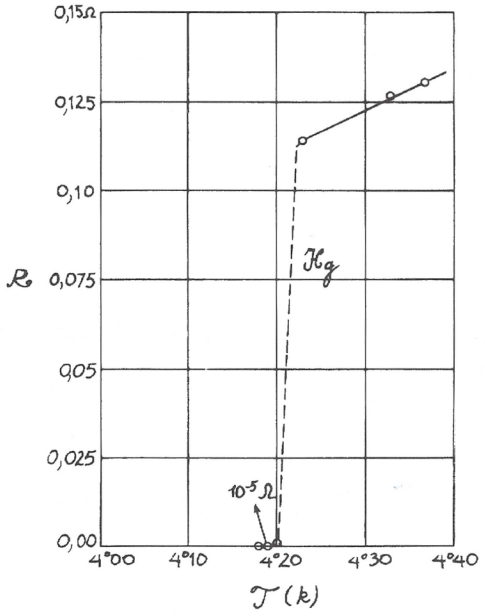

FIGURE 2.1: Historic plot of resistance (Ω) versus temperature (° K) for mercury measured by Kamerlingh Onnes in 1911 [71]. The SC transition happens at 4.20 K, within 0.01 K, when the resistance jumps to an unmeasurable small value (at least 10^7 times smaller). Adapted from [66].

the transition temperature of very high purity samples of niobium indicate transition widths of 0.3 mK around a critical temperature $T_c = (9.288 \pm 0.002)$ K, which reveals to be very stable [74].

The first superconductors to be discovered were pure metals and metal alloys. The most commonly used LTS are: pure Nb, pure Pb, and the alloys NbTi and Nb_3Sn. In order to reach the low transition temperatures of these materials, liquid helium is

[1]More recent direct resistivity measurements allow to measure that this is at least 17 orders of magnitude smaller than the resistance of copper at room temperature [73].

the most commonly used, which always represents considerable cost and an experimental limitation. During the second half of the 1980s the first cuprate (copper-oxide) HTSs were discovered. This sprung a new interest in superconductivity research and resulted in the discovery of materials that have critical temperatures above the liquid nitrogen transition temperature, from which the most promising are $YBa_2Cu_3O_7$ and $Bi_2Sr_2Ca_2Cu_3O_{10}$. However, these new HTS materials are ceramic materials with complex crystalline structures which are usually difficult to produce. Being brittle materials, it is almost impossible to form these into wires or complex bulk geometries [75]. This represents a strong limitation in the fabrication of SC magnetic shields and coupling circuit for the CCC monitors.

2.1.2 Meissner-Ochsenfeld effect

Materials in the superconducting state have zero electrical resistance, similar to perfect conductors for which the resistivity $\rho = 0$. This is, however, not sufficient to explain the SC behaviour. In 1933 Meissner and Ochsenfeld [76] found that under appropriate conditions a material in the SC state completely expels the magnetic field from its interior. This happens if the magnetic field is applied after the element is already in the SC state, as would happen in a perfect conductor due to the action of screening eddy currents, but more surprisingly, they also observed that the same happens if the magnetic field is statically applied before it goes through the SC phase transition. In the latter case the expulsion of the magnetic field occurs exactly when the sample is cooled below T_c. The difference in behaviour between perfect conductors and superconductors going through their phase transitions is shown in Figure 2.2. Meissner and Ochsenfeld

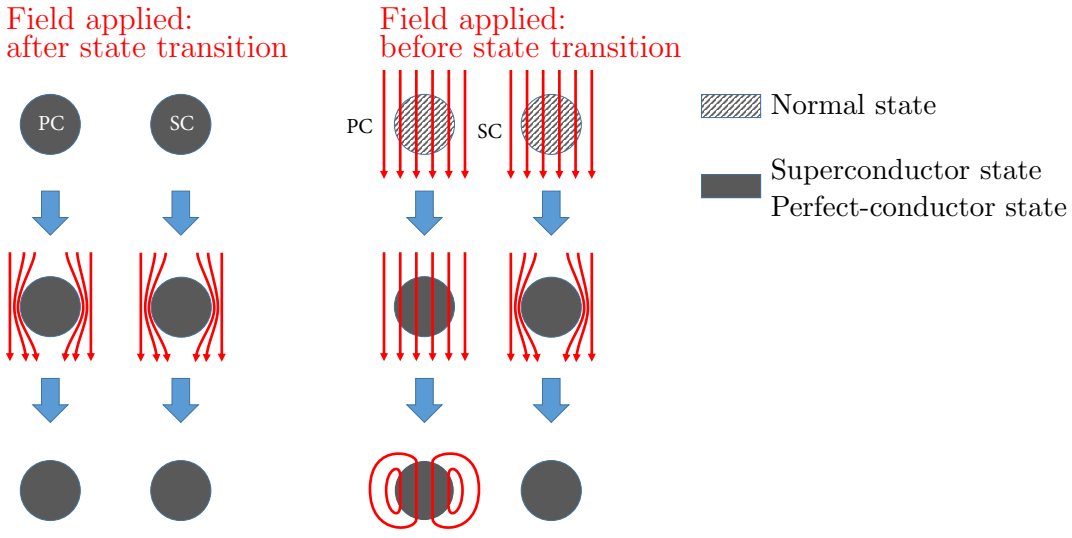

FIGURE 2.2: Response to a magnetic field of between a perfect conductor and a superconductor going through the state transition.

also observed that applying a strong magnetic field above a certain threshold critical

field B_c (dependent on the temperature), the superconductivity state was destroyed and the material returned to its normal state.

2.2 The macroscopic wavefunction and London's theory

Understanding of the microscopic interactions that give rise to the properties of "conventional" superconductors was first possible with BCS theory proposed by Bardeen, Cooper and Schrieffer in 1957 [77], after important contributions from Fröhlich [78].

The fundamental ideas behind the BCS theory are: 1) the effective forces between electrons in a solid can sometimes be attractive rather than repulsive due to coupling between the electrons and the phonons (quantum mechanical description of the vibration modes) of the underlying crystal lattice; 2) under certain conditions this interaction is able to bind electrons in a stable bounded pair state of charge $q_s = 2e$ and mass $m_s = 2m_e$, a so called Cooper pair [2]; 3) all the superconducting electrons forming Cooper pairs can be described by a many-particle coherent wavefunction similar to those arising in the scope of superfluidity and Bose-Einstein Condensates.

The description of the superconducting electrons by a coherent wavefunction is possible because the Cooper pairs form a singlet state with zero spin and thus behave in many aspects like bosons. Unlike fermions, which obey the Pauli exclusion principle, multiple bosons can occupy the same quantum energy state. At sufficiently low-temperatures these tend to form a large Bose-Einstein condensate, where a large fraction of the Cooper pairs occupy the lowest energy quantum state. Thus, the many electron-pairs tend to lock their phases coherently, and this coherence persists over the macroscopic scale of the superconductor. This electron-pair condensate can be described by a macroscopic many-body quantum wavefunction $\Psi(\boldsymbol{r}, t)$, which is the spatial average of the many coherent wavefunctions of individual pairs. See for example [66, 79] for more details.

The energy of the Cooper pair bound state is very weak, of the order of $1 \times 10^{-3}\,\mathrm{eV}$ and can be easily broken by thermal vibrations of the material lattice nucleus. This is the reason why superconductivity only emerges at very low-temperatures.

If the macroscopic wavefunction Ψ describes the ensemble of SC electrons, then, with appropriate normalisation $|\Psi|^2 = n_S(\boldsymbol{r}, t)$, where n_s is the local density of superconducting charges, and

$$\Psi(\boldsymbol{r}, t) = \sqrt{n_s(\boldsymbol{r}, t)} e^{i\theta(\boldsymbol{r}, t)}, \tag{2.1}$$

where $\theta(\boldsymbol{r})$ is the phase of the wavefunction. The below equations, called London's equations, were derived following [66].

When the electric field $\boldsymbol{E}$ and the magnetic field $\boldsymbol{H}$ are weak, and since the relaxation time in most materials is typically very fast, of the order of 10 ps, the charge distribution can be assumed to be homogeneous, $n_s(\boldsymbol{r}, t) = \text{constant}$. This is one of the assumptions of the London theory of superconductivity.

[2] Surprisingly the formation of stable Cooper pairs is possible even for low values of the attractive force.

In the presence of an electromagnetic field, described by the vector potential $\boldsymbol{A}$, such that $\boldsymbol{B} = \nabla \times \boldsymbol{A}$, the classical canonical momentum operator for a particle of charge q_s, mass m_s and velocity v_s is

$$\boldsymbol{p} = m_s v_s + q_s \boldsymbol{A}. \tag{2.2}$$

Knowing that the canonical classical momentum $\boldsymbol{p}$ must be the result of computing the expectation value of the quantum mechanical momentum operator $\hat{\boldsymbol{p}} = -i\hbar\nabla$, one can write,

$$\langle \Psi | -i\hbar\nabla | \Psi \rangle = \boldsymbol{p}. \tag{2.3}$$

Resolving the left-hand side for Equation 2.1 and replacing the right side by Equation 2.2 one obtains,

$$\boldsymbol{p} = \hbar\nabla\theta = m_s \boldsymbol{v}_s + q_s \boldsymbol{A}. \tag{2.4}$$

Using Equation 2.4, the pair current density, given by $\boldsymbol{J}_s = n_s q_s \boldsymbol{v}_s$, can be written as

$$\boldsymbol{J_s} = q_s\, n_s \underbrace{\left(\frac{\hbar}{m_s} \nabla\theta(\boldsymbol{r}, t) - \frac{q_s}{m_s} \boldsymbol{A}(\boldsymbol{r}, t) \right)}_{v_s}, \tag{2.5}$$

where the expression in parentheses corresponds to the velocity v_s of the SC electron pairs. Applying the curl operator to both sides of Equation 2.5 results in the "second" London equation,

$$\boxed{\nabla \times \boldsymbol{J_s} = -\frac{1}{\Lambda} \boldsymbol{B}}, \tag{2.6}$$

where $\Lambda = m_s/(n_s q_s^2)$ is the London parameter. If the SC electrons are to behave as free particles inside the superconductor material, they should be subject to externally applied electromagnetic fields. Using the Lorentz force law together with the partial time derivative of Equation 2.5 it is possible to derive that,

$$\frac{\partial \boldsymbol{J_s}}{\partial t} = \frac{1}{\Lambda} \boldsymbol{E} - \frac{1}{2 n_s q_s} \nabla \left(\boldsymbol{J_s}^2 \right). \tag{2.7}$$

In the limit where $|\boldsymbol{E}| \gg |\boldsymbol{v_s}||\boldsymbol{B}|$, which is almost always the case in superconductors since strong magnetic fields break the superconductivity state and high kinetic energy of the SC electrons breaks the binding of Cooper pairs, the second term in Equation 2.7 can be ignored resulting in the "first" London equation,

$$\boxed{\frac{\partial \boldsymbol{J_s}}{\partial t} = \frac{1}{\Lambda} \boldsymbol{E}.} \tag{2.8}$$

When solving an electromagnetic problem in a normal material, the Ohm law $\boldsymbol{J} = \sigma \boldsymbol{E}$ is the constitutive relation required to close the Maxwell equations. In an SC medium the "first" London equation plays the role of the constitutive relation, describing electron-pairs as free particle, freely accelerated by electric fields as given by the Lorentz force.

2.2.1 Mathematical simplification of London equations

The electric and magnetic fields can be defined by the scalar and vector potential fields through,

$$\boldsymbol{E} = -\nabla\Phi - \frac{\partial \boldsymbol{A}}{\partial t}, \tag{2.9}$$

$$\boldsymbol{B} = \nabla \times \boldsymbol{A}. \tag{2.10}$$

The electric potential Φ and the vector potential $\boldsymbol{A}$ are defined in terms of their derivatives and so are not uniquely defined. These contain some redundant degrees of freedom which can be changed by a set of transformations without altering the physical $\boldsymbol{E}$ and $\boldsymbol{B}$ fields being described. This is called the gauge invariance of electromagnetic theory, and the allowed gauge transformations are

$$\boldsymbol{A} \rightarrow \boldsymbol{A} + \nabla\chi, \tag{2.11}$$

$$\Phi \rightarrow \Phi - \frac{\partial \chi}{\partial t}, \tag{2.12}$$

where χ is a scalar function. Such a transformation can always be performed without changing the physical results. An additional gauge fixing condition can be imposed by choosing χ, and this can be used to simplify the calculations.

It is possible to show that one can always find a gauge where $\nabla \cdot \boldsymbol{A} = 0$, and this condition defines the Coulomb gauge. The London gauge assumes, in addition to the Coulomb gauge, that the electric potential is constant inside a superconductor, which is valid in the low-field and low frequency regime. This implies that $\nabla\Phi = 0$. Assuming the London gauge in Equation 2.6 the "second" London equation can be written as

$$\boxed{\boldsymbol{J_s} = -\frac{1}{\Lambda}\boldsymbol{A}}. \tag{2.13}$$

2.2.2 Understanding the Meissner state

The greatest success of the London theory was the explanation of the observed exclusion of the magnetic field from the interior of Type-I superconductors. This is a result of superconducting currents flowing near the surface such that the resulting field inside the superconductor exactly cancels the applied external field. These currents flow on a thin surface layer described by the London penetration depth, and any change of the externally applied field will cause an immediate change of the screening to cancel the field. It was seen that assuming perfect conductivity is not sufficient to account for the exclusion of static magnetic fields from a superconductor, but London's "second" equation (Equation 2.13), does precisely this by allowing a current distribution to appear in the presence of a static magnetic field.

In the quasi-stationary limit where the electric displacement current is zero, Maxwell-Ampère law is simplified to $\nabla \times \boldsymbol{H} = \boldsymbol{J_s}$. Combining this with Equation 2.6, and using

the vector calculus identity for the curl of a curl, and since $\nabla \cdot \boldsymbol{H} = 0$, one obtains the following equations for $\boldsymbol{H}$ and $\boldsymbol{J_s}$,

$$\nabla^2 \boldsymbol{H} = \left(\frac{1}{\lambda_L^2}\right) \boldsymbol{H}, \tag{2.14}$$

$$\nabla^2 \boldsymbol{J_s} = \left(\frac{1}{\lambda_L^2}\right) \boldsymbol{J_s}, \tag{2.15}$$

where

$$\lambda_L = \sqrt{\frac{\Lambda}{\mu_0}} \tag{2.16}$$

is the London penetration depth. These correspond to the well-known Helmholtz equation for each vector component. The solutions of the magnetic field in the interior of SC materials therefore exhibit an exponential decay with characteristic length equal to λ_L. For the case of a superconductor occupying the half-space $x > 0$, and a parallel magnetic field applied at $x = 0$, the magnetic field and current in the interior of the superconductor, shown in Figure 2.3, are given by

$$B(x) \propto \exp\left(-x/\lambda_L\right), \qquad J_s(x) \propto \exp\left(-x/\lambda_L\right). \tag{2.17}$$

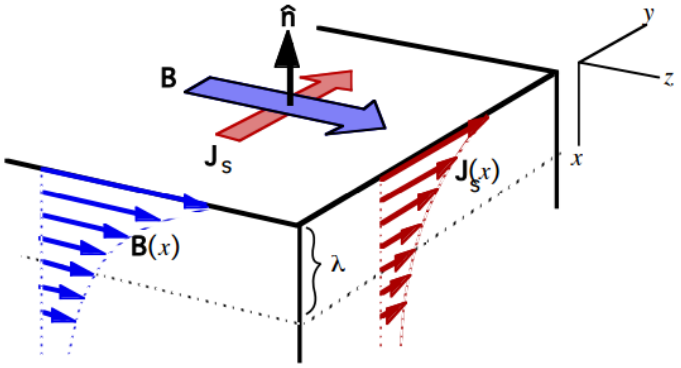

FIGURE 2.3: Attenuation of magnetic field inside a superconductor occupying the half-space $x > 0$, due to the Meissner-Ochsenfeld.

When the superconductor element has a cylindrical shape, the magnetic field and currents in the interior of the cylinder will depend on modified Bessel functions of the first kind.

When the macroscopic dimensions of the superconductor material are much bigger than λ_L, on can assume that the magnetic field is completely excluded from the interior of the superconductor material, and the response to an applied field is given by surface currents. This is called the bulk limit. The field distribution outside of the superconductor almost equally matches that caused by a perfectly diamagnetic material. Hence, this is also called the ideal diamagnetic limit.

2.2.3 Flux conservation and quantisation

Writing the line integral of the "first" London Equation in 2.8 along a contour C in a multiple connected region inside a bulk superconductor of Type-I, as shown in Figure 2.4, together with Maxwell-Faraday law in the integral form results in,

$$\frac{\partial}{\partial t}\left[\Phi_S + \oint_C \Lambda \boldsymbol{J} \cdot d\boldsymbol{s}\right] = 0. \tag{2.18}$$

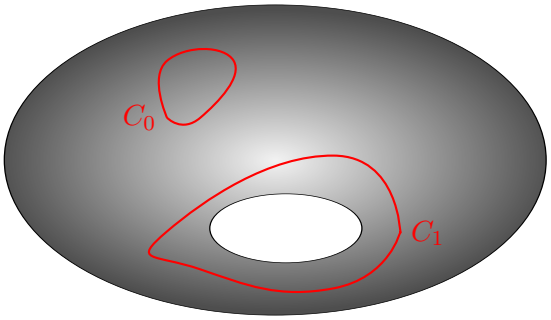

FIGURE 2.4: Superconductor sample with a multiple connected region. Path C_1 includes the multiple connected region in its interior, while path C_0 does not. The "fluxoid" traversing path C_1 is conserved as long as the sample is in the superconducting state.

For a contour within the superconductor where $\boldsymbol{J} = 0$, the total magnetic flux through the hole remains constant, and is thus conserved independently of any time varying external field, as long as the SC state is maintained. The resulting magnetic field in the region around a SC ring subject to different external magnetic fields is shown in Figure 2.5.

More than being conserved, the magnetic flux threading a multiple connected region of a superconductor is also quantised. This is a macroscopic quantum mechanical quantisation effect, and one of the most striking properties of superconductivity as it puts in evidence the existence of the long-range macroscopic wavefunction of the Cooper pairs condensate. Calculating the line integral of the SC current density defined in Equation 2.5 around the same multiple connected contour C_1, as shown in Figure 2.4, results in

$$\oint_{C_1} \Lambda \boldsymbol{J_s} \cdot d\boldsymbol{l} = -\oint_{C_1} \left(\boldsymbol{A}(\boldsymbol{r}, t) - \frac{\hbar}{q_s}\nabla\theta(\boldsymbol{r}, t)\right) \cdot d\boldsymbol{l}. \tag{2.19}$$

The first term on the right-hand side is simply the magnetic flux through C_1. The second term, although being the line integral of a gradient function over a closed path, it is not necessarily zero since $\theta(\boldsymbol{r}, t)$ is only defined in the interior of the SC element. However, the wavefunction, defined in Equation 2.1, must be single valued and so $\theta(\boldsymbol{r}, t)$ can only

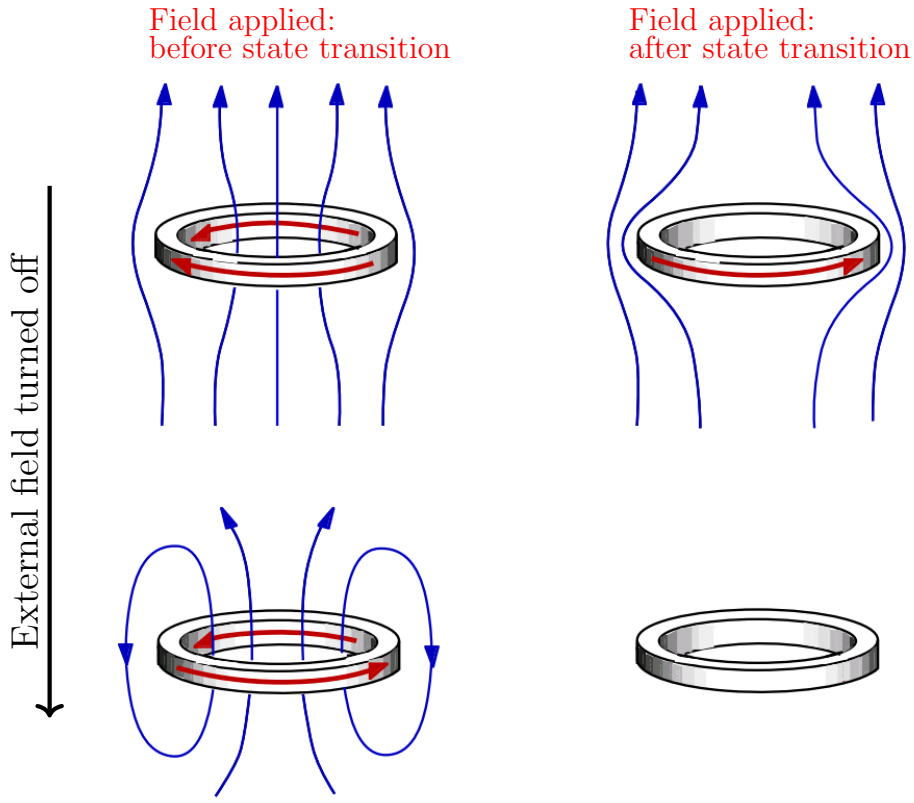

FIGURE 2.5: Different situations showing how an SC ring reacts to changes in the external magnetic field in order to keep the total flux through the ring constant. a) magnetic field is first applied when $T > T_c$ before the SC transition; b) initial conditions similar to previous case, but external field is turned off when $T < T_c$; c) initial magnetic field before SC transition is zero, and applied only after $T < T_c$.

vary by integer multiples of 2π when going around C_1. Hence, Equation 2.19 results in

$$\underbrace{\Lambda \oint_{C_1} \boldsymbol{J_s} \cdot d\boldsymbol{l} + \Phi_c}_{\text{fluxoid}} = \phi_0 n, \qquad \text{with} \qquad n = 0, 1, \ldots \tag{2.20}$$

where the flux quantum is [80],

$$\phi_0 = \frac{h}{2e} = (2.067\,833\,831 \pm 0.000\,000\,013) \times 10^{-15}\,\text{Wb}. \tag{2.21}$$

In a contour around a multiply connected region of a superconductor, the "fluxoid" defined in Equation 2.20, which is the sum of the flux penetrating the integration contour plus the line integral of the current density along the same contour is always a multiple of ϕ_0. When C_0 covers a simply connected region, as shown in Figure 2.4, the "fluxoid" will always be equal to zero, and one recovers the "second" London equation in its integral form.

In the bulk limit, where it is assumed that no current flows in the interior of the superconductor, it is possible to choose a contour such that the first term of the "fluxoid"

in Equation 2.19 is zero. In this limit case it is the flux alone that is quantised,

$$\Phi_C \equiv \int_C \boldsymbol{B} \cdot d\boldsymbol{s} = n\,\phi_0. \tag{2.22}$$

It should be noted that while the total flux resulting from externally applied magnetic fields plus the field created by shielding currents in the superconductor is quantised, the external magnetic fields can assume any continuous value.

This quantisation phenomenon is fundamental in the physics of many SC devices as is the case for the Josephson junctions and the SQUID.

2.3 Josephson junctions

Electron quantum tunnelling in metal junctions separated by a thin insulation layer is a well known effect, that is explained by the leakage of the electron wavefunction outside of the metal region. In 1962 Josephson predicted that a similar phenomenon should happen for Cooper pairs in weakly coupled SC junctions [81]. Since these are SC electrons, this should be possible even when no potential difference is applied across the junction. These junctions can be formed by a thin insulating layer, a short section of non-SC metal or a physical constriction that weakens the superconductivity, between two SC elements. Many different geometries and fabrication processes have been proposed for various Josephson junctions types. In the widely used Superconductor-Insulator-Superconductor junctions, shown in Figure 2.6, the current transport occurs via tunnelling of Cooper pairs and quasiparticles. Quasiparticles are a idealised theoretical particles resulting from approximating the complex microscopic behaviour interactions, occurring in a many-body system context, by the simpler behaviour of effective particles with properties that may differ from the original particles intervening at the microscopic level (e.g. conducting electrons in a metal are quasiparticles that effectively behave as normal free electrons but with a different mass). In superconductors these account for the electron and hole charge carriers resulting from the breaking up of superconducting Copper pairs.

Each SC electrode, on both sides of the junction, will have their own macroscopic wavefunction. If these are made of the same material, the electron-pair density n_s will be equal for both wavefunctions, but the phases θ_1 and θ_2 are allowed to differ. When the separation is small enough, a weak link is formed by the wavefunctions that penetrate the barrier sufficiently to couple to each other. This allows pairs to pass through without any energy loss establishing a current (the Josephson current) without any voltage drop $V = 0$.

As shown in Equation 2.5, the gauge invariant supercurrent density is proportional to the gauge invariant phase gradient, equal to $\boldsymbol{v}_s$, and the charge density n_s. In the case of a Josephson junction where there is a constriction to the supercurrent flow, the charge density in the barrier will be much smaller. But since the current density must be constant on both electrodes and on the junction, then the phase gradient will be

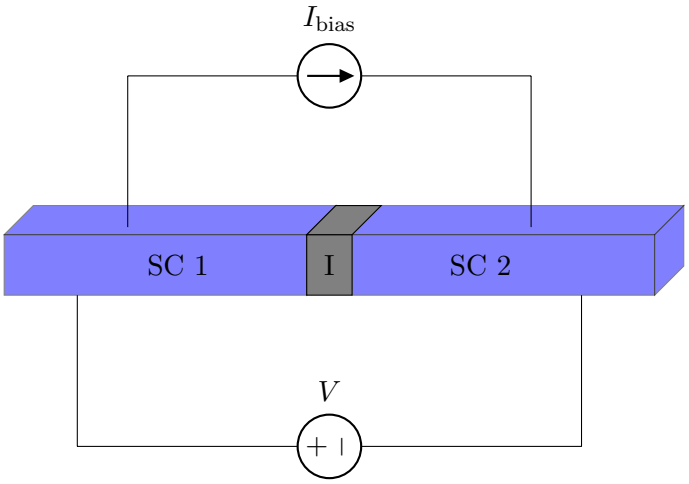

FIGURE 2.6: Schematic of a Josephson element formed by a SC-insulation-SC junction.

much larger in the junction. This sharp change in the phase at the junction allows us to define a macroscopic gauge invariant phase difference given by,

$$\gamma(t) = \theta_2(t) - \theta_1(t) - \frac{q_s}{\hbar}\int_1^2 \boldsymbol{A}(\boldsymbol{r},t)\cdot d\boldsymbol{l}. \tag{2.23}$$

The Josephson current shall obey the following conditions 1) be a function of γ; 2) be zero in case the phase difference is also zero; 3) any variation by 2π of γ should maintain the wave functions unchanged. Under these assumptions it can be demonstrated that that this current is given by the first Josephson equation,

$$\boxed{I_s = I_c \sin\gamma,} \tag{2.24}$$

where the constant I_c is the critical current. Equation 2.24 says that if there is a vector potential or voltage applied across the junction, the phases become locked. In this case γ = const. and a constant SC current develops bounded to the values of $|I_c|$. At low temperatures, the critical current density is typically in the range (10^2-10^4) A/cm^2. For a junction area of 10 µm^2, this results in a critical current in the range (10-100) µA.

Tunnelling of Copper pairs does still occur when a voltage V is applied across the junction, but in this case the wavefunctions phases are not locked anymore. Instead, their γ changes at a rate proportional to the voltage, as given by the second Josephson equation,

$$\boxed{\frac{\partial\gamma}{\partial t} = \frac{q_s}{\hbar}V} = \frac{2\pi}{\phi_0}V. \tag{2.25}$$

Solving this equation shows that when a constant voltage is applied, an oscillatory current develops across the junction,

$$\gamma = \gamma_0 + (2\pi V/\phi_0)\ t, \tag{2.26}$$

$$I = I_c \sin\left(\gamma_0 + 2\pi\, f\, t\right). \tag{2.27}$$

This is the so called AC Josephson effect. The value of this voltage dependent frequency is

$$f = \frac{1}{\phi_0} V. \tag{2.28}$$

Since $\phi_0^{-1} = 483.6\,\mathrm{MHz/\mu V}$, this frequency falls for most practical cases in the microwave regime. This allows Josephson junctions to be used as voltage controlled oscillators in the GHz and THz regime. And the fact that voltage and frequency are related by the fundamental constants e and h opens the possibility for Josephson junctions to be used as voltage standards.

2.3.1 Response to an external magnetic field

The critical current I_c is the main parameter in a Josephson junction. But this is not a constant value and it changes in the presence of a magnetic field. It can be shown that any magnetic field applied in the plane transverse to the junction direction will modulate the critical current I_c in such away that

$$I_c(\phi) = I_c(0) \left| \frac{\sin(\pi\Phi/\phi_0)}{(\pi\Phi/\phi_0)} \right|. \tag{2.29}$$

This dependency gives rise to the Josephson-Fraunhofer interference pattern that is shown in Figure 2.7

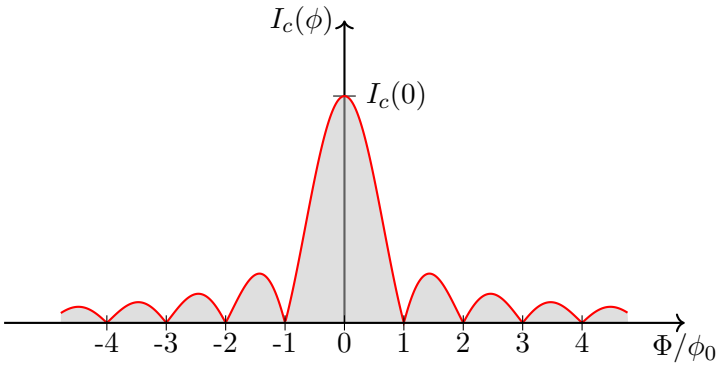

FIGURE 2.7: Modulation of the critical current as a function of the applied magnetic flux. The shaded grey area indicates the allowed region for the Josephson supercurrent.

In principle, this dependence of critical current of a single junction on the magnetic flux could be used to perform measurements of the magnetic field. But since the area of the Josephson junction A_J is in general small, the sensitivity to the magnetic field of such a device would also be small since $|\boldsymbol{B}| = \phi/A_J$.

2.3.2 I-V characteristic of Josephson junctions

The tunnelling of Cooper pairs across a Josephson junctions described by the Josephson equations gives rise to the SC current I_s. However, this is not sufficient to describe a real device, and it is necessary to also take into account the tunnelling current of

Quasi-particle (QP) at finite voltages I_{qp}, as well as a displacement current I_d across the insulation layer, acting as a dielectric in a capacitor.

There are two mechanisms leading to the generation of QPs. Above 0 K there is a probability for the Cooper pairs to brake up due to thermal excitation, or by externally applying some energy to the circuit e.g. through a voltage. The properties of these un-paired electrons mixed with the Bose-Einstein condensate however differs from that of normal conducting electrons. Hence, the quasi-particles current depends in a complicated way on the voltage V. However, if V is kept small these can still be treated as normal electrons forming an ohmic current flow [66].

The separation between the two SC electrodes also works like a capacitor with the insulation barrier being the dielectric. This gives rise to a displacement current that can be approximated by the current flowing through a linear capacitance I_d.

The capacitively-shunted junction (RCSJ) model, first proposed by the Stewart and McCumber [82, 83], is a lumped-element model that takes into account these three current contributions. Under certain assumptions [64], the dynamic behaviour and the Current-to-Voltage (I-V) characteristic of a Josephson tunnel junction can be accurately described by this model. The RCSJ model consists of a circuit element obeying Equations 2.24 and 2.25 through which flows a current I_s, corresponding to an ideal Josephson junction connected in parallel with a resistance R, accounting for I_{qp}, and a capacitance C modelling I_d. The most import simplification of the model is the assumption of a linear R. It also assumes a point-like junction and overlooks any spatial dependencies. The electrical schematic of the RCSJ model is shown Figure 2.8 with the different currents I_s, I_{qp} and I_d flowing through each branch element.

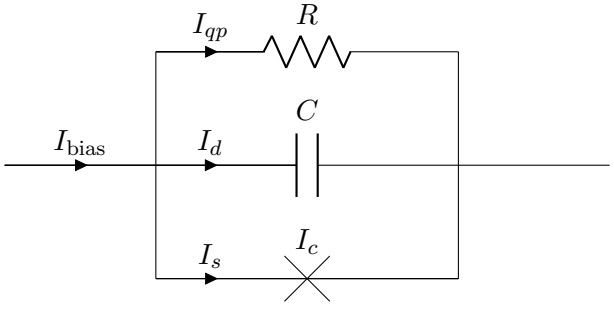

FIGURE 2.8: Lumped element RCSJ model of a real Josephson junction.

Using the second Josephson Equation 2.25, and writing the expression for the total current flowing across the junction, it is possible to write a second order non-linear differential equation for the dynamics of the phase difference γ that governs the behaviour of the junction,

$$I = I_c \sin\gamma + \frac{1}{R}\left(\frac{\phi_0}{2\pi}\right)\frac{\mathrm{d}\gamma}{\mathrm{d}t} + C\left(\frac{\phi_0}{2\pi}\right)\frac{\mathrm{d}^2\gamma}{\mathrm{d}t^2}. \tag{2.30}$$

This equation can be simplified by writing it in terms of the dimensionless variables $i = I/I_c$, $v = V/(I_cR)$, $\tau = t/\tau_c$, and defining the parameters β_c and τ_c,

$$\beta_c = \frac{2\pi I_c R^2 C}{\phi_0}, \tag{2.31}$$

$$\tau_c = \frac{\phi_0}{2\pi I_c R}. \tag{2.32}$$

Using these transformations, Equation 2.30 is rewritten as,

$$i = \sin\gamma + \frac{\mathrm{d}\gamma}{\mathrm{d}\tau} + \beta_c \frac{\mathrm{d}^2\gamma}{\mathrm{d}\tau^2}, \tag{2.33}$$

where β_c is the Stewart-McCumber parameter, which determines the behaviour of the Josephson junction, and $\omega_c = 1/\tau_c$ is Josephson frequency at the characteristic voltage $V_c = I_cR$.

This equation is analogous to that of the mechanical system of a mass m and friction coefficient ξ, moving down a varying potential profile with which it is constantly in contact, resulting from a fixed term $w(x)$ plus a varying term driven by a force F_d [3]. The dynamics of this mechanical system is described by

$$m\ddot{x} + \xi\dot{x} = -\frac{\partial[w(x) - F_d x]}{\partial x}. \tag{2.34}$$

To make this clear in Equation 2.33, the driving term, i, and constant potential term, $\sin\gamma$, can be combined in a generalised energy potential u_J equal to,

$$u_J(\gamma, i) = 1 - \cos\gamma - i\gamma, \tag{2.35}$$

and Equation 2.33 can now be rewritten as,

$$\beta_c \frac{\mathrm{d}^2\gamma}{\mathrm{d}\tau^2} + \frac{\mathrm{d}\gamma}{\mathrm{d}\tau} = -\frac{\partial u_J}{\partial\gamma}. \tag{2.36}$$

To complete the analogy with the mechanical system, the mass m corresponds to the capacitance C, the friction coefficient ξ corresponds to the conductance $1/R$, and the bias current I_{bias} corresponds to the external force F_d that tilts the cosine-shaped potential, this is sometimes also called a "washboard" potential.

Equations 2.36 and 2.34 describe a non-linear system that can only be solved numerically and under certain conditions[4] these may even show chaotic behaviour [84]. The system's behaviour will be determined by the shape of the energy potential, and is analysed next for the following cases $i = 0$, $i < 1$ and $i > 1$, whose potentials are illustrated in Figure 2.9.

[3] Another mechanical system analogous to the Josephson junction is that of a damped pendulum with a rigid rod driven by an angular force.

[4] This is a well known phenomenon in driven non-linear oscillators. In Josephson junctions this happens for underdamped junctions driven at microwave frequencies below the Josephson plasma frequency.

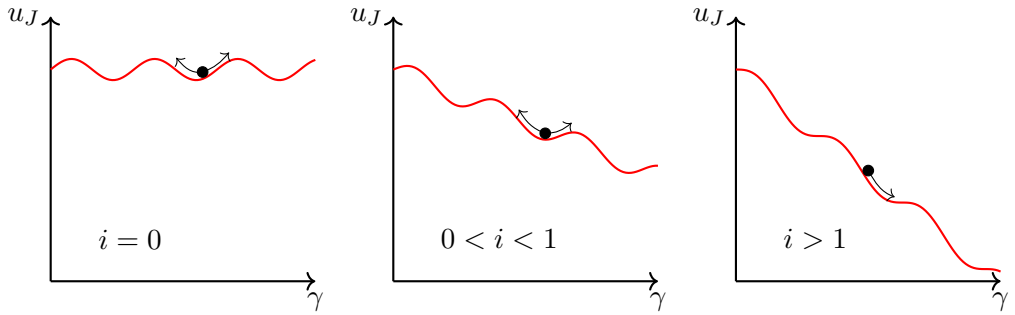

FIGURE 2.9: Potential driving the dynamics in a Josephson junction according to Equation 2.33, for different values of the bias current. The moving particle represents the instantaneous phase difference $\gamma(t)$.

The junction phase difference $\gamma(t)$ is represented by the "particle" in the previously described analogy with a mechanical system and shown in Figure 2.9. The voltage v across the junction results from the time derivative of $\gamma(t)$ as given by Equation 2.25.

When $i = 0$ (or $I_{\text{bias}} = 0$) the potential presents no tilting and $\gamma(t)$ oscillates back and forth trapped in a energy potential minimum. As the current increases up to $i \leq 1$ (or equivalently $I_{\text{bias}} \leq I_c$) the potential still presents no local minima and $\gamma(t)$ remains bounded in a potential minimum. When i reaches $i \geq 1$ (or $I \geq I_c$) the potential has no longer any local minima, and γ starts sliding down the undulating potential. This behaviour was simulated using the Simulink model shown in Appendix A. The obtained time evolution of the voltage for different values of a bias current is shown in Fig 2.10. When $i < 1$, as shown for the case $i = 0.95$ the particle is confined to one a potential

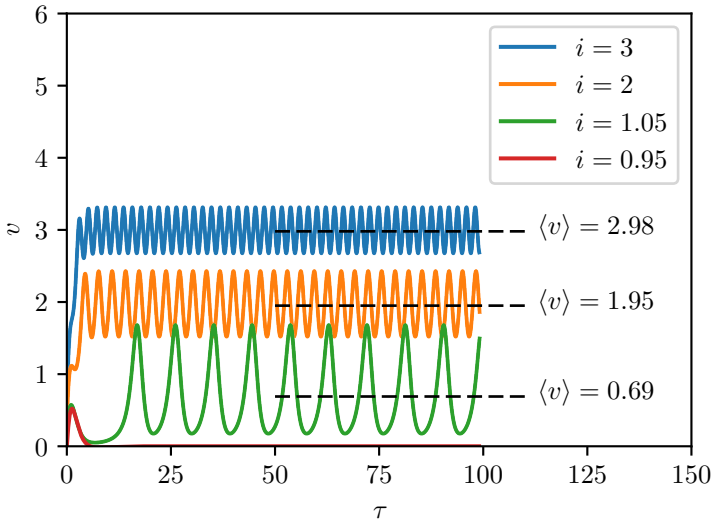

FIGURE 2.10: Time evolution of the voltage across a Josephson junction for different values of the bias current.

minima where it oscillates back and forth resulting in a zero average voltage $\langle v \rangle$. In this case the I-V relation exhibits a superconducting behaviour. The oscillations occur at

the so called plasma frequency [85], which for $i = 0$ is given by

$$\omega_p^2 = \left(\frac{2\pi}{\phi_0}\frac{I_c}{C}\right). \tag{2.37}$$

This is in general much higher than what is "visible" in most applications. For example, for a typical shunt capacitance $C = 1\,\mathrm{pF}$ and critical current $I_c = 10\,\mu\mathrm{A}$, when $i = 0$ the oscillation frequency is 27 GHz. Hence, in most systems only the time average of the voltage curves, shown in Figure 2.10, is accessible to be measured, and it is this value that will give origin to the typical I-V characteristic shown in Figure 2.11.

The transition from a bounded value of γ to a sliding one occurs when $i > 1$, inducing a transition into a finite average voltage as indicated by the dashed trace in Figure 2.11. This transition occurs within an interval of the order of 1 ps, and if i is further increased, the average rate at which the γ slides down increases proportionally to i and the I-V relation enter the ohmic regime.

When reducing the current starting from a value $i > 1$, different dynamics can occur depending on the parameter β_c of the junction. When the current reaches $i = 1$, the potential exhibits again the local minima, but γ is not immediately trapped in one of these minima and keeps sliding down the undulating potential inducing a finite average voltage across the junction even for $i < 1$. This can be understood in the analogous mechanical system this by the particle inertia which makes it overcome the potential valleys until the tilting of the potential is sufficiently reduced to trap again the particle in a stable minimum.

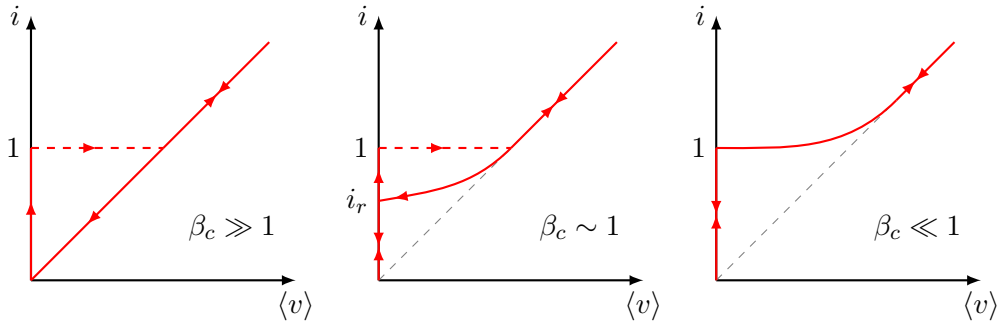

FIGURE 2.11: Dynamic I-V characteristic of Josephson junctions with different values of β_c. Left-plot: strongly underdamped junction; Middle-plot: balanced junction; Right-plot: strongly overdamped junction.

In the Josephson junction, the return current i_r is defined as the current when γ becomes locked again, and hence returning to the superconducting regime with $\langle v \rangle = 0$. Since this current is smaller than the critical current the I-V characteristic presents in general a hysteretic behaviour. There exists two important limit cases concerning the value of the junction parameter β_c. When $\beta_c \gg 1$ the junction is said to be strongly underdamped and the I-V curve is highly hysteretic. After reaching the ohmic phase the junction does not recover to the superconducting regime until the current is reduced to zero ($i_r = 0$). This happens in junctions with a high capacitance value and resistance

values, or in the analogy with the mechanical system, it corresponds to particles with a very high mass and low friction coefficient. When $\beta_c \ll 1$ the junction is strongly overdamped and the I-V curve presents no hysteresis ($i_r = 1$). This corresponds to junctions with a small capacitance or resistance, which is equivalent in the mechanical system to particles of negligible mass and high friction coefficient. These two limit cases are shown in Figure 2.11.

2.3.3 Effect of thermal noise

The resistance R in a real Josephson junction induces thermal noise that causes the total current to fluctuate around its mean value. A qualitative description of the effect of thermal noise on the junction characteristic can be obtained by resorting again to the picture of the tilted undulating potential. The current noise will cause the potential u_J tilt to fluctuate up and down. Even when $i < 1$, the current noise may cause the total current to exceed the critical current, over tilting the potential u_J and permitting the particle to roll to next potential minimum. In the overdamped junction this will induce a series of voltage pulses randomly spaced in time, whose average will be a finite DC voltage v. Hence the I-V curve will show a rounding effect at low voltages, as shown in Figure 2.12 for different noise values. The amount of noise is usually defined by the parameter Γ, which is the ratio of the thermal energy $I_T = k_B T$ and the Josephson coupling energy $I_c\phi_0/2\pi$,

$$\Gamma = \frac{2\pi k_B T}{I_c \phi_0}. \tag{2.38}$$

This parameter can also be written as a current ratio $\Gamma = I_T/I_c$, where I_T is the equivalent thermal noise current, which at $T = 4.2\,\mathrm{K}$ equates to $I_T \approx 0.15\,\mu\mathrm{A}$.

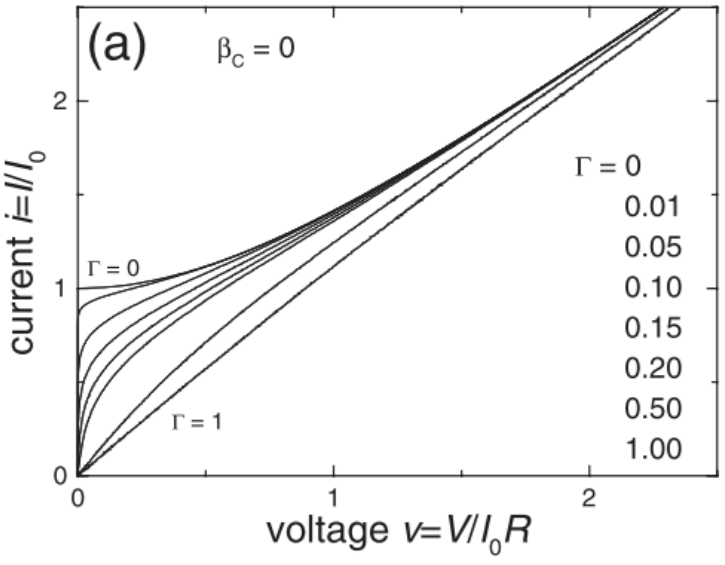

FIGURE 2.12: Rounding effect of the I-V curve in the presence of current noise in the limit case of strongly overdamped junctions. Adapted from [85].

Increasing the noise levels will cause a decrease in the critical current I_c, and for $\Gamma \approx 0.2$, I_c vanishes completely.

2.4 Superconducting QUantum Interference Devices

A SQUIDs consist of an SC loop interrupted by one or two Josephson junctions. The former are known as rf-SQUIDs, which rely on the AC-Josephson effect, and the latter are named DC-SQUIDs, since they are based on the DC-Josephson effect. Their name and principle of operation derive from the observed interference of the SC wavefunctions across the junction. Nowadays, DC-SQUIDs present several advantages over rf-SQUIDs for the measurement of low-frequency magnetic fields, and are usually preferred in most applications. The following comprehensive references have been used [85–87].

DC-SQUIDs can be seen as a generalisation of a single Josephson junction. In order to increase the sensitivity of the critical current modulation by a magnetic field in a Josephson junction (discussed in Section 2.3.1), the simplest possibility is to increase the junction area A_J. However this causes some undesired effects, as e.g. the increase of the junction capacitance, and it is generally preferable to have small junction areas. However, if the junction is stretched and split into two, keeping an SC loop connection, then it would be possible to have bigger sensing areas for the magnetic field while keeping small Josephson junctions.

Very high-quality Josephson junctions tend to have a high value of β_c and present a strongly hysteretic I-V characteristic. This is undesirable for conventional SQUIDs and is usually compensated for by adding a parallel resistance to the junction, thus forcing an overdamped behaviour. Also, in LTS SQUIDs the noise parameter Γ is usually kept below 0.1. Figure 2.13 show the schematic of the DC-SQUID and its equivalent RSCJ model circuit. The SC ring is biased by a current I_{bias} that is split by the two arms of the SQUID, where each of the Josephson junctions is present. The SQUID behaviour

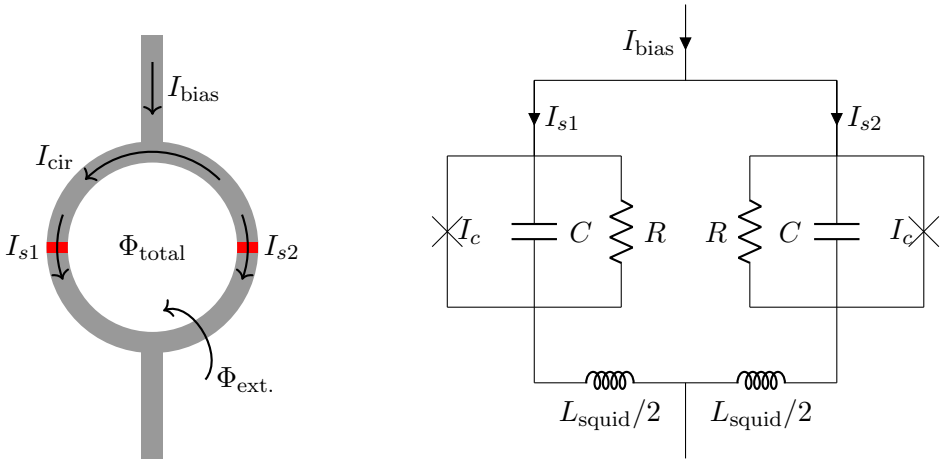

FIGURE 2.13: Schematics of a symmetric SQUID. Left: diagram with the various circulating currents and magnetic fluxes; Right: Equivalent RSCJ-model circuit.

will be determined by the relation between the SC wavefunctions on each branch of the loop, which will depend on the magnetic flux through the SQUID loop.

Proceeding as in Section 2.2.3 to derive the flux quantisation in an SC loop, using the bulk approximation, one can generalise Equation 2.20 for the case of a DC-SQUID loop by adding the phase difference terms across each junction, such that

$$\Phi_{\text{total}} = \phi_0\, n + \frac{\phi_0}{2\pi} \underbrace{(\gamma_1 - \gamma_2)}_{\text{Josephson}}, \qquad \text{with} \qquad n = 0, 1, \ldots \tag{2.39}$$

For an ideal and symmetric SQUID the total supercurrent I_{bias} is given by,

$$I_{\text{bias}} = I_{s1} + I_{s2} = I_c(\sin\gamma_1 + \sin\gamma_2), \tag{2.40}$$

which when combined with Equation 2.39 results in

$$I_{\text{bias}} = 2I_c\, \cos\left(\frac{\pi\,\Phi_{\text{total}}}{\phi_0}\right) \sin\left(\gamma_2 + \frac{\pi\,\Phi_{\text{total}}}{\phi_0}\right), \tag{2.41}$$

after rearranging both terms using fundamental trigonometric identities. Equation 2.39 indicates that the maximum value of the superconducting current that can flow through the SQUID is $2I_c$, but this maximum critical current of the SQUID can change depending on the total magnetic flux, and possibly even become zero. Solving Equation 2.41 is in general difficult since the flux Φ_{total} depends on the external flux and the loop current, which on their own also affect the phase difference in the junctions. However, the principle of operation of the DC-SQUID can be qualitatively understood by the following argument: the total SQUID magnetic flux Φ_{total} can be written as

$$\Phi_{\text{total}} = \Phi_{\text{ext}} + \Phi_{\text{cir}} \tag{2.42}$$

$$= \Phi_{\text{ext}} + L_{\text{squid}}\, I_{\text{cir}}, \tag{2.43}$$

where L_{squid} is the SQUID loop inductance. Starting from a situation with no flux applied, $\Phi_{\text{ext}} = 0$, in the SQUID loop, the total bias current I_{bias} will split equally between the two junctions, 1 and 2, such that $I_{s1,2} = I_{\text{bias}}/2$. In this case the I-V curve of the SQUID (I_{bias} versus V) will be identical to that of a single Josephson junction but with a critical current that is the double, $2I_c$. If the external magnetic flux Φ_{ext} is increased from zero, and due to the flux quantisation seen in Section 2.2.3, a screening current I_{cir} will appear in the loop inducing a flux Φ_{cir} such that the total magnetic field is kept constant, $\Phi_{\text{total}} = \Phi_{\text{ext}} + \Phi_{\text{cir}} = 0$. On one side of the SQUID the current I_{cir} will add to the bias current and on the other side it will subtract from it. Hence, the current on the SQUID branches will be

$$I_{s1} = I_{\text{bias}}/2 + I_{\text{cir}}, \qquad I_{s2} = I_{\text{bias}}/2 - I_{\text{cir}}, \tag{2.44}$$

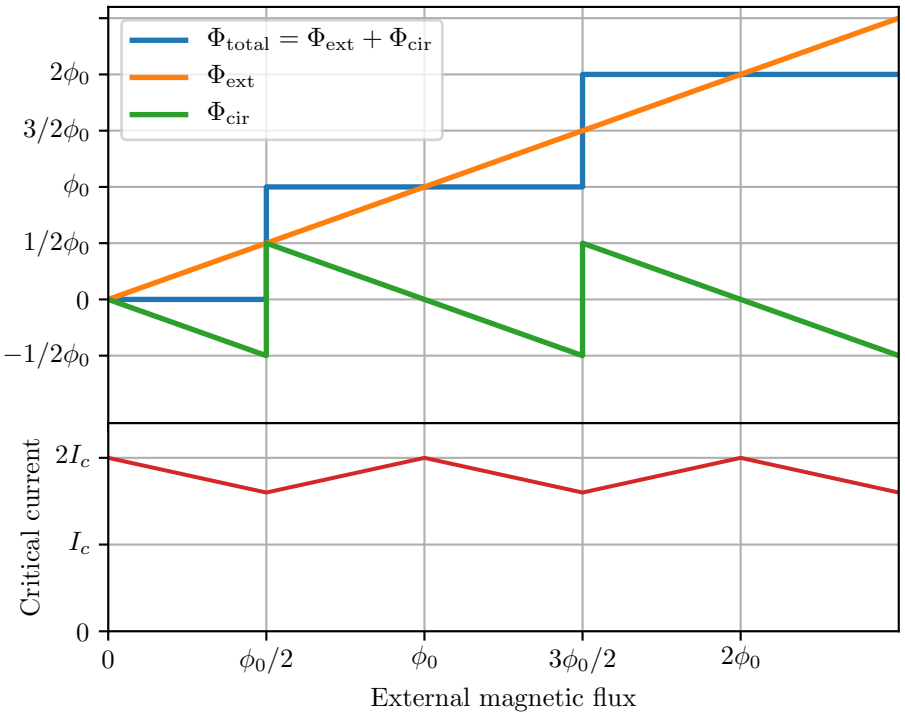

FIGURE 2.14: Modulation of the SQUID critical current (red trace) by an externally applied magnetic flux (orange trace), which causes a circulating loop current inducing a counteracting flux (orange trace). The exact quantisation of the total flux in the SQUID (blue trace) occurs only in the case of devices with a large self-inductance. In the case of a smaller L_{SQUID}, the total flux is not exactly quantised.

and

$$I_{\text{cir}} = \frac{1}{2}\left(I_{s1} - I_{s2}\right). \tag{2.45}$$

Junction 1 will reach its critical current I_c before junction 2, and when this occurs a voltage $V \neq 0$ will appear across the SQUID. This happens for a current $I_{\text{bias}} < 2I_c$, hence the effective critical current of the SQUID will be reduce. If the external flux is further increased, once it reaches $\phi_0/2$ it becomes energetically more favourable for the SQUID to allow for one flux-quanta $\Phi_{\text{squid}} = 1\phi_0$ to enter its loop by reversing the sense of the screening current I_{cir}. If the Φ_{ext} continues to increase the current I_{cir} will again decrease to maintain the loop flux at $1\phi_0$ until $\Phi_{\text{ext}} = 1\phi_0$ when $I_{\text{cir}} = 0$. With the reduction of the current I_{cir}, the critical current of the SQUID will increase until its initial value, $2I_c$, is recovered. This results in a periodic modulation of the SQUID critical current by the external magnetic flux, with period equal to ϕ_0, as shown in Figure 2.14.

The previous description of the SQUID assumes that L_{squid} is large enough for the flux generated by the screening current I_{cir} to reach at least $\phi_0/2$ (when $I_{\text{cir}} = I_c$), in order to guarantee the perfect quantisation of the total SQUID flux. In order to assess how big the magnitude of the flux created by the screening current when compared to

$\phi_0/2$, the dimensionless parameter β_L is commonly used,

$$\beta_L = \frac{I_c\, L_{\text{squid}}}{\phi_0/2}. \tag{2.46}$$

The perfect quantisation of the total SQUID flux is only possible if $\beta_L \geq 1$. However, this also results in a reduced modulation depth $\Delta I_c^{\text{squid}}$ of the SQUID critical current, as was the case in Figure 2.14 [85]. Therefore, devices used to measure magnetic fields typically have $\beta_L \ll 1$ for an increased sensitivity to variations in the magnetic field. In this case, the total SQUID flux is not perfectly quantised, but the general principle behind the modulation of the critical current as the result of a circulating current induced to try to preserve the flux quantisation still holds true. In the limit case when $\beta_L \ll 1$, the modulation of the critical current will be maximum, corresponding to the case where the sine factor in Equation 2.41 equals 1 and

$$I_c^{\text{squid}} = 2I_c \left| \cos\left(\frac{\pi\, \Phi_{\text{ext}}}{\phi_0}\right) \right|. \tag{2.47}$$

For higher values of β_L, the modulation depth of the critical current will decrease as shown in Figure 2.15.

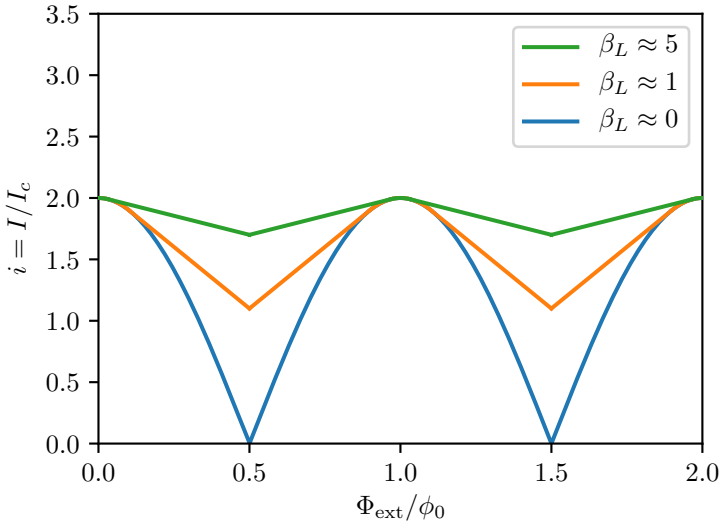

FIGURE 2.15: Modulation of the SQUID critical current by action of an externally applied magnetic flux, for different value of the parameter β_L. Adapted from [85].

In order to use the SQUID as a magnetometer the modulation of its critical current by the applied flux needs to be converted into a voltage-flux or current-flux modulation. Considering the RCSJ-model of a SQUID, shown in Figure 2.13, where each junction has resistance R, capacitance C and critical current I_c, and in the limit where $\beta_L \ll 1$ and no magnetic field is applied, the SQUID observes the same dynamics as a single Josephson junction [85], given by Equation 2.30, with resistance equal to $R/2$, capacitance $2C$ and critical current $2I_c \cos(\pi\Phi_{\text{ext}}/\phi_0)$. Consequently, the I-V curve will assume the same

shape as that of a single Josephson junction, like the one shown in Figure 2.11. But in the SQUID case, the I-V curve is periodically modulated between two limit curves, with varying critical current, as shown in Figure 2.16. This allows the SQUID to be used as flux to voltage (or current) transducer. For example, if a constant bias current is applied to the SQUID, the average voltage will be modulated by the magnetic flux as shown in Figure 2.16 by the Voltage-to-Flux (V-Φ) in the right-hand side plot. This curve exhibits a period of ϕ_0 and presents a peak-to-peak voltage swing V_{pp} which is typically in the order of tens of micro-volt. The highest sensitivity occurs at points where $\Phi = (2n+1)/4\,\phi_0$, and for an approximately sinusoidal characteristic with $V_{pp} = 100\,\mu V$ this has a value of $V_\Phi = \partial V/\partial\Phi = 314\,\mu V/\phi_0$. When thermal noise is not taken into account the SQUID I-V curve is not continuously differentiable at the critical current point and this would cause a divergence in the V-Φ curve at points where $\Phi = n\phi_0$, when $I_{\text{bias}} < 2I_c$. However, in a real SQUID the thermal noise will round the I-V curve near the critical current transition as was described in Section 2.3.3. Hence, the SQUID V-Φ curve will be free of any divergence, independently of the bias current.

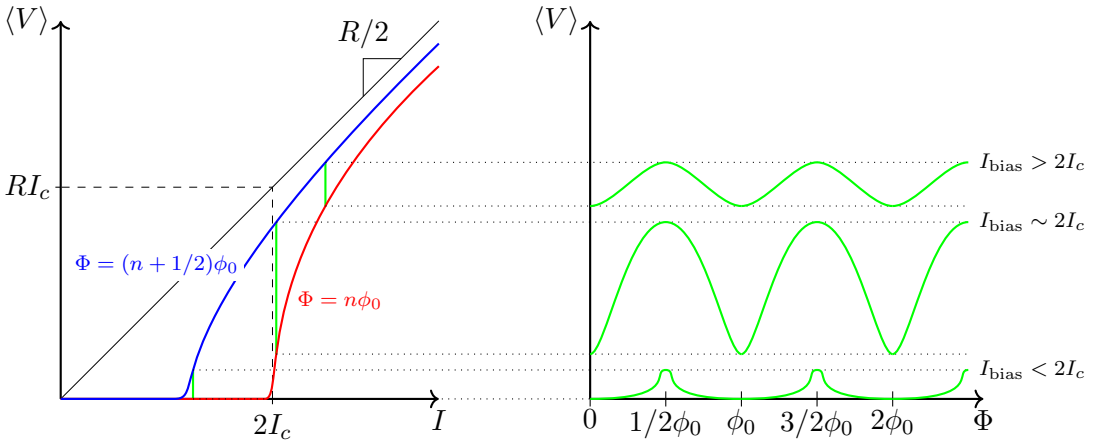

FIGURE 2.16: Modulation of the SQUID characteristic curves by an external magnetic field. Left-plot: limit I-V curves for different values of the magnetic flux. Right-plot: Voltage-flux response of a SQUID when different bias currents are applied.

2.4.1 Flux Lock Loop readout

After biasing the DC-SQUID with a constant current it behaves as a flux-to-voltage converter with a periodic and non-linear $V - \Phi$ characteristic. A readout electronic circuit is required to convert the SQUID changing voltage into a measure of the magnetic flux. Most often a setup with a constant bias current is used with the SQUID becoming a flux-voltage transducer as shown in the Figure 2.16. The vertical and horizontal position of characteristic curve V-Φ can also be adjusted by means of an auxiliary bias voltage V_{bias} and a bias flux Φ_{bias}, as shown in Figure 2.17.

A SQUID can be operated in a small-signal mode around a optimum working point usually in the steepest part of the $V - \Phi$ curve, where V_Φ is maximum. This working point is obtained by properly setting a bias flux Φ_{bias}. This readout requires just an

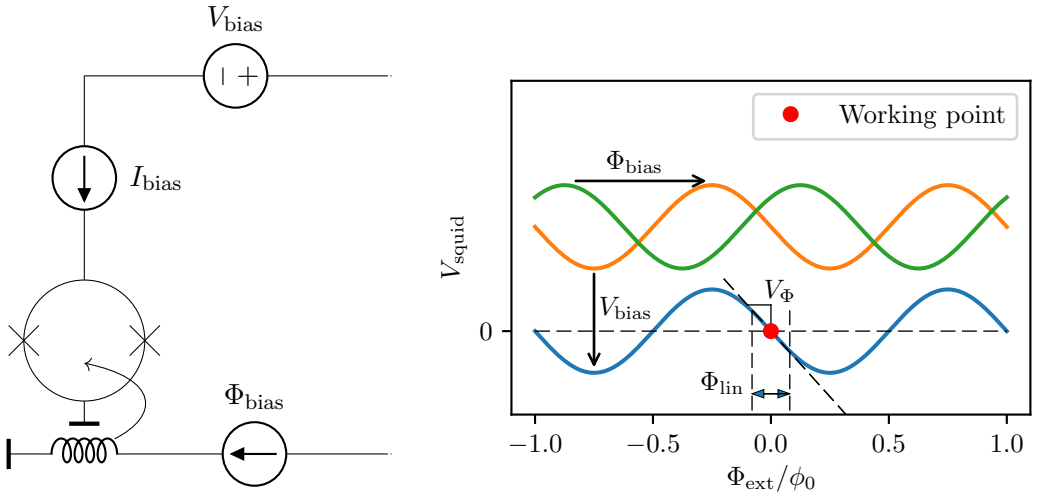

FIGURE 2.17: Left: Schematic of the SQUID biasing when this is used in a constant bias current mode. Right: V-Φ curves resulting from adjusting the values of V_{bias} and Φ_{bias} in order to properly adjust the SQUID working point.

amplifier to increase the voltage across the SQUID without introducing too much noise. However, the $V - \Phi$ curve is linear only in a small region Φ_{lin}, shown in Figure 2.17, which assuming a sinusoidal curve can be approximated by

$$\Phi_{\text{lin}} \lesssim \frac{\phi_0}{\pi}. \tag{2.48}$$

This reduced linear range enables a limited dynamic range when the SQUID is operated in a small-signal mode.

The dynamic range can be considerably increased by using a more sophisticated readout scheme called a FLL. This circuit is shown in Figure 2.18, and it performs two functions: it amplifies the weak voltage across the SQUID, and it linearises the SQUID transfer function to increase the available dynamic range. Assuming that the SQUID

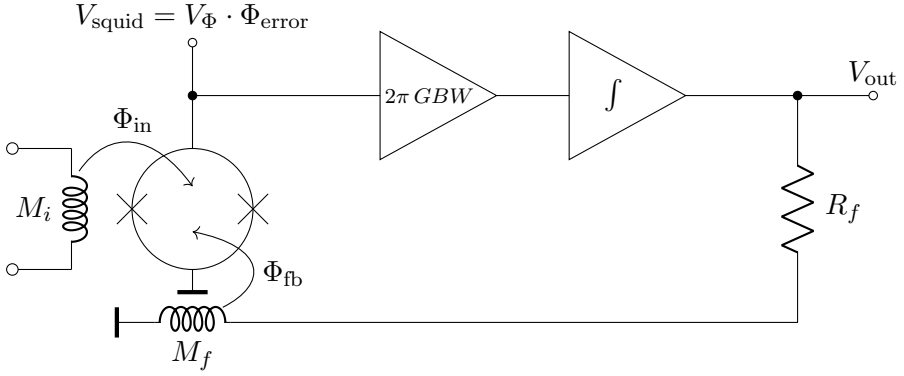

FIGURE 2.18: SQUID with FLL readout schematic, consisting of a negative feedback loop with an integrator ensuring a constant magnetic flux working point. The pre-amplifier gain is $2\pi GBW$ where GBW is the gain bandwidth constant product of the feedback loop in hertz.

is correctly biased, any applied flux change $\delta\Phi_{\text{in}}$ in the SQUID will induce a deviation of the voltage around the working point (according to $V - \Phi$ curve). This voltage variation is pre-amplified with a gain of $2\pi GBW$ (where GBW is the gain bandwidth constant product of the feedback loop), integrated and negatively fed back into the SQUID via the resistor R_f and a feedback coil which is coupled to the SQUID with mutual inductance M_f. The negative feedback integrator will generate a flux signal Φ_{fb} that will compensate any variation in the input flux, Φ_{in}, $\delta\Phi_{\text{fb}} + \delta\Phi_{\text{in}} = 0$, such that the total SQUID flux, $\Phi_{\text{error}} = \Phi_{\text{in}} - \Phi_{\text{fb}}$, is brought to zero $\Phi_{\text{error}} \to 0$. The small-signal transfer function of the FLL circuit when locked around a stable working point, given by $G_{\text{FLL}}(s) = V_{\text{out}}(s)/\phi_{\text{in}}(s)$, can be calculated by solving the following system of equations in the Laplace domain:

$$V_{\text{out}} = \frac{2\pi GBW}{s} \cdot V_\Phi \cdot \Phi_{\text{error}}, \tag{2.49}$$

$$\Phi_{\text{error}} = \Phi_{\text{in}} - \Phi_{\text{fb}}, \tag{2.50}$$

$$\Phi_{\text{fb}} = \frac{M_f}{R_f} \cdot V_{\text{out}}. \tag{2.51}$$

The resulting SQUID/FLL transfer function has a first order low-pass behaviour,

$$G_{\text{FLL}}(s) = \frac{G_{\text{FLL}}}{1 + s/\omega_p}, \tag{2.52}$$

with the DC-gain and pole frequency given by

$$G_{\text{FLL}} = \frac{R_f}{M_f}, \tag{2.53}$$

and

$$\begin{aligned} f_p = \frac{\omega_p}{2\pi} &= \frac{V_\Phi \cdot GBW \cdot M_f}{R_f} \\ &= V_\Phi \cdot \frac{GBW}{G_{\text{FLL}}}, \end{aligned} \tag{2.54}$$

respectively. At low-frequencies the output voltage V_{out} becomes linearly dependent on the applied flux Φ_{in}, for an extended range which is primarily limited by the saturation of the pre-amplifier and the integrator. Contrary to the small-signal readout, the gain factor G_{FLL} becomes independent of the SQUID gain at the working point, depending only on the circuit parameters R_f and M_f. The pole frequency on the other hand depends on the V_Φ flux-voltage coefficient, and pre-amplifier gain $2\pi GBW$. For a single-pole transfer function the $-3\,\text{dB}$ system bandwidth is identical to the pole frequency $BW_{\text{FLL}} = f_p$. However, if a time delay is considered in the system this equivalence will no longer hold true.

The system maximum Slew Rate (SR) defines how fast the input signal can change in time. It is defined in terms of the feedback flux Φ_{fb} by,

$$\dot{\Phi}_{\text{fb}} = \left| \frac{\mathrm{d}\Phi_{\text{fb}}}{\mathrm{d}t} \right|_{\text{max}}. \tag{2.55}$$

The feedback flux can be written as a function of the variation of the flux error $\delta\Phi_{\text{error}}$ times the open loop gain function give by $G_{\text{OPEN}} = f/f_p$, such that $\Phi_{\text{fb}} = G_{\text{OPEN}} \cdot \delta\Phi_{\text{error}}$. In the case of a sine wave input signal, the SR can then be written as,

$$\dot{\Phi}_{\text{fb}} = 2\pi f \, |\Phi_{\text{fb}}|_{\text{amp}} = 2\pi \, f_p \, |\delta\Phi_{\text{error}}|. \tag{2.56}$$

Two conditions can be defined for the maximum allowed flux error. A more restrictive one specifies that the system must be able to linearly track any changes in the input signal, which implies that the flux error should only vary within the linear region of the SQUID transfer function Φ_{lin}. Using Equation 2.48 and writing $|\delta\Phi_{\text{error}}| \leq \Phi_{\text{lin}}/2$, this results in

$$\dot{\Phi}_{\text{fb}} \leq 2\pi \, f_p \, \Phi_{\text{lin}}/2 = f_p \, \phi_0. \tag{2.57}$$

And a less restrictive condition which allows for the system response to become non-linear when the SR of the input signal is maximum, but still requires that the FLL feedback loop is able to stably operate at a fixed working point, and that not flux-jump occurs due to excessive excursions of the $\delta\Phi_{\text{error}}$ flux above $\phi_0/2$ or $|\delta\Phi_{\text{error}}| \leq \phi_0/2$. This results in

$$\dot{\Phi}_{\text{fb}} \leq \pi f_p \, \phi_0. \tag{2.58}$$

Both conditions are independent of the frequency, but this only holds for the case of a single-pole feedback loop [88]. As an example, for a SQUID/FLL system with a 1 MHz bandwidth, the maximum allowed SR of the input signal that preserves the system stability would be $SR = 3.14\,\text{M}\phi_0/\text{s}$. However, this stability estimation does not take into account the system noise which will be superimposed in the $\delta\Phi_{\text{error}}$ signal and may also cause flux jumps occur. An analysis of the SQUID/FLL stability taking into account the system noise and bandwidth will be presented in Section 3.3.

In the ideal case where there is no group delay in feedback loop SQUID/FLL bandwidth is exactly equal to the pole frequency $BW_{\text{FLL}} = f_p$. But any group delay t_d will distort the gain of the frequency transfer function $|G_{\text{FLL}}(s)|$, as a function of the product $f_p t_d$. For low values $f_p t_d \ll 0.08$ the effect of t_d is negligible and $BW_{\text{FLL}} = f_p$. The maximally flat gain response is obtained when $f_p t_d = 0.08$, resulting in a FLL bandwidth which is increased to $BW_{\text{FLL}} = 2.25 f_p = 0.18/t_d$. For higher values of $f_p t_d$ the transfer function starts showing a resonant peak which for excessive values compromises the system stability [88].

In the FLL readout scheme the voltage noise of the pre-amplifier is commonly the dominant noise source. To compensate this a flux modulation technique that defines a working frequency above the $1/f$-noise of the electronics was normally used in the

past. However, this solution requires a more complex electronics readout and limits the maximum bandwidth of the system. An alternative to the flux modulation is to use the Additional Positive Feedback (APF) technique [89]. The APF circuit consists of a resistor R_{APF} and a coil L_{APF} in series, with the coil magnetically coupled to the SQUID, and fed by the SQUID voltage, as shown in Figure 2.19. The APF technique considerably increases the SQUID's maximum sensitivity V_Φ, which results in a decrease of the weight of the noise induced by electronics readout. This makes it possible to implement a simpler direct-coupled FLL feedback loop, where the squid voltage V_{squid} is measured by a pre-amplifier without the need for any modulation. Higher SQUID/FLL bandwidth can also be achieved using the APF scheme [90], and systems with bandwidths higher than 15 MHz have been implemented [91]. However, increasing the SQUID transfer coefficient V_Φ at the expense of a reduced Φ_{lin} may result in an overall reduction of the SR according to Equation 2.57.

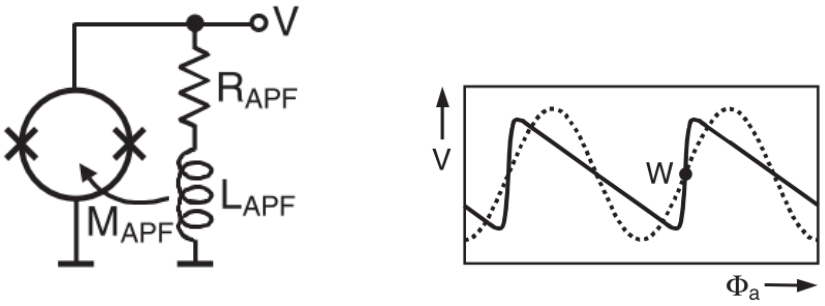

FIGURE 2.19: SQUID using APF technique. Left: circuit schematic; Right: Modified V-Φ transfer function with solid line representing the modified transfer function with the APF technique.

In a direct readout electronics working at room temperature, as the one used in the current project with a cable length of 1 m between the electronics box and the SQUID sensor $t_d \approx 2 \times 5\,\mathrm{ns}$. Hence the maximum flat bandwidth obtainable is $BW_{\mathrm{FLL}} = 18\,\mathrm{MHz}$. For values much higher than this, the system will become unstable.

For a comprehensive review of the different electronic readout techniques see [92].

2.5 CCC working principle

The CCC was invented by Harvey in 1972 [47] as a metrology device to compare two currents with a high precision. For a review of CCC devices please see [93]. Its functioning primarily rests on Maxwell-Ampère law and the perfect diamagnetism of the superconductors in the Meissner state. The simplest form of a CCC is that of a hollow SC cylinder where the wall thickness is sufficiently large for the bulk approximation to be valid as shown in Figure 2.20. If two currents I_1 and I_2 pass through the cylinder, there will a shielding supercurrent I flowing at the surface of the SC cylinder that will ensure that the magnetic field $\boldsymbol{B}$ inside the cylinder is equal to zero, independently of

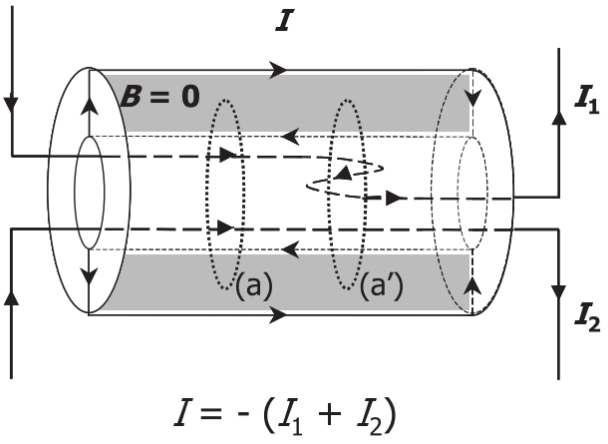

FIGURE 2.20: Superconducting cylinder shielding structure. Adapted from [93].

the trajectories and spatial distribution of the currents I_1 and I_2. Applying Maxwell-Ampère's law to a closed contour C passing in the interior of the cylinder and around its aperture,

$$\oint_C \boldsymbol{B} \cdot d\boldsymbol{l} = \mu_0 \left(I_1 + I_2 - I\right), \tag{2.59}$$

results in that,

$$I = -(I_1 + I_2). \tag{2.60}$$

This equality is valid independently of the path of the current inside the tube. More than this, the distribution of the supercurrent I will tend to be homogeneous on the outer surface of the cylinder, even for asymmetric paths of I_1 and I_2. Due to this fact, a precise measurement of the imbalance in currents I_1 and I_2 can be obtained by measuring the magnetic field $\boldsymbol{B}_{\text{ext}}$ induced by current I in the exterior of the cylinder.

2.5.1 Magnetic shielding structure

This shielding structure relies on the Meissner-Ochsenfeld effect to shape the magnetic field, and rejects the unwanted field components. In order to better understand the shielding effect of the CCC shield structure, it is instructive to analyse the behaviour of the field distribution of an off-centre current passing through a hollow cylinder depicted in Figure 2.21. Assuming that the cylinder has infinite length, thickness d, and that the SC material's London penetration depth is λ, the expressions for the potential vector inside and outside of the cylinder are [94]:

Inside the cylinder

$$A_z(\rho,\phi) \cong \frac{\mu_0 I}{2\pi}\left[-\ln\frac{r(\rho,\phi)}{K_1} - \sum_{n=1}^{\infty}\left(\frac{R_l}{R_i}\right)^n\left(\frac{1}{n} - 2\frac{\lambda}{R_i}\right)\left(\frac{\rho}{R_i}\right)^n \cos n\phi\right] \tag{2.61}$$

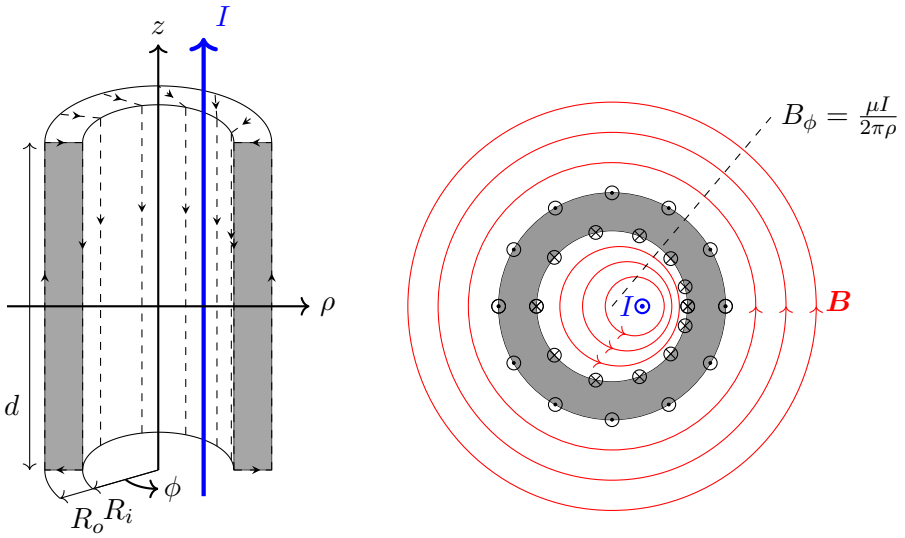

FIGURE 2.21: Superconducting hollow cylinder with a traversing off-centre current. The induced magnetic field inside the tube is asymmetric as expected, but the magnetic field in the outside region will tend to be symmetric due to the SC shielding currents flowing in the tube surface. This symmetrisation will only be perfect for a tube of infinite length.

Outside of the cylinder

$$A_z(\rho,\phi) \cong \frac{\mu_0 I}{2\pi}\left[-\ln\frac{\rho}{K_2} + \frac{4\lambda}{\sqrt{R_i R_o}}e^{-d/\lambda}\sum_{n=1}^{\infty}\left(\frac{R_1}{R_i}\right)^n\left(\frac{R_o}{\rho}\right)^n\cos n\phi\right] \tag{2.62}$$

Equation 2.62 shows that for the field outside the cylinder the terms dependent on the azimuthal position ϕ are highly suppressed by the factor $e^{-d/\lambda}$. In the bulk limit, where cylinder thickness is much larger than the London penetration depth this factor goes to zero, and the resulting magnetic field is

$$\boldsymbol{H} = \left(\frac{I}{2\pi\rho}\right)\boldsymbol{e_\phi}. \tag{2.63}$$

Only the azimuthal magnetic field component is present outside of the cylinder and all other components are suppressed. This is identical to the case where the field was created by a current passing through the centre $\boldsymbol{e}_z$ axis. It is as if the hollow SC cylinder removed any information about the spatial position of the wire passing through it. In CCC monitors measuring a particle beam current, this property is important to that have the measurement that is has much as possible independent from the beam position.

The analysis of how the outside field deviates from a perfectly azimuthal field in case of finite length cylinder can be found in [94].

2.5.2 Type I and Type II CCCs

The first developed CCCs, based on the principle described in the previous section is usually said to be of the Type I. This designation refers only to the CCC geometry

and has nothing to do with type I and type II superconductors. It would be rather unpractical to have a very long shielding tube. In order to reduce the size of the shield, and to try to mitigate the edge effects due to its finite length, in type I CCCs the tube is in a torus with overlapping ends, as shown in Figure 2.22. The longer is the overlap, the more efficient is the screening of the magnetic flux which tends to leak through the gap of the overlap [95]. The wires carrying the currents to be compared pass through the interior of the torus, and a small opening is made to bring them out and connect them to their respective current sources. The external magnetic flux, which for this geometry will assume a dipole distribution, will be proportional to the difference of the turn-current products $N_l I_l$, and almost independent of their spatial arrangement. Different aspects can be optimised to increase the resolution and accuracy of the current comparison. However, with this design it is not possible to measure the current from a beam of particles, since it would be impossible to make it pass through the interior of the torus shield.

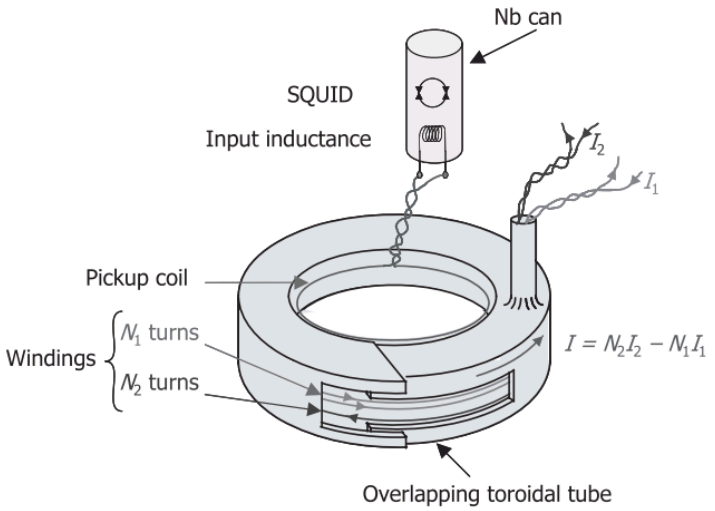

FIGURE 2.22: SC shield of type I CCC. Adapted from [93]

Another CCC design was proposed by Grohmann *et al.* [94], which is commonly referred to as being a CCC of the type II. This design inverts the two relevant space regions that are separated by the SC shielding barrier. In the cylinder type I CCC, the region inside the shielding torus is where the currents flow and the magnetic fields are asymmetric, while in the outside space is the region where the magnetic field to be measured is symmetric. By continuous deformation of the type I CCC it is possible to invert the hollow cylinder into a type II CCC, as shown in Figure 2.23. In the type II CCC, the region outside the torus is where the currents and asymmetric fields are, and the inside region of the resulting toroid is the region of highest symmetrisation, where the magnetic field becomes suitable to be measured.

The type II CCC presents the advantage that the magnetic field sensing region is enclosed inside the SC toroid geometry. This way, besides helping with the symmetrisation of the current fields, it also provides shielding against magnetic field perturbations

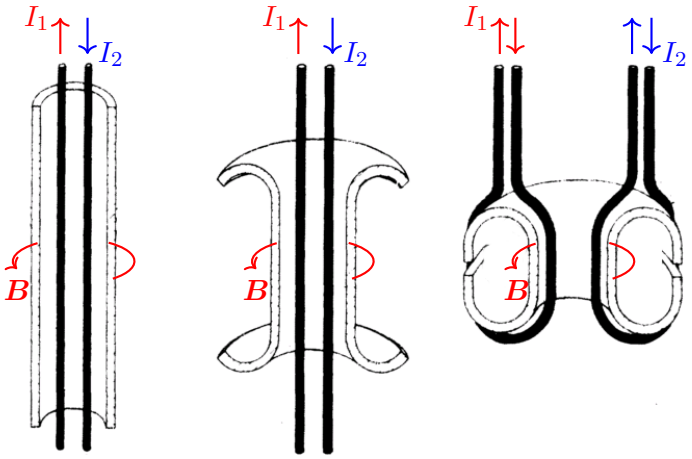

FIGURE 2.23: Transformation of the Type-I CCC into a Type-II CCC. Adapted from [96].

from external sources. In the type I systems a second shield enclosing is commonly used for the purpose of shielding external perturbations [97].

Different geometries are possible for the type II shield, and these can be evaluated concerning the symmetry, the magnetic fields induced by the currents one wants to measure, and also the shielding they provide for externally applied fields. Earlier studies and

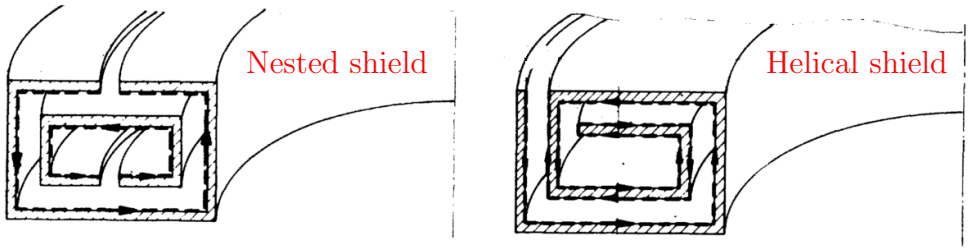

FIGURE 2.24: Different structures of Type-II CCC shields. Left: nested shield; Right: helical shield.

measurements of the attenuation A of non-azimuthal components in the two geometries in Figure 2.24 by Grohmann *et al.* [96], showed that this follows an exponential law that is a function of the effective length l_{eff}, related to the path of the screening currents in the inner surfaces. These measurements did not directly measure the magnetic field attenuation factors but instead the current ratio error obtained when comparing two known currents through input windings. By using these improved shield geometry errors $< 10^{-10}$ were obtained. It was also found that for DC and low frequency fields, the helical configuration was better than the nested one by more than 3 orders of magnitude. Additionally, increasing the number of folded surfaces or reducing the gap d, improved the attenuation of non-azimuthal components. For higher frequencies the attenuation decreased, and a convergence between the different geometries, for equivalent dimensions was observed.

A way of increasing the effective length while keeping a compact geometry is to have a meander shaped geometry [96], as shown in Figure 2.25. By increasing the number

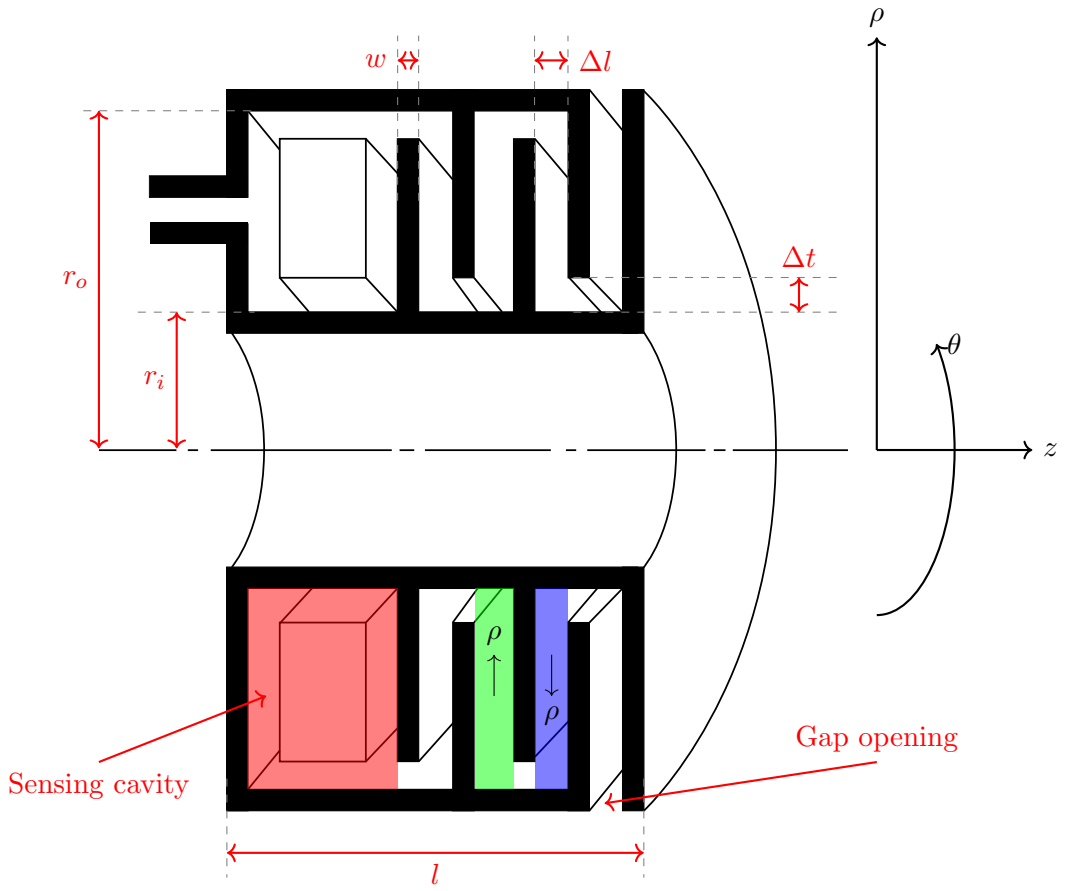

FIGURE 2.25: Meander shaped Type-II CCC shield. Region in red indicates the sensing cavity where sits the pickup ferromagnetic core; region in green indicates a ring cavity with decreasing ρ; region in blue indicates a ring cavity with increasing ρ.

of meanders it is possible to increase the effective length of the path connecting the gap opening of the shield to the sensing cavity where the signal magnetic field is picked up, without increasing much the total length of the shield. The following analysis of the shielding geometry uses the system of coordinates shown in Figure 2.25, where z is the direction oriented along the central aperture of the shield, ρ is the outward radial direction and θ is the azimuthal angular direction.

Analytic solutions of the magnetic field distribution inside the shield and respective attenuation factor have been calculated for the ring and coaxial geometries that combined form the more complex shapes shown in Figure 2.25 [59, 60]. In the bulk limit, the magnetic field distribution outside of the SC regions is obtained from the Maxwell-Ampère law by imposing the appropriate boundary conditions. Under magnetostatic conditions, Maxwell-Ampère equation can be simplified to $\nabla \times \boldsymbol{H} = 0$, and the magnetic field can be represented by a scalar potential $\boldsymbol{H} = -\nabla V$ which obeys the Laplace equation,

$$\nabla^2 V = 0. \tag{2.64}$$

The boundary condition that imposes the exclusion of all magnetic field from the SC material is given by

$$\frac{\partial V}{\partial \boldsymbol{n}} = 0, \tag{2.65}$$

where $\partial/\partial \boldsymbol{n}$ denotes the derivative with respect to the vector normal to the material surface.

All solutions without any dependence on z, can be written as a sum of cylindrical multipole multipole modes,

$$V(\rho, \phi, z) = V_0 \sum_{k=1}^{\infty} \left(\frac{1}{\rho^k}\right) \left(a_k \cos k\phi + b_k \sin k\phi\right), \tag{2.66}$$

where k indicates the order of the multipole mode. In the limit case where Δt is much smaller than r_i and r_o, the meander geometry can be seen as being formed by a succession of the two types of ring cavities highlighted in green and blue in Figure 2.25. The cavities where ρ increases (blue cavity), when going from the outside gap opening to the interior sensing cavity, and those where ρ is decreasing along the same path (green cavity). Neglecting the field distribution in corners of that connect the two type of ring cavities, one can assume that at the radial edges of each cavity, where $\rho = r_{i,o}$, the following conditions holds for the radial field component $B_\rho^+(r_{i,o}, \phi) = -B_\rho^-(r_{i,o}, \phi)$. This approximation is only valid for small w and when $\Delta l = \Delta t$. In this case the solutions for the magnetic potential inside the two types of ring cavities is,

$$\text{Increasing } \rho\text{: } V(\rho, \phi, z) = V_0 \left(\frac{\rho}{r_o}\right)^{-k} \cos k\phi, \tag{2.67}$$

$$\text{Decreasing } \rho\text{: } V(\rho, \phi, z) = V_0 \left(\frac{\rho}{r_o}\right)^{k} \cos k\phi. \tag{2.68}$$

From these expressions it is possible to compute the attenuation factors A per cavity for the transverse magnetic field components B_ρ and B_θ, which for a cavity with inner radius r_i are given by [98],

$$\text{Increasing } \rho\text{: } A^+ = \left(\frac{r_i}{r_o}\right)^{k+1}, \tag{2.69}$$

$$\text{Decreasing } \rho\text{: } A^- = \left(\frac{r_i}{r_o}\right)^{k-1}. \tag{2.70}$$

The mode that is less attenuate is the dipole mode $k = 1$, corresponding to a homogeneous transverse field. In this case the cavities with increasing ρ provide an attenuation factor of $A^+ = (r_i/r_0)^2$ and the cavities with decreasing ρ provide no attenuation $A^- = 1$, and are necessary only to connect consecutive cavities with increasing ρ.

2.5.3 Simulations of magnetic shield

At the beginning of the project it was planned that a new CCC shield was going to be designed and fabricated. As a starting point for the study of the optimal dimensions for a new meander shaped shielding, the prototype that had been fabricated by GSI and the University of Jena for the FAIR CCC project was used. The dimensions of the FAIR CCC shield are shown in Table 2.1. The very narrow gap between successive meander rings of $\Delta_l = 0.5\,\text{mm}$ makes the shield fabrication very challenging and requires tight tolerances to avoid any contact between the plates. During the assembly process, the welding of the different ring structures together, using electron beam welding, may cause surface deformations which may put different meander rings in contact. Additionally, the presence of any small particles may also cause electrical contacts. These possible issues are aggravated by the tight spacing of the ring cavities.

r_i [mm]	r_o [mm]	l [mm]	w [mm]	Δl [mm]	Δt [mm]	N_{meander}
92.5	140	182	3	0.5	1	10

TABLE 2.1: Dimensions of the prototype magnetic shield fabricated for the FAIR CCC

To investigate whether some of these dimensions could be increased, thus relaxing the mechanical fabrication constraints without a significant loss in the obtained shielding factors, different simulations where performed using the magnetostatic solver of the CST Electromagnetic Studio [99]. Different geometries with varying dimensions of the ring cavities, and varying number of meanders were simulated. In these simulations an external dipole field with magnitude $10\,\text{A/m}$ was considered, since this is the mode of smallest attenuation. Figures 2.27 and 2.28 shows the resulting magnetic vector field in the longitudinal plane parallel to the applied field, and how this field penetrates inside the SC shield.

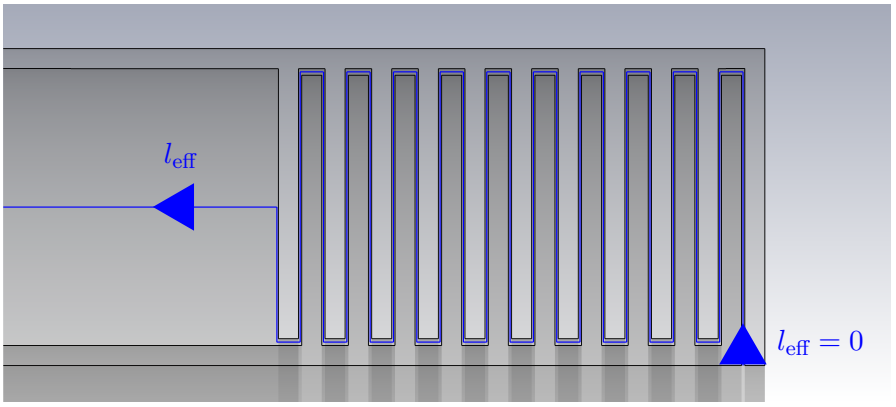

FIGURE 2.26: Path starting at shield opening and following through all meanders into the sensing cavity. Results of magnetic field simulations are shown along this path.

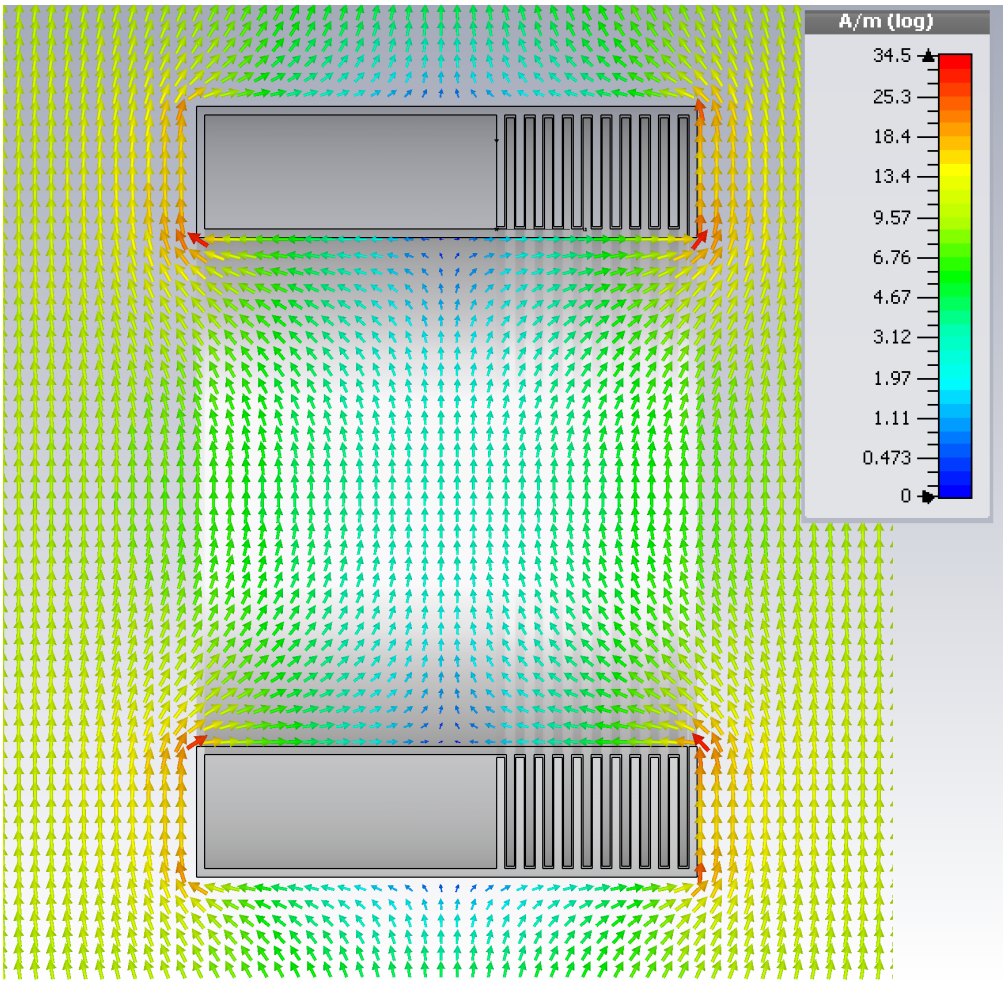

FIGURE 2.27: Field distribution around the shield geometry.

To compare the attenuation provided by the different geometries, the simulated magnitude of the magnetic field was plotted along the path shown in Figure 2.26, traversing through the meanders into the sensing. The obtained results are shown in Figure 2.29, these are inline with the ones obtained in previous similar simulation [100]. In the top-left plot is the attenuation obtained for geometries with different number of meanders together with attenuation obtained from the analytic solution of Equations 2.69 and 2.70. One observes that the analytic approximation accurately reproduces the simulation results in the ring cavities when the shielding geometry is formed by a reduced number of meanders, with differences increasing with the number of meanders. In the top-right plot are the simulation results for geometries with varying width of the longitudinal gap Δt. And in the bottom-left plot are the results for two different values of the width of the transverse gap Δl.

From these results one concludes that the most effective way of achieving a higher attenuation, for a fixed r_i/r_o ratio, is to increase the number of meanders. With the considered dimensions, changing the ring cavities dimensions does not have a significant impact in the obtained attenuation, resulting for example in an attenuation decrease of $\approx 5\,\text{dB}$ when Δl is increased from $0.5\,\text{mm}$ to $2\,\text{mm}$. Also, the increase of the Δt

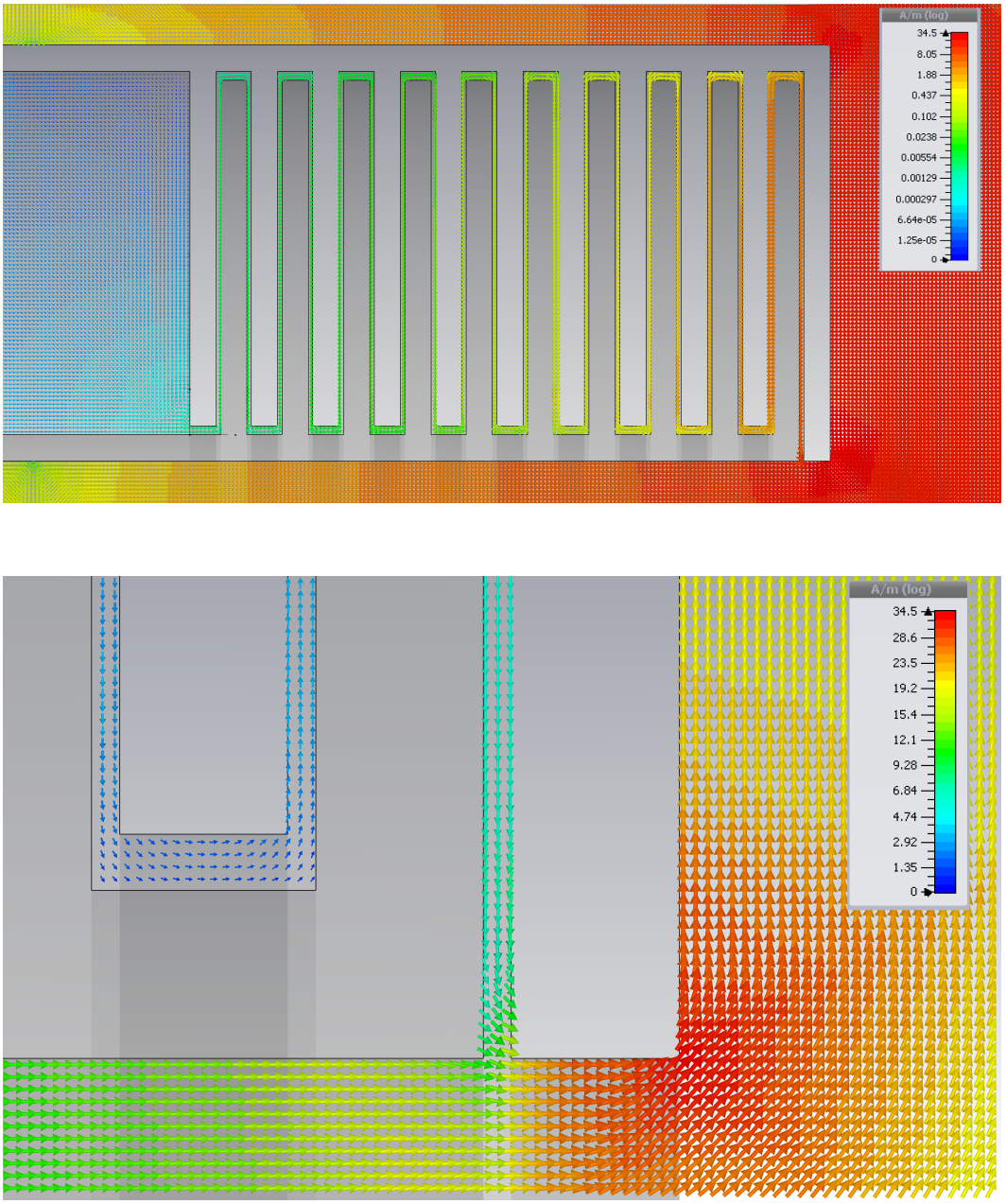

FIGURE 2.28: Top-image: detail of how the magnetic $|\boldsymbol{H}|$ field is attenuated through the meanders until reaching the sensing cavity. Bottom-image: detail of field entering the shield gap opening.

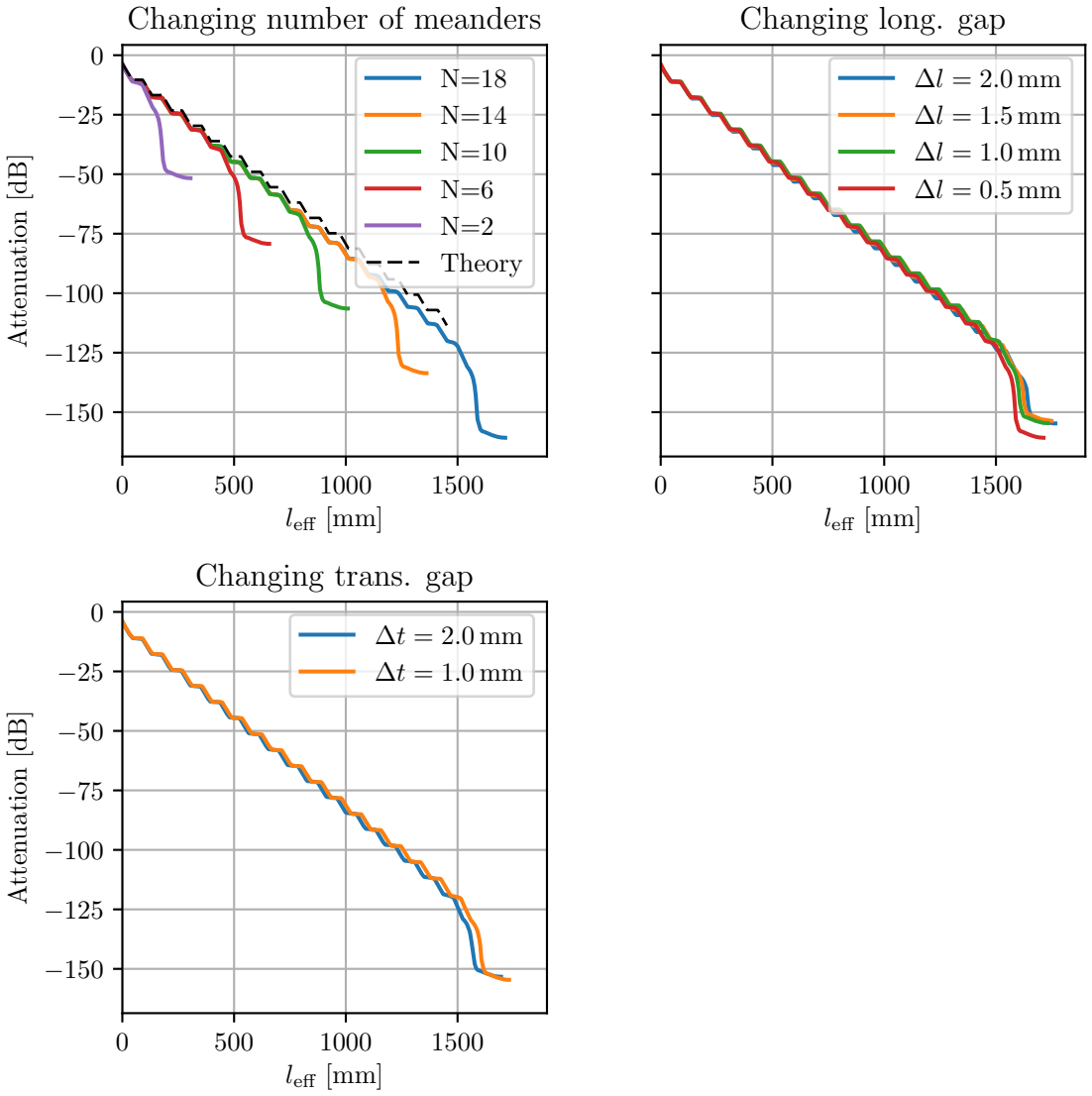

FIGURE 2.29: Magnetic field attenuation along path shown in Figure 2.26 for varying dimensions of the shield meanders. Top-left: Fix longitudinal and transverse gap and changing number of meanders; Top-right: Changing longitudinal gap; Bottom-left: Changing transverse gap.

parameter had almost no impact on the resulting attenuation, as shown in bottom-left plot of Figure 2.29. One concludes, that increasing the ring cavities dimensions Δ_l and Δ_t does not have a significant impact on the shielding effectiveness, while significantly contributing to less challenging mechanical constraints.

The obtained attenuation for the FAIR prototype geometry was $\approx -105\,\text{dB}$. Taking the Earth's magnetic field of $\approx 50\,\mu\text{T}$ as a reference, inside the sensing cavity this field would be attenuated to $\approx 300\,\text{pT}$, which is still two orders of magnitude above the lowest induced fields by the AD beam. However, it is important to note that the effect of a dipole field inside the sensing cavity on a toroid inductor will be much further attenuated due to the symmetry of the toroid geometry. In the ideal case, where the pickup core

presents a perfect cylindrical symmetry, the coupling of the dipole field to the pickup inductance would in fact be zero. But in a real pickup inductor, the cylindrical symmetry is broken by inhomogeneities in the core's ferromagnetic material and by the position of the coil wires. Estimating this additional attenuation factor is quite a difficult problem that could be better studied by real measurements.

After this study it was decided, under the collaboration with GSI and Jena University, that the CCC shield that had already been fabricated for FAIR was to be used in the current project in the AD.

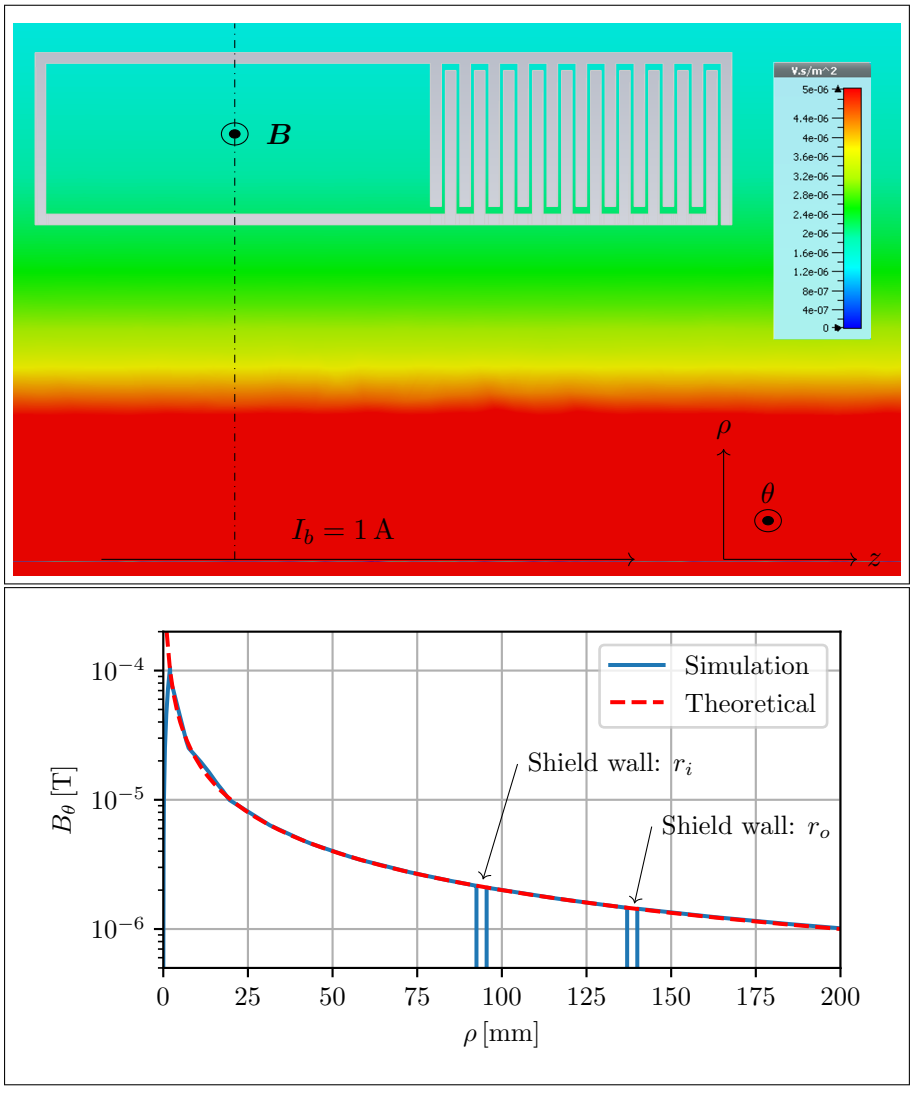

FIGURE 2.30: Simulation of the azimuthal magnetic field distribution induced by a beam current $I_b = 1$ A passing through the centre of the magnetic shield. Top plot: colour map of absolute value of the magnetic field $\boldsymbol{B} = B_\theta \, \boldsymbol{e_\theta}$; Bottom plot: amplitude of the field in radial direction along the dash-dotted line shown in top plot.

Besides the attenuation of the different multipole modes it is also fundamental that the azimuthal magnetic field distribution of the beam is not attenuated. In the absence of any magnetic structure a beam passing through the centre of the shield structure, at $\rho = 0$, induces a field distribution that only has an azimuthal component $\boldsymbol{B} = B_\theta \, \boldsymbol{e_\theta}$,

given by Equation 1.3. In the presence of the meander magnetic shield, this azimuthal field distribution is always tangential to the magnetic shield surface, hence the condition in Equation 2.65 is still satisfied even without a reconfiguration of the shield distribution. This implies that the magnetic field reaching the sensing cavity will be the same and follow the same radial dependence as if the shield structure was not present, $B_\theta \sim 1/\rho$. A simulation of this situation was performed, and the field induced by a beam current passing through the centre of the shield structure is shown in Figure 2.30. The bottom plot shows the comparison between the radial dependence of the field amplitude in vacuum, given by Equation , and the simulated field amplitude when the magnetic shield structure is present.

2.6 Conclusion

In this chapter the fundamental aspects of superconductivity theory that enable the CCC device to achieve its current measurement accuracy are introduced. The approach taken sought to arrive at the main results starting from first SC principles, by combining a classical description under London brother's theory with a quantum description based on the macroscopic superconducting quantum wavefunction. In this framework, it was derived the Meissner-Ochsenfeld effect that describes the expulsion of magnetic fields from the interior of a SC; the flux conservation and quantisation in a SC ring threaded by a magnetic field; the behaviour of Josephson junctions with their critical current modulation by applied magnetic fields; and the functioning of the SQUID device whose building blocks are Josephson junctions.

The Meissner-Ochsenfeld effects repels the magnetic field from the interior of Type-I superconductors except for the narrow region near the surface determined by the London penetration depth. In the bulk limit, where the dimensions of the SC are much larger that the London penetration depth, one can assume that no field can penetrate the interior of the SC, and the static field distribution for any given geometry can be obtained by solving the Laplace equation for a magnetic field scalar potential.

The behaviour of the Josephson junctions was explained using the common analogy with a point mass moving along a tilted undulating potential, which provides an intuitive analogy to understand the dynamics of the Josephson junction's V-Φ curve. The equivalent lumped-element circuit RCSJ-model of the Josephson junction was also introduced. Then, the DC-SQUID, with two Josephson junctions, was discussed as a generalisation of the single Josephson junction. When no magnetic fields are applied to the SQUID, this behaves as one Josephson junction with RCSJ-model components that result from paralleling components of the individual models. When a magnetic field is applied the flux quantisation unbalances the two branches of the SQUID, which results in the modulation of the critical current. It is from this modulation, which has period equal to ϕ_0, that results the exceptional sensitivity of SQUIDs to magnetic fields variations. This effect is exploited in SQUID magnetometers which have a noise resolution

power of (1-10) $\mathrm{fT}/\sqrt{\mathrm{Hz}}$. But in order to linearise and amplify the periodic low voltage SQUID output an appropriate electronic readout scheme is required. The analogue technique that can achieve the highest system bandwidths, required to cope with the high SR of the AD bunched signals, is the directly coupled FLL feedback loop.

It is worth restating that what is usually perceived as a constant voltage across the SQUID, is in fact the average of a high-frequency oscillations. These high-frequency signals are above the bandwidth of most applications, but, in case a similar-frequency signal is coupled to the SQUID, the resulting down-mixed signals may show at lower frequencies, which could perturb the "visible" V-Φ characteristic, and consequently affect the SQUID measurement. Thus, in most SQUIDs the input and feedback inductances, M_i and M_f (both defined in Figure 2.18), are protected by internal low-pass filters with cutoff frequencies at a few mega-hertz. Additional filtering at the SQUID input can help in further attenuating high-frequency perturbations.

After discussing the SQUID, the basic principles of the CCC devices were presented. The equations of the field distribution in cylinder geometry shield which is the simplest possible one, show the resulting symmetrisation of the magnetic field induced in the exterior region. Other types of geometry are obtained from the this simple geometry, and for measuring the current of a particle beam only the option of a Type-II CCC geometry can be used. One advantage of this type of geometry is that, besides symmetrising the beam field it also shields against external fields.

The CCC of this PhD project used the meander-shaped shield that had been previously fabricated as a prototype for the FAIR CCC. The dimensions of this shield are presented in Table 2.1. The attenuation of a dipole field component obtained with this shield geometry was simulated, and the results are inline with the theoretical prediction. This simulation was repeated for different geometric dimensions of the model to see their effect on the field attenuation. From the scanned parameters, the number of meanders is the one with the strongest impact on the attenuation as expected. It was also seen that increasing the longitudinal Δl and transverse Δt gaps of the meander almost does not affect the attenuation. This is an important conclusion which may used to justify the increase in the gaps Δl and Δt width, which would simplify requirements for the mechanical fabrication process. During the fabrication of the current shield, several problems due to short-circuits between the meanders showed up, particularly due to the very tight longitudinal gap equal to $\Delta l = 0.5\,\mathrm{mm}$.

Chapter 3

CCC Design for the AD

This chapter presents all the studies performed for the design of the CCC monitor optimised to measure the AD beam, and concludes by presenting the implemented device and auxiliary data acquisition systems. It starts by introducing the used SQUID device and presenting the measurement of its main parameters in Section 3.1. Section 3.2 covers the coupling circuit between the pickup inductor and the SQUID input, and different options and configurations are analysed. The current sensitivity and the low-frequency current noise resolution are estimated for different configurations of the coupling circuit. The SR of the AD beam at injection will impose a stringent constrain on the stability of the SQUID/FLL system. Section 3.3 starts by discussing SQUID/FLL SR limitations, and how these affect the measurement stability, and in Section 3.3.1 the beam parameters during the AD bunched beam phases are presented. These limits and behaviour are analysed using a theoretical and a simulation model. With these design tools the coupling circuit is modified in order to reduce the signal SR, and the main results are presented in Section 3.3.2. The implemented CCC monitor is presented in Section 3.4. This chapter concludes with a description of the installed acquisition and control system, designed to automatise the data acquisition during the AD cycle.

3.1 SQUID sensor measurements

Modern thin-film SQUIDs, with integrated input coil, have an input inductance L_i typically limited to a few micro henries. For modern low-noise devices the noise spectrum of the combined intrinsic SQUID noise and the readout electronics noise, presents a $1/f$-noise at low frequencies with corner frequency $\sim 1\,\mathrm{Hz}$, and white noise spectrum for higher frequencies with amplitude spectral density $\sim 1\,\phi_0/\sqrt{\mathrm{Hz}}$ [101]. These devices may achieve an input sensitivity $1/M_i$ of the order of $\gtrsim 0.1\,\mu\mathrm{A}/\phi_0$. The input sensitivity is correlated with the input inductance.

For the current project a commercially available SQUID system from Magnicon GmbH was used. This consists of the high performance low noise DC-SQUID sensor model C6L1 [102], combined with a low noise and high bandwidth FLL electronics model [103]. This device uses the APF technique enabling a directly-coupled FLL readout.

This sensor was chosen for its relatively high input inductance and current sensitivity, which is important when coupling the sensor to a pickup coil with a much higher self-inductance. Also its very low noise levels ensure the proper operation when used with a high bandwidth FLL readout, which will be required to cope with the high SR of the AD beam. The XXF-1 FLL electronics, also from Magnicon, was chosen for its low noise and high bandwidth, together with the fact that it is highly customisable, being possible to remotely configure many operation parameters, such as the SQUID bias current and voltage, as well as the FLL R_f and GBW parameters, with a wide range of possible values. Below are the main specifications of the used system [102].

- Input inductance L_i: 400 nH
- Input coupling $1/M_i$: 0.51 µA/ϕ_0
- Feedback sensitivity $1/M_f$: 43 µA/ϕ_0
- Maximum voltage swing $\Delta V_{\max}$: 53 µV
- Transfer coefficient V_Φ: $\approx$ 570 µV/ϕ_0
- White noise: 0.7 µ$\phi_0/\sqrt{\text{Hz}}$
- $1/f$-noise corner: 0.7 Hz

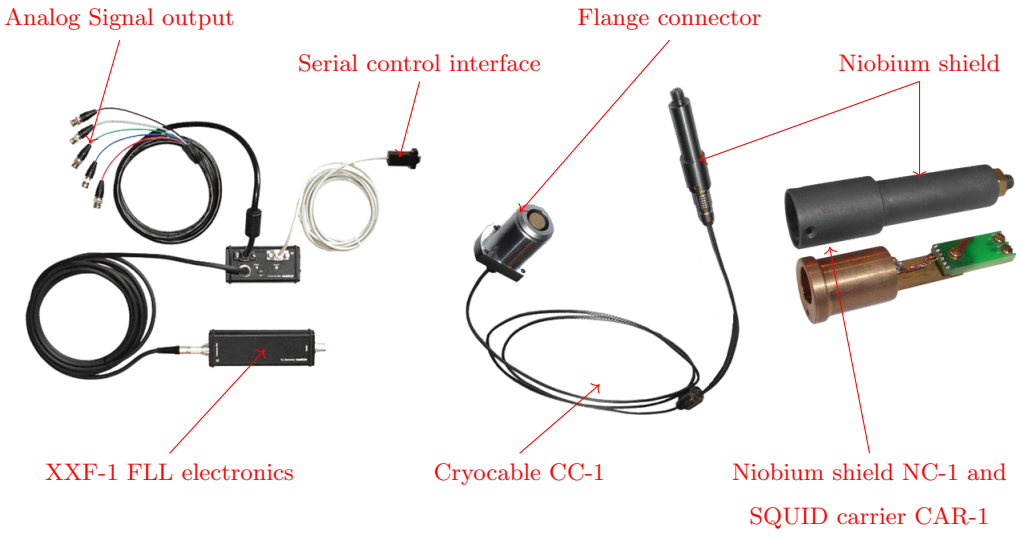

FIGURE 3.1: Different components of the Magnicon SQUID/FLL system. Magnicon images.

The different components of the Magnicon SQUID system are shown in Figure 3.1 [102–104]. The SQUID is installed in a printed circuit board carrier (CAR-1) which is inserted inside a cylindrical niobium shield (NC-1) for shielding the device from external magnetic fields. The signals to be measured are coupled to the SQUID input inductance through two screw pressure contacts, and the connections for biasing, reading and controlling the remaining SQUID signals is made through the cryocable (CC-1)

with a vacuum tight flange connector. This flange connector is to be installed in the exterior vessel of the cryostat container used to cool down the SQUID. Directly at the flange port is connected the FLL electronics box in order to reduce the length and time delay between the SQUID and the feedback loop. All the XXF-1 FLL analogue and control signals are distributed through a connector box which also implements a 10 kHz low-pass filter in the FLL measurement output V_{out}.

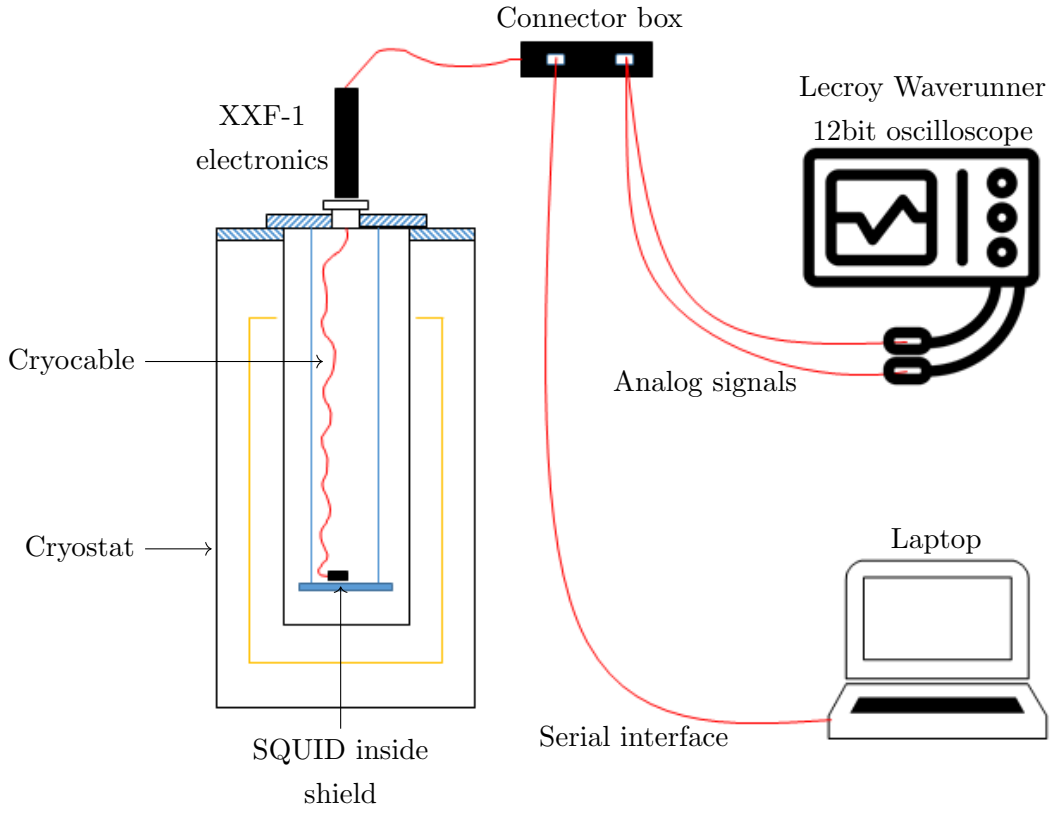

FIGURE 3.2: Setup used to measure the characteristic curves of the selected Magnicon SQUID alone.

Measurements of the characteristic curves of the SQUID with its input inductance disconnected from any source were performed to verify some of the SQUID parameters and characteristic curves. These measurements were performed with the SQUID inside the niobium cylindrical shield and placed inside a general purpose wide-neck liquid-helium bath cryostat for cooling, as shown in Figure 3.2. The XXF-1 electronics implements two signal generators which can be used to sweep the I_{bias} current or generate magnetic flux signal Φ_{SQUID} in the SQUID, through the M_f feedback mutual inductance. The readout electronics also implements an amplifier with $\times 2000$ gain, which is used to measure the low-voltage V_{SQUID}. In the following measurements this gain was deducted from the measured signals, so that the plotted voltages correspond to voltage across the terminals SQUID.

The measured I-V curve is shown in Figure 3.3. For $I_{\text{bias}} < I_c$ the SQUID is operating in the superconducting regime , and for $I_{\text{bias}} > I_c$ it starts developing a voltage with a

ohmic behaviour. This curve can be compared to the expected curves shown in the left plot of Figure 2.16, when Φ_{SQUID} is kept constant.

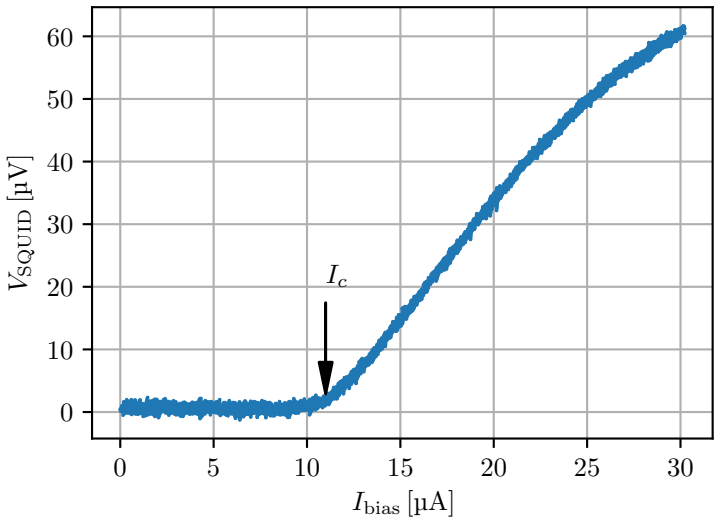

FIGURE 3.3: Measured I-V curve of the selected SQUID from Magnicon. The observed skewed shape of the transfer functions is a consequence of the implemented APF technique.

The V-Φ curve was measured by first applying a constant bias current I_{bias} and then modulating the flux coupled to the SQUID. The three curves shown in Figure 3.4 were measured for three different values of the bias current I_{bias}. The value of M_f can be

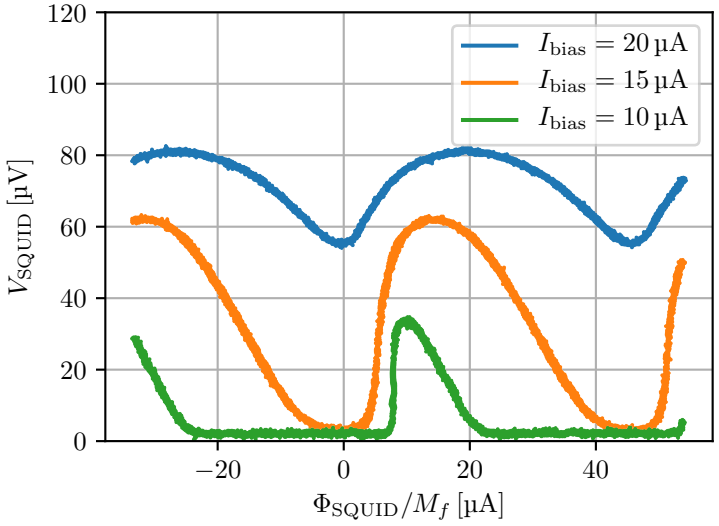

FIGURE 3.4: Measured V-Φ curve of the selected SQUID from Magnicon, for various values of bias current I_{bias}.

estimated from the obtained curves by dividing on ϕ_0, equal to the curves period, by the current required to produce that same variation.

In order to properly setup the SQUID, the bias current needs to be adjusted to the point that produces the maximum voltage excursion ΔV_{SQUID} of the V-Φ curve, and the bias voltage is adjusted so that the curve is vertically centreed around $V_{\text{SQUID}} = 0$. Once the SQUID is correctly biased, it is possible to measure its transfer coefficient V_Φ, by computing the curve slopes at the intersections with the horizontal axis. This procedure is shown in Figure 3.5, after the V-Φ curve was smoothed by an averaging filter. The estimated optimal SQUID transfer coefficients at the negative and positive

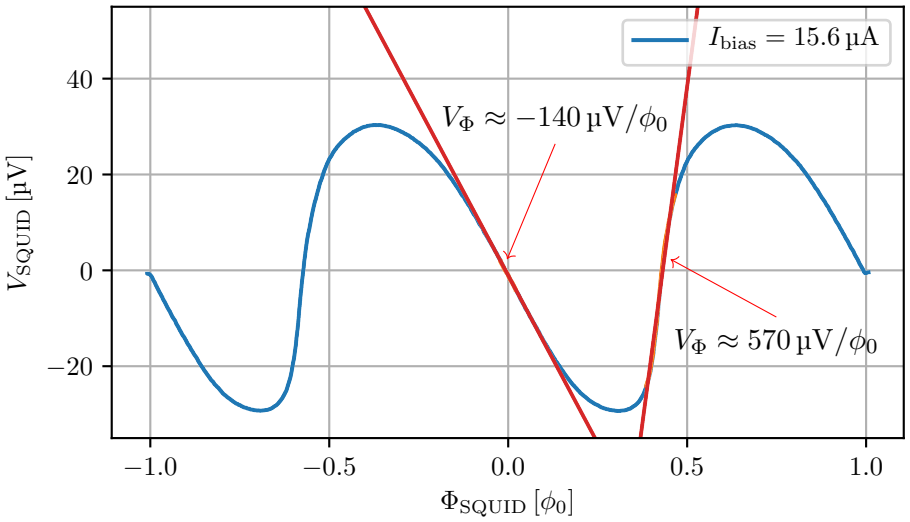

FIGURE 3.5: Measured optimal V-Φ curve for a bias current $I_{\text{bias}} = 15.6\,\mu\text{A}$. Curve has been smoothed by applying a window averaging filter. Bias voltage has also been adjusted to $V_{\text{bias}} = 31.6\,\mu\text{V}$, so that optimal working point crosses the zero volt line.

crests of the V-Φ curve are $\approx 140\,\mu\text{V}/\phi_0$ and $\approx 570\,\mu\text{V}/\phi_0$. These values should be seen as approximate values, since any small variations in the SQUID bias V_{bias} or I_{bias} will considerably affect the transfer coefficient V-Φ curve. Additionally the linear region, particularly in the high slope side of SQUIDs with APF is limited, and any signals that drive the SQUID flux Φ_{SQUID} outside of this region will reduce the transfer coefficient. Hence, there is always some uncertainty in the closed loop FLL bandwidth BW_{FLL} estimation using Equation 2.54.

3.2 Coupling circuit

In most SQUID applications a coupling circuit is required to couple the magnetic field to be measure to the SQUID loop. SQUIDs present a very low intrinsic magnetic flux noise, which of the order of $\Phi^{\text{noise}}_{\text{SQUID}} \approx 1 \times 10^{-6}\,\phi_0/\sqrt{\text{Hz}}$, but since their loop area A_s needs to be kept small, the magnetic field noise $B^{\text{noise}}_{\text{SQUID}} = \Phi^{\text{noise}}_{\text{SQUID}}/A_S$ is often too high. To increase the magnetic field resolution it becomes necessary to enhance the effective area. Simply increasing the SQUID geometric area would result in an increase of the SQUID inductance L_{squid} and β_L with an associated reduction of the modulation depth

and sensitivity as seen in Figure 2.14. In the case of LTS SQUIDs this can be easily overcome by using a superconducting pickup circuit with a sensing input coil connected to the SQUID input inductance, this is known as a flux transformer [105]. The flux transformer integrates the magnetic field to be measured over a large surface at the expenses of spatial resolution, and tightly couples the amplified magnetic field to the SQUID loop.

In the current analysis it will be neglected that the presence of the flux transformer reduces the SQUID inductance and consequently the coupling M_i. This changes the optimal coupling conditions although this is a minor effect.

3.2.1 Flux transformer

Considering a closed SC circuit with multiple inductors connected in series as shown in Figure 3.6, the total flux linkage must remain constant as long as the loop stays in the SC state, due the magnetic flux conservation in a SC loop discussed in Section 2.2.3.

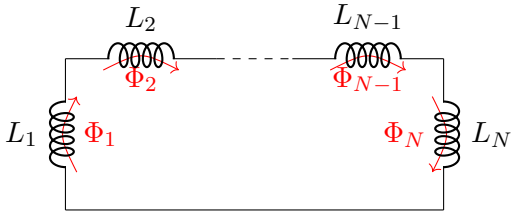

FIGURE 3.6: Superconducting loop with multiple inductors, each with its associated magnetic flux.

Assuming that there are N inductive elements in series forming a loop, then

$$\Phi_1(t) + \Phi_2(t) + \ldots + \Phi_N(t) = \text{constant}, \tag{3.1}$$

where the sources of flux linkage can be: self-inductances L_a, mutual inductances M_{ab}, or externally applied fluxes Φ_{ext}, such that

$$\Phi_a = L_a i_a + M_{ab} i_b + \ldots + \Phi_{\text{ext}}. \tag{3.2}$$

Such a circuit can be used as a flux transformer to transport magnetic flux signals, and also to amplify magnetic field $\boldsymbol{B}$ signals.

In the case where one wants to couple the magnetic field induced by a beam current into SQUID sensor, the simplest possible circuit is that shown in Figure 3.7, for which,

$$\delta\Phi_p + \delta\Phi_i = 0, \qquad \rightarrow \qquad M_p I_{\text{beam}} + L_p i = -L_i i, \tag{3.3}$$

where M_p is mutual inductance between the source current and the pickup inductance L_p as shown in Figure 3.7. Considering that the flux in L_i is coupled to the SQUID loop with mutual inductance M_i, the coupling S_{I_b} of the source current into the SQUID

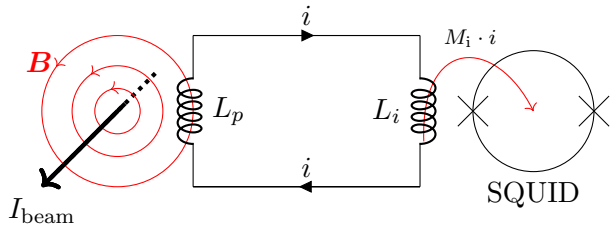

FIGURE 3.7: SC flux transformer used to couple magnetic fields from a current source into a SQUID sensor. DC magnetic field signals can also be coupled due to the total flux conservation in the SC loop.

magnetic flux is given by,

$$S_{I_b} = \frac{\Phi_{\text{squid}}(t)}{I_{\text{beam}}(t)} = \frac{M_p}{L_p + L_i} M_i. \tag{3.4}$$

One important characteristic of SC flux transformers is that they do not have a low cutoff frequency and are able to couple fields and currents down to DC.

In general any mutual inductance can be written as function of the two self-inductances $L_{1,2}$ and the coupling factor k, which accounts for any leakage flux occurring when the inductances are not tightly coupled and $k < 1$,

$$M_p = k\sqrt{L_1 L_2}. \tag{3.5}$$

For high permeability materials, $L_{1,2}$ can be written in terms of the inductance factor (self inductance per turn) A_L,

$$L_{1,2} = N_{1,2}^2 \, A_L. \tag{3.6}$$

When measuring a beam current using a high permeability pickup core with an inductance L_p and mutual inductance M_p, the number of turns in the primary side is equivalent to 1, while the number of turns in the secondary N_p may be freely chosen. Hence, assuming a perfect coupling $k = 1$ which is a good approximation when the relative permeability of the core's magnetic material is very high $\mu_r \gg 1$,

$$M_p = N_p L_p. \tag{3.7}$$

In this case, Equation 3.4 is simplified to,

$$S_{I_b} = \frac{\Phi_{\text{squid}}(t)}{I_b(t)} = \frac{1}{N_p} \frac{L_p}{L_p + L_i} M_i. \tag{3.8}$$

To maximise S_{I_b} the number of turns N_p should be the smallest possible, hence it is almost always 1, although it could be possible to have a fractional equivalent number of turns as described in [106]. The parameters L_i and M_i are fixed by the chosen SQUID and for a single stage dc-SQUID L_i is typically limited to $\leq 1\,\mu\text{H}$, and $M_i \leq 5\,\phi_0/\mu\text{A}$. The pickup core inductance L_p should be large, although it is useless to have it much

bigger than L_i since the sensitivity of this coupling circuit is limited to $S_{I_b} \approx M_i$ for $L_p \gg L_i$. Higher magnetic field concentrations and consequently higher inductances are achieved by forming the core in a closed magnetic circuit in a toroid. Because of their symmetry, toroidal cores allow a minimum flux leakage. An inductor with a toroidal geometry of height h, inner radius r_i, outer radius r_o and made of a material with relative permeability μ_r, has a self-inductance.

$$L = \frac{\mu_o \mu_r}{2\pi} \cdot h \cdot N^2 \cdot \log \frac{r_o}{r_i}. \tag{3.9}$$

To increase L, without changing $N = 1$, one can change the geometry, although this is normally constrained, or increase μ_r. In the here-presented project the core geometry was already set by the SC shield dimensions, described in Section 2.5.3.

The current resolution of the monitor will be fundamentally limited by the different noise contributions. Increasing the pickup inductance L_p with a ferromagnetic core of large dimensions will increase the sensitivity but will also add additional thermal magnetisation noise. However, the additional flux noise is proportional to $\sqrt{L_p}$ while the sensitivity increases with L_p (as long as $L_p < L_i$), hence, the SNR will increase with $\sqrt{L_p}$,

$$\frac{\Phi^{\text{in}}}{\Phi^{\text{noise}}} \propto \sqrt{L_p}. \tag{3.10}$$

By choosing an appropriate ferromagnetic core material it is possible to increase L_p by many orders of magnitude.

3.2.2 Ferromagnetic cores

Ferromagnetic materials have a high magnetic permeability $\mu_r \gg 1$, but also present a non-linear behaviour with saturation and hysteresis effects as shown in the $B - H$ magnetisation curve in Figure 3.8. Hysteresis in the $B - H$ curve is due to irreversible expansion or rotation of the ferromagnetic domains. Materials that have a high permeability but where fields are easily reversed due to a narrow hysteresis loop are known as soft ferromagnetic materials. These are the materials normally used in magnetic applications. Additionally, for small enough variation of H around a fixed working point, the domain walls perform reversible movements around some equilibrium position. This occurs if $\delta|H| \ll H_c$, and if $|H| < H_c$, where H_c is the coercive field of the material. In the reversible regime, of small δH, the relation between H and B is approximately linear and the magnetic permeability μ almost constant. If the core's material is electrically conducting, eddy currents will induce thermal losses and delays in the magnetisation response. For all ferromagnetic materials the permeability is in general dependent on the frequency, and for high frequencies $\mu_r \to 1$.

The magnetic noise of magnetic materials is normally associated with the different loss mechanisms occurring in the material [107–109]. Losses in inductors are modelled by a complex permeability $\mu^* = \mu' - j\mu''$, which results in a real and imaginary part

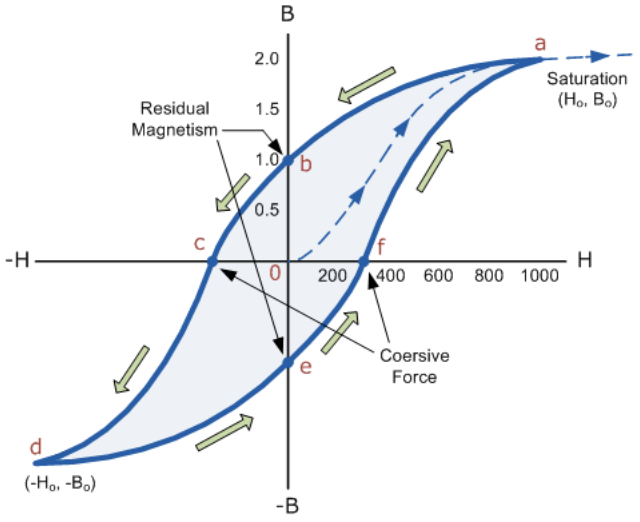

FIGURE 3.8: Magnetisation curve of ferromagnetic materials.

inductance, L' and L'', respectively, such that

$$L = L' - jL'' = (\mu' - j\mu'')L^{\text{air}}k_f, \tag{3.11}$$

where L^{air} is the equivalent inductance of an inductor with the same geometry but without any core material, $\mu = \mu_0$. The filling factor k_f of the core material, needs to be considered in real inductors, as it accounts for the active area of the magnetic material. From a circuit perspective, the complex inductance results in a resistance in series with a lossless inductor, with impedance

$$\begin{aligned} Z(\omega) &= j\omega L \\ &= \underbrace{\omega\mu'' L^{\text{air}}\, k_f}_{R_s} + j\omega \underbrace{(\mu' L^{\text{air}}\, k_f)}_{L_s}. \end{aligned} \tag{3.12}$$

Both R_s and L_s can be measured using an impedance analyser, and from these one can derive the real and imaginary parts of the permeability using,

$$\mu' = \frac{L_s}{L^{\text{air}}k_f}, \tag{3.13}$$

$$\mu'' = \frac{R_s}{\omega L^{\text{air}}\, k_f}. \tag{3.14}$$

At small variations of the magnetisation fields, $H \ll 1\,\text{mT}$, the noise in the response magnetic field comes either from eddy currents or from thermal losses mechanisms related to magnetisation relaxation and rotation processes within fixed magnetic domains [107]. At larger magnetisation variations, losses related to domain wall jumps, will induce Barkhausen noise [110], which will become the dominant noise source. For cores

made of tightly wound thin insulated ribbons, the eddy currents are strongly attenuated and the thermal noise becomes dominant. In this case the magnetisation noise can be treated as thermal fluctuations, originating from various dissipation mechanisms, and it can be estimated using the fluctuation-dissipation theorem [108, 111]. If the complex magnetic permeability of the material is known, the magnetisation noise can be calculated by computing the equivalent Johnson-Nyquist noise of the resistor R_s in Equation 3.12. For the circuit in Figure 3.7 consisting of a inductor with ferromagnetic core under analysis L_p, in parallel with another inductor L_i, as is the case of the simplest SQUID coupling circuit, the power spectral density of the core flux noise coupled in the SQUID is given by [108],

$$\langle \Phi^2_{\text{squid}} \rangle = \frac{2k_B T}{\omega} \cdot \frac{L''_p(\omega)}{|L_i + L_p(\omega)|^2} \cdot M_i^2, \tag{3.15}$$

where T is the temperature and k_B is the Boltzman constant.

The following properties are desired in a ferromagnetic core to be used for low intensity current measurement:

- high value of real permeability;
- constant permeability up to frequency of interest;
- low hysteresis losses in the frequency range of interest;

Additionally, the permeability of most materials varies considerably with the working temperature. Particularly relevant for the case of the CCC core is the fact that many materials with high permeability at room temperature will have its permeability strongly decreased when cooled down to cryogenic temperatures. For this reason it is important to select an appropriate material that is able to keep the desired properties even at cryogenic temperatures.

Amorphous and nanocrystalline alloys are good candidate for applications requiring magnetically soft materials such as transformers and inductive devices, due to their very high permeability and small magnetostrictive coefficient [1]. Cobalt-based amorphous alloys, iron-based amorphous alloys, and nanocrystalline alloys have evolved over the past decades with soft magnetic properties which now exceed those of the bulk alloys based on iron, cobalt and iron-cobalt [112]. Figure 3.9 shows the relation between the magnetic permeability and saturation field for different classes of materials.

Initially it was planned that a new core was to be used in the current project and preliminary measurements were performed to compare properties of different types of materials. Measurements of the permeability, at Room Temperature (RT) and liquid helium temperature (4.2 K), were performed on two toroidal core samples, one made of a general cobalt based amorphous material (core A), and another made of a nanocrystaline material, Vitroperm 500F fabricated by VACUUMSCHMELZE GmbH (core B).

[1] Magnetostriction is a property of ferromagnetic materials causing them to change their shape or dimensions during the process of magnetisation.

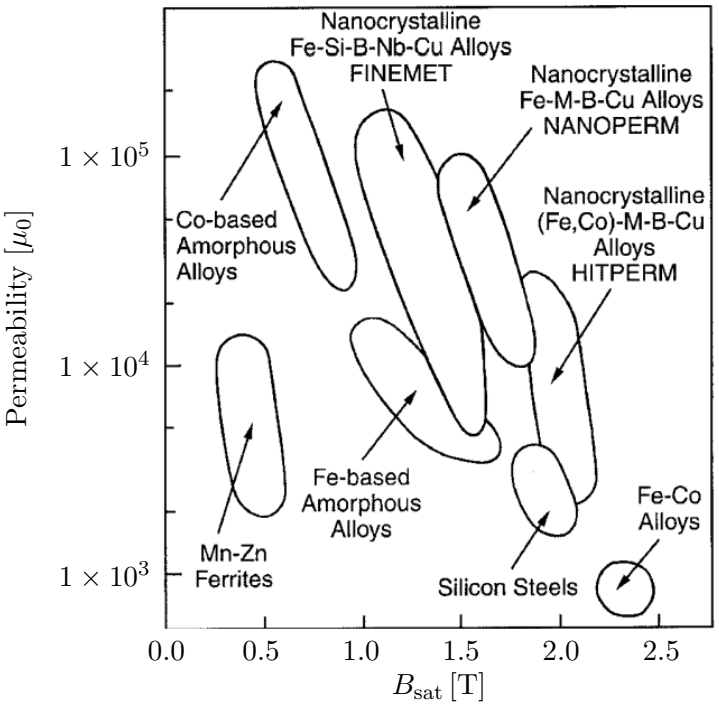

FIGURE 3.9: Relationship between magnetic permeability and saturation field for soft magnetic materials. Adapted from [112].

The measurements were performed on small core samples of these materials with the dimensions shown in Table 3.1. The cores were placed inside a general purpose wide neck cryostat and cooled down with a liquid helium bath. Each core was wound with a 10 loop coil, and each coil was connected inside the cryostat to the vacuum BNC connector feedthrough using a coaxial cable. Outside the cryostat another coaxial cable was used to connect to an impedance analyser.

Core	r_o [mm]	r_i [mm]	h [mm]	N
Core A (amorphous)	24	14	5	10
Core B (nanocrystaline)	8	5	6	10

TABLE 3.1: Dimensions of the sample cores made of an amorphous material and nanocrystaline one.

A Keysight 4294A impedance analyser was used, configured to measure a series inductance L_s and resistance R_s, over a frequency range from 40 Hz to 1 MHz. The impedance analyser was calibrated taking into account the cables length outside of the cryostat, but not the cable located inside the cryostat. However, this should not have any significant impact in the measurement frequency range. From this measurement, the complex permeability was calculated using Equations 3.13 and 3.14. The obtained complex permeabilities of core A and core B, both at room temperature and 4.2 K, are shown in Figure 3.10. The nanocrystaline material of core B shows superior properties

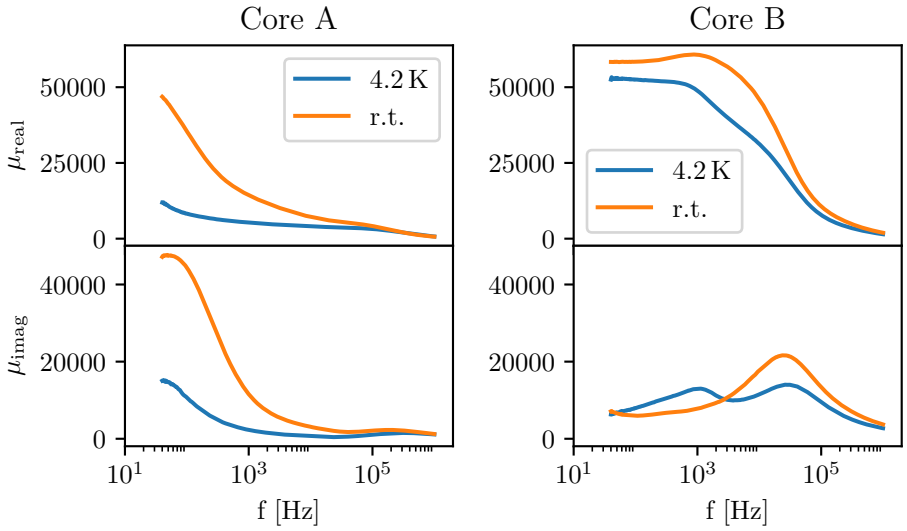

FIGURE 3.10: Measurement of the complex relative permeability of core A (in the left hand side) and core B (in the right hand side) at room temperature and at 4.2 K, performed with a impedance analyser. Top plots: real part of the permeability; Bottom plots: imaginary part of the permeability.

when compared with the amorphous material of core A already at RT, having much smaller μ'' at low frequencies, and constant μ' up to $\approx$ 1 kHz. But more important, when cooled down to 4.2 K the real permeability of core B is reduced only by $\approx$ 10 %, while in the case of core B the initial permeability is reduced by $\approx$ 75 %.

These measurements are inline with results from other comparative studies of nanocrystaline magnetic materials at low temperatures, which have shown that these behave better at very low temperatures when compared to amorphous materials [113, 114]. Nanocrystaline soft magnetic materials are thus good candidates to be used in CCCs due to their high real permeability and low losses particularly at low-frequencies. Additionally, the change in their properties when cooled down to cryogenic temperatures is not as strong as for other types of materials. The amorphous material Metglas, produced by the company Metglas Inc., contrary to most amorphous materials is also able to keep most of its permeability at cryogenic temperatures [111]. However, nanocrystaline materials still exhibit better properties at cryogenic temperatures.

Despite these initial measurements, it was later decided that the already existing FAIR CCC magnetic shield was going to be used in the current project under the established collaboration agreement. This shield already had assembled in its interior a ferromagnetic core, made of the material Nanoperm, which is a nanocrystaline material produced by Magnetec GmbH. The complex permeability of the FAIR CCC core had been previously measured by [115] and is shown in Figure 3.11. Similarly to the material Vitroperm of core B, Nanoperm also presents a very high real permeability and low imaginary permeability at low frequencies. It also presents a better frequency response with constant permeability up to $\approx$ 100 kHz, and lower losses at lower frequencies.

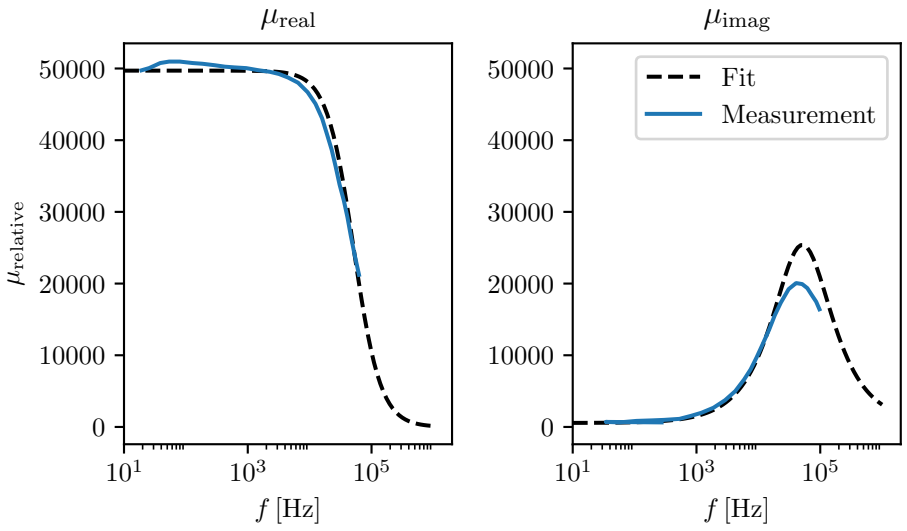

FIGURE 3.11: Complex relative permeability of Nanoperm ferromagnetic cores. Measurements [114] and curve fitting at $T = 4.2\,\text{K}$.

In general there are multiple mechanisms at various scales that account for material magnetisation, and different models have been proposed to describe the frequency dependent permeability. The permeability curves in Figure 3.11 can be fitted to reasonable agreement, with a first-order relaxation Debye model [116, 117],

$$\mu_r(f) = 1 + \frac{K_{\text{spin}}}{1 + j\frac{f}{f_{\text{spin}}}}. \tag{3.16}$$

This model accounts for the gyromagnetic rotation of the material magnetic moments. However, it does not account for the constant imaginary term observed at low frequencies. Such a term $-iK_{1/f}$ will originate a $1/f$ noise spectrum and is known as viscosity term [118],

$$\mu_r(f) = 1 + \frac{K_{\text{spin}}}{1 + j\frac{f}{f_{\text{spin}}}} - iK_{1/f}. \tag{3.17}$$

The measured complex permeability of the Nanoperm material was fitted to the model of Equation 3.17. The resulting parameters were $K_{spin} = 49700$ for the DC magnetic susceptibility, $f_{spin} = 51.5\,\text{kHz}$ for the resonant frequency, and imaginary permeability term at low-frequencies $K_{1/f} = 556$.

The dimensions of the core in the FAIR shield that was used in this project has the following dimensions: $h = 90\,\text{mm}$, $r_0 = 130\,\text{mm}$, $r_i = 102.5\,\text{mm}$, and a single turn winding $N = 1$. At low frequencies the fitted permeability was $\mu_r(f = 0) = 49700$, and an area correction factor must be considered to take into account the proportion of the active magnetic material, which equals $k_f = 0.5$ [114]. Using these parameters, the inductance obtained using Equation 3.9 and 3.11 is 106 µH. This is very close to the measured value at $T = 4.2\,\text{K}$,

$$L_p = 104\,\mu\text{H}. \tag{3.18}$$

The theoretical flux noise induced by the SQUID/FLL and the ferromagnetic core were estimated for the case of the simple coupling circuit in Figure 3.7. The SQUID spectral noise parameters were provided by the manufacturer and are indicated in the beginning of Section 3.1. These are $\approx 0.7\,\mu\phi_0/\sqrt{\text{Hz}}$ for the white noise flux density, and $\approx 0.7\,\text{Hz}$ for the $1/f$-noise corner frequency The theoretical flux noise in the SQUID induced by the ferromagnetic core was estimated using Equation 3.15. The previously modelled complex permeability and pickup inductance as well as the following SQUID parameters $L_i = 400\,\text{nH}$ and $M_i = 2\,\phi_0/\mu\text{A}$ we used. Both noise spectra are plotted in Figure 3.12. The core noise is the dominant contribution up to frequencies of several

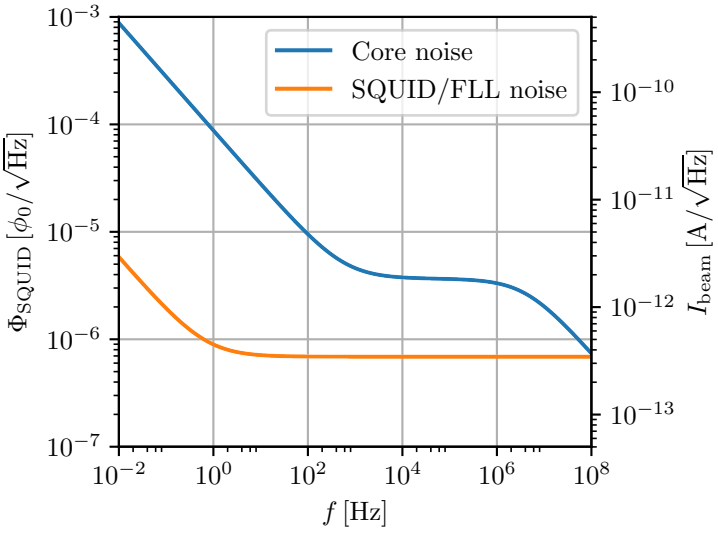

FIGURE 3.12: Theoretical flux spectral density of ferromagnetic thermal noise and SQUID noise. The SQUID/FLL noise spectrum is obtained from the manu

10 MHz, and the combined (core plus SQUID/FLL noise) integrated noise density over the bandwidth $[0.01\,\text{Hz}; 1\,\text{kHz}]$ is 1.65 nA.

3.2.3 Current sensitivity and resolution

If the pickup inductance L_p is much higher than the SQUID input inductance, as is usually the case, the sensitivity of the circuit in Figure 3.7 will be limited to $S_{I_b} = M_i$ as obtained from Equation 3.4. In order to further increase the sensitivity an inductance matching transformer can be used to adapt the larger pickup inductance to the smaller SQUID input inductance, resulting in the circuit shown in Figure 3.13. The sensitivity of this coupling circuit is given by,

$$S_{I_B} = \left[\frac{M_i M_p M_f}{(L_p + L_1)(L_2 + L_i) - M_f^2} \right], \tag{3.19}$$

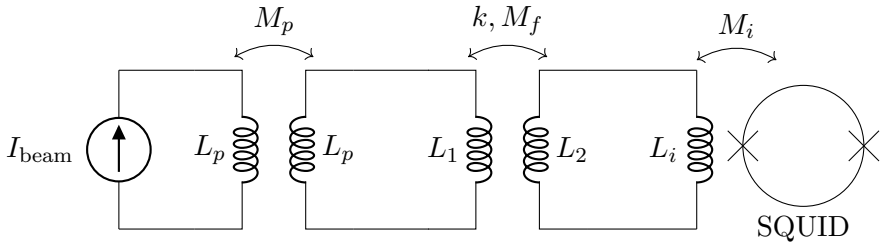

FIGURE 3.13: Coupling circuit with an inductance matching transformer. A coupling factor k is assumed for the matching transformer.

where L_1 and L_2 are the inductances of the primary and secondary of the matching transformer, and M_f is the respective mutual-inductance. This circuit can be transformed into an equivalent simpler circuit as the one without the matching transformer, by applying the following transformation to the SQUID input self inductance and mutual inductance [119],

$$L_i' = L_1 - \frac{M_f^2}{L_i + L_2}, \tag{3.20}$$

$$M_i' = \frac{M_i M_f}{L_i + L_2}. \tag{3.21}$$

For a matching transformer with coupling factor k, the optimal coupling is obtained by making the primary and secondary inductances equal to,

$$L_1 = \frac{L_p}{\sqrt{1-k^2}}, \tag{3.22}$$

$$L_2 = \frac{L_i}{\sqrt{1-k^2}}. \tag{3.23}$$

Figure 3.14 shows the calculated beam current sensitivity S_{I_b} and the beam current resolution $\sigma(I_b)$ as a function of the pickup inductance L_p for different combinations of the coupling circuit and pickup inductance. The geometric dimensions of L_p were kept constant and equal to the dimensions of the used SC shield, shown in Figure 2.25. Then two options were considered: one where L_p is simply an "air" core with inductance $L_p = L^{\text{air}}$ (blue traces), and another where a ferromagnetic core of the Nanoperm material with permeability shown in Figure 3.11 is used, and $L_p = \mu_r L^{\text{air}}$ (orange traces). The same plot also shows the comparison between a coupling circuit where L_p is directly connected to L_i (dashed traces), and a coupling circuit where a matching transformer with high coupling factor $k_f = 0.99$ (this value is usually even higher) is used (continuous traces). In the beam current resolution calculations a SNR= 1 and a bandwidth up to 1 kHz were considered.

Introducing the matching transformer considerably improves the sensitivity. The bigger the difference between L_p and L_i, the bigger the improvement brought by the matching transformer is. When $L_p \sim L_i$, having or not having the matching transformer plays no difference. A similar improvement occurs for the current resolution, although

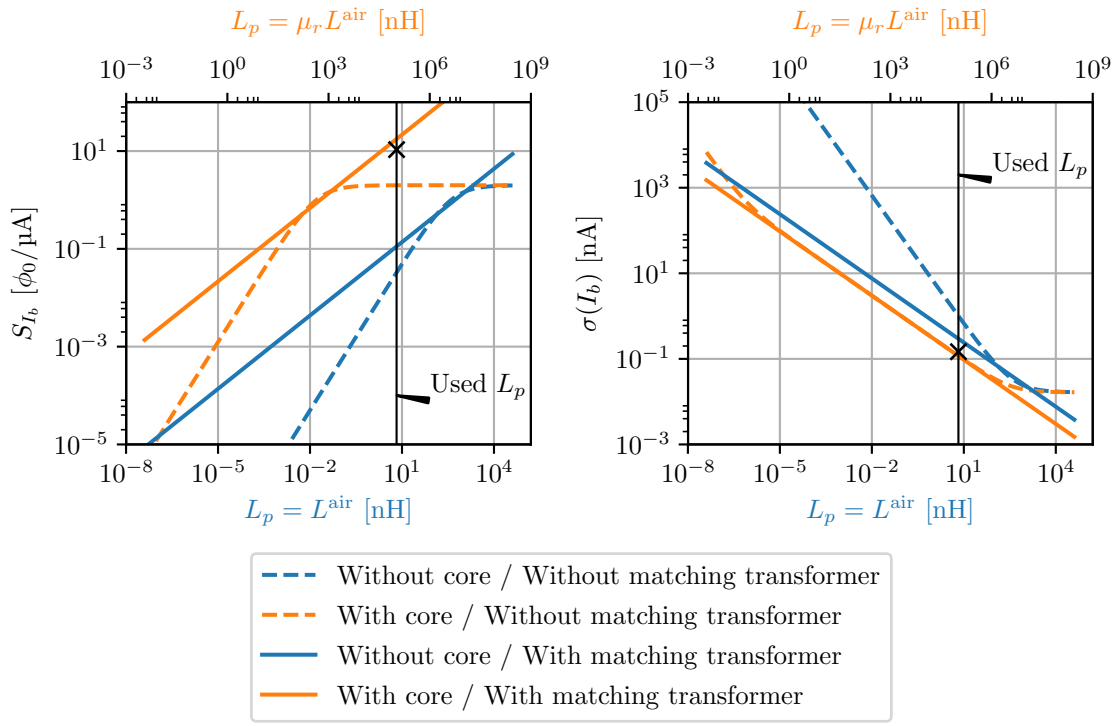

FIGURE 3.14: Coupling circuit sensitivity and beam current resolution computed as a function of the pickup inductance L_p for different configurations of the coupling circuit, with SQUID parameters given in Section 3.1. Left plot: sensitivity; Right plot: current resolution. The crosses indicated the theoretical parameters of the implemented circuit.

in the case where L_p has a magnetic core, this difference becomes relevant only when L_p and L_i are separated by more than 4 orders of magnitude.

Having L_p with a magnetic core increases the sensitivity by more than 2 orders of magnitude when a matching transformer is used, and by more than 4 orders of magnitude when no transformer is used. However, the improvements in current resolution are much less significant and of a factor slightly higher than 2, when comparing two circuits with matched inductances.

The inductance $L_p = 104\,\mu\text{H}$ of the pickup inductor with a magnetic core used in the current project is indicated by a vertical line in Figure 3.14. It was decided to use the option with a magnetic core pickup and matching transformer, which provides the best theoretical resolution for equivalent dimensions.

For the coupling factor $k_f = 0.99$, the optimal values of L_1 and L_2 would imply a large number of winding turns on a relatively large core, which would be unpractical to be installed near the SQUID inside a small SC shielding cartridge as shown in Figure 1.12. A sub optimal coupling was chosen with a matching transformer with the following parameters, this results in a small decrease in sensitivity and current resolution:

$$L_1 = 101\,\mu\text{H}, \qquad N_1 = 15; \tag{3.24}$$

$$L_2 = 450\,\text{nH}, \qquad N_2 = 1. \tag{3.25}$$

This results in the following theoretical coupling sensitivity and beam current resolution (marked by a cross in Figure 3.14),

$$S_{I_b} = 10.7\,\phi_0/\mu\text{A}, \tag{3.26}$$

$$\sigma(I_b) = 0.15\,\text{nA}. \tag{3.27}$$

The spectral density of the flux noise coupled to the SQUID due to the magnetic core alone, over a 10 MHz and 20 MHz bandwidth, amounts to,

$$\Phi^{\text{core}} = 3.34 \times 10^{-6}\,\phi_0/\sqrt{\text{Hz}}, \qquad BW = 10\,\text{MHz}, \tag{3.28}$$

$$\Phi^{\text{core}} = 2.38 \times 10^{-6}\,\phi_0/\sqrt{\text{Hz}}, \qquad BW = 20\,\text{MHz}. \tag{3.29}$$

These values will be important to estimate stability of the SQUID/FLL feedback system.

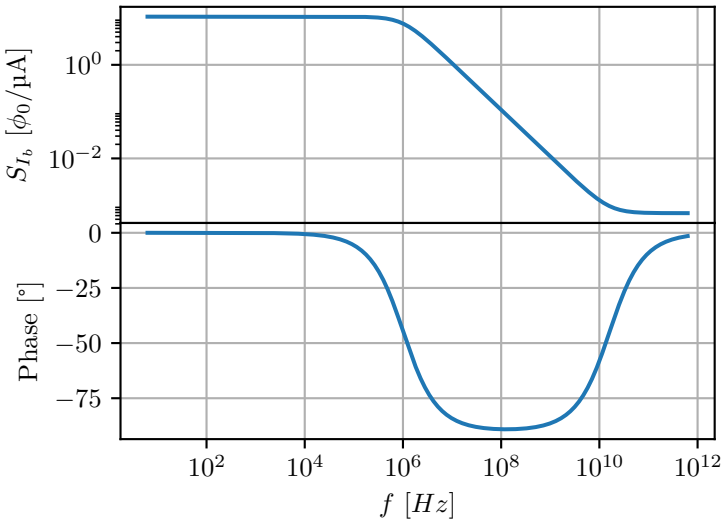

FIGURE 3.15: Theoretical transfer function of the coupling circuit computed using the modelled frequency dependent permeability of the ferromagnetic core in L_p.

The decreasing permeability for $\gtrsim 10\,\text{kHz}$ results in a decreased sensitivity S_{I_b} above these frequencies. It is possible to use the permeability model in Equation 3.16 to compute the frequency dependent sensitivity, or transfer function of the coupling circuit, by replacing $L_p(s)$ as given by,

$$L_p(s) = L_p^{\text{air}}\left(1 + \frac{K_{\text{spin}}}{1 + s/s_0}\right) \qquad \text{and} \qquad L_p = L_p(0) = L_p^{\text{air}}(1 + K_{\text{spin}}), \tag{3.30}$$

in Equation 3.19 resulting in

$$S_{I_b}(s) = \frac{\left[(M_f M_i L_p^{\text{air}})\right](s/s_0) + M_f M_i L_p}{\left[(L_1 + L_p^{\text{air}})(L_2 + L_i) - M_f^2\right](s/s_0) + (L_2 + L_i)(L_1 + L_p) - M_f^2}, \tag{3.31}$$

where $s_0 = 2\pi f_{\text{spin}}^{\text{res}}$. For low frequencies ($s \ll s_0$) the constant coupling function of Equation 3.19 with pickup inductance given by L_p is recovered, and for high frequencies ($s \gg s_0$) S_{I_b} assumes the same form but with the pickup core inductance given by L_p^{air} as expected due to the vanishing permeability of the core. The magnitude and phase plots of this transfer function are shown in Figure 3.15.

3.3 SQUID/FLL bandwidth and slew rate limits

Due to the non-linear and periodic nature of the SQUID V-Φ transfer function, the SQUID/FLL systems may present an unstable behaviour if the feedback loop is not able to lock into any working point, or if the working point jumps from crest to crest in the V-Φ curve. This may happen due to excess noise in the system or too large slew rate of the input signal.

When a SQUID is operated in the FLL mode with the circuit shown in Figure 2.18, the SQUID output noise as well as the pre-amplifier noise will be amplified by the feedback chain, and reintroduced into the SQUID. For a constant input signal the flux error $\Phi_{\text{error}} = \Phi_{\text{in}} - \Phi_{\text{fb}}$, in Equation 2.50, should be ideally zero, but due the injected noise Φ_{error} will always be non-zero. When the amplitude of the error exceeds $1/2\phi_0$, the working point of the SQUID feedback circuit may undergo a flux jump by one or more periods along the $V - \Phi$ characteristic, as shown in Figure 3.16. The error signal

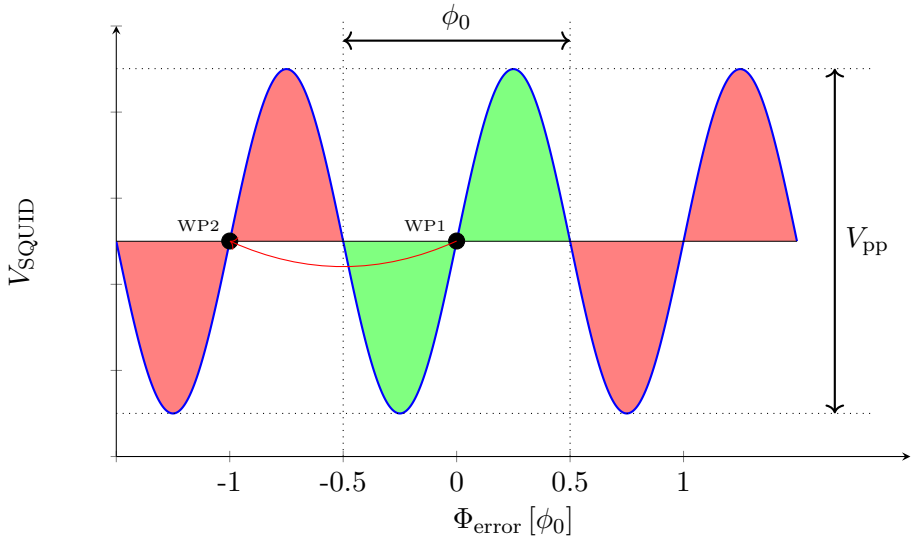

FIGURE 3.16: SQUID V-Φ transfer function, indicating an instability event resulting in a flux jump that forces the FLL stable working point to change from WP1 to WP2. This may occur if Φ_{error} goes over the stability $\pm\phi_0/2$ region highlighted in green.

may exceed this limit either because the system noise level is too high, or because the SR (defined in Equation 2.55) of the applied signal Φ_{in} is too fast for the feedback loop to be able to track its change. Both these situations may cause the amplitude of Φ_{error} to exceed the stability limit.

To measure input signals with a high SR, the FLL bandwidth should be sufficiently large to be able to continuously track the input signal. However, a larger the system bandwidth will also increase the noise integrated by the feedback loop and coupled to the SQUID. Hence, there imposes an upper limit in the FLL bandwidth. The following analysis studies the system stability and the bandwidth limits derived from these conditions. This follows from the work presented in [120].

A flux jump condition can be defined by looking at the probability for the noise to exceed $\pm 1/2\phi_0$ at any given instant. If the distribution function of the noise values in time can be modelled by a Gaussian distribution $P(\Phi^{\text{noise}})$, the probability for a flux jump to occur will correspond to the integral of side bands shown in Figure 3.17. The

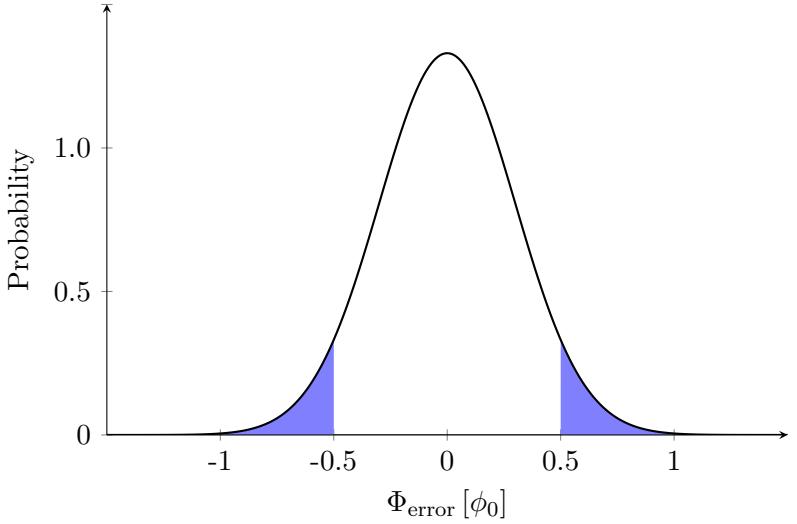

FIGURE 3.17: Probability density of the flux distribution with no input signal applied. In blue is indicated the instability region where flux jumps are likely to occur.

flux jump rate ν_{FJ}, can be estimated by the ratio of the probability of the noise to go above the stability point over its correlation time. If the noise also has a white noise power spectrum, it is reasonable to estimate the correlation time by the inverse of the bandwidth of the noise coupled to the SQUID, which equals the FLL loop bandwidth given by the frequency of its single-pole $BW = f_p$, resulting in,

$$\nu_{FJ} = BW_{\text{noise}} \cdot P(|\Phi^{\text{noise}}| > \phi_0/2). \tag{3.32}$$

Using this equation the flux jump rate was computed as a function of the bandwidth for different levels of total flux noise in the SQUID, with the resulting curves shown in Figure 3.18

A simulation of the dynamic of the SQUID/FLL in Figure 3.16 was performed using the Mathworks Inc./Simulink. This simulation used the SQUID transfer function that was measured in Figure 3.5, and it considered a single source of white noise. The details of the model can be found in Appendix A. Configuring the FLL loop with $R_f = 1\,\text{k}\Omega$, $GBW = 1\,\text{GHz}$, working point in a negative slope of the V-Φ-curve results in

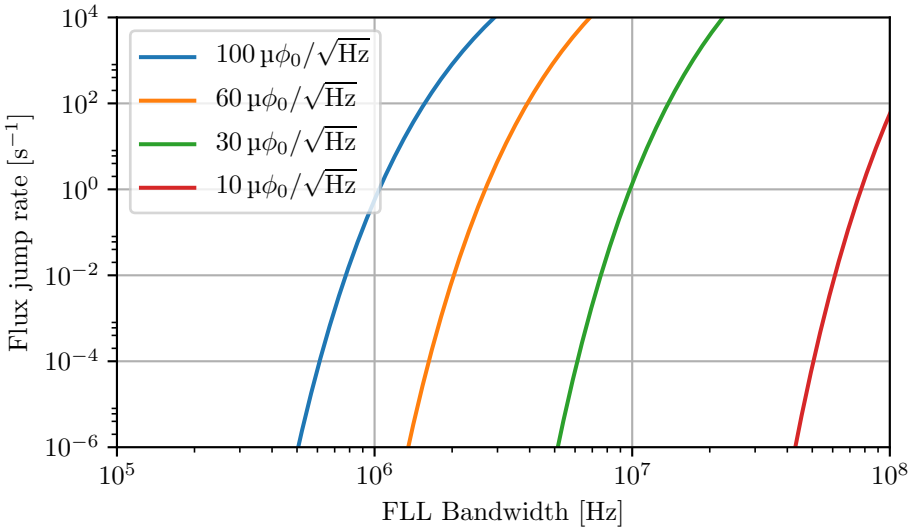

FIGURE 3.18: Flux jump rate for different values of average flux noise coupled to the SQUID, as a function of the bandwidth of the feedback loop.

a FLL bandwidth $BW_{\text{FLL}} = 15.9\,\text{MHz}$ and gain $G_{\text{FLL}} = 43\,\text{mV}/\phi_0$, obtained from Equations 2.54 and 2.53, respectively. For example, adding to the SQUID flux a level of white Gaussian noise with spectral density equal to $\Phi^{\text{noise}} = 30.5\,\mu\phi_0/\sqrt{\text{Hz}}$ and no input signal, results in an unstable system with flux jumps occurring as shown in the simulation results in Figure 3.19. A simulation step of $t_s = 1\,\text{ns}$ was used to ensure that all the dynamics of the system was captured.

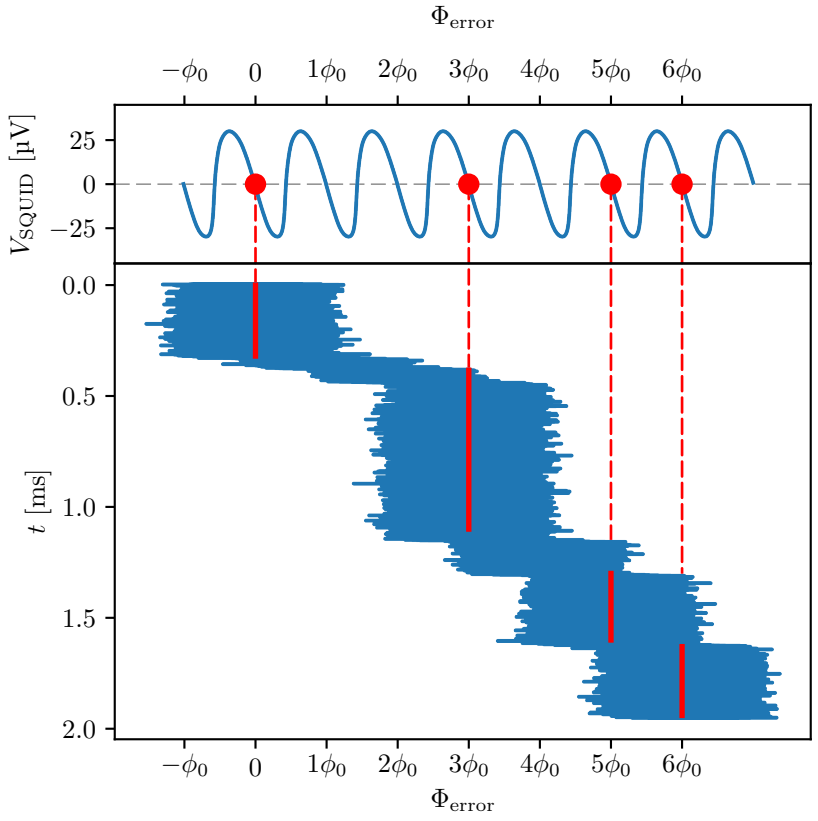

FIGURE 3.19: Simulation of the SQUID/FLL dynamics when a conjugation of excess noise and high bandwidth causes successive flux jumps of the working point. Top: V-Φ curve with the temporarily stable working points indicated in red; Bottom: time evolution of the total SQUID flux $\Phi^{\text{total}} = \Phi^{\text{noise}} + \Phi^{\text{fb}}$.

The amplitude of the flux jumps can be a single flux quantum ϕ_0, or multiple ϕ_0 can be covered between the temporary lock at two different working points. These jumps show up in the measurement output V_{out} like jumps in the zero signal offset, as shown in Figure 3.20. For a sensitivity of the coupling circuit equal to $S_{I_b} = 10\,\phi_0/\mu\text{A}$, each flux jump would correspond to a measured beam current offset of $\delta I_b = 100\,\text{nA}$ which is one order of magnitude above the desired current resolution for the CCC monitor. Hence, it is fundamental to guarantee that no flux jumps occur in the designed monitor.

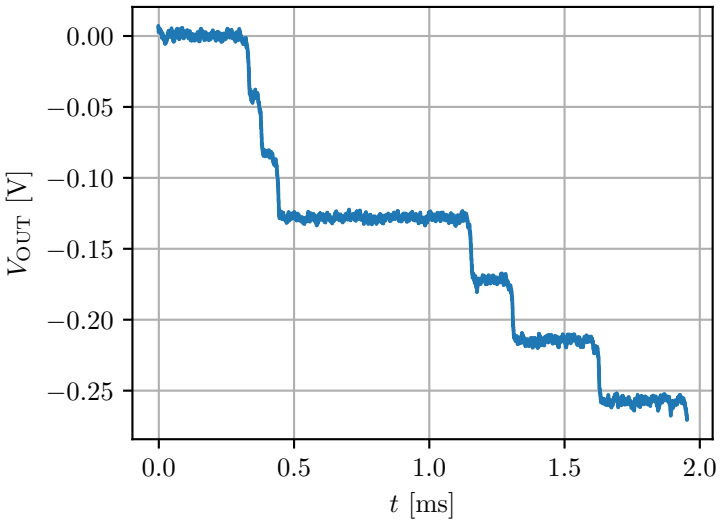

FIGURE 3.20: Voltage output signal resulting from the simulation of the SQUID/FLL dynamics, where the successive flux jumps of the working point cause a jump in the zero signal offset.

The previous analysis assumed that no signal was present at the SQUID input. But when a time-varying signal Φ_{in} is present, and since the open loop gain is finite, there will be a non zero value of the flux error $\Phi_{\text{error}} = \Phi_{\Delta}^{\text{signal}}$ in the SQUID. Considering that the FLL closed loop transfer function has a single pole at $2\pi f_p$, and that the input signal is a sine wave with frequency much below the cutoff frequency, then the SQUID flux error caused by an input signal with slew rate, SR, will be approximately given by[2],

$$\Phi_{\Delta}^{\text{signal}} \approx \frac{SR}{2\pi f_p}. \tag{3.33}$$

This flux error will add up to the Gaussian flux noise,

$$\Phi_{\text{error}} = \Phi^{\text{noise}} + \Phi_{\Delta}^{\text{signal}}, \tag{3.34}$$

and shift the probability distribution as shown in Figure 3.21.

[2]Only valid for the case where the closed loop transfer functions is of the first-order low-pass type.

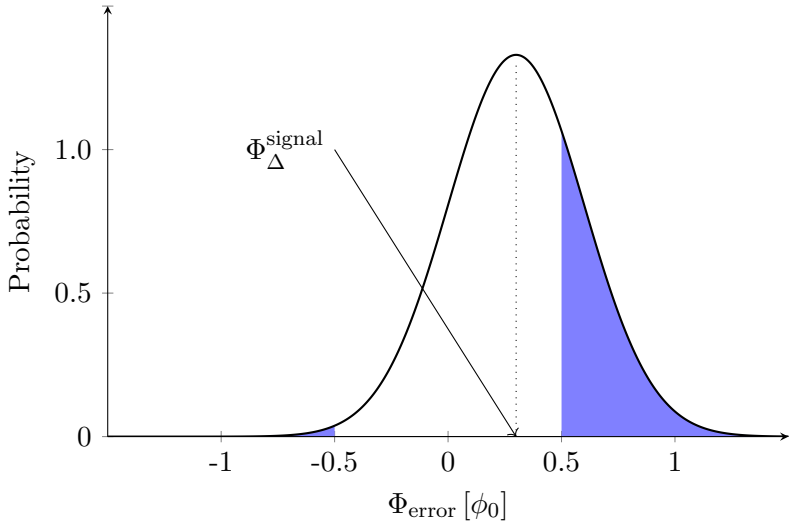

FIGURE 3.21: Probability density of the flux distribution with a time-varying signal applied. The slew rate of the signal induces a flux error equal to Φ_Δ In blue is indicated the instability region where flux jumps are likely to occur.

This shift will increase the area of the Gaussian distribution falling beyond $\phi_0/2$ and thus increase the probability for a flux jump to occur, which is now given by

$$\nu_{\text{FJ}} = BW_{\text{noise}} \cdot P\left(|\Phi^{\text{noise}} + \Phi_\Delta^{\text{signal}}| > \phi_0/2\right). \tag{3.35}$$

By specifying a value for the maximum allowed jump rate ν_{FJ}, it is possible to compute back what the maximum allowed SR of the signal at SQUID input must be. The AD cycle has a typical duration of $\approx 100\,\text{s}$, hence it was considered that a single jump occur could occur only every $10\,000\,\text{s}$ which is two orders of magnitude longer than the AD cycle. This corresponds to a flux jump rate $\nu_{\text{FJ}} = 10^{-4}/\text{s}$. The maximum SR was computed by using an iterative method, where for each value of the noise bandwidth BW_{noise} and flux noise Φ^{noise}, the flux jump rate ν_{FJ} is computed for an array of $\Phi_\Delta^{\text{signal}}$ values. From the resulting array of flux jump rates, the one closest to the maximum specified value for this parameter is selected. Assuming that the input signal is a sine wave it is trivial to obtain the SR from $\Phi_\Delta^{\text{signal}}$ using Equation 3.33. The resulting plot of the maximum allowed SR as a function of the bandwidth is shown in Figure 3.22 for various levels of flux noise density.

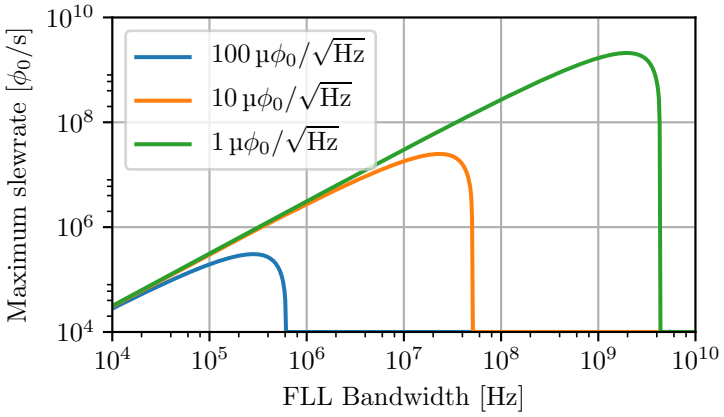

FIGURE 3.22: Maximum allowed slew rate of the magnetic flux input signal as a function of the FLL bandwidth, assuming a flux jump rate smaller than 1 per hour. Different curves correspond to different average flux spectral noise density.

As an example of what happens when the signal slew rate renders the system unstable, a simulation was run using a sine wave input with $f = 10\,\text{kHz}$ and amplitude $10\,\phi_0$. The previous Simulink simulation was used but with a smaller noise level equal to $\Phi^{\text{noise}} = 10 \times 10^{-6}\,\phi_0/\sqrt{\text{Hz}}$, and with the GBW parameter set to 0.4 GHz, and 0.8 GHz. These result in the following pole frequencies $f_p \approx 5.3\,\text{MHz}$ and $f_p \approx 10.6\,\text{MHz}$, which for the present case of a first-order system is identical to the FLL bandwidth. The SR of the input signal is $0.63\,\text{M}\phi_0/\text{s}$. The resulting SQUID flux and output voltage signals are shown in Figure 3.23.

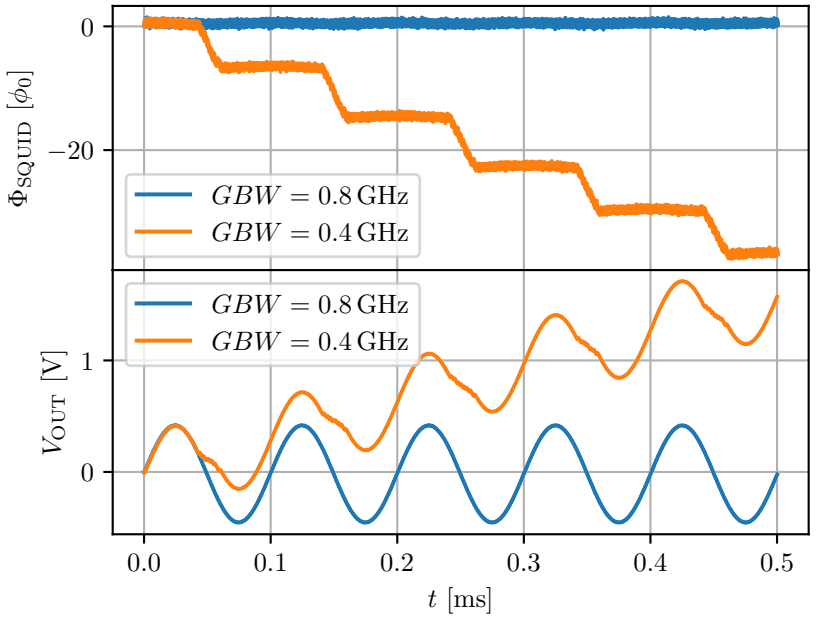

FIGURE 3.23: Simulation of the response of two SQUID/FLL systems to a sinusoidal input signal with slew rate near stability limit. Top plot: SQUID flux signal; Bottom plot: measurement output.

Momentum [GeV/c]	f_{rf} [MHz]	*RF* harmonic	Number of bunches	Bunch length [ns]	SR [kA/s]
Injection: 3.57	9.54	6	4	30	8.60
3.57 - 2.00	1.59 - 1.49	1	1	172 - 420	1.05 - 0.18
2.00 - 0.30	1.49 - 0.50	1	1	136 - 859	1.67 - 0.04
0.30 - 0.10	1.50 - 0.52	3	3	104 - 370	0.95 - 0.08
Extraction: 0.10	0.17	1	1	110	2.56

TABLE 3.2: Parameters of the AD beam during the different bunched phases of the cycle shown in Figure 1.3.

With the smaller bandwidth the feedback loop is not able to track the input signal, resulting in a distorted output due to the flux jumps occurring when the input signal goes through its highest SR points, while the system with the higher bandwidth is already able to accurately track the input signal at all moments.

More details about the stability of SQUID/FLL systems when subject to high SR signals can be found in [121].

3.3.1 AD bunched beam parameters

For a nominal injection, with $N = 5 \times 10^7\,\overline{p}$ the average beam current ranges from 12.7 µA, at injection, to 1.4 µA, at extraction. The main beam parameters at the different energy plateaus of the AD cycle were presented in Table 1.1. The parameters related to the beam bunch structure are presented in Table 3.2. These will be used to compute the SR of the beam current.

The average current profile during the deceleration is depicted in Figure 3.25 assuming a constant number of antiprotons $N = 5 \times 10^7\,\overline{p}$. The beam is injected with a relativistic velocity factor of $\beta = 0.97$, and by the end of the cycle the beam is already non-relativistic with $\beta = 0.11$. This transition to a non-relativistic regime is clearly visible in the deceleration ramps, where in the first two the current changes non linearly with the momentum, and by the last ramp this variation is almost linear.

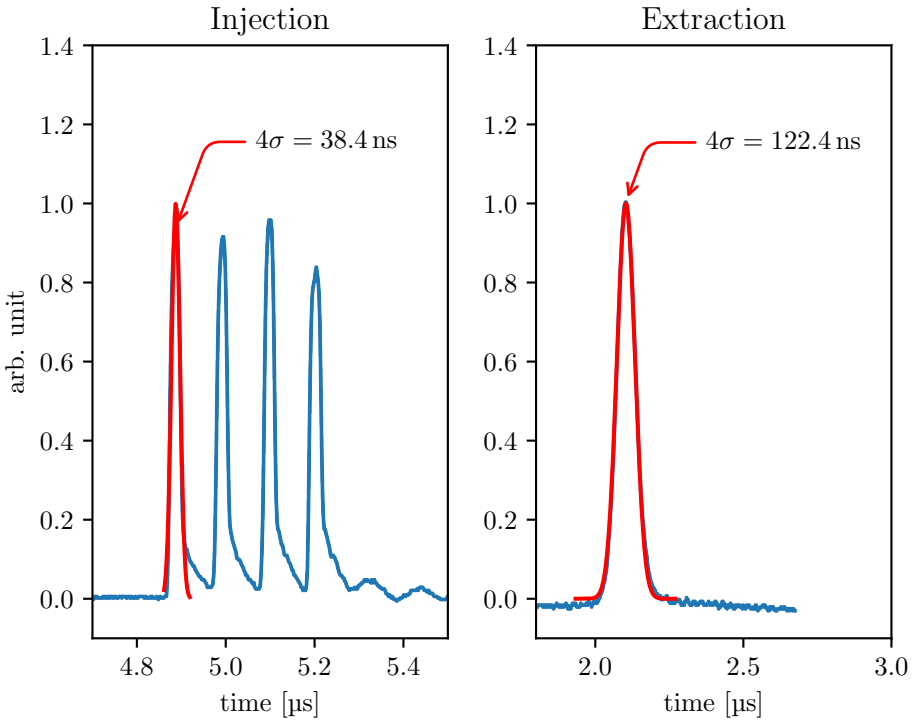

FIGURE 3.24: AD bunch shape at injection and extraction determined by the Fast-BCT.

Assuming a Gaussian longitudinal charge distribution for the bunches during the bunched phases, which is a reasonable assumption as seen in Figure 3.24, the instantaneous beam current is given by,

$$I_b(t) = \frac{Q}{\sqrt{2\pi}\sigma_t} \exp\left(-\frac{(t-t_0)^2}{2\sigma_t^2}\right), \tag{3.36}$$

where $Q = N \cdot e$ is the total charge in bunch and $4\,\sigma_t$ is the bunch length in time. The SQUID systems using a FLL readout scheme are limited by the SR of the input magnetic flux signal. Hence, it is fundamental to assess the SR of the beam during its different bunched phases. The maximum value of the first derivative of Eq. 3.36 results in,

$$SR = \max\left(\frac{\mathrm{d}I_b}{\mathrm{d}t}\right) = \pm\frac{Q}{\sqrt{2\pi}\sigma_t^2} \exp(-1/2). \tag{3.37}$$

Using this equation and the bunch "length" in time for the different bunched beam phases, specified in Table 3.2 for a $4\sigma_t$ length, together with the number of bunches, allows to calculate the maximum SR of the beam current SR for each bunched phase. This quantity is shown in the last column of the table. The highest observed SR is 8.60 kA/s occurring at injection when the beam is composed of 4 bunches, each one populated with $N = 1.25 \times 10^7\,\overline{p}$ and length equal to $4\sigma_t = 30\,\mathrm{ns}$. From the signals of wide-band BCTs at the injection and extraction lines of the AD, shown in Figure 3.24, it was possible to observe that in the real beam the bunches length should be even slightly

higher. Nevertheless, the more demanding nominal shorter bunch lengths were used in the SR estimation.

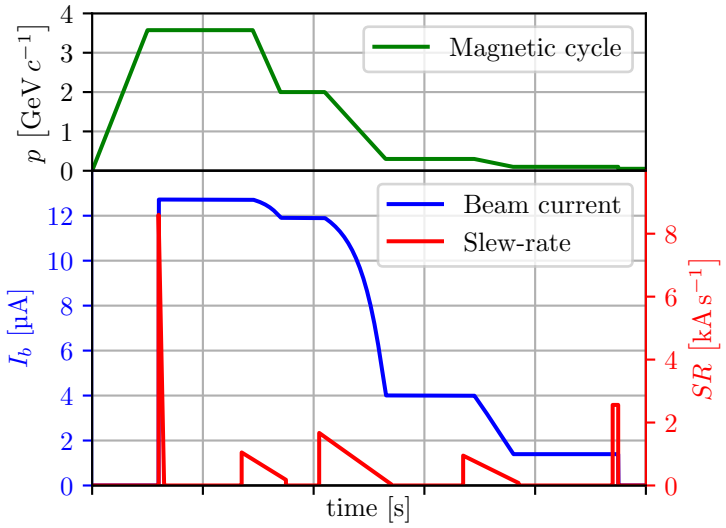

FIGURE 3.25: Evolution of the beam current and SR during the AD cycle, assuming a nominal injection and 100 % deceleration efficiency. During the coasting beam phases the particle velocity is kept constant, and during the bunched phases particles are decelerated.

The SR of the AD bunched beam at injection reaches a value of 8.6 kA/s, which for a constant sensitivity given by Equation 3.26 would result in flux signal coupled to the SQUID with SR 86 Gϕ_0/s, this is more than 4 orders of magnitude higher than the achievable FLL stability limits. Considering now the frequency dependent sensitivity due to the ferromagnetic core given in Equation 3.31, and computing the response of this system to the AD injection beam results in a SR of 1.2 Gϕ_0/s. This value is still too high and additional filtering needs to be performed in the coupling circuit before the flux signal reaches the SQUID to reduce the its SR.

3.3.2 Reducing the AD beam slew rate

The fact that the circuit loops connecting the pickup inductance to the SQUID input need to be kept superconducting in order to couple DC fields imposes strong constraints on the exact configuration and the order of the filter, since it is not possible to add any series resistance in these loops. One of the simplest ways of further reducing the SR is to use a *RC* filter inserted in parallel with the inductances of the coupling circuit

An *RC*-filter in the CCC coupling circuit could be inserted in the primary or secondary side of the matching transformer. As it results from the calculations, for the same values of R and C a lower cutoff frequency can be achieved by placing the filter in the primary side of the circuit. The two simplest possible configurations are having an *RC*-series filter as shown in Figure 3.26, or having an *RC*-parallel filter as shown in Figure 3.27. This option was the first to be considered since it was initially thought that

the suppression of the additional Johnson-Nyquist noise at low frequencies due to the series capacitor and resistive element would result in an overall noise reduction across the entire FLL bandwidth. Computing the transfer function for this circuit one obtains

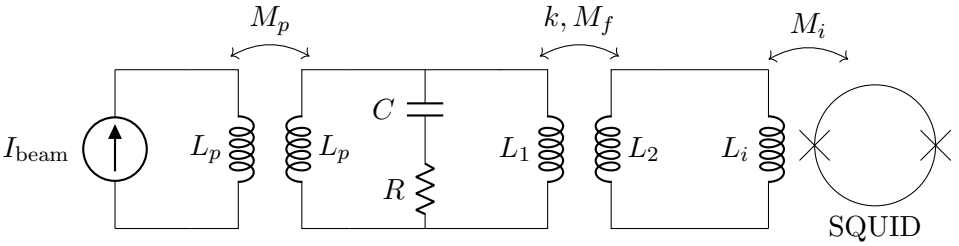

FIGURE 3.26: Coupling circuit with a matching transformer and a RC-series filter.

$$S_{I_b}(s) = \frac{M_i' R}{L_i'} \left[\frac{s + 1/(RC)}{s^2 + s\left(R/\overline{L}\right) + 1/\left(\overline{L}C\right)} \right], \tag{3.38}$$

with L_i' and M_i' defined in Equations 3.20 and 3.21, and $\overline{L}$ as

$$\overline{L} = \frac{L_i' L_p}{L_i' + L_p}. \tag{3.39}$$

This second order transfer function has two poles and one zero, hence the high-frequency roll-off attenuation will be limited to $-20\,\text{dB/dec}$. Also, depending on the poles locations the transfer function may present a resonance near the cutoff frequency.

Since the coupling network needs to be cooled down to cryogenic temperatures, this limits the type of capacitors and resistors that can be used. Most commonly used capacitors at cryogenic temperatures are NPO/C0G[3] ceramic [122], although these exhibit nearly the same capacitance when cold, they are limited in value up to $\approx 100\,\text{nF}$. Some metalised film capacitors also maintain a good performance at cryogenic temperatures, specially ECPU series capacitors from Panasonic [123, 124], which are available up to $\approx 1\,\mu\text{F}$ and loose only about 20 % of their room-temperature capacitance. So the value of C is limited up to $\approx 10\,\mu\text{F}$, obtainable by connecting a few capacitors in parallel. For the resistances there is a wider range of components suitable for working at cryogenic temperatures. Carbon composition and ceramic resistors show a higher change in value ($> 15\,\%$) when cooled to cryogenic temperatures, while metal film and wire wound resistors are extremely stable [125]. Other types of resistor construction can also be used in cryogenic applications depending on the required precision. All these are usually available in a wide range of values.

[3]NPO, for the type of ceramic material, and C0G, for the very low temperature coefficients and strict tolerances, are both designations according to the EIA-RS-198 standard.

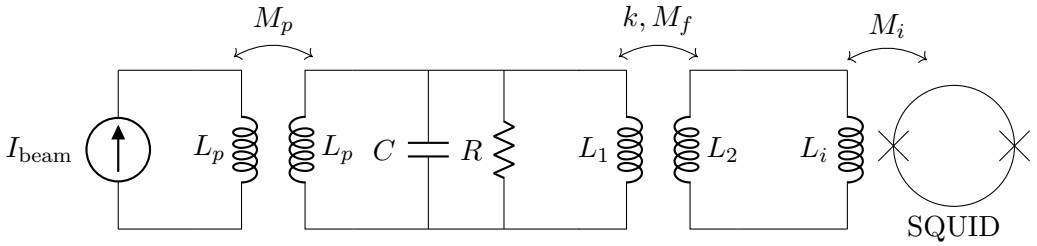

FIGURE 3.27: Coupling circuit with a matching transformer and a RC-parallel filter.

Parameter	RC-series	RC-parallel
ω_n	$1/\sqrt{\overline{L}C}$	$1/\sqrt{\overline{L}C}$
ξ	$R/2 \cdot \sqrt{C/\overline{L}}$	$1/2R \cdot \sqrt{\overline{L}/C}$
ω_{zero}	$1/RC$	no zero

TABLE 3.3: Parameters of second-order system obtained for the coupling circuit with the RC-series and RC-parallel filter.

Instead of a RC-series filter, a second possible configuration is that of a parallel RC-filter as shown in Figure 3.27. The transfer on for this circuit is given by,

$$S_{I_B}(s) = \frac{M_i'}{L_i' C} \left[\frac{1}{s^2 + s(1/RC) + 1/(\overline{L}C)} \right]. \tag{3.40}$$

This second-order low pass system has no zeroes and hence the roll-off attenuation at high frequencies is $-40\,\text{dB/dec}$. The pole location will also be different from the RC-series filter.

Considering the following general form for the denominator of a second order system

$$D(s) = s^2 + 2\xi\omega_n s + \omega_n^2, \tag{3.41}$$

where ω_n is the natural frequency, and ξ is the damping ratio. If $\xi < 1$ the system is underdamped and the step response will present some oscillation, while if $\xi > 1$ the step response does not oscillate. In Table 3.3 are the equations of the second order parameters for both coupling circuits with the RC filter. Appendix B contains a summary of how these parameters affect the shape of the time and frequency responses. The frequency responses of the two circuits for $R = 1\,\Omega$ and $C = 1\,\mu\text{F}$ or $C = 10\,\mu\text{F}$ were computed using Equations 3.40 and 3.38, and are shown in Figure 3.28. For the same parameters, the cutoff frequency of the RC-series is higher and it also presents a resonant peak, which is not present in the RC-parallel case. Looking into reducing the resonant peak by increasing the damping factor ξ, given in Table 3.3, of the RC-series circuit one could consider further increasing C, or increasing R. But a higher R will decrease the frequency of the zero, which will reduce the available attenuation to $20\,\text{dB/dec}$ at lower frequency. Therefore, the circuit with the RC-parallel filter was chosen.

Using the values of the different inductances of the implemented coupling circuit

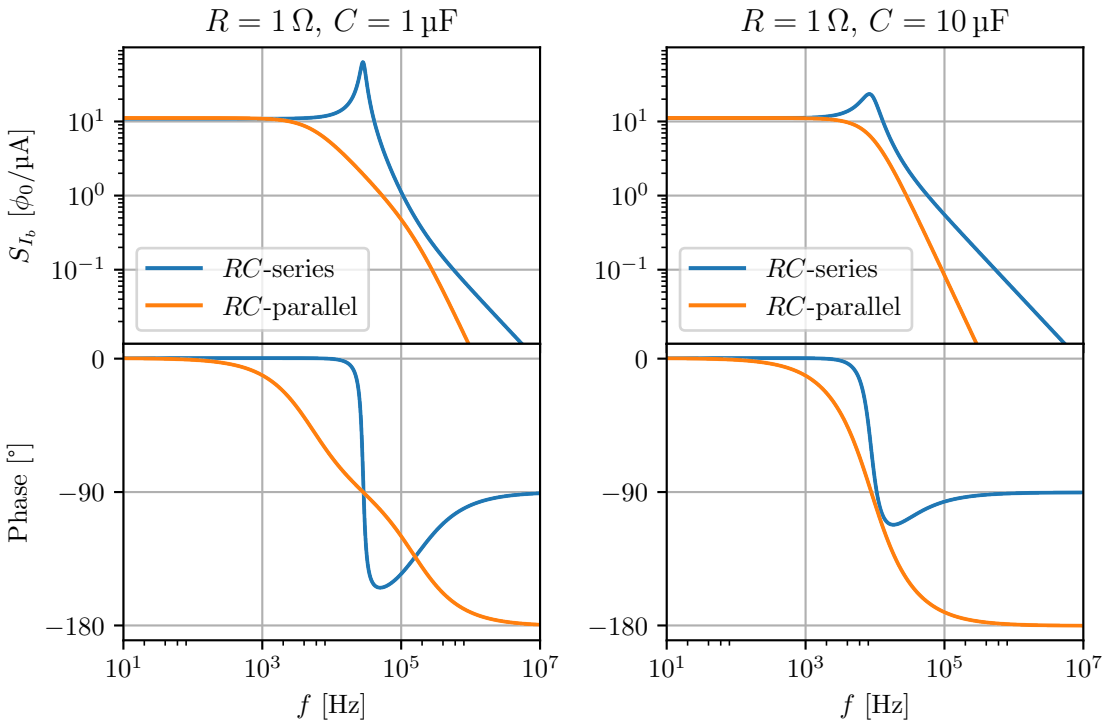

FIGURE 3.28: Comparison of the transfer function of the coupling circuit with an *RC*-series and an *RC*-parallel filter. Left plot: with $R = 1\,\Omega$, $C = 1\,\mu$F. Right plot: with $R = 1\,\Omega$, $C = 10\,\mu$F.

presented in Section 3.2.3, , the resulting value of $\overline{L}$ (Equation 3.39) is $\overline{L} = 32.5\,\mu$H. To have a cutoff frequency of 1 kHz and a system that is close to critical damping would require that $C \approx 779\,\mu$F. This value is too high to be practically achievable. Instead, the values $C = 10\,\mu$F ($C = 12\,\mu$F at room temperature) and $R = 0.225\,\Omega$ ($R = 0.25\,\Omega$ at room temperature) were selected. This results in two real poles located at $f_1 = 1.12$ kHz and $f_2 = 69.61$ kHz. The magnitude and phase of the resulting transfer function is shown in Figure 3.29.

One of the arguments for the *RC*-series circuit was a smaller amount of Johnson-Nyquist noise from the resistor coupled to the SQUID. To compare the noise level introduced by both filter configurations and for different values of R the expressions have been computed. The thermal noise can be modelled by a current source i_n in parallel with the resistor, with the one sided power spectral density given by,

$$\mathrm{PSD}(i_n) = \frac{4k_B T}{R}. \tag{3.42}$$

For the *RC*-series circuit this results in

$$\Phi^{\mathrm{noise}} = \frac{L_p M_i'}{L_p + L_i'} \cdot \frac{s(R/\overline{L})}{s^2 + s(R/\overline{L}) + 1/(\overline{L}C)} \cdot i_n. \tag{3.43}$$

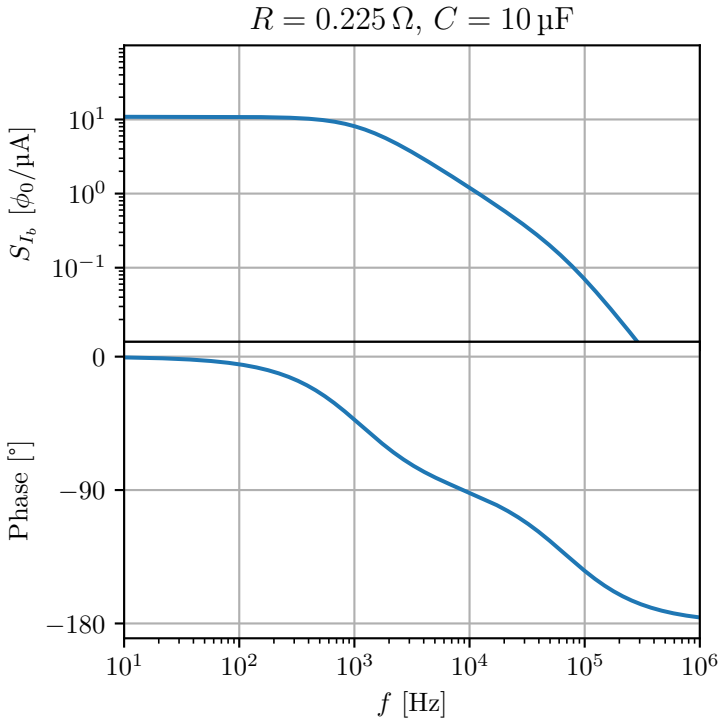

FIGURE 3.29: Transfer function of the implemented coupling circuit with an *RC*-parallel filter, with $R = 0.225\,\Omega$, $C = 10\,\mu$F.

For the *RC*-parallel circuit this results in a flux noise at the SQUID equal to,

$$\Phi^{\text{noise}} = \frac{M_i'}{L_i' + C} \cdot \frac{1}{s^2 + s(1/RC) + 1/(\overline{L}C)} \cdot i_n. \tag{3.44}$$

The spectrum of the thermal noise induced by the resistor R alone was computed for both circuits using Equations 3.43 and 3.44. This is shown in Figure 3.30 for both the *RC*-series and *RC*-parallel circuits, with $R = 0.225\,\Omega$ and $C = 10\,\mu$F. The noise at low-frequencies which is more severe in the *RC*-parallel case will reduce the resolution of the average beam current measurement. The Root Mean Square (RMS) flux noise in the desired measurement bandwidth of 1 kHz, referred to the input beam current is,

$$\sigma(I_\text{b}) = 8.35\,\text{pA}, \qquad RC\text{-series}, \tag{3.45}$$

$$\sigma(I_\text{b}) = 0.92\,\text{nA}, \qquad RC\text{-parallel}. \tag{3.46}$$

This value should not compromise the desired current resolution of $\sigma(I_\text{b}) \leq 10\,\text{nA}$. The additional noise will also increase the probability of flux jumps to occur.

Figure 3.30 shows that for both circuits the resistor noise is concentrated below 1 MHz, and for both circuit it results in a total flux noise equal to $14.5 \times 10^{-3}\,\phi_0$. This is equivalent to the following white noise spectral densities over a 10 MHz and 20 MHz

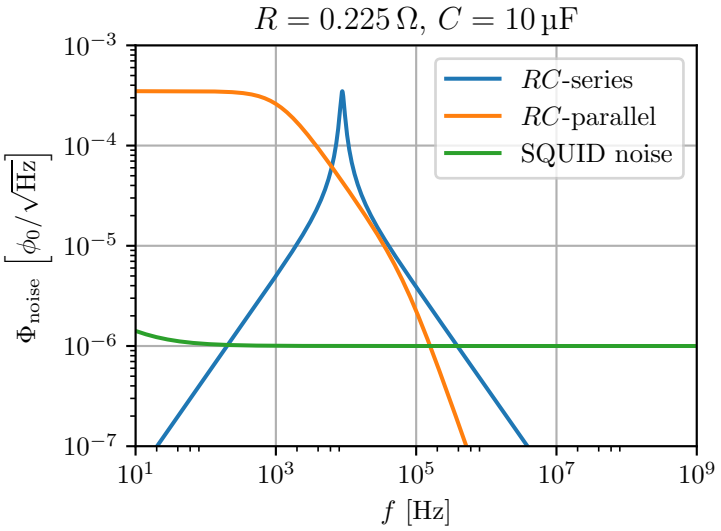

FIGURE 3.30: Comparison of the additional SQUID flux noise spectrum from the resistor R in the two coupling circuit configurations under analysis.

bandwidth

$$\Phi^{\text{core}} = 4.60 \times 10^{-6}\,\phi_0/\sqrt{\text{Hz}}, \qquad BW = 10\,\text{MHz}, \tag{3.47}$$

$$\Phi^{\text{core}} = 3.25 \times 10^{-6}\,\phi_0/\sqrt{\text{Hz}}, \qquad BW = 20\,\text{MHz}. \tag{3.48}$$

The flux output of the coupling circuit for the AD injection current is shown in Figure 3.31. The parameters for the injection beam are those in Table 3.2, and it was assumed that the beam kept this structure for the entire period of the calculation. This reduces the SR of the flux coupled to the SQUID to $0.936\,\text{M}\phi_0/\text{s}$, which should

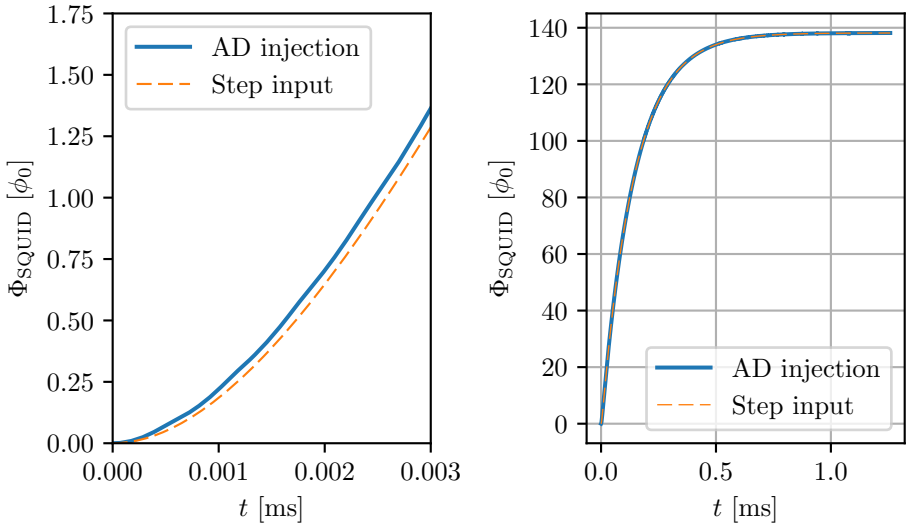

FIGURE 3.31: Time-response of the coupling circuit with the *RC*-parallel filter to the AD beam current at injection, and to a step input signal.

be already under the stability limits discussed before. If in the coupling circuit the frequency dependent core permeability is also taken into account as in Equation 3.31, the additional SR reduction is minimal to $0.930\,\mathrm{M}\phi_0/\mathrm{s}$. The response of the coupling circuit to a step function was also computed and it behaves almost exactly as the response to the AD-injection signal. This is due to the fact that the Gaussian bunches in the AD signal have a repetition frequency much higher than the cutoff frequency of the coupling circuit.

In reality, the bunch rotation in the longitudinal phase-space takes place $\approx 50\,\mu\mathrm{s}$ after injection, which reduces the beam momentum spread and increases the bunches length. However, the maximum SR coupled to the SQUID occurs at $\approx 10\,\mu\mathrm{s}$, hence the bunch rotation should not affect maximum SR that the SQUID/FLL will have to cope with.

The flux signal in Figure 3.31 was used as input to the Simulink model of the SQUID/FLL system, and a single white noise source was used to account for the total noise from the different sources. The total equivalent white noise spectral density for different FLL bandwidth is shown in Table 3.4. For the simulation of the

Noise source	10 MHz $\left[\mu\phi_0/\sqrt{\mathrm{Hz}}\right]$	15 MHz $\left[\mu\phi_0/\sqrt{\mathrm{Hz}}\right]$	20 MHz $\left[\phi_0/\sqrt{\mathrm{Hz}}\right]$
SQUID	0.7	0.7	0.7
Core	3.5	2.7	2.6
RC-filter	4.6	3.8	3.3
Total	5.8	4.7	4.3

TABLE 3.4: Comparison of average flux spectral noise density from different sources, for different averaging bandwidths.

SQUID/FLL stability when measuring the AD injection signal, the used flux noise amplitude was $\Phi^{\mathrm{noise}} = 10\,\mu\phi_0/\sqrt{\mathrm{Hz}}$, which doubles the total expected from the sources described before. The simulation was performed for different values of the gain bandwidth product parameter, $GBW = 0.01\,\mathrm{GHz}$, $GBW = 0.1\,\mathrm{GHz}$, $GBW = 1.0\,\mathrm{GHz}$ and $GBW = 10\,\mathrm{GHz}$, when the SQUID working point is on the high slope side of the V-Φ characteristic in Figure 3.5, these correspond to the approximate FLL bandwidths, $BW_{\mathrm{FLL}} \approx 160\mathrm{kHz}$, $BW_{\mathrm{FLL}} \approx 1.6\mathrm{MHz}$, $BW_{\mathrm{FLL}} \approx 16\mathrm{MHz}$ and $BW_{\mathrm{FLL}} \approx 160\mathrm{MHz}$, respectively. The resulting current measurement and total flux at the SQUID are shown in Figure 3.32. The output voltage was calibrated to current using the total circuit gain

$$\begin{aligned} V_{\mathrm{out}}/I_b &= S_{I_b} \cdot G_{\mathrm{FLL}} \\ &= 10.7\,\phi_0/\mu\mathrm{A} \times 43\,\mathrm{mV}/\phi_0 \\ &= 460\,\mathrm{mV}/\mu\mathrm{A}. \end{aligned} \tag{3.49}$$

From the simulated responses, the FLL feedback system is only able to reliably track the input current signal when $GBW = 1\,\mathrm{GHz}$, or $BW_{\mathrm{FLL}} \approx 16\mathrm{MHz}$. For smaller

bandwidths the feedback loop is too slow to follow the high SR of the input signal, and large flux jumps, as can be seen in the bottom plot of Figure 3.32. For example,

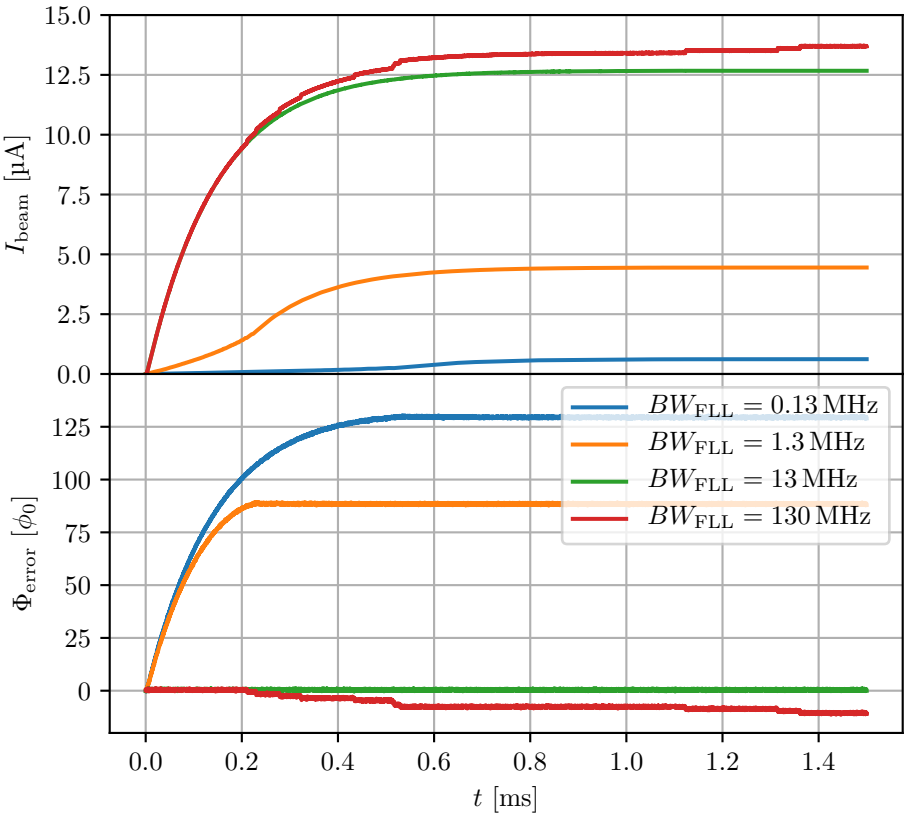

FIGURE 3.32: Simulation of the SQUID/FLL dynamics the AD injection signal, after filtering by the coupling circuit, for various values of the FLL closed loop bandwidth. Top: Measured current calibrated using voltage to current gain of total circuit. Bottom: Evolution of the total flux (error signal) coupled to the SQUID.

when $BW_{\text{FLL}} = 1.6\,\text{MHz}$ (orange trace) a total of $88\,\phi_0$ jumps occur, which results in a final current measurement under valued by $\approx 8.3\,\mu\text{A}$. On the other hand, when $BW_{\text{FLL}} = 160\,\text{MHz}$ (red trace), the feedback loop is fast enough to track the initial high SR current increase, but since the bandwidth is too large, the amount of integrated noise will cause occasional stochastic flux jumps which distort the measured signal.

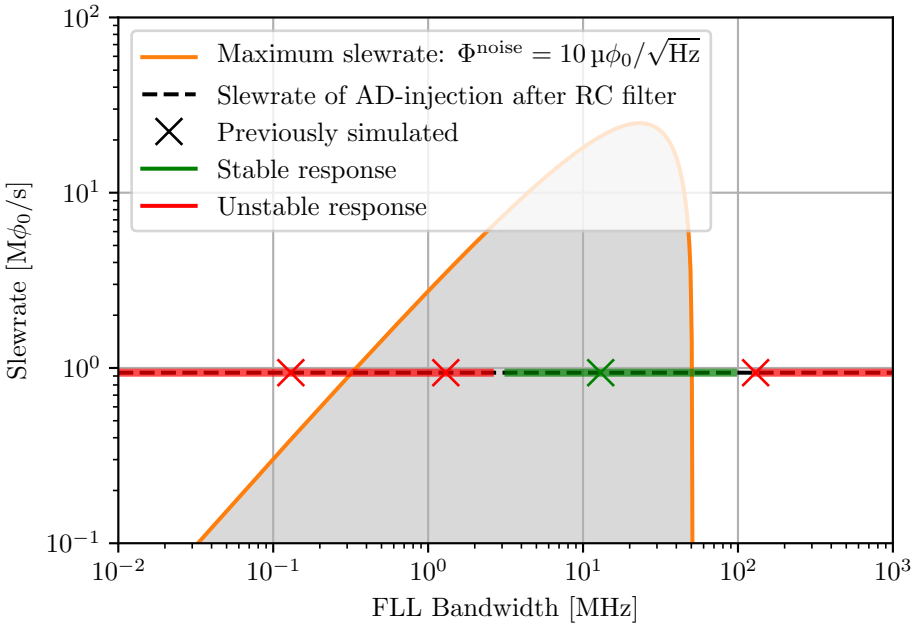

FIGURE 3.33: Maximum allowed slew rate of the input signal as a function of the FLL bandwidth. The grey region corresponds to the theoretically stable region and the dashed line corresponds to the SR at AD injection, and . The cross markers indicate the simulations from Figure 3.32. The red lines indicate the configurations for which the response to the coupled AD injection signal was unstable, and the green line the stable ones.

Figure 3.33 shows the expected SR stability region as a function of the FLL bandwidth. This region is highlighted in grey and it follows from the analysis presented in Section 3.3, for a flux noise spectral density $\Phi^{\text{noise}} = 10\,\mu\phi_0/\sqrt{\text{Hz}}$, and a maximum allowed flux jump rate of $\nu_{\text{FJ}} = 10^{-4}$/s. The four simulations previously performed of the AD injection signal coupled to the SQUID through the dimensioned coupling circuit with the *RC*-parallel low-pass filter are indicated by cross markers. Simulations for other FLL bandwidths were also performed, and their stability is indicated by red (unstable) and green (stable) line segments.

The stable bandwidth region resulting from the simulations is considerably smaller in the low-frequency end when compared with the theoretical analysis. One possible reason for this is that the theoretical model does not consider any reduction in $V_\Phi = \partial V/\partial\Phi$ due to the non-linear nature of the V-Φ transfer function. This is only valid when the Φ_{error} signal has a small amplitude excursion. Additionally, the real APF V-Φ curve used in the simulation, shown in Figure 3.5, although presenting a bigger V_Φ when $\Phi_{\text{error}} = 0$ (and consequently a higher FLL bandwidth), also has a reduced Φ_{lin} region outside of which V_Φ is significantly reduced. This makes the model approximation of a constant V_Φ a crude approximation. In the high-frequency end the simulation results indicate that the system response is stable for higher bandwidths than predicted by the model. This is due to the fact that the stability condition used for the model was that the flux jump rate should be smaller than 1 per 10 000 s, while the simulations were run only

for periods of few milliseconds. Hence the chances that any jump occurred during these shorter simulation periods was much reduced.

3.4 Complete assembly

The printed circuit board and assembly of the coupling circuit resulting from the circuit specified in the previous section was performed at Jena University, and is shown in Figure 3.34. The mechanical drawings can be found in Appendix C. This printed circuit

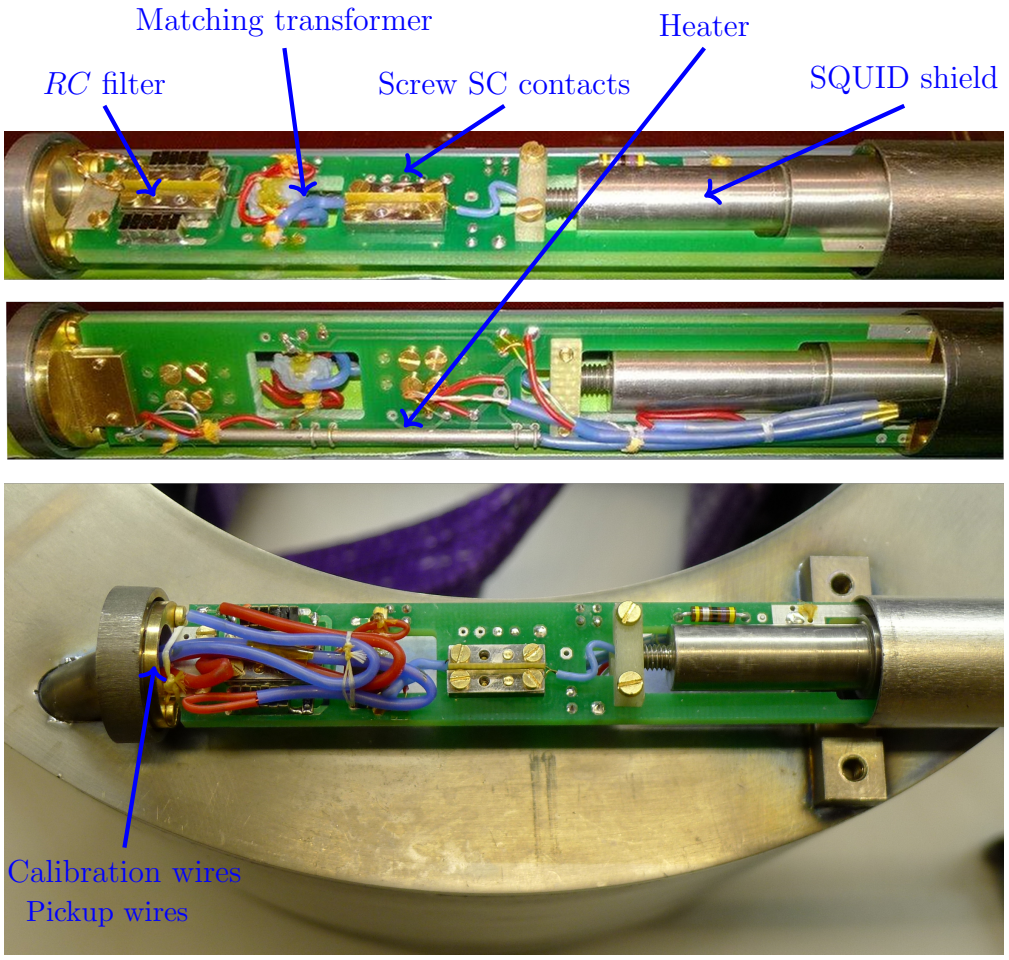

FIGURE 3.34: SQUID cartridge containing the printed circuit board with coupling circuit and SQUID. Top: top view before installation; Middle: bottom view before installation; Bottom: Top view after installation and connection to the pickup core and calibration winding.

board is placed inside a superconducting cylinder for magnetic shielding and attached to the CCC meander shield structure as shown in Figure 3.35.

Figure 3.35 shows the complete assembly of the CCC before welding the cap that closes and locks the ferromagnetic pickup inductance inside the sensing cavity of the shield. This single turn winding around the pickup core is formed not by a single wire, but by a casing that covers the entire surface of the toroid core, except for a small gap, where a pair of wires is welded and connected into the interior of the cartridge cylinder

attached to the outside of the shield cap. Inside this cylinder is installed the coupling circuit and the SQUID show in Figure 3.34.

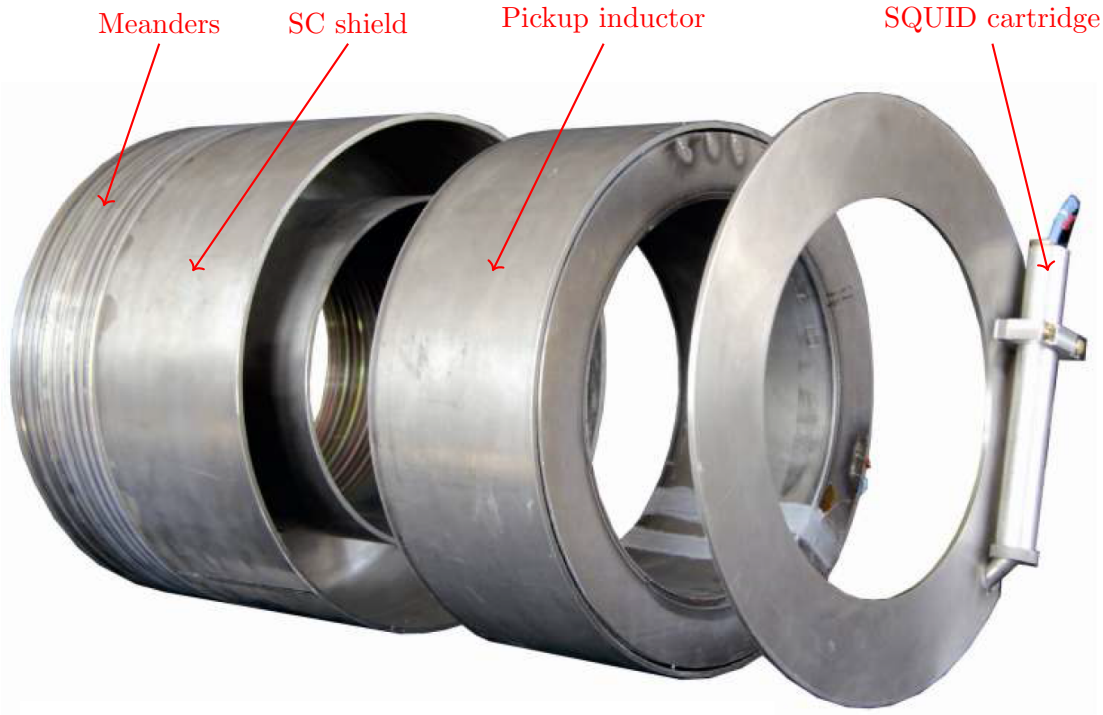

FIGURE 3.35: Exploded view of the CCC assembly, with the meander shield, the pickup inductor with the ferromagnetic core and the end cap with the cartridge.

3.5 CCC acquisition and control system

A control and acquisition system was implemented to automatise the CCC measurement of the beam current and beam intensity for every AD cycle. In order to dimension the acquisition system it is necessary to specify the dynamic range of the CCC voltage output for the expected input current signals.

3.5.1 FLL electronics and measurement output

The maximum expected AD beam average current is 12.7 µA as shown in Table 1.1, and the expected input sensitivity is $S_{I_b} = 10.7\,\phi_0/\mu\text{A}$, given in Equation 3.26. The Magnicon FLL electronics has an output voltage range between $V_{\text{out}} = \pm 10\,\text{V}$, and voltage output gain G_{FLL}, given by Equation 2.53, with the SQUID parameters in Section 3.1 is $G_{\text{FLL}} = (43 \times R_f)\,\mu\text{V}/\phi_0$. From the FLL feedback resistor R_f values that it is possible to select in the Magnicon electronics, the best fitting one is $R_f = 1\,\text{k}\Omega$, which results in,

$$V_{\text{out}}/I_b = G_{\text{FLL}} \cdot S_{I_b} = 0.46\,\text{mV/nA}. \tag{3.50}$$

With this gain the FLL voltage output for the expected beam current is $0 < V_{\text{out}} < 6\,\text{V}$, which is within the saturation limits of the electronics.

The FLL output voltage is to be acquired by an Analogue-to-Digital Converter (ADC) card which needs to be able to provide the sufficient resolution and dynamic range. The gain of the complete chain from the beam current to the ADC bin output is given by,

$$G_{\mathrm{CCC}} = G_{\mathrm{ADC}} \cdot G_{\mathrm{FLL}} \cdot S_{I_b} \tag{3.51}$$

$$= \frac{2^{N_{\mathrm{bin}}}}{\Delta V_{\mathrm{ADC}}} \cdot \frac{R_f}{M_f} \cdot S_{I_b}, \tag{3.52}$$

where N_{bin} is the number of ADC bins and, ΔV_{ADC} is the input voltage range. The selected ADC acquisition card, VD80 from INCAA Computers BV, has 16-bit and voltage input range $\Delta V_{\mathrm{ADC}} = \pm 10\,\mathrm{V}$ [126]. With these parameters the G_{CCC} gain is,

$$G_{\mathrm{CCC}} = 1.507\,\mathrm{bin/nA}, \quad \text{or} \quad G_{\mathrm{CCC}}^{-1} = 0.663\,\mathrm{nA/bin}. \tag{3.53}$$

Additionally, and since the frequency range of the sampled signals is small, $f < 1\,\mathrm{kHz}$, the signal wave length is much bigger than the length of the cable connecting the CCC to the ADC, $l \approx 100\,\mathrm{m}$. This means it is not necessary to have matched impedances between the different systems, and a ADC with high input impedance can be used. The selected ADC has $800\,\mathrm{k\Omega}$ of differential input impedance. The quoted full-scale SNR ratio of the selected ADC at $f_s = 10\,\mathrm{kHz}$ is $> 80\,\mathrm{dB}$, which is equivalent to $\approx 6\,\mathrm{bin}$. Considering the current sensitivity in Equation 3.50, and voltage range of $\pm 10\,\mathrm{V}$ this would represent a current measurement noise of $\approx 4\,\mathrm{nA}$. This value is slightly higher than the desired current resolution of $3\,\mathrm{nA}$, however in reality the ADC noise level was observed to be considerably smaller $\approx 1\,\mathrm{bin}$ which corresponds to $\approx 0.7\,\mathrm{nA}$.

The main requirements for the CCC acquisition and control system are to:

- control SQUID/FLL electronics in order to bias the SQUID, setup the FLL working point, reset the FLL integrator and check the SQUID functioning;
- control the current calibration source;
- acquire the CCC current measurement and other auxiliary signals, as e.g. the magnetic cycle;
- compute the beam intensity from the acquired beam current measurements and magnetic cycle;
- publish the data in a consistent format on a per cycle basis.

The architecture of the implemented system is shown in Figure 3.36 [127]. The data acquisition system used for control and measurements is based on the VME standard and comprised of a MEN-A20 CPU card, a VD80 ADC card, and a CERN Timing Receiver (CTRV) card. All these devices are commonly used in CERN's acquisition and control systems. Additionally serial interface (RS-232) to Ethernet converter is used

to allow the VME server to communicate and control the SQUID electronics and the calibration current source.

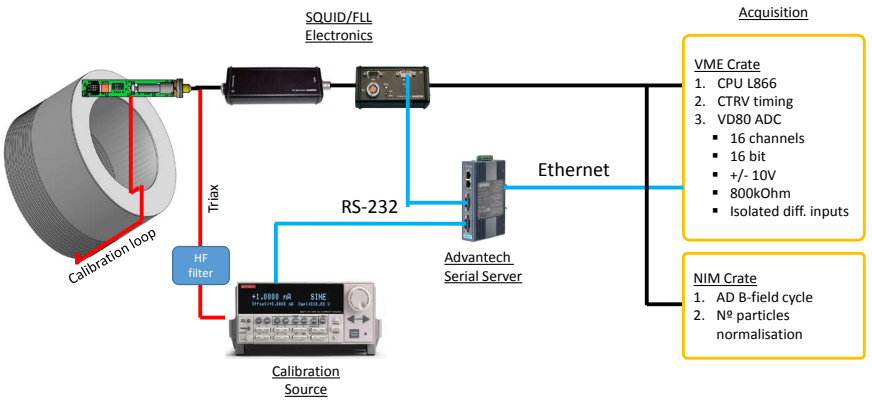

FIGURE 3.36: Architecture of the control and acquisition system.

- the CPU card hosts a dual core INTEL Core 2 Duo L7400 64-bit processor running at 1.5 GHz with 4 GB of RAM;
- the VD80 ADC is a 16-bit card that can sample in simultaneous 16 channels (32 MB per channel) at a maximum frequency of 200 kHz. All ADC inputs are fully differential and galvanically isolated;
- the CTRV is a CERN timing receiver used to provide information on the occurrence of different accelerator events and triggers, via software interrupts or TTL hardware outputs.

A real-time server application was developed by the Software section in the CERN's Beam Instrumentation group, to automate the configuration, calibration, acquisition and publishing of the measurements. The architecture of this server is based on the CERN Front-End Software Architecture (FESA) C++ framework [128].

The FESA server implements the instruction protocols used to configure the SQUID electronics and calibration source according to the user settings. These settings include important SQUID configuration parameters such as the bias current, bias voltage, gain bandwidth and feedback resistance for the SQUID, and calibration steps and duration for the current source. The time diagram in Figure 3.37 shows the main events, triggers and actions performed during the acquisition of an AD cycle. At the start of each cycle, and before the beam injection a reset of the SQUID integrator is performed to guarantee the maximum dynamic range is available even when flux jumps may have occurred previously, and also a sequence of calibration pulses is triggered. Time markers produced by the CTRV card are registered for the beam injection, and the start and end of each magnetic cycle plateau. The injection event is used in real-time for re-setting the SQUID integrator in order to ensure a zero offset. The plateau markers are subsequently

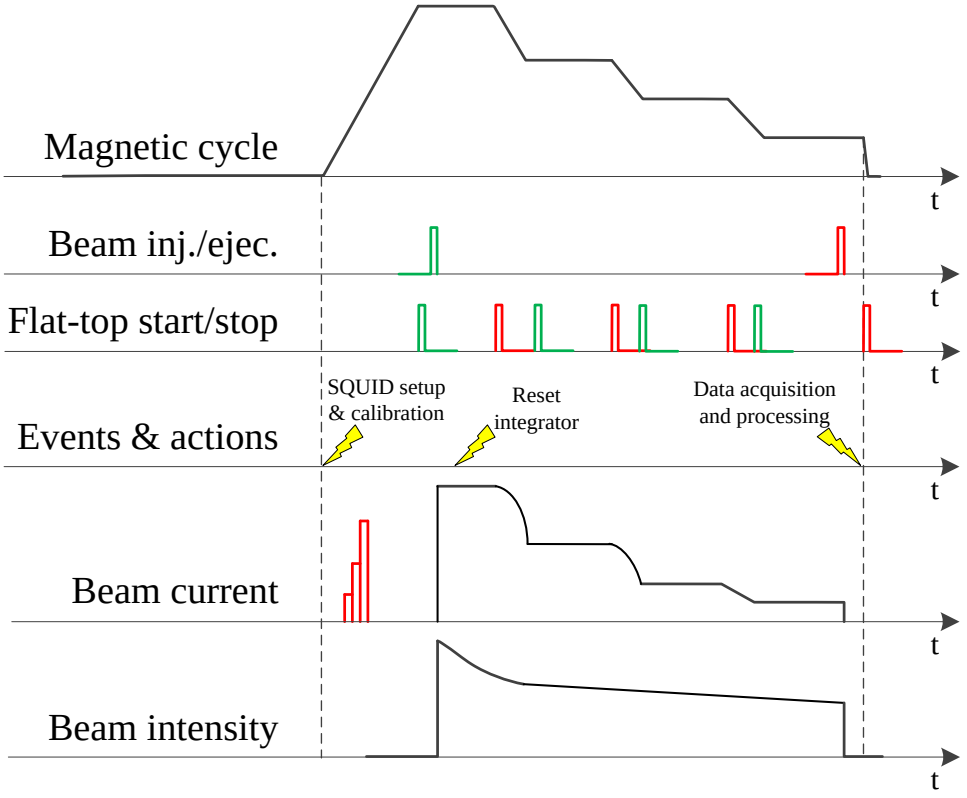

FIGURE 3.37: Different actions and events occurring during the AD cycle acquisition. Adapted from [127]

used to automatically detect the beginning and the end of each phase time window for which intensity measurements are particularly relevant for the operators.

With the first implementation of the acquisition FESA software the used sampling rate was fixed at 1 kHz. Since the CCC bandwidth is $BW_{\mathrm{FLL}} = 1\,\mathrm{kHz}$, the sampling rate does not fulfill with the Nyquist sampling theorem, according to which the sampling frequency should be at least twice the maximum bandwidth of the sampled signal. However, future modifications are already planned to allow higher sampling frequencies allowing to capture the full available measurement dynamics and avoiding aliasing effects. However, the obtained RMS noise should be the same as with the current sampling rate.

3.5.2 Current calibration source

A commercial available precision current source manufactured by Keithley (model 6221), was used for the test and calibration of the CCC. This current generator is able to source and sink both DC and AC signals up to 100 kHz. The specified current accuracy of this source is summarised in Table 3.5.

Range	Accuracy (23 °C ± 5 °C)	Typical noise (RMS)
0.2 µA	0.3 % ± 0.1 nA	4 pA
2 µA	0.1 % ± 1 nA	40 pA
20 µA	0.05 % ± 10 nA	400 pA

TABLE 3.5: Accuracy and noise levels of the precision low intensity current source used for the CCC calibration [129].

3.6 Conclusion

This chapter covered the design of the CCC coupling circuit, both in the static limit and in the frequency domain. The beam's magnetic field is concentrated in the pickup core, and then transferred to SQUID via a flux transformer circuit, which by the fact of being a superconducting loop is able to couple DC fields. This is a mandatory requirement in order to measure the beam's average current. It is shown that using a high-permeability ferromagnetic core in the pickup inductor increases the coupling sensitivity, and although the thermal noise also increases with the permeability, the measurement the signal to noise ratio is still improved being proportional to $\sqrt{\mu}$. At cryogenic temperatures many high-permeability materials loose their room-temperature properties, so it is important to appropriately choose a material that when cooled down keeps its real part of the permeability much bigger than the imaginary one.

Two sample cores were measured at liquid-helium temperatures to demonstrate this effect, showing that nanocrystaline material keep most of their properties unchanged when cooled down. The FAIR CCC shield used in this project already had integrated a ferromagnetic core made of the material Nanoperm.

The beam current sensitivity and resolution were computed for different configurations of the coupling circuits. This was done for a circuit with and without a ferromagnetic core, and with and without an intermediate inductance matching transformer. Using a ferromagnetic core and a matching transformer increases the sensitivity by several orders of magnitude, but the gains in current resolution are not so significant. However, in the current project both were used and a theoretical sensitivity of $S_{I_b} = 10.7\,\mu\text{A}$ and resolution of $\sigma(I_b) = 0.15\,\text{nA}$, which at this point took only into account the core thermal noise and the SQUID noise were estimated.

Next the analysis of the dynamic behaviour of the SQUID/FLL was presented. The mechanism of the flux jumps of the SQUID/FLL readout is described as well as its impact on the current measurements. An estimation of the maximum input signal SR and stability limits was performed using a simple theoretical model and a simulation model that used the measured SQUID V-Φ characteristic.This study was critical to ensure the stable measurement of the high SR AD bunched beam, which presented the most challenging requirements at injection. The SR stability limit of SQUID/FLL systems is typically limited to a few Mϕ_0/s, while the AD injection beam after being filtered

by the frequency dependent permeability core imposed a SR of $1.2\,\mathrm{G}\phi_0/\mathrm{s}$. In order to reduce the slew rate, a modification of the coupling circuit was performed in order to filter and reduce the SR of the signal reaching the SQUID. Two filter configurations were considered, one with a *RC*-parallel and another with a *RC*-series shunt in the coupling circuit. The design was done taking into account the amount of filtering provided, the additional noise introduced by the resistor and the limited availability of component values suitable to work at cryogenic temperatures. The *RC*-parallel option presented the strongest attenuation, and despite adding more noise in the measurement bandwidth, $\sigma(I_b) = 0.92\,\mathrm{nA}$, this was still under the resolution requirement. Matlab/Simulink simulations of the system dynamics were performed and resulted in a stable system as long as the FLL feedback loop bandwidth was set to $\approx 10\,\mathrm{MHz}$, which is a reasonable value for the used direct-readout FLL electronics. This chapter 3 concludes with the description of the acquisition and control system that was installed in the AD to automatise all the data taking of the deceleration cycles during AD operation. This acquisition system was essential make the installed CCC an operations ready device, and to allow the consistent data taking of many AD cycles which was used to perform the long-term performance and stability analysis.

Chapter 4

AD Integration and Cryostat Design

This chapter is divided in two parts. In the first part the performed studies concerning the installation of the new CCC monitor in the AD are presented. Section 4.1 introduces the installation location and presents the performed analysis of the expected background magnetic fields. The beam pipe aperture constraints are also presented, and the possibility of reducing this aperture in view of the dimensions of the developed CCC monitor is also studied. In the second part, starting in Section 4.3, the design of the cryostat fabricated to host the CCC monitor is presented. This discussion covers the mechanical and thermal design, as well as the installed instrumentation and obtained performance.

4.1 Installation location

In a particle accelerator space for installing equipment in the beam line is always a scarce resource. For installing the cryostat housing the CCC monitor at least 1 m of longitudinal space was required.

The installation location for the CCC monitor was Section 15, in Sector 2A of the AD, in between two quadrupoles, QDS15 and QFN16, as shown in Figure 4.1. This section has a length of 1.7 m, and only a ion getter pump was present, which could be shifted to open space for the new monitor to be installed in the middle of the section.

This was one of the few locations available but at the same time it also complied with most of the desired properties. There are no dipole magnets in its immediate vicinity. And it is also relatively distant to the following elements which may cause considerable EMI problems, such as RF-cavities and kicker magnets. The relative location of these elements to the CCC is shown in Figure 1.2.

4.1.1 Magnetic field environment

Different magnetic noise sources are present in a particle accelerator. Focusing and bending magnets' stray fields usually create the strongest perturbations, and this can

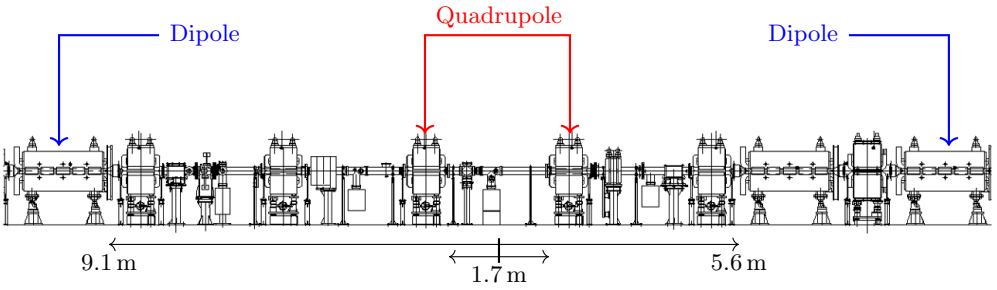

FIGURE 4.1: Profile of part of the AD accelerator. The location selected for the installation of the CCC monitor, corresponds to the middle point of the image. This is Section 15, located between the quadrupoles QDS15 and QFN16.. The localisation of this section in the full ring is indicated in Figure 1.2.

potentially affect the CCC performance. In order to assess the field levels in the CCC installation location simulations of the accelerator magnets stray fields were performed. As shown in Figure 4.1 the two closest magnet elements are two focusing and defocusing quadrupoles located 1.6 m away from the mid-point of the proposed CCC location. These two elements have been modeled and simulated using the magnetostatic solver from the CST EM Studio software. The models created replicate the real iron yokes, the poles shape, and the quadrupole coils, as shown in Figure 4.2. Both magnets are powered in

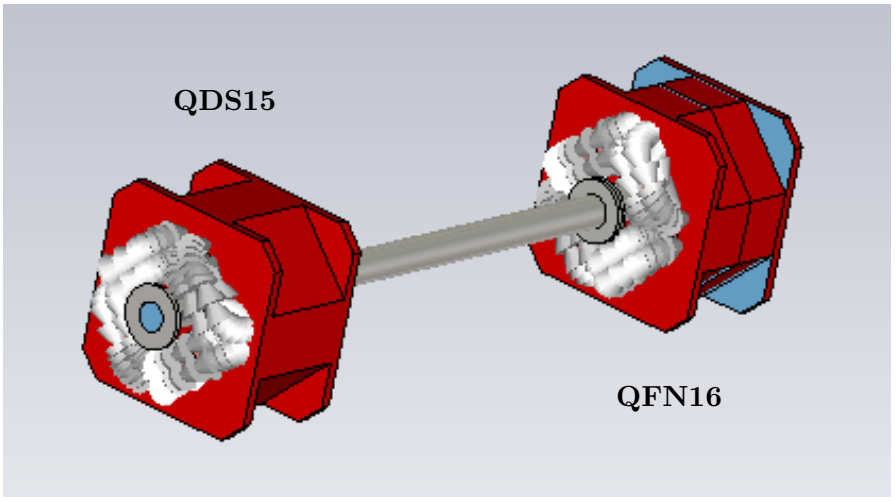

FIGURE 4.2: Model of the two quadrupoles magnets near the foreseen CCC installation location.

series with the same current, which attains the maximum value of $I_{\text{quad}} = 2005\,\text{A}$ during the first energy flat top of the AD cycle in Figure 1.3. The coils in quadrupole QDS15 have 17 turns, while the QFN16 one have 19. The obtained magnetic values are shown in Figure 4.3

The plots in Figure 4.3 show the magnitude of the transverse and longitudinal magnetic field component in the XZ plane rotated by 45° around the Z axis, at different radius values. This is the plane where the longitudinal components of the magnetic field is maximum, while the transverse component has approximately the same magnitude as

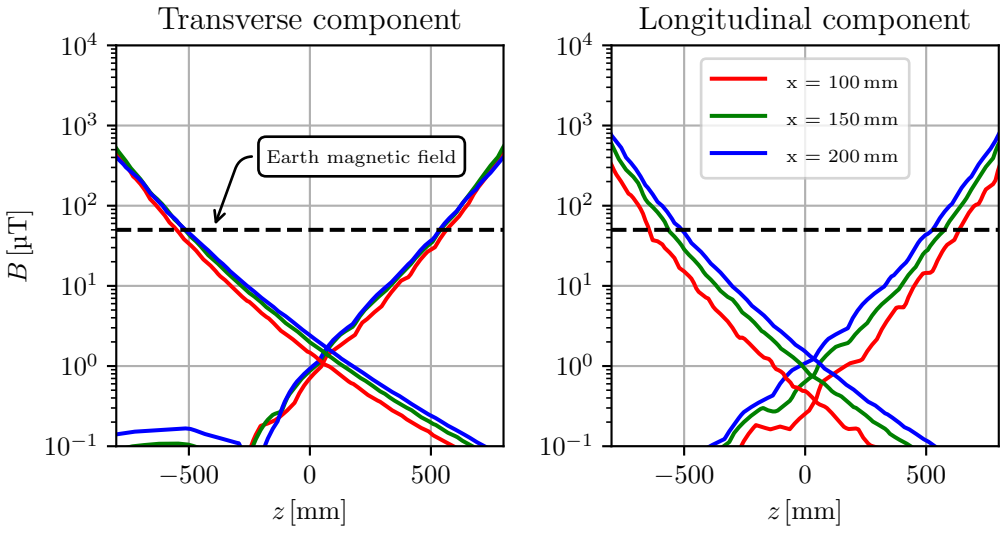

FIGURE 4.3: Simulated absolute value of the stray magnetic fields created by the two adjacent quadrupoles at the maximum field condition. Left: absolute value of the transverse component; Right: longitudinal component. The dashed line indicates the magnitude of the Earth's magnetic field. The CCC monitor will be located close to the $z = 0$ position.

in the XZ plane. In the the region $|z| < 1\,\text{m}$, both the transverse and longitudinal components of the stray magnetic fields are smaller than the Earth's magnetic field which is $\approx 50\,\mu\text{T}$ with a minimum of $\approx 2\,\mu\text{T}$.

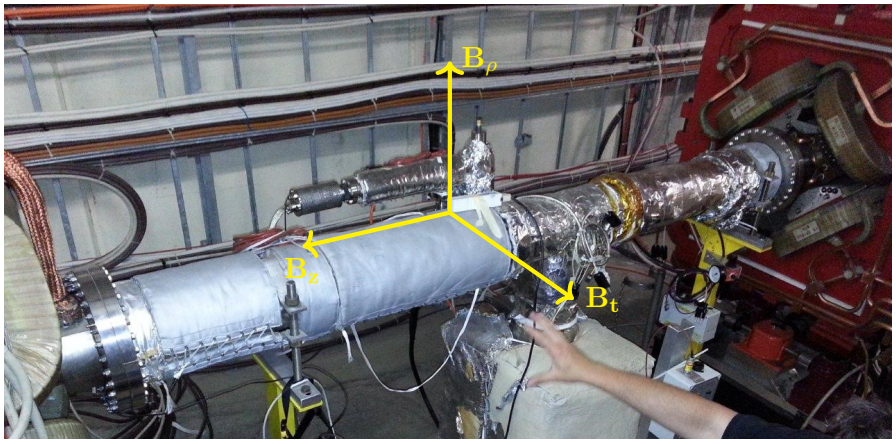

FIGURE 4.4: Magnetic field probe location during the measurements of magnetic stray field during the AD magnetic cycle.

After performing these simulations it was possible to measure the actual magnetic field in the center of the installation AD section, as shown in Figure 4.4. This measurement was performed using a 3-dimensional fluxgate probe, MAG 03S-1000 from Bartington Instruments Ltd. Additionally, a Hall effect sensor was placed inside one of the quadrupoles to acquire a synchronisation reference measurement of the AD cycle.

The measured magnetic field components throughout the AD cycle are shown in Figure 4.5. At the highest energy plateau the amplitude of the magnetic field is $\approx 30\,\mu T$, which is one order of magnitude higher than the value obtained by simulation at the same location. This discrepancy is most likely explained by the inaccurate modelling of the magnets' iron yokes. In particular their real magnetic permeability, as well as the fact that the iron works were not a single piece but were composed of many laminated plates joined together, which was not taken into account in the simulation. Nevertheless,

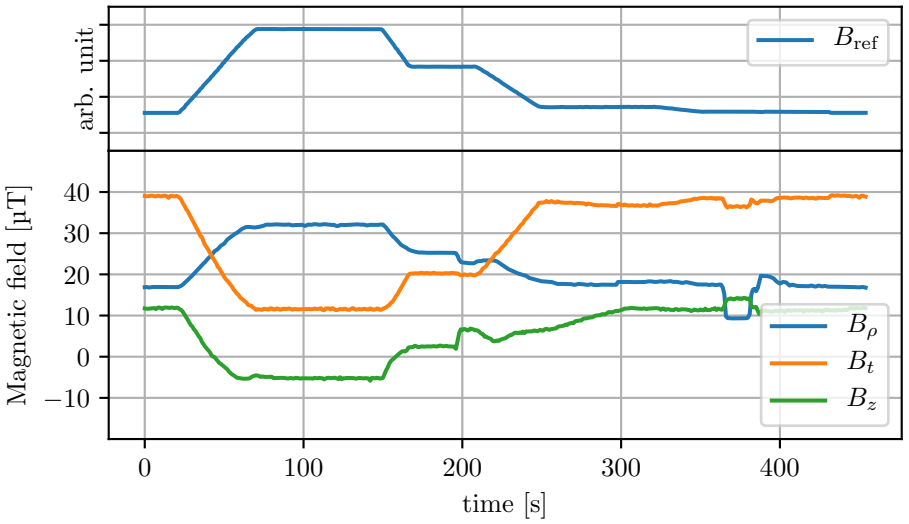

FIGURE 4.5: Measured magnetic fields during the AD cycle, in the midpoint of the section selected for installation of the CCC monitor. In the top plot is a reference measurement of the AD cycle.

the measured magnetic fields are in the order of magnitude of the Earths' magnetic field and should not have a significant impact in the CCC monitor current measurement.

4.1.2 Beam pipe aperture

The vacuum beam pipe in the installation AD section has a diameter of 160 mm. In order to use the niobium magnetic shield prototype that had already been developed for FAIR it was necessary to reduce the beam pipe diameter. The FAIR shield has an inner diameter of only 185 mm, and it would be impossible to integrate this reduced diameter in the existing beam pipe aperture of 160 mm, since the 25 mm gap would not be sufficient to fit the different isolation layers between the accelerator vacuum pipe wall and the cryostat liquid helium vessel wall. Hence, the possibility of reducing the beam vacuum pipe diameter to at least 100 mm was studied.

To analyse the impact of reducing the beam pipe aperture on the available space for the beam, some concepts of transverse beam dynamics need to be used [130]. The transverse region occupied by the beam, $X_{h,v}(s)$ in the horizontal (h) and vertical plane

(v), along the longitudinal coordinate s is given by,

$$X_{h,v}(s) = \sqrt{\epsilon_{h,v}\,\beta_{h,v}(s)} + O.C._{h,v}, \tag{4.1}$$

where $\epsilon_{h,v}$ is the beam emittance and $\beta_{h,v}(s)$ is the accelerator beta function at position s, which is solely dependent on the accelerator "optics". The "optics" is defined by the ensemble of the bending, focusing and correcting magnets, as well as by the drift sections in between. Usually, there would also be a dispersion term accounting for the off-momentum particles which was not included in Equation 4.1 since this is quite small in this straight section. The AD beam emittance at injection, which corresponds to the highest value observed during the entire cycle, is $\epsilon_h \approx 200\pi\,\text{mm mrad}$ and $\epsilon_v \approx 40\pi\,\text{mm mrad}$, in the horizontal and vertical plane respectively. These are defined as the 2σ state-space region occupied by the beam, which contains $\approx 95\,\%$ of the particles.

Both the emittance and the beta function are defined in the vertical and horizontal plane. The quantity $O.C._{h,v}$ refers to the excursion of the beam orbit center around beam pipe center, during the accelerator normal operation. The beta functions at any point s of a drift section can be calculated from the parameters β, α and γ (so called Twiss parameters) defined at a single point $s = 0$ using the following expression,

$$\beta_{h,v}(s) = \beta_{h,v}(0) - 2\alpha_{h,v}(0)\,s + \gamma_{h,v}(0)\,s^2. \tag{4.2}$$

At the magnetic edge of the quadrupole QDS15, $s = s_1$ (indicated by a cross in Figure 4.6), the Twiss parameters values are:

- $\beta_h = 2.460\,\text{m}$, $\alpha_h = -0.896\,\text{m}$,
- $\beta_v = 12.351\,\text{m}$, $\alpha_v = 2.273\,\text{m}$,

while γ can be calculated using $\gamma_{h,v} = (1 + \alpha_{h,v}^2)/\beta_{h,v}$. In order to compute the largest transverse region that the beam can occupy in the CCC location, the AD acceptance was used in place of the emittance in Equation 4.1, since part of the beam is still located outside of the emittance region that accounts only for 95 % of the beam. The acceptance $A_{h,v}$, however, corresponds to the widest region in phase-space that the beam particles can occupy and still be captured by the machine optics. In the AD the horizontal and vertical acceptances at injection are $A_h = 220\pi\,\text{mm mrad}$ and $A_v = 200\pi\,\text{mm mrad}$, respectively.

In Figure 4.6 is shown the beam pipe section where the space occupied by the beam satisfies $|X_h|, |X_v| < 100\,\text{mm}$, which is located between $-0.94\,\text{m} < s < 0.81\,\text{m}$. This interval represents the length available for the installation of the CCC cryostat.

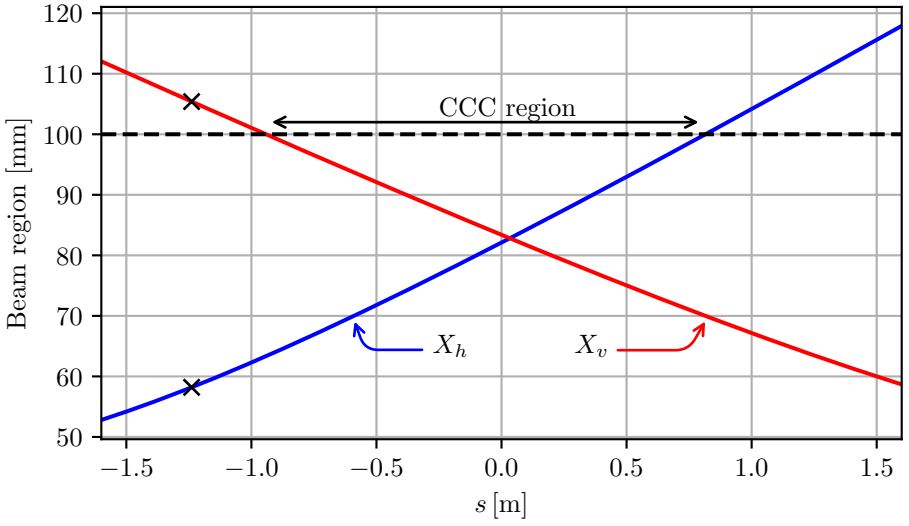

FIGURE 4.6: Region occupied by the beam in the drift section allocated to the CCC installation, in the horizontal (blue trace) and vertical plane(red trace), along the longitudinal direction.

4.2 Radiation levels

The expected radiation level in the installation location was measured, since the FLL electronics needs to be installed close to the cryostat. The used Magnicon system combines both analogue and digital electronics which were not designed to be radiation hard. The radiation level was monitored over a period of 6 months, before the cryostat installation, using a RADiation-sensitive Field-Effect Transistor (RadFET) sensor [131] for the total dose, and a SRAM memory sensor to measure the high energy hadron fluence, located $\approx 10\,\text{cm}$ below the beam pipe. The dose was estimated to be of the order of $5\,\text{Gy/yr}$ with a $\pm 50\,\%$ uncertainty, and the measured fluence was in the order of $10^7/\text{cm}^2$. These values are inline with the expected low levels of radiation, and are below $< 10\,\text{Gy/yr}$, what should pose no problems to the electronics. After installation of the cryostat the general radiation level is probably higher due to the reduction of the beam pipe aperture, but the electronics box is also installed farther away from the beam pipe, than the radiation sensors, and off the horizontal where most beam losses should in principle happen.

4.3 Cryostat

A new cryostat was developed at CERN to house the CCC monitor and to be installed in the AD beam line. The conceptual, cryogenic and mechanical design was undertaken by A. Lees, from the Cryogenic group [132], and the detailed drawings and fabrications were undertaken by the Mechanical and Materials Engineering group. T. Koettig and the Cryolab team, also from the Cryogenic group, were responsible for the tests and

commissioning of all the cryogenic systems, and were also involved in the cryostat design. The main requirements for the cryostat were:

- Long term operation at around 4.2 K;
- Annular cryostat with the inner wall of the vacuum vessel acting as the beam pipe;
- Thermal insulation vacuum separated from accelerator vacuum;
- Ceramic electric insulating rings to break the beam image current;
- Supporting structure optimised for stiffness and to minimise mechanical perturbation of the CCC;
- Accessibility to the CCC device without the need to break the beam vacuum.

The general schematic of the cryostat structure is shown in Figure 4.7. It consists of three main toroidal volumes, which are the external Vacuum Vessel (VV), an intermediate Thermal Shield (TS) and the inner Helium Vessel (HV) which contains the CCC monitor. The inner diameter pipes of the three components are coaxial, with the beam pipe of the VV connecting directly to the beam pipe of the AD ring. Ceramic insulators were required in the beam pipe and in the inner diameter of the HV, to break the path of the beam induced mirror currents that would otherwise highly attenuate the measured magnetic fields down to low-frequencies.

As in most common liquid-helium cryostats, a good insulation vacuum is required to reduce the thermal load on the cold mass due to residual gas convection. The TS, which is cooled to a intermediate temperature in order to reduce the thermal radiation heat load between the room temperature outer vessel and the HV. Additionally, multiple layers of Multi Layer Insulation (MLI), reflective sheets made from aluminised mylar are added to the cold surfaces to minimise the thermal radiation heat loads.

The CCC will be cooled by a liquid helium bath supplied by an external re-condensation unit based on a pulse tube cryocooler. The decision to have a liquid bath cooling was made in order to ensure a higher stability of the CCC temperature. A pulse-tube type of cryocooler was selected due to the low level of mechanical vibrations it creates when compared to other cryocoolers, as for example the Gifford-McMahon cryocooler [134]. The PT415 helium reliquefier unit from Cryomech [133], shown in Figure 4.7, was selected. The decision of having an external reliquefying unit, instead of directly integrating the cryocooler cold-head into the cryostat HV, was taken in order to reduce the coupling of mechanical vibrations produced by the cryocooler unit into the CCC.

The closed loop operation was designed to work in the following way. The helium evaporated from the HV is circulated through a cooling pipe of the TS (shown in Figure 4.9), cooling the TS using the enthalpy of the evaporated helium to temperature in the range $(75 - 90)$ K. After leaving the TS the gaseous helium is heated to approximately 300 K and then returned to the reliquifying unit to be recondensed and transferred back to the HV as liquid. If the recondensation rate (or equivalently the cooling power) of the reliquefying unit is higher than the boil off rate of the cryostat (or

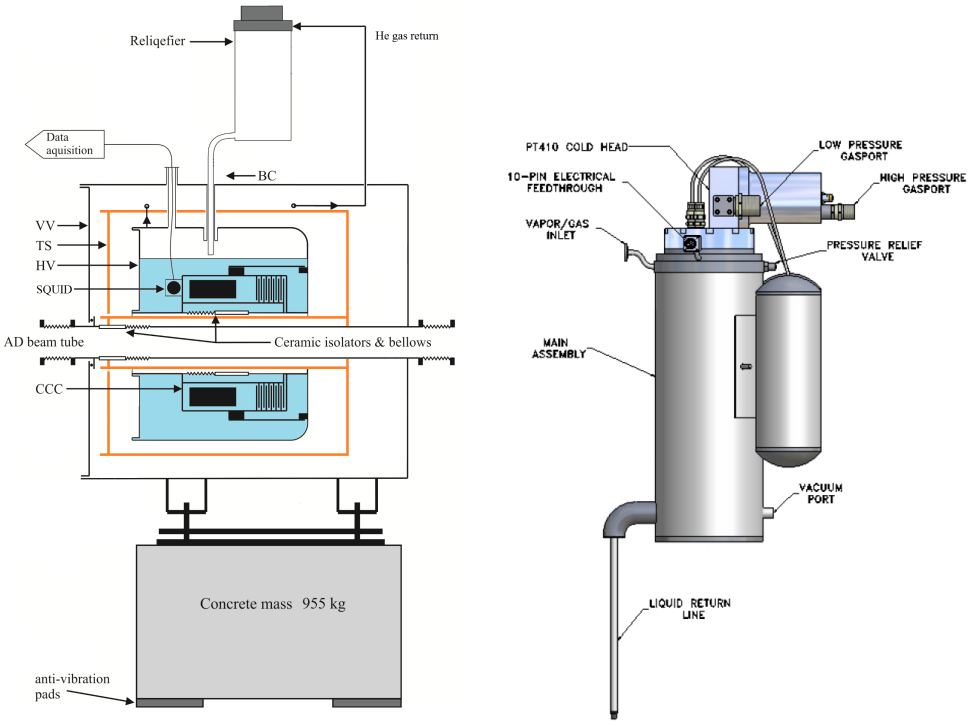

FIGURE 4.7: Left: Schematic view of the cryostat and cryogenic systems. Adapted from [127, 132]; Right: helium reliquefier unit from Cryomech containing in its interior the PT415 pulse-tube cryocooler cold head [133].

equivalently the total heat in-leak rate) the system will work in a closed-cycle, without the need for periodic refills. This will enable the stand-alone and continuous operation of the CCC monitor. Modern, commercially available, pulse tube cryocoolers can provide approximately 1.5 W of cooling power at 4.2 K. But when integrated in a reliquefier unit, an inferior performance is obtained due to the helium gas convection around the cold head. The selected unit from Cryomech specifies a reliquefaction rate of $\geq 15\,\mathrm{l/d}$ from room temperature gas, and $\geq 27\,\mathrm{l/d}$ from cold gas, this is equivalent to $\geq 0.45\,\mathrm{W}$ and $\geq 0.80\,\mathrm{W}$, respectively [133]. To balance the boil off rate and recondensation rate, two heater/temperature controllers are available. One directly at the cryocooler cold-head, and another at the warm helium gas return line.

4.3.1 Mechanical and thermal design

The main design challenge was to optimise the thermal and mechanical performance of the cryostat to retain a stable amount of liquid helium while minimising the transmission of vibrations to the CCC. Additionally, the space available between the inner diameter of the CCC magnetic shield (185 mm) and the minimum allowed diameter for the accelerator vacuum beam pipe (103 mm) made the integration of the HV inner diameter, TS inner diameter, ceramic insulation rings, bellows and MLI very challenging.

Table 4.1 shows calculated heat load for each of the main sources. The total estimated heat load in the 4.2 K cold mass equals 0.57 W, which is $\approx 30\,\%$ inferior to the cooling

power of the reliquefying unit. Different views of the main components of the designed

	TS [W]	**HV** [W]
Thermal radiation	2.84	0.12
Support rods	4.61	0.26
Bayonet connection	0.49	0.05
Safety valves line	0.56	0.02
SQUID feedthrough	0.53	0.06
Instrumentation	0.06	0.04
Heater line	0.09	0.01
Total	**9.17**	**0.57**

TABLE 4.1: Estimated heat load in the TS surface (at $< 75\,\mathrm{K}$) and HV (at $4.2\,\mathrm{K}$) [132].

cryostat are shown in Figure 4.8, 4.9 and 4.10.

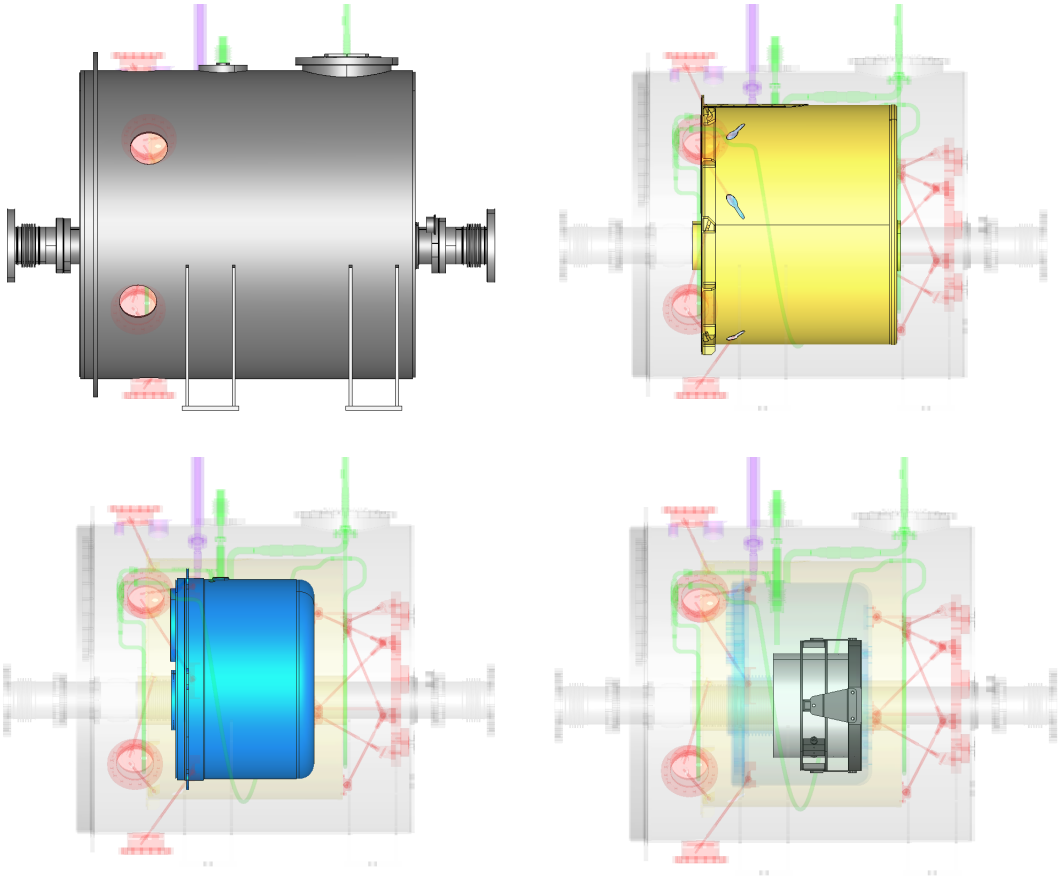

FIGURE 4.8: Lateral view of the main components of the CCC cryostat. Top-left: External VV highlighted in grey; Top-right: TS highlighted in yellow; Bottom-left: HV highlighted in blue; Bottom-right: CCC and respective support highlighted in grey.

Two main sources of mechanical vibrations affect the CCC. Firstly the helium compressor located $\approx 20\,\mathrm{m}$ away from the cryostat, and connected to the cryocooler via

two high-pressure helium flexible lines (inlet and outlet) that drive the operation cycle happening in the cryocooler. The compressor motor with main vibration frequency measured at 48 Hz, delivers a steady flow of high-pressure helium gas to the cryocooler at ≈ 20 barg [1], where it undergoes a series of compression and expansions in the cold head before returning at ≈ 8 barg. This cryogenic cycle in the cold head operates at the frequency 1.4 Hz, inducing a strong beating in the helium gas flow. The helium gas circuit between the compressor and the cryocooler is separated form the cryostat liquid helium circuit.

The motor running in the cryocooler generates the second source of vibrations with dominant components measured at 96 Hz and 139 Hz. On some occasions, a primary rotary vacuum pump and a secondary turbomolecular pump were running and connected to the VV. The first one uses a motor rotating at 50 Hz and the second uses a motor with magnetic bearings rotating at 1.5 kHz.

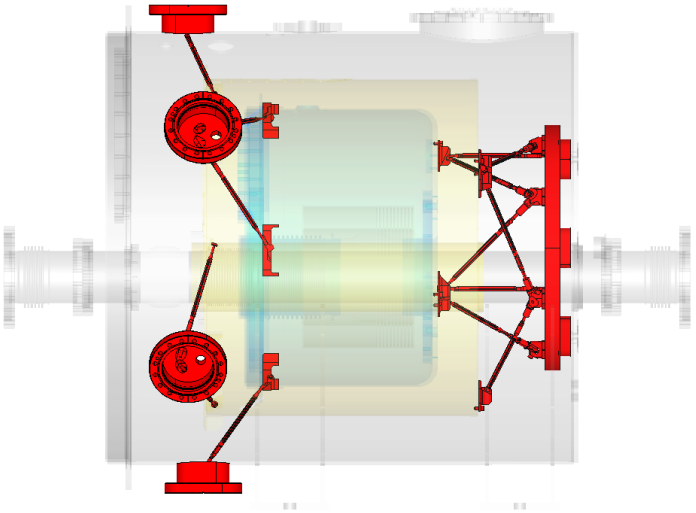

FIGURE 4.9: Structure of rods supporting the HV and the TS highlighted in red.

Another requirement for the cryostat design and installation was to isolate as much as possible the CCC from any mechanical vibrations, which were a strong affected previous CCCs projects [50, 51, 56]. In order to avoid resonance with external vibrations, the design of the cryostats internal support systems were optimised to ensure that the vibration resonant mode frequencies of the HV and TS where above 50 Hz. This was achieved by optimising the layout, number, material and cross-sectional area of the support rods to increase stiffness while keeping heat in-leak by thermal conduction to a minimum. In the resulting design, the masses of the HV (145 kg including 55 kg for the CCC), and the mass of the TS 55 kg are independently supported by 24 titanium support

[1] The unit barg represents a gauge pressure measured in bar measured with relation to the atmospheric pressure.

rods in a hyperstatic configuration, as shown in Figure 4.9. Titanium was used due to its high yield strength to thermal conductivity ratio, when compared to stainless steel. The frequencies of the first mechanical vibration modes obtained through simulations are 64.7 Hz for the HV and 68.1 Hz for the TS [132].

A longitudinal section of the different cryostat vessels annotated with its main dimensions is shown in Figure 4.7. The location of the ceramic breaks in the beam pipe and HV, and of an opening in the TS also for the purpose of breaking the path of the beam induced mirror currents is also shown.

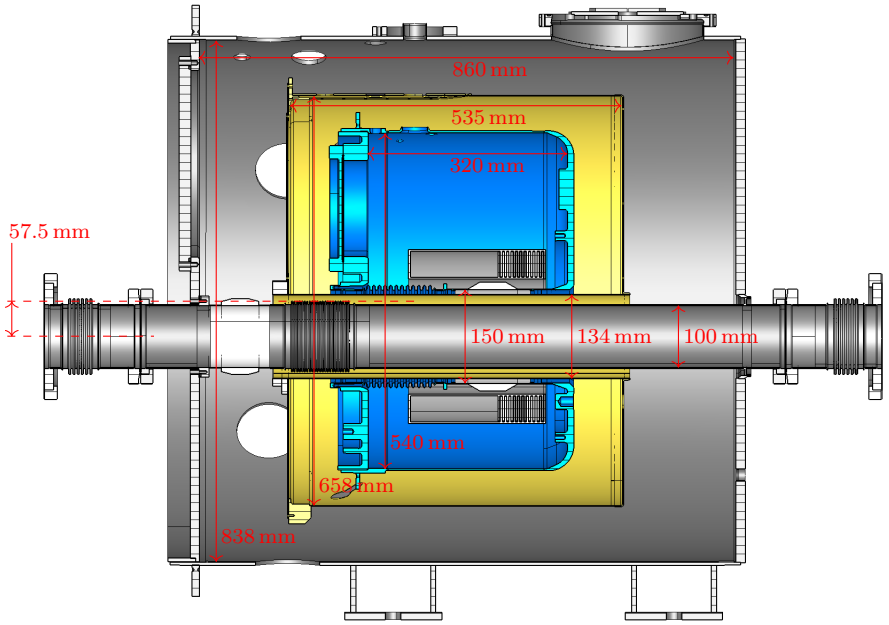

FIGURE 4.10: Cross section of the cryostat, showing the coaxial structure of its main components, as well dimensions.

In order to increase the attenuation of the beam higher frequencies, and thus further reduce the SR of the signal coupled to the SQUID, a so called RF-bypass was initially installed in the ceramic gap of the beam pipe. This bypass consisted of a series of capacitors and resistors distributed in parallel around the ceramic amounting to a total capacitance of $C = 150\,\mu F$ and $R = 1\,\Omega$ [135]. This capacitance opens a path for the beam induced mirror currents to flow through the beam pipe instead of the outer shell of the cryostat, attenuating the beam current. But will also allow stray currents flowing in the beam pipe to pass through the CCC and be picked up as a beam current.

To further improve the isolation from the cryocooler vibrations, the helium reliquefier vessel was installed in an aluminium support "bridge", placed across the cryostat. A flexible bayonet connection was designed to mechanically isolate the two systems. Vibrations propagating through the ground floor could also impact the CCC performance, and so the 850 kg cryostat assembly was mounted on a 955 kg concrete mass sitting on top of four anti-vibration mats. Additionally, to mitigate the impact of any vibrations

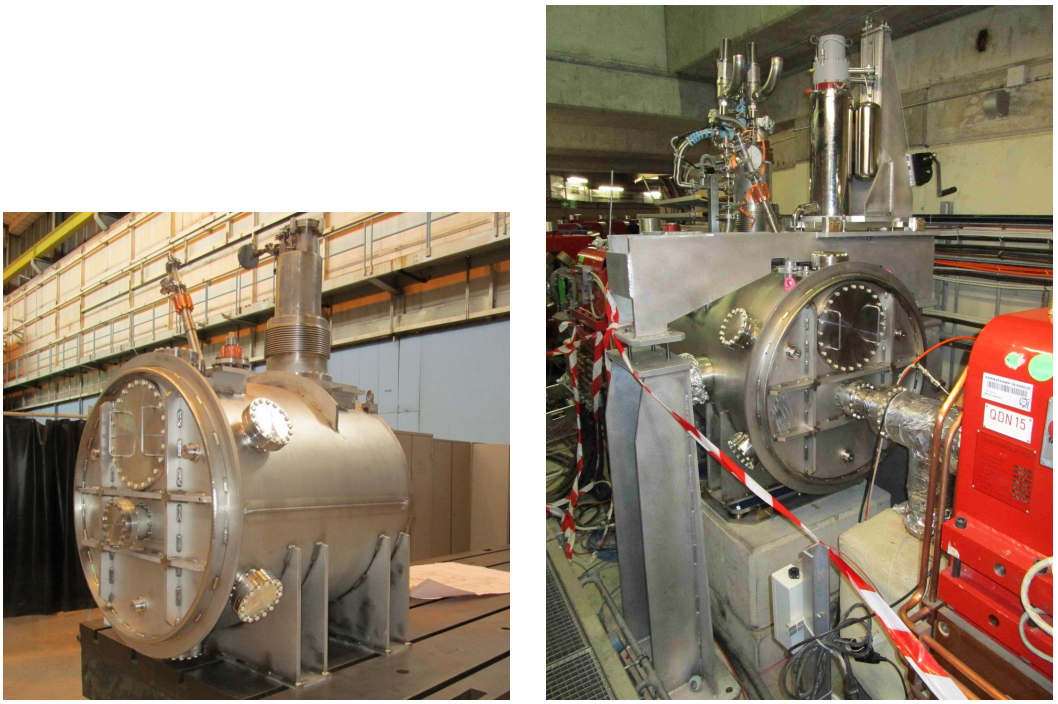

FIGURE 4.11: Left: fabricated cryostat, designed to house the CCC monitor; Right: cryostat installation in the AD accelerator together with the cryocooler installed in a separate support "bridge".

propagating through the accelerator beam pipe, flexible bellows were used on both sides of the cryostat connection to the adjacent accelerator sections.

All the vacuum components were fabricated from 316LN stainless steel, which has low-magnetic permeability, and exhibits almost no hysteresis. Figure 4.11 shows the completed cryostat before and after installation in the AD accelerator.

4.3.2 Instrumentation

A Programmable Logic Controller (PLC) based system was implemented to monitor and control the cryostat operating conditions, relying on the following set of sensors and heaters installed in the cryostat:

- Temperature: 2× low-temperature sensors on the HV, 6× Pt100 sensors in the TS, 1× diode sensor in the cryocooler cold-head, and 1× Pt100 sensor in the helium gas return line.
- Pressure: 1× pressure sensor to measure the gas pressure in the HV.
- Vacuum: vacuum pressure gauge to monitor the insulation vacuum.
- Heaters: 2× heaters in the HV, 2× heaters on the TS, 1× heater in the helium gas return line, and 1× heater in the cryocooler cold-head.
- Level: a liquid helium level gauge was installed inside the HV.

A screenshot of the monitoring application with the different monitoring parameters is shown in Figure 4.12.

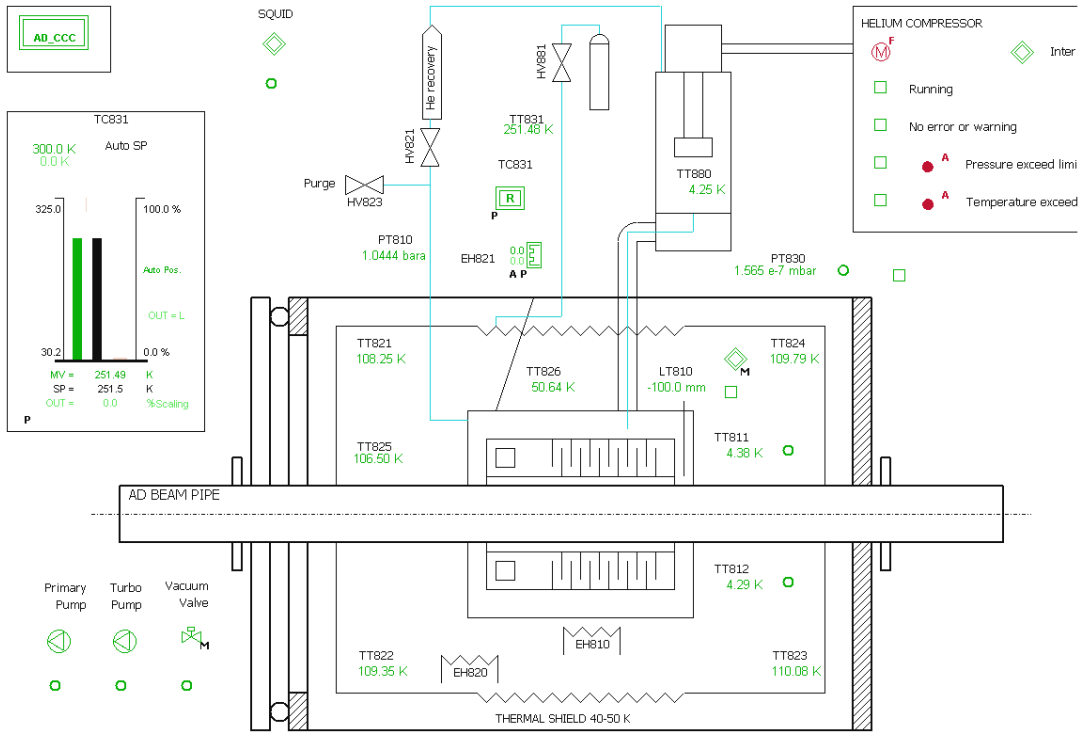

FIGURE 4.12: Screenshot of the PLC application interface, showing the different monitored cryostat parameters.

4.3.3 Performance

In the first year's run the cryostat thermal performance was limited and it was not possible to keep the CCC within working temperatures range for more than 3 days. This was due to an excess of heat in-leak in the cryostat. After implementing corrective and improvement modifications, it was possible in 2016 to extend the cold periods first to 20 days, and later in the year continual operation was attained [132], as shown in Figure 4.13.

Different kinds of pressure variations in the HV were observed. Thermo-acoustic oscillations which severely compromise the cryogenic performance usually appeared during the initial refill of the cryostat. These could be solved by adjusting the helium gas flow between the HV and the reliquefier. Pressure variations and drifts were also observed on a longer time scale. Figure 4.14 shows the pressure measurement during the last period of 2016, this while the cryogenic system was continuously running with a filled cryostat. The maximum pressure was limited by a pressure check valve opening at $\approx 250\,\text{mbarg}$ [2]. These pressure variations have an impact on the CCC measurement, since the induced temperature variation of the SQUID will make its V-Φ curve to drift. This results in fluctuations of the CCC zero current baseline.

[2]This is independent of the two safety valves adjusted to open at 1.5 barg, which were also installed in the cryostat.

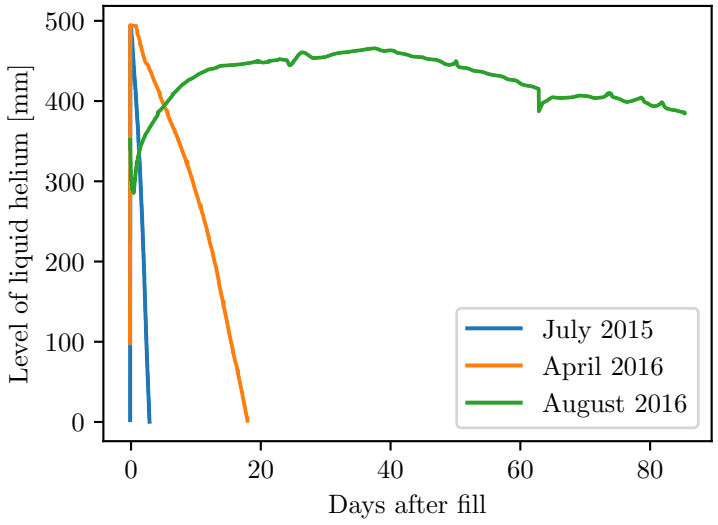

FIGURE 4.13: Evolution of the level of liquid helium inside the cryostat after the improvement modifications.

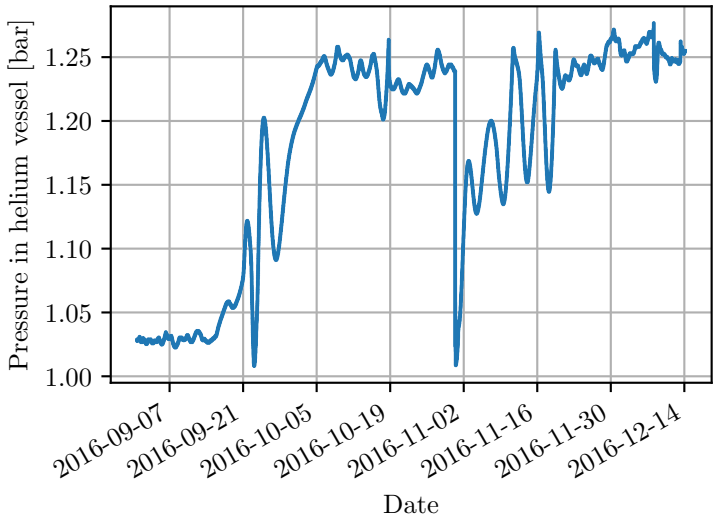

FIGURE 4.14: Long-term pressure variations in the liquid helium vessel.

4.4 Conclusion

In this chapter different aspects concerning the installation and integration of the CCC monitor in the AD were presented, as well as the developed cryostat and cryogenic system.

The diameter of the FAIR CCC shield was too small to enable the integration of the monitor and cryostat in the allocated AD section, taking into account the diameter of the existing vacuum beam pipe. However, due to modifications of the machine optics that have occurred over the years, the beam size in this location permitted the reduction of the aperture of the beam pipe to 100 mm. This was verified by looking into the machine

optics functions and computing the maximum transverse space occupied by the beam along the drift section.

An estimation of the stray magnetic field expected in this section was performed, by simulating the field induced by the closest accelerator quadrupole magnets. These were estimated to be smaller than the Earth's magnetic field, with fields of the order of $\sim 1\,\mu T$. Afterwards, it was possible to measure the magnetic field . This measurement revealed that the stray field present in the installation location is one order of magnitude higher than expected from the simulation. This was probably due to inaccurate modelling of the magnetic properties of the magnets' yokes in the performed simulation. Also, only the adjacent quadrupole magnets were considered in the simulation, while stray fields could also be induced by magnets, although these contributions should not entirely explain the observed difference. Nevertheless, the magnitude of the measured field was under $100\,\mu T$, and hence, the CCC performance should not be strongly affected by the magnetic stray fields present the AD cycle.

Chapter 5

Measurements and results

The measurements performed with the designed CCC are presented in this chapter. Section 5.1 covers all the measurements performed in laboratory setting, to characterise the device in terms of its current sensitivity, noise spectrum and frequency transfer functions. These measurements are compared with the expected theoretical values obtained in Chapter 3. The measurement dependency with current horizontal position is also presented, as well as the dependency to an external magnetic field. Finally, the response of the CCC to a current signal simulating the expected AD injection was also measured in laboratory.

In Section 5.2 the beam measurements obtained after installation of the CCC in the AD are presented. The beam current measurements performed with and without the *RF*-bypass are presented in Section 5.2.1. The measurement of the beam intensity is presented in Section 5.2.2, and this is compared with the similar measurement obtained with the Schottky monitor. Section 5.3 covers the performance analysis performed over the set of acquired AD cycles during the year 2017. This includes the analysis of the beam current and intensity resolution, as well as the observed drifts and variations of the zero-current baseline. The chapter concludes in Section 5.3.1 with a discussion of observed flux jump at injection, including the measurements that have been performed to try to identify the root cause.

5.1 CCC characterisation

The assembled CCC monitor was first measured and characterised alone in laboratory. These measurements were performed in the University of Jena. The CCC schematic of the is shown in Figure 5.1. Two single-turn current loops were used to inject a current to be measured by the monitor: one through a loop directly wound around the ferromagnetic core inside the magnetic shield, and a second through a loop wound through the magnetic shield. Figure 5.2 is shows the setup used to measure the current calibration curves and background noise spectrum.

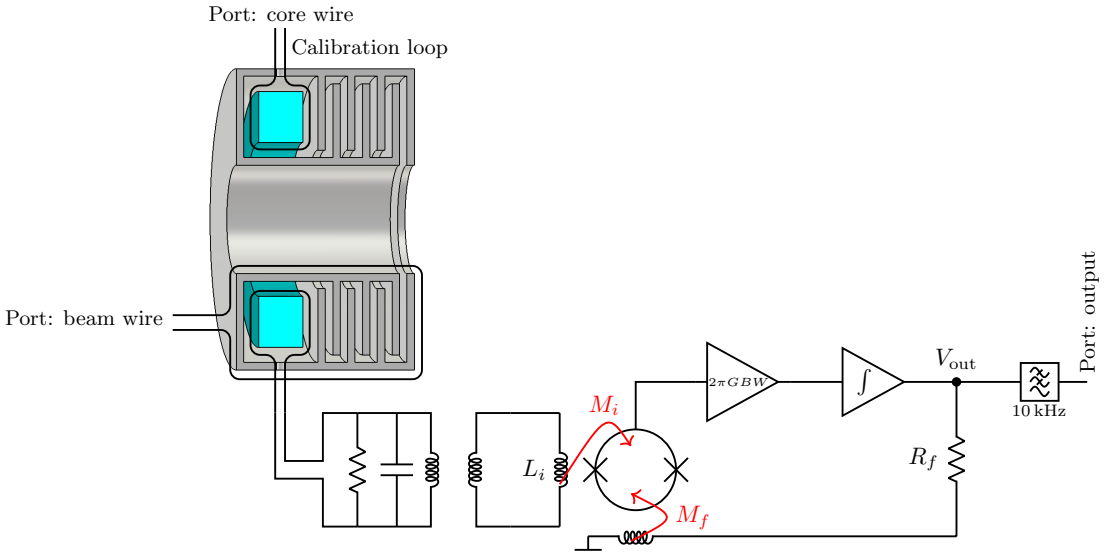

FIGURE 5.1: Schematic of the stand-alone CCC used.

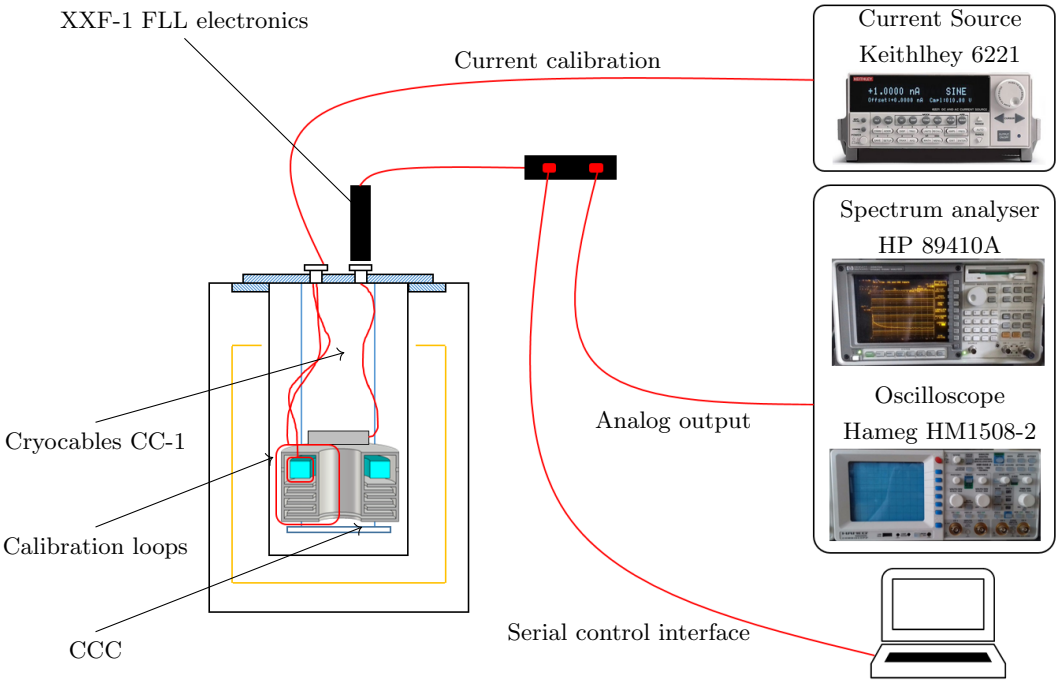

FIGURE 5.2: Setup used in the laboratory measurements of the CCC alone. Measurement of the current calibration used the current source and oscilloscope. Measurement of the background noise spectrum used the signal analyser as a spectrum analyser.

5.1.1 Current calibration of CCC alone

A current calibration was performed to determine the S_{I_b} parameter. The current was performed with the reference current injected through: the single turn calibration loop wound directly around the pickup core, and via wire passing through the CCC shield structure. The first one will be referred to as "core wire", and the second one as "beam

wire" for beam simulation purpose. For generating the calibration currents the Keithley 6221 precision source described in Section 3.5.2 was used, and for measuring the SQUID/FLL voltage output the analogue oscilloscope Hameg HM1508-2 was used.

The precision current source was used to generate 100 Hz sine wave of variable amplitude. The FLL feedback resistor was set to $R_f = 2.73\,\mathrm{k\Omega}$ [1], which represents a flux to voltage gain of $G_{\mathrm{FLL}} = 2.73\,\mathrm{k\Omega} \times 44\,\mu\mathrm{A}/\phi_0 = 120.12\,\mathrm{mV}/\phi_0$. Figure 5.3 shows the measured voltage signals and fitted sine curves for the calibration using the "beam wire". From the amplitude values obtained with the fit of the acquired signals to the original

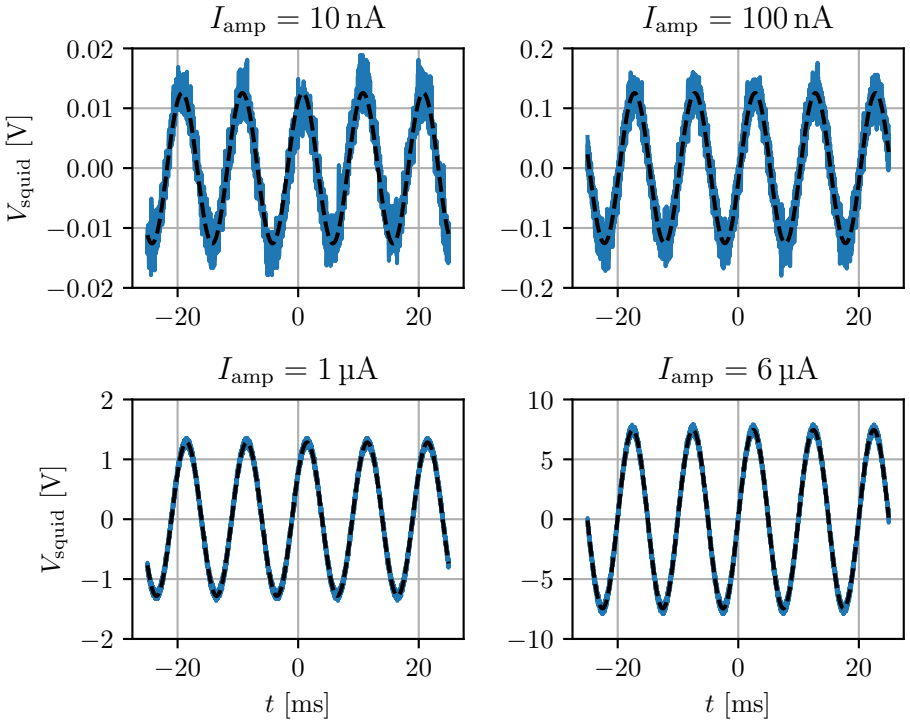

FIGURE 5.3: Measured current calibration signals from the "beam wire", with increasing current amplitude.

sine wave function, the calibration parameters were determined using the least squares method to the linear relation,

$$\Phi_{\mathrm{SQUID}} = \Phi_{\mathrm{offset}} + I_{\mathrm{b}} \cdot S_{I_b}. \tag{5.1}$$

Each current point was weighted by its respective error, as described in Appendix D. The obtained linear calibration curves are shown Figure 5.4, and the numerical values are in Table 5.1. The measured calibration factors are very close to the theoretical one $S_{I_b} = 10.7\,\phi_0$ obtained in Equation 3.26, exhibiting a difference of $\approx 3\,\%$. The CCC sensitivity to a current injected in the "core wire" is 0.6 % smaller than a current passing trough the "beam wire".

[1] At this point both R_f values of 1 kΩ and 2.73 kΩ were being considered for the final system parameters. Eventually it was decided to use 1 kΩ, but these early measurements were done using 2.73 kΩ.

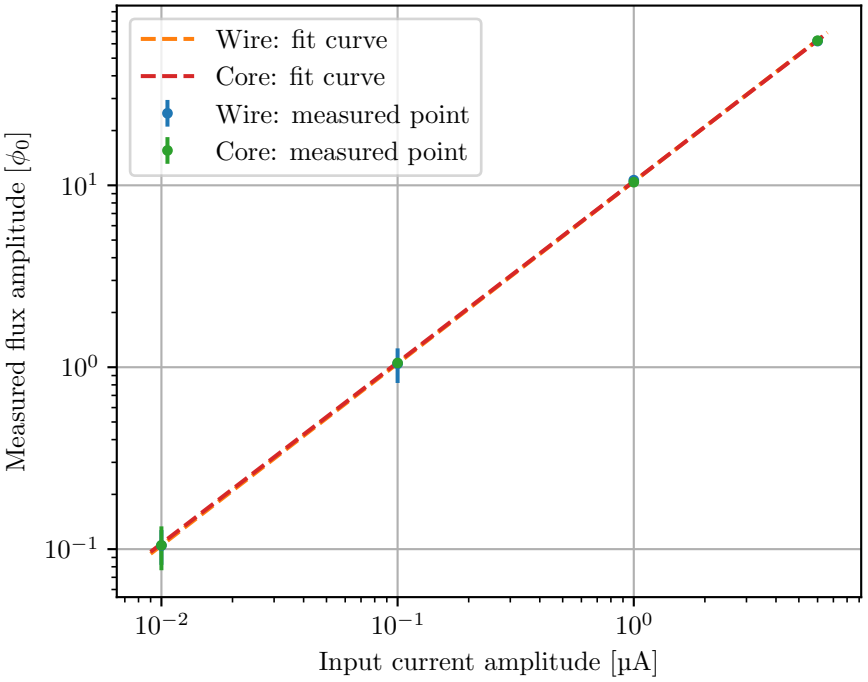

FIGURE 5.4: Current to magnetic flux calibration curve.

Calibration	Φ_{offset} $[\phi_0]$	S_{I_b} $[\phi_0/\mu\text{A}]$
Beam wire	0.00 ± 0.03	10.49 ± 0.01
Core wire	0.00 ± 0.04	10.43 ± 0.01

TABLE 5.1: Results of current calibration performed on the CCC alone.

5.1.2 Noise spectral density of CCC alone

The noise spectral density of the CCC alone in the test cryostat was measured using the spectrum analyser HP 89410A. This instrument is based on the superheterodyne architecture and provides a very good frequency resolution down to 0.01 Hz, covering very low-frequency ranges from 1 Hz up to 10 MHz. In order to have a good compromise between frequency resolution and sweep times, several acquisition of the noise spectral density were performed with different frequency resolution for different frequency ranges. Afterwards, these were concatenated together in measurement which is shown in Figure 5.5. During the acquisitions it was also important to keep any mechanical vibrations to a minimum level. For example, even the footsteps of people waling in the nearby corridor would show up as a very strong spectral component. This was normalised to the measured beam current using the previously obtained current calibration factor. The spectrum shows a good agreement with the theoretical curve of the noise induced by the *RC*-filter which is the dominant contribution at low frequencies. At around 100 kHz the

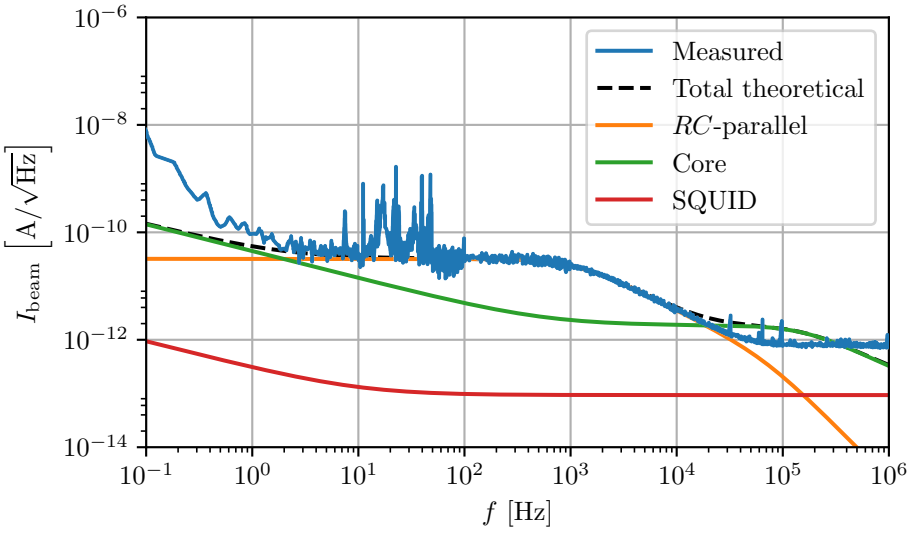

FIGURE 5.5: Measured current spectral density noise, compared with the theoretical predictions.

measured noise is below the predicted core thermal noise, although this can be understood by the overestimated imaginary component of the complex permeability obtained in the fit of Figure 3.11 at these frequencies. On the other hand, between 5 Hz and 50 Hz, the core noise seems to be slightly underestimated. Additional perturbations are visible in the range (8-100) Hz which are thought to be caused mostly by mechanical vibrations and electrical power lines at 50 Hz. The obtained current resolution in the 1 kHz bandwidth was ≈ 2 nA.

5.1.3 Sensitivity to a magnetic dipole field

The sensitivity of the CCC to an external dipole magnetic field was measured using a Helmholtz coil. First the field generated at the center of the Helmholtz coil was measured using a magnetic field probe. After this, the Helmholtz coil was installed around the wide-neck cryostat with the CCC inside. Very low-frequency sinusoidal signals of different amplitude were imposed, and the CCC response was recorded. The SQUID/FLL gain was set to a high value, with $R_f = 30\,\text{k}\Omega$, to increase the measurement sensitivity. Two orientations of the magnetic field were measured, as shown in Figure 5.6. The observed sensitivities were much higher than the expected values taking into the account the magnetic shielding provided by the meander-shaped geometry. It was also observed that when the field was parallel to the SQUID cartridge the sensitivity was higher than the one obtained when the field was orthogonal to the cartridge. The obtained values were:

- Sensitivity to parallel field: 179 nA/mT
- Sensitivity to orthogonal field: 72 nA/mT

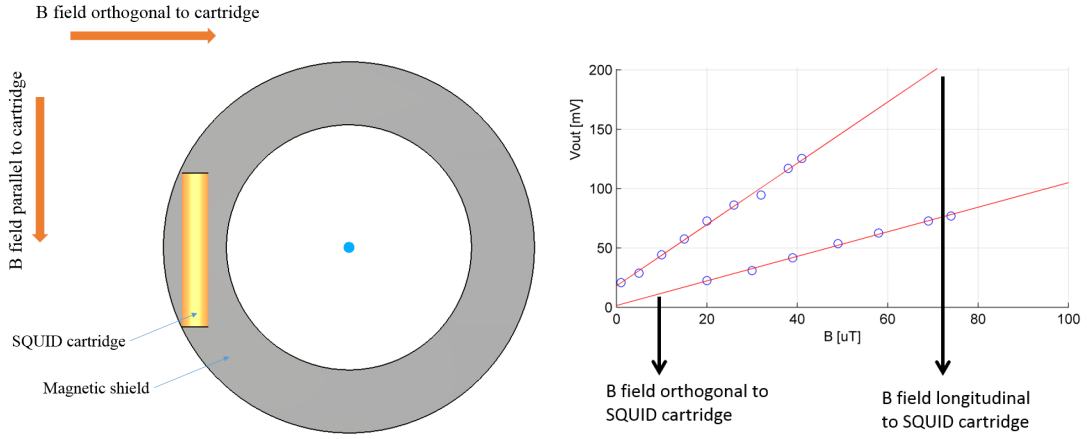

FIGURE 5.6: Measurement of the CCC sensitivity to an external dipole magnetic field

If the magnetic field was being coupled to the pickup core shielded inside the meander shaped geometry, no difference in sensitivity would be expected for the two orientations. Hence the coupling of the magnetic field to the CCC is thought to happen directly in the coupling circuit and SQUID inside the tube cartridge.

5.1.4 Current calibration of the CCC in the new cryostat

After installation of the CCC in the new cryostat its characteristics were again measured in a laboratory environment before the installation in the AD. The CCC configuration is the same as in the previous measurements except for the beam simulating current that was not injected through a stretched wire passing through the beam pipe aperture as shown in Figure 5.7. These measurements were performed in the cryogenics labora-

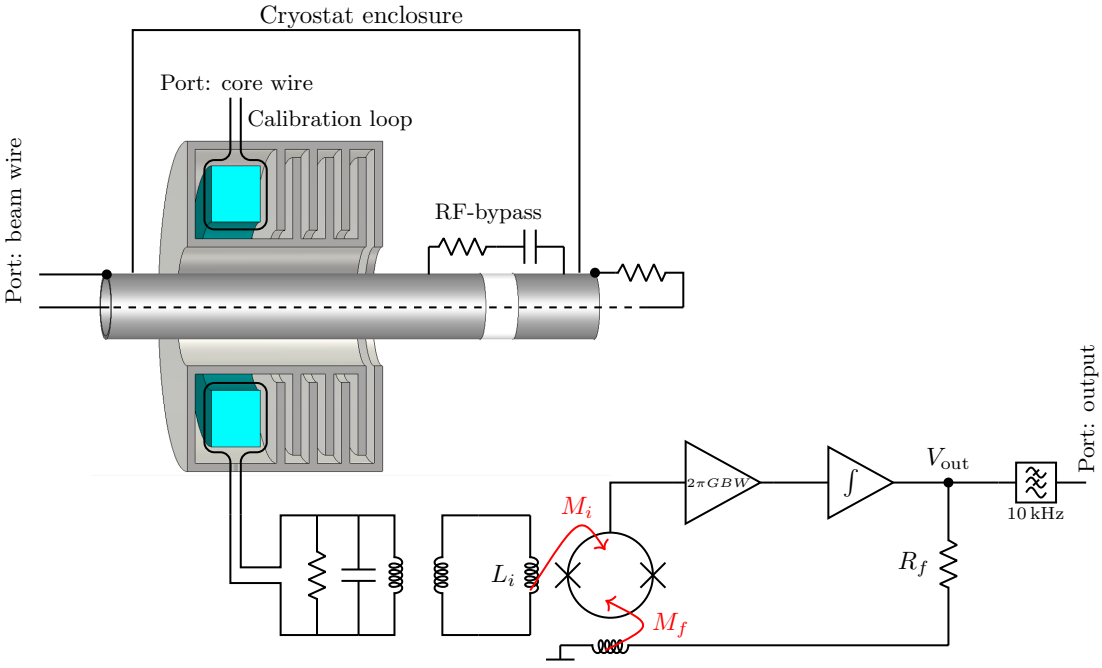

FIGURE 5.7: Schematic of the CCC and beam pipe.

tory at CERN, in which, running equipment such as vacuum pumps, compressors and reliquifiers, might perturb the CCC measurements. Also the liquid helium reliquifier was already installed in the cryostat, with its compressor located right next to the cryostat, and running at the same time that the measurements were being taken. Additionally, the *RF*-bypass installed in the ceramic break of the cryostat beam pipe, shown in Figure 5.7, was responsible for an observed high sensitivity to EMI interferences. All these factors contributed to an excess of noise and perturbations in the performed measurements.

The same Keithley 6221 current source was used for generating the precision calibration currents, the SQUID/FLL voltage output was measured using the 12-bit oscilloscope Lecroy HRO 6Zi. The complete measurement setup is shown in Figure 5.8 The Magni-

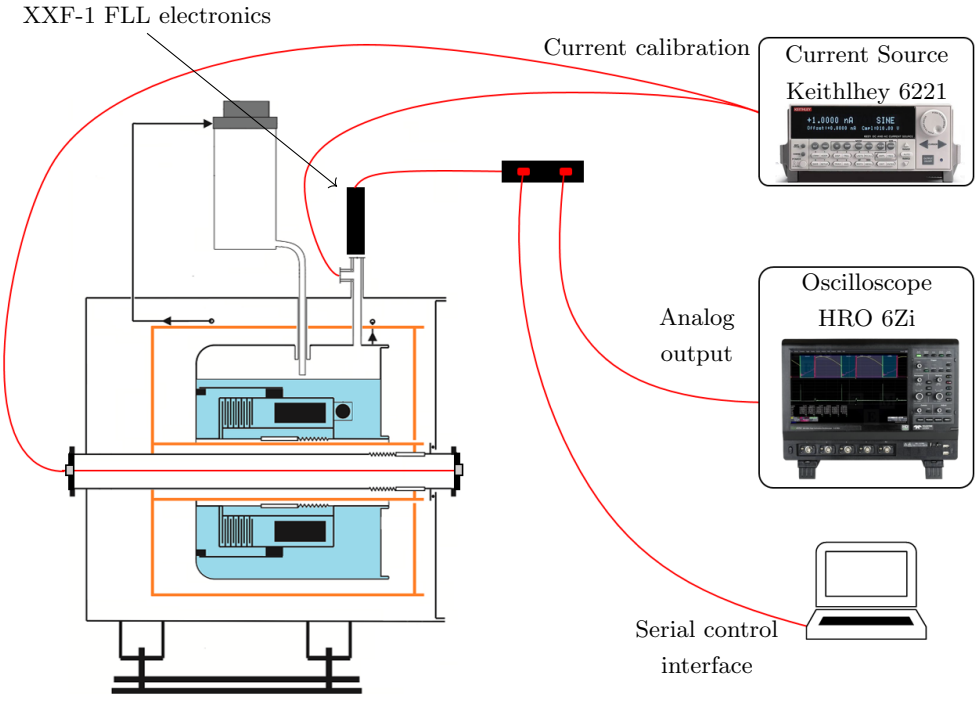

FIGURE 5.8: Setup used in the laboratory measurements of the CCC installed in the new cryostat.

con SQUID/FLL electronics has a second-order Butterworth[2] 10 kHz low-pass filter at the output of the feedback loop, as shown in Figure 5.7. For most of the measurements shown in this chapter, the filter was turned on.

As before, a current calibration was performed using sine waves of various amplitudes and constant frequency, equal to 100 Hz. The FLL feedback resistor was set to $R_f = 1\,\mathrm{k}\Omega$, which represents a flux to voltage gain of $G_{\mathrm{FLL}} = 44\,\mathrm{mV}/\phi_0$. The measured and fitted curves are shown in Figure 5.9.

Two different calibrations were performed. As before a current was injected through the so-called "core wire". And a second calibration was performed using a wire stretched through the vacuum beam pipe opening of the cryostat, as shown schematically in

[2]The Butterworth filter is a type of signal processing filter designed to have a frequency response as flat as possible in the passband.

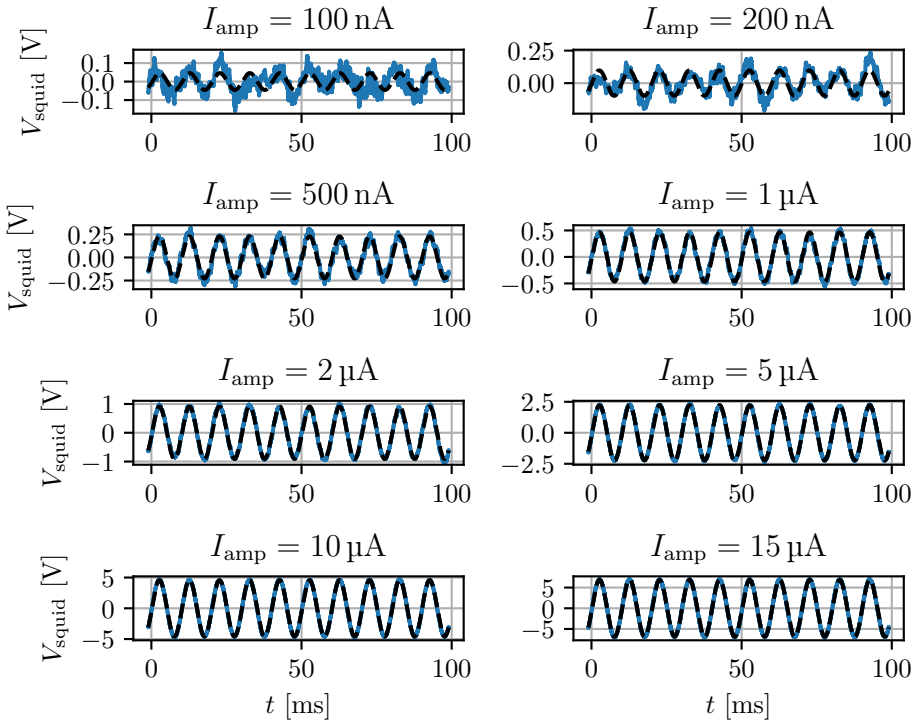

FIGURE 5.9: Measured current calibration signals from the "beam wire", with increasing current amplitude. The measurement was perturbed by many interferences which limited the capture of the lower current signals.

Figure 5.7, which will also be referred to as "beam wire" port. In this configuration the current source is connected to one side of the cryostat beam pipe, and the other side is terminated with a resistive load. The injected DC current returns back to the source through the cryostat vacuum vessel.

The obtained calibration curves are shown in Figure 5.10, and the values of the fitted parameters in Table 5.2.

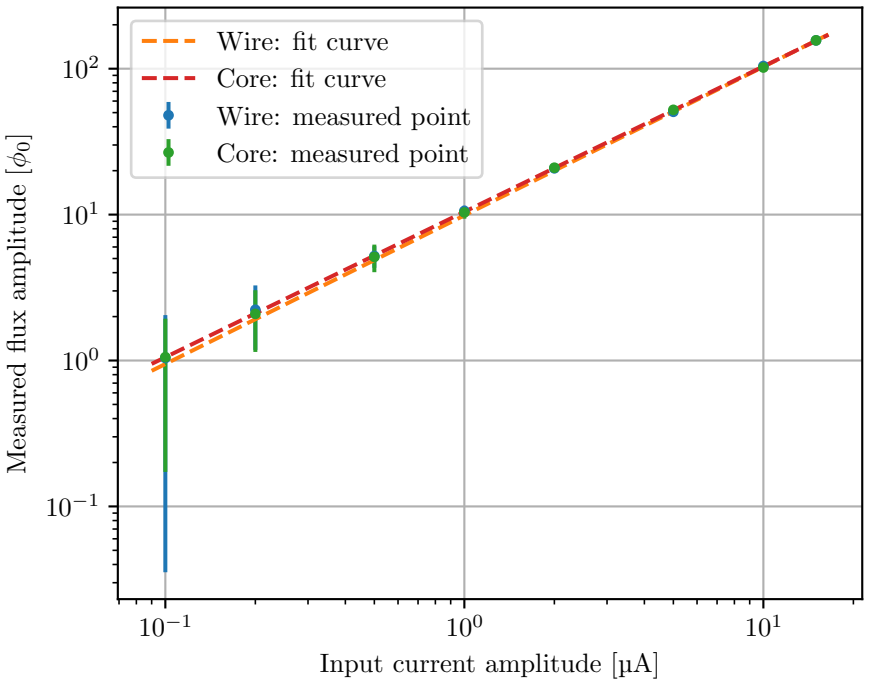

FIGURE 5.10: Current to magnetic flux calibration curve.

Calibration	Φ_{offset} $[\phi_0]$	S_{I_b} $[\phi_0/\mu\text{A}]$
Beam wire	0.1 ± 0.5	10.41 ± 0.01
Core loop	0.0 ± 0.4	10.34 ± 0.01

TABLE 5.2: Results of current calibration performed on the CCC installed inside the cryostat.

The fit of the smaller calibration currents is much less accurate, since these signals were affected by the many strong interferences picked up by the CCC. The obtained sensitivities are smaller than the ones previously obtained for the CCC alone by $\approx 0.8\,\%$, and the difference between the calibration through the "core wire" and the "beam wire" is $0.7\,\%$ in line with what had been observed before. For a current sensitivity $S_{I_b} = 10.4\,\phi_0/\mu\text{A}$, this represents an uncertainty of $\delta I_b = 7\,\text{nA}$ over a $I_b = 1\,\mu\text{A}$ current span.

5.1.5 Noise spectral density of the CCC in the new cryostat

The noise spectrum was estimated from the acquired time signals with the 12 bit oscilloscope, since a low frequency spectrum analyser was not available during these measurement. The power spectral density was obtained by averaging the Fast Fourier Transform (FFT) of multiple windowed segments, using the periodogram Welch's method [136]. The obtained spectrum is shown in Figure 5.11. The general purpose Hann window was

used to scale each segment before the FFT computation. The main perturbations were observed at 72 Hz, which was thought to be originating in some mechanical equipment running nearby; 1.4 Hz which is the cryocooler beating frequency; and at 50 Hz from the electric network. The obtained current resolution in the 1 kHz bandwidth was between 50 nA and 100 nA, depending on the measurement conditions and other running equipment.

When using discrete Fourier transforms different effects introduce errors in the spectrum shape amplitudes, and these affect differently the coherent and incoherent noise components. The main example of such effects is spectral leakage, which is mitigated by the use of weighing windows although never fully eliminated. Different windows also introduce different coherent power gain errors affecting coherent components, and equivalent noise bandwidth error overestimating the noise floor due the side lobes in the windows spectrum. In the spectrum of Figure 5.11 the equivalent noise bandwidth error was corrected by using the factor −1.76 dB corresponding to the Hann window [137]. Despite this correction it is not possible to observe, in the measured spectrum, the good agreement of the noise floor with the theoretical prediction, as was the case with the measurement in Figure 5.5. It is thought that this is mainly due to the fact that there are many coherent perturbation components at adjacent frequencies, which mask the noise floor due the spectral leakage effect.

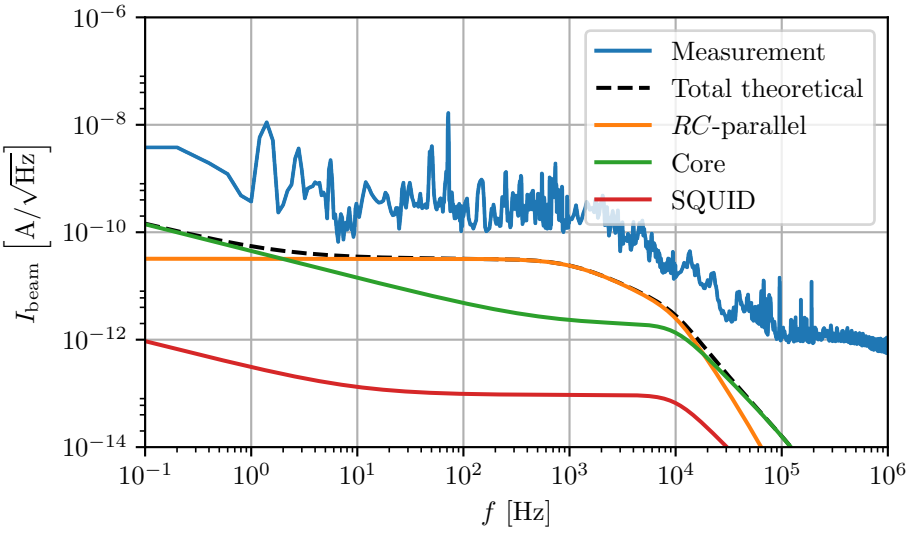

FIGURE 5.11: Measured current noise spectrum in laboratory.

5.1.6 Transfer function of the CCC

With the CCC already installed in the cryostat the frequency dependent transfer function of the CCC was measured using a Keysight E5061B vector network analyser. This is instrument is able to measure down to 5 Hz. The transfer function was derived from the measurement of the S_{21} parameter with port 2 of the network analyser connected

to the output of the FLL electronics. Two transfer functions were measured, depending where the excitation current was applied. In one measurement this current was injected the "beam wire" by connecting it to the port 1. And a second measurement was taken by connecting the port 1 to the "core wire". A schematic of the measurement setup is shown in Figure 5.12. In order to perform the measurement a weak excitation signal

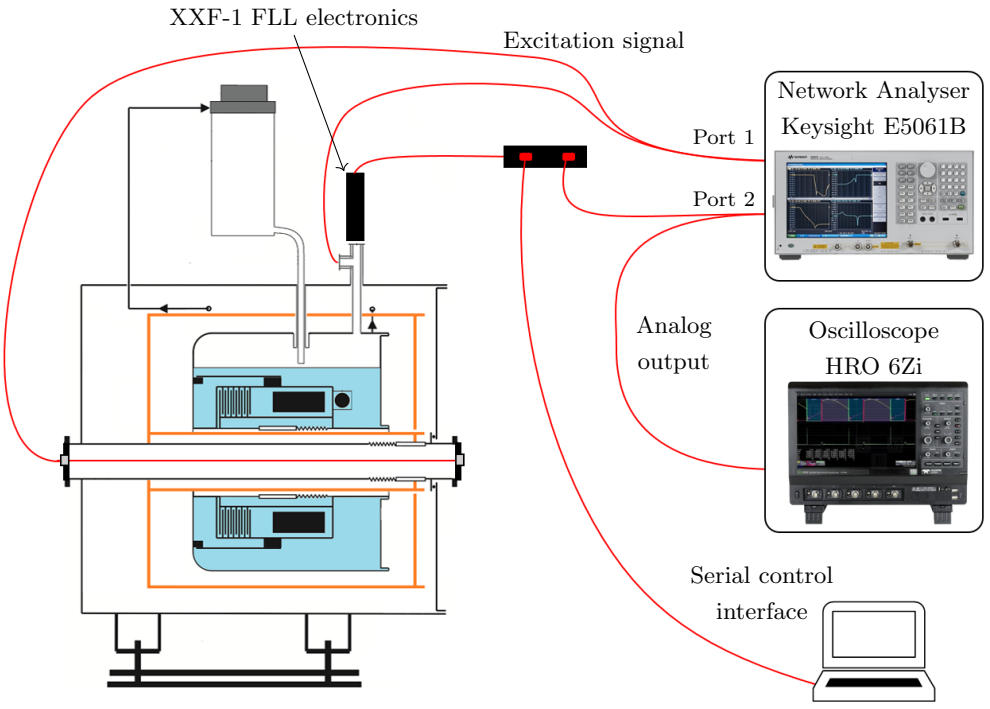

FIGURE 5.12: Setup used in the laboratory measurement of the transfer function of the CCC installed in the new cryostat. This was measured with network analyser excitation injected in the core wire and in the beam wire calibration loops.

was emitted by port 1, to guarantee that the currents being measured by the CCC were sufficiently small to avoid the saturation or instability of the FLL circuit. For that purpose, before each acquisition, the CCC output was observed in an oscilloscope to make sure that the signal was not being distorted by the frequency scan of the network analyser.

To account for low-pass 10 kHz filter at the output of the FLL electronics, the theoretical transfer function that had been derived in Equation 3.40, was convoluted with the filter transfer function in order to compare with the performed measurements. Hence the theoretical curves shown here differ from the one in Figure 3.29.

The DC-gain of the measured transfer functions was $7\,\phi_0/\mu A$, this difference of -3.5 dB was most probably due to the setup and the fact that no precise calibration of the network analyser was performed. Since the aim of this measured was to compare the evolution of the frequency response with the theoretical curves, the former were normalised so that they exhibit the same gain at low-frequencies.

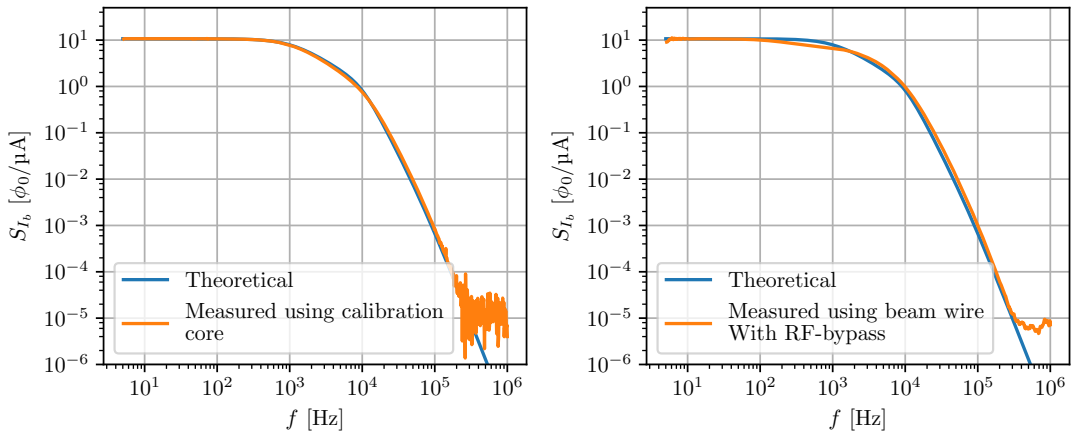

FIGURE 5.13: Measured gain of the CCC transfer function, referred back to the sensitivity of the coupling circuit. Left plot: signal injected through calibration loop - "core wire", right plot: signal injected through "beam wire", with the *RF*-bypass installed in the ceramic break. Both graphics should the same theoretical transfer function.

The left-hand side of Figure 5.13 shows the measured gain of the transfer function with a current being injected directly through the "core wire". The measured shape shows a very good agreement with the theoretical curve, with the first pole very close to the design frequency of 1.12 kHz, due to the fact that the 10 kHz filter was active at the time of the measurement, it is not possible to verify the location of the second pole at 69.61 kHz. However, it could be observed from the phase function that indeed a second pole was present, although the file with this plot was not correctly saved. The measured transfer function with the current being injected through the "beam wire" is shown in the right-hand side of Figure 5.13. In this measurement the cryostat geometry and the *RF*-bypass do change the transfer function although it is possible to observe that this has a reduced effect in this range of frequencies.

The RF-bypass was causing the CCC to pick up stray currents flowing in the accelerator beam pipe which strongly perturbed the beam current measurement. At the same time it was observed from the comparison of the two transfer functions measured in Figure 5.13 that the RF-bypass was almost not affecting transfer function of the CCC and hence was not having a significant impact in reducing the signals SR. Hence, it was decided to remove the RF-bypass. One year after the first measurements it was possible to measure again the transfer function from the "beam wire" port, after having removed the *RF*-bypass from the ceramic break. The resulting measurement is shown in Figure 5.14.

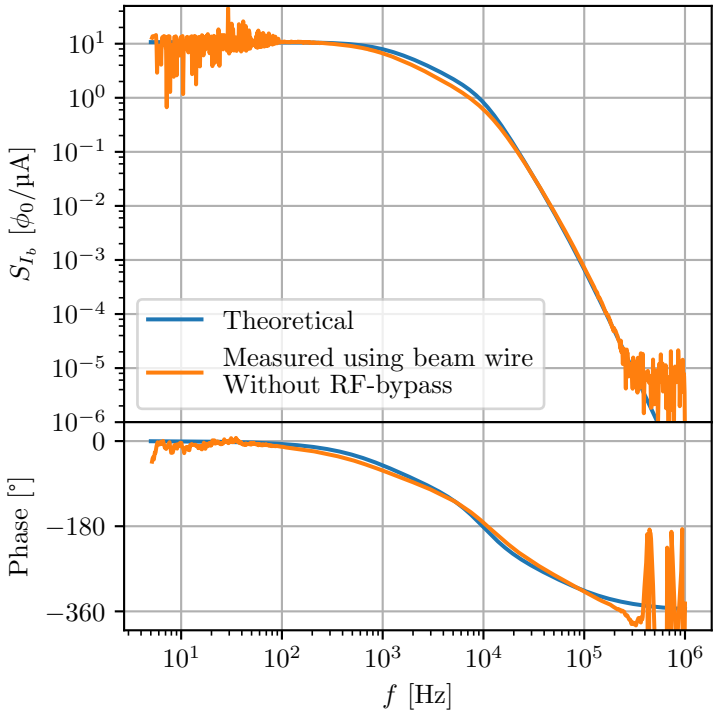

FIGURE 5.14: Measured transfer function with signal injected through "beam wire" port, and the *RF*-bypass removed from the ceramic break.

The measurement noise observed at low-frequencies is due to the improper setup of the network analyser while taking this measurement, namely the frequency sweep time, which was too fast, and the Intermediate Frequency filter Bandwidth (IFBW), which was too large. In reality, the transfer function still maintained the flat response at low-frequencies as expected theoretically and as had been previously measured.

5.1.7 Position dependency

The dependency of the CCC measurement with respect to the horizontal position of the "beam wire" was measured using the same setup used for measuring the "beam wire" current calibration shown in Figure 5.8. A movable current port, shown in Figure 5.15, was used on both sides of the cryostat beam pipe to inject and change the position of the wire along the horizontal axis. Similarly to what was done for the calibration, different sine wave currents of constant amplitude were injected and the measured output were measured for the different displacement values. The amplitude variations, calculated with respect to the average of amplitude for the combined positions, as a function of the wire position were fit the linear function,

$$\Delta I_b^{\text{obs}} = a + x_{\text{pos}} \cdot b. \tag{5.2}$$

Figure 5.16 shows the measured current variations, and Table 5.3 shows the obtained fit parameters.

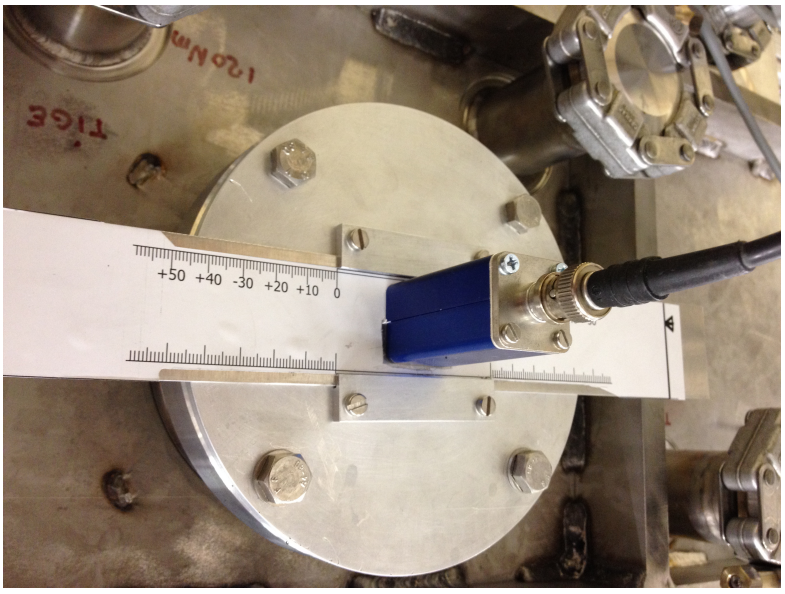

FIGURE 5.15: Setup used to change the position of the beam simulating wire passing through the cryostat beam pipe.

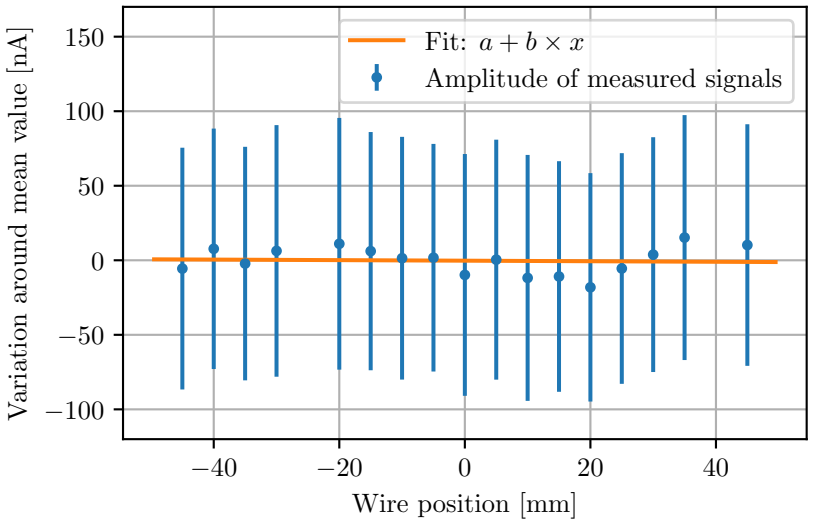

FIGURE 5.16: Measurement of the horizontal position dependency to currents injected in the "beam wire".

Position	a [nA]	b [nA/mm]
Beam wire	-0.27 ± 19.44	-0.018 ± 0.734

TABLE 5.3: Measurement of the CCC beam current position dependency, obtained by measuring the CCC signal for different horizontal positions of the "beam wire".

No correlation could be observed and the calculated position dependency factor is compatible with zero. The measurement errors are large since this measurement was

performed while the cryostat was still placed in the noisy environment of the Cryolab, and with the *RF*-bypass was still installed in the ceramic break.

5.1.8 Measurement of an AD injection like signal

The stability of the SQUID/FLL system to a current identical to the AD beam injection was also measured in laboratory by injecting a current signal through the "beam wire" generated with the waveform generator Keysight 33522A. This generator allows to generate point-by-point arbitrary waveforms with bandwidths up to 30 MHz and with 16 bit precision. This allows to accurately reproduce the injection current as specified by the parameters in Table 3.2. The measurement setup is shown in Figure 5.17.

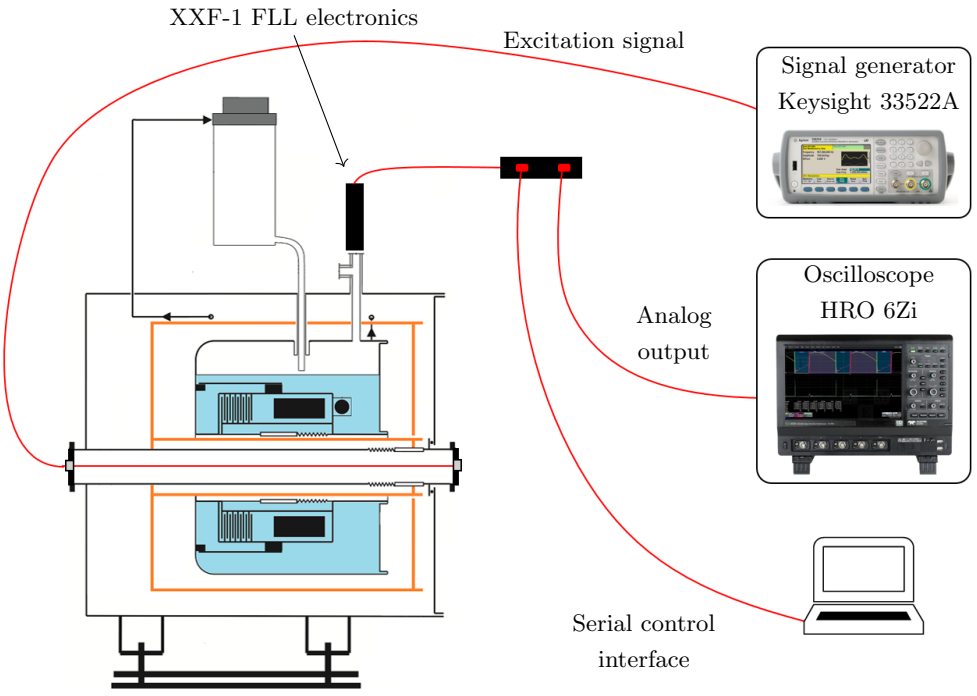

FIGURE 5.17: Setup used in the laboratory measurement of the transfer function of the CCC installed in the new cryostat. This was measured with network analyser excitation injected in the core wire and in the beam wire calibration loops.

Figure. 5.18 shows the measurement for successive injections of the bunched signal. The generated signal had the same time structure as the AD injection current and an average voltage equal to 6 mV (peak-to-peak voltage was set to 70 mV). By injecting this signal in port 1 of Figure 5.7, an average current equal to $\approx 17\,\mu A$ should be measured by the CCC. This is almost 50 % above the expected current amplitude during AD injection.

The absence of a sustained strong drift, and the fact that the amplitude of the measured signal is inline with expected value indicates that the system should able to cope with the AD injection high slew rate signal without significant flux jumps. The observed long-term variation of the mean values of the current reading at the top and

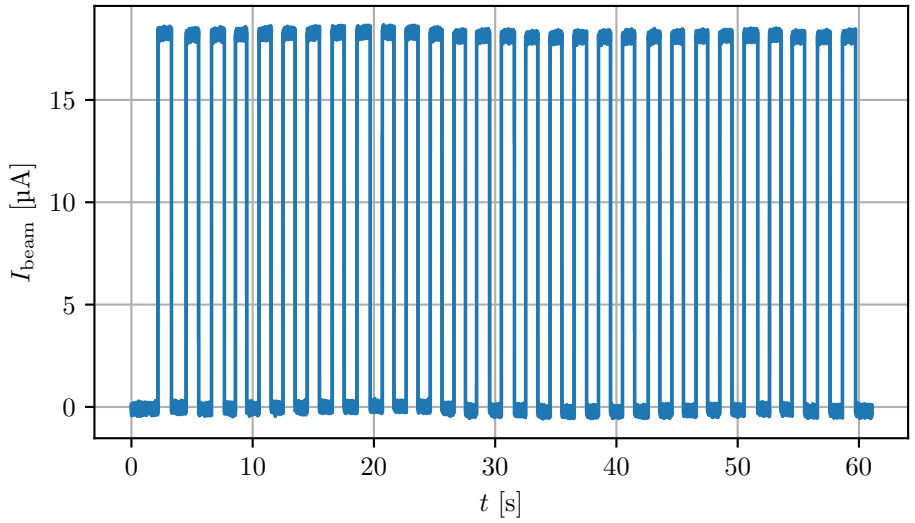

FIGURE 5.18: Laboratory measurement of a current signal with the same structure found during the AD injection. This signal was repeatedly switched on and off [138] .

bottom values is thought to be due to external perturbations, as e.g. fluctuations in the pressure of the cryostat or any source of $1/f$-noise.

5.2 Beam measurements in the AD

After the laboratory measurements the cryostat and the CCC were installed in the AD, and measurements with real beam could be taken. For some measurements an oscilloscope was used and on others the acquisition system described in Section 3.5 was used.

During commissioning and before the first beams were injected excessive noise was observed, with components mostly at odd harmonics of 50 Hz, as shown in the spectra of Figure 5.19. Besides the interferences at 50 Hz and harmonics, it is possible to observe another expected perturbation at 1.4 Hz which is caused by the functioning of the cryocooler in the reliquefying unit. Different configurations for the ground connection of the cryostat, SQUID electronics were tried and a minimum RMS zero current noise of $\sigma(I_b) \approx 180\,\text{nA}$, was obtained when most of the AD equipment were turned off, and no beam was circulating.

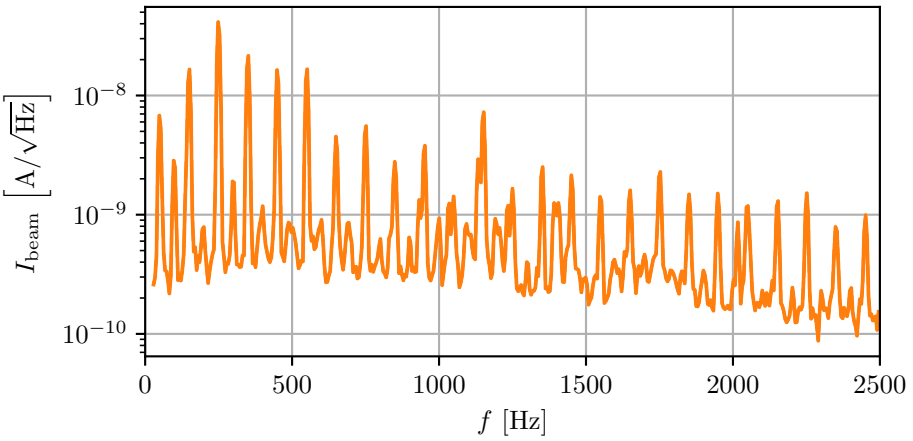

FIGURE 5.19: Noise spectrum measurement obtained right after installation of the CCC in the AD and before improving grounding. The RMS noise level was $\sigma(I_{\text{b}}) = 450\,\text{nA}$ in the current measurement, and this was later reduced to $\sigma(I_{\text{b}}) = 180\,\text{nA}$ by improving the system grounding. Strong perturbation components are observed at 50 Hz and harmonics.

5.2.1 Current measurement

When all the AD equipment was running and the first $\overline{p}$ beams injected, the noise level increased to $\approx$ 250 nA. Additionally it was observed that at the moment of beam injection, the zero current offset changed abruptly due to a flux jump of the SQUID/FLL working point. This is visible in the measured raw output voltage shown in the middle plot of Figure 5.20. This is the very first beam measurement obtained with the CCC. In it the V_{out} signal was acquired using a Lecroy Wavejet 354-A digital scope. This scope has only 8 bit what in the measurement range limits its voltage resolution to 150 mV, producing the quantisation noise visible in Figure 5.20.

When injection, happens instead of measuring a current increase as expected, the SQUID/FLL shows an unphysical sharp decrease in the voltage output V_{OUT}. This can be corrected for at the end of the cycle after beam ejection (or beam loss as in the current example), when one knows that the current should be zero, allowing for a correction of the measurement baseline, before and after injection. The bottom plot of Figure 5.20 shows the current measurement, after applying this offset correction, and after applying the previously measured calibration factor.

The measurement noise could also be greatly reduced by applying a time-domain moving average low-pass filter, with a window length multiple of the perturbation period. This resulted in the averaged signal shown in Figure 5.20, with a current resolution of $\approx 30\,\text{nA}$, at the expenses of a bandwidth reduction to 11 Hz.

The *RF*-bypass, installed in the ceramic gap shown in Fig. 5.7, intended to provide additional reduction of the beam signal slew rate, was thought to be responsible for the excess of noise observed, by providing a path for stray currents flowing in the beam pipe to pass through the CCC and be measured by it. Additionally, in the hypothesis that

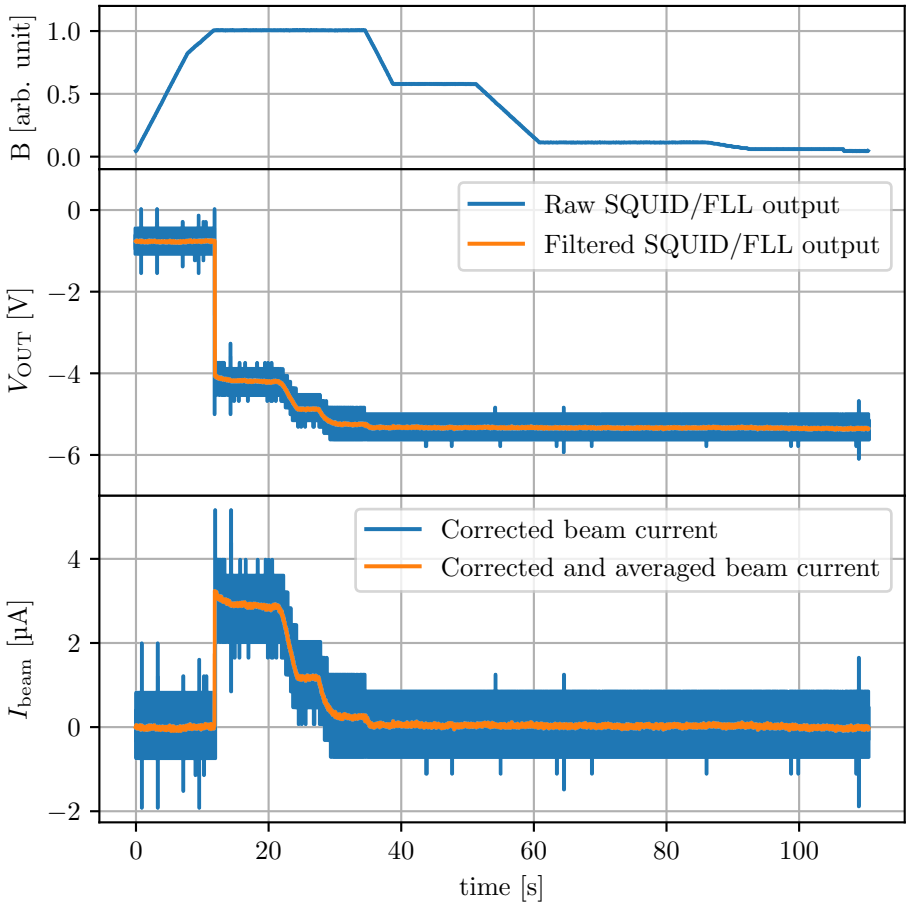

FIGURE 5.20: First measurements of the AD beam with the CCC. Uncalibrated measurement showing the raw voltage signal obtained at the output of the FLL electronics, sampled with an 8 bit oscilloscope at 2.5 kHz. Top plot: magnetic cycle of AD dipoles in arbitrary units; Middle plot: measured SQUID/FLL output raw signal (in blue), and same signal filtered with a moving average (in red); Bottom plot: calibrated beam current measurement after filtering and baseline recovery (before beam injection and after beam extraction).

the flux jump occurring at injection is caused by an excess of the beam current slew rate, the RF-bypass was not able provide the required slew rate reduction. Hence, this was removed for the measurements performed in 2016 and 2017. Indeed, removing the RF-bypass eliminated most of the interference at 50 Hz and harmonics, and strongly reduced the overall background perturbation level. Figure 5.21 shows the example of an AD cycle with the corresponding CCC current measurement. The value obtained for the current measurement noise resolution is

$$\sigma(I_b) \approx 2.8\,\text{nA}, \tag{5.3}$$

and this is observed to be constant during the entire cycle. On some occasions the jump observed at injection limited the dynamic range available for the current variation during the remaining of the cycle. To compensate the CCC control system was configured to

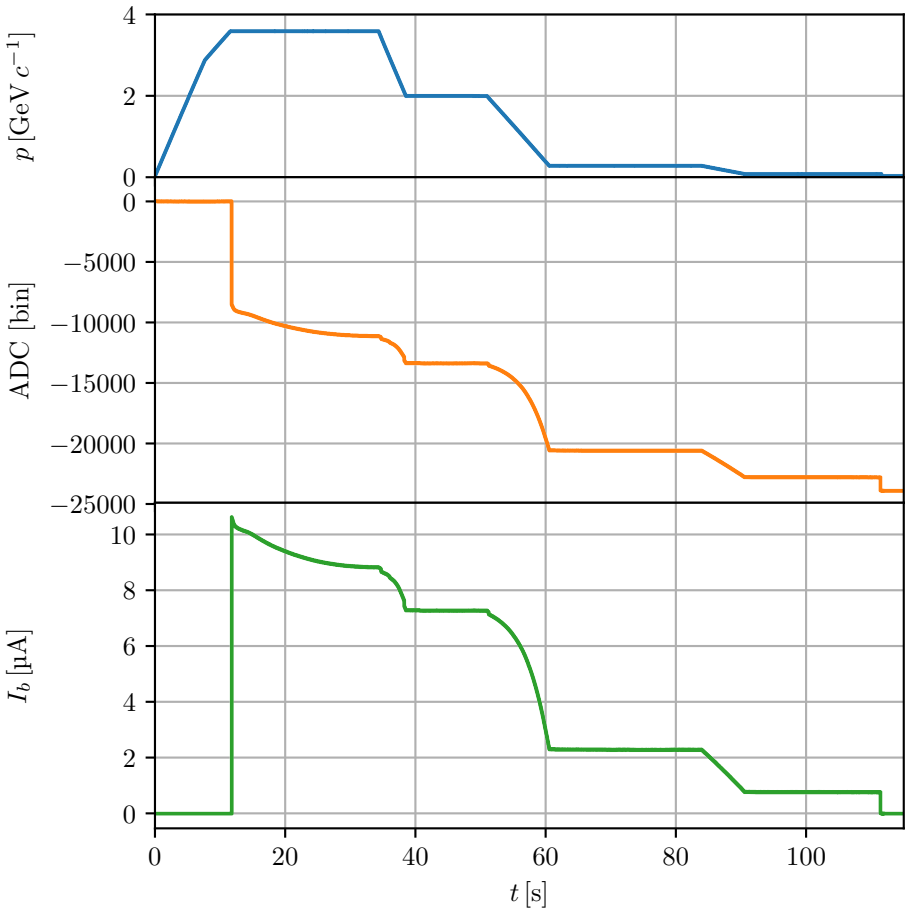

FIGURE 5.21: Measurement of the AD beam current. Top: magnetic cycle; Middle: unfiltered CCC output signal acquired by 16 bit ADC; Bottom: Current measurement obtained after calibration and offset correction.

perform a reset of the SQUID integrator right after the beam injection, as shown in Figure 5.22. In this Figure is also shown the current steps generated by the precision current source that are used to calibrate each cycle. Figure 5.23 shows a zoom in of the different cycles phases of the measured current. During the first deceleration ramp it is possible to observe two moments where the current decreases more abruptly, which could be due to a flux jump in the SQUID/FLL. However, at these instants the currents vary by $\approx 70\,\text{nA}$ while a jump by 1 flux quantum corresponds to 96 nA, since $S_{I_b} = 10.4\,\phi_0/\mu\text{A}$. Additionally these current variations occur over a period of $\approx 10\,\text{ms}$, while the flux jumps observed in the simulations happened in a much shorter time scale. Hence, the observed variations are thought be real current variations due to particle losses.

5.2.2 Intensity measurement and comparison with Schottky monitor

During the operational use of the CCC monitor the following procedure is used to acquire and compute the beam intensity measurement. When the timing signal indicating the start of a new AD cycle arrives, the integrator of the FLL feedback loop is reset to

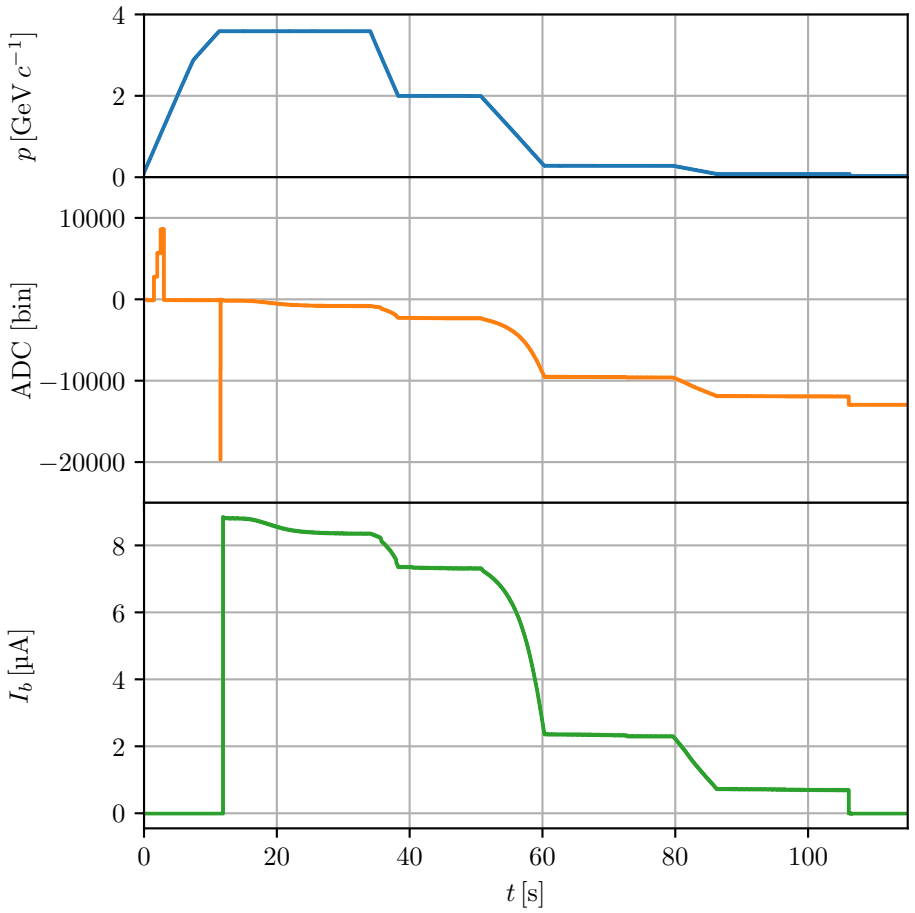

FIGURE 5.22: Measurement of the AD beam current with a reset performed after injection and calibration pulses. Top: magnetic cycle; Middle: CCC output acquisition by 16 bit ADC; Bottom: Current measurement obtained after calibration and offset correction.

zero the voltage output V_{OUT}, and the acquisition ADC is started and kept acquiring until the end of the cycle. Right after this, and before the beam is injected, a set of programmable calibration pulses are sent to the monitor by controlling the calibration current source. At the moment of injection, a significant flux jump occurs rendering the measurement zero offset unknown, and the FLL integrator is reset again. Due to this problem, throughout the cycle only a relative measurement is possible. After the beam is extracted, the zero current offset is acquired making it possible to determine the absolute current measurement. It is also at the end of the cycle that ADC is stopped and its buffers are read. Then a post-processing computation is performed to apply the measured calibration factor to the acquired signal, thus converting it from ADC bins into current units. Finally the beam intensity (number of particles) is computed using the revolution frequency which is computed from the acquired magnetic cycle of the AD as explained next.

The CCC measures primarily the beam current, while the most relevant figure for the AD operations and experiments is the number of circulating particles, often referred to

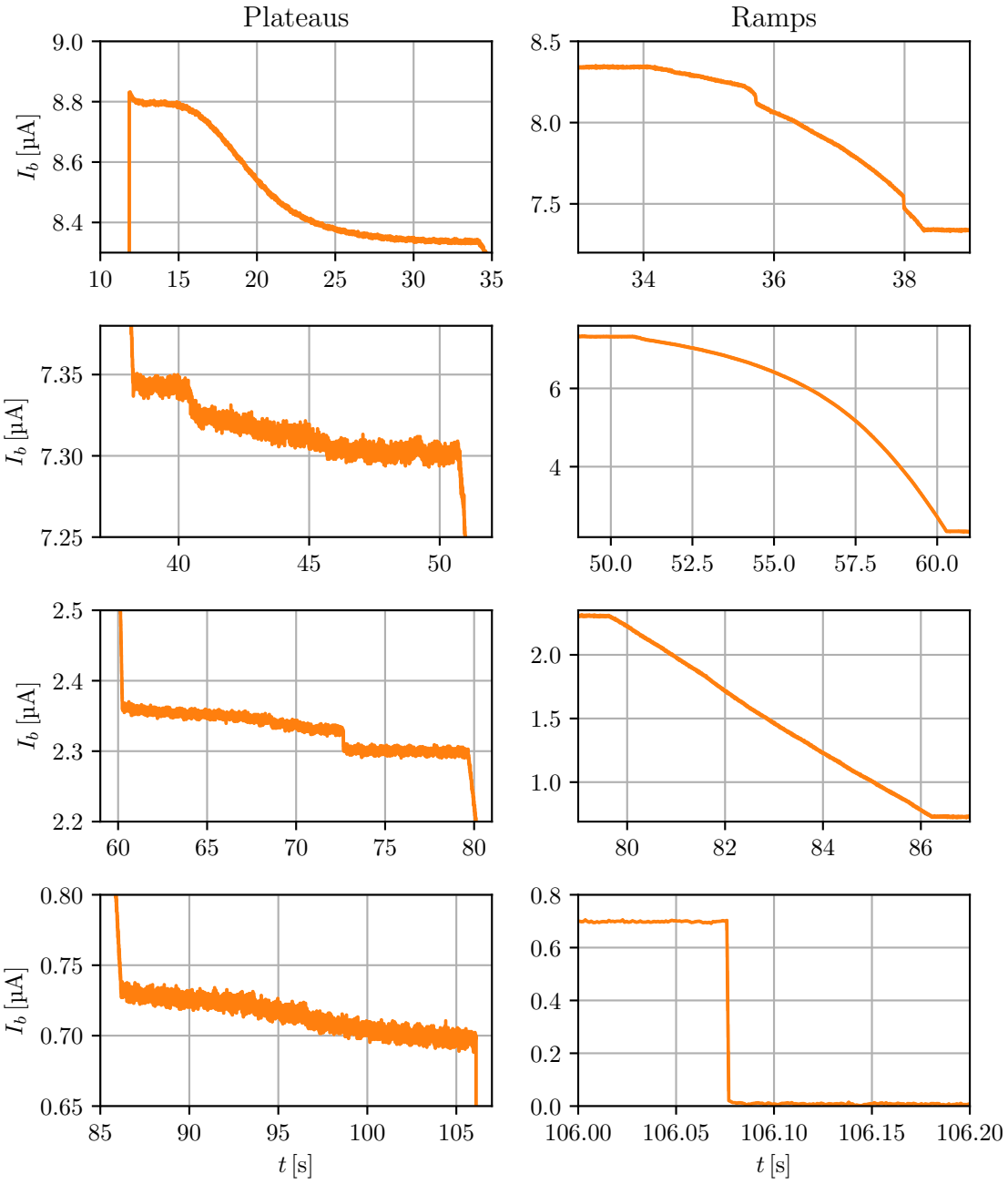

FIGURE 5.23: Zoom in on measured current during the different AD phases. Left plots: show the energy plateaus. Right plots: show the deceleration ramps and ejection.

as "beam intensity". This value can be calculated by normalising the current measurement with revolution frequency, as indicated in Equation 1.2. The revolution frequency was obtained by synchronously acquiring in one of the ADC channels a voltage signal proportional to the dipole magnetic field B_{dipole} created by the AD bending magnets. This signal is proportional to the momentum of the circulating particles p, as given by,

$$B_{\text{dipole}} \cdot \rho = \frac{p\,c}{e}, \tag{5.4}$$

where ρ is the bending radius of the particle travelling across the dipole. The revolution frequency f_{rev} can be calculated from the particle momentum using,

$$f_{\text{rev}} = \frac{c}{L} \frac{p}{\sqrt{m^2 c^2 + p^2}}, \tag{5.5}$$

where m is the antiproton mass, and $L = 182.5\,\text{m}$ is the length of the center orbit in the AD. The revolution frequency is computed from the acquired magnetic field signal, and the beam intensity N can be obtained using Equation 1.2, with $Q = 1$.

The top plot of Figure 5.24 shows the revolution frequency curve derived from the acquired magnetic cycle, and the bottom plot shows the resulting intensity measurement.

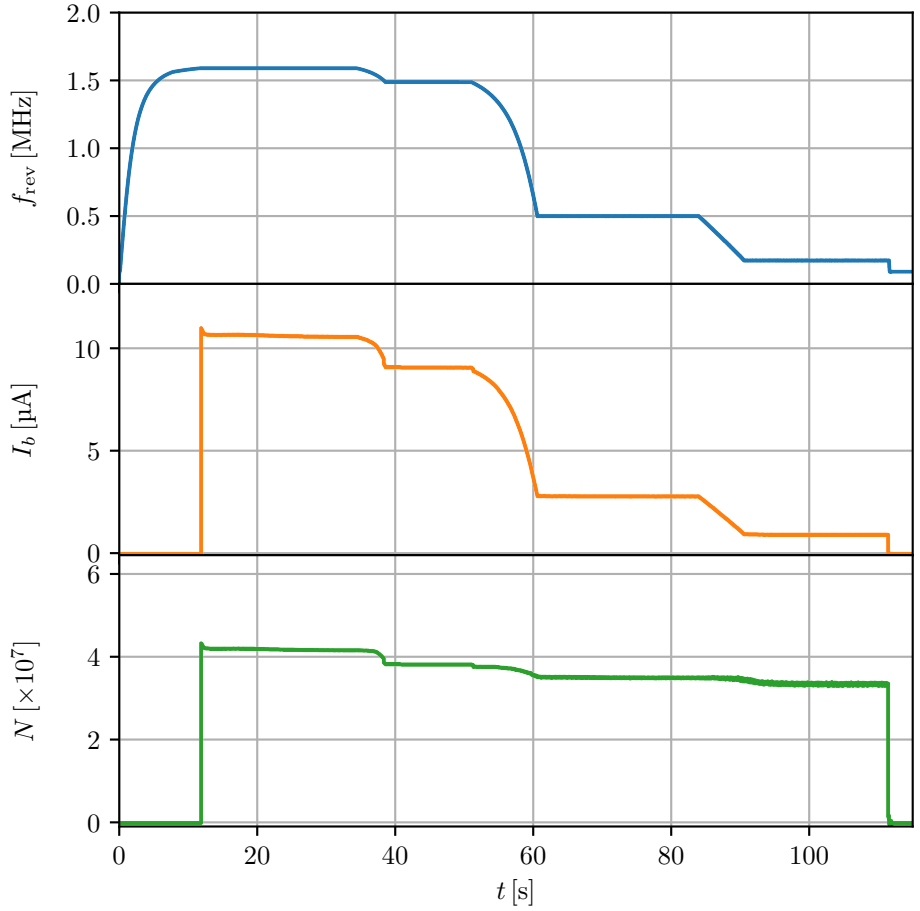

FIGURE 5.24: Beam intensity measurement. Top plot: revolution frequency profile; Middle plot: measured beam current; Bottom plot: beam intensity obtained from normalising the beam current by the revolution frequency.

The noise resolution of the beam intensity measurement depends on the revolution frequency. For smaller values of f_{rev} the absolute intensity noise increases. For the cycle

in Figure 5.24 the intensity resolution values at each momentum plateau are,

$$\sigma(N) \approx 0.0012 \times 10^7\,\overline{p} \qquad \text{at } 3.5\,\text{GeV}/c, \tag{5.6}$$

$$\sigma(N) \approx 0.0012 \times 10^7\,\overline{p} \qquad \text{at } 2.0\,\text{GeV}/c, \tag{5.7}$$

$$\sigma(N) \approx 0.0042 \times 10^7\,\overline{p} \qquad \text{at } 0.3\,\text{GeV}/c, \tag{5.8}$$

$$\sigma(N) \approx 0.0130 \times 10^7\,\overline{p} \qquad \text{at } 0.1\,\text{GeV}/c. \tag{5.9}$$

These are long the best values that could be obtained for the acquired cycles.

With this current and intensity resolution it is possible to clearly observe that on some occasions some beam is left circulating in the AD ring even after ejection, as shown in Figure 5.25. This left portion of the beam is definitely lost only after the dipole magnetic field is reduced to an equivalent momentum of 50 MeV/c without the corresponding particle deceleration. Figure 5.25 shows a zoom of the period right after ejection, where the CCC measurement clearly shows that a portion of the beam stays in the AD and continues circulating until a change in the dipoles magnetic field causes the residual beam loss in the accelerator.

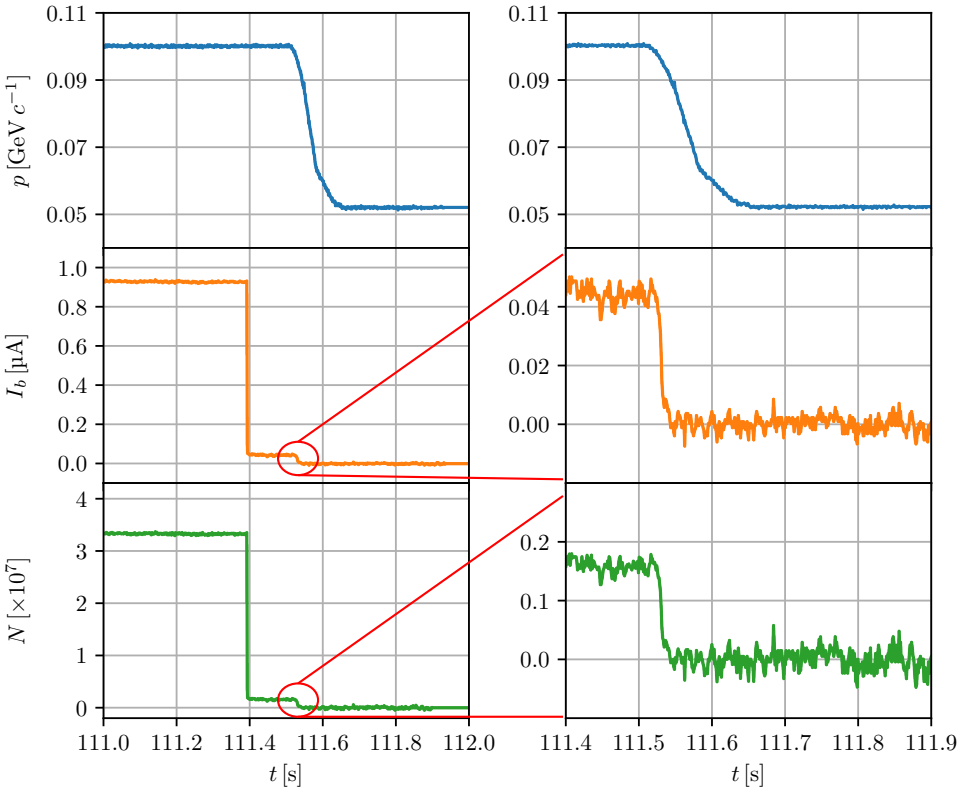

FIGURE 5.25: Measurement of the beam left after ejection.

By measuring the baseline corresponding to $I_b = 0$, when no beam was circulating, it was possible to observe that several effects in the very low-frequency range could affect the measurement accuracy. Figure 5.26 shows an example of a cycle where different fluctuations can be observed.

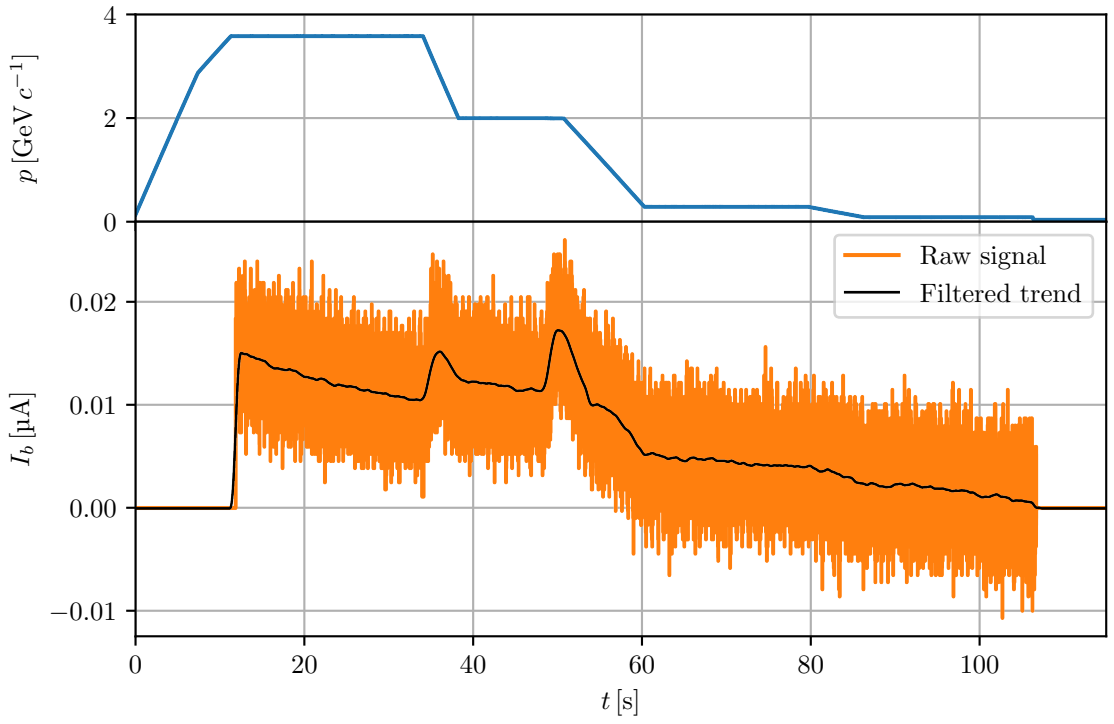

FIGURE 5.26: Baseline variation of the current measurement during a cycle where no beam was injected.

There is a constant drift which in this case, and for the duration of one cycle amounts to $\Delta I_b \approx 15\,\text{nA}$, this was observed to be correlated with variations of the pressure in the HV of the cryostat. There are fluctuations occurring at $t \approx 38\,\text{s}$ and $t \approx 50\,\text{s}$, which were correlated with the first two ramps of the magnetic cycle and amounted to $\Delta I_b \approx 10\,\text{nA}$.

The CCC beam intensity measurement was also compared to the measurement obtained with the Schottky monitor. Figures 5.27 and 5.28 show two cycles, with the Schottky measurement (red dots) superimposed to the CCC one (green trace). When the beam is debunched during the cooling plateaus, the CCC measurement presents a clearly superior current and time resolution compared to the measurement obtained from the analysis of the Schottky noise spectrum. When the beam is bunched (excluding the points observed while the beam is being bunched or debunched) there is an agreement between the CCC measurement and the intensity measurement obtained from the analysis of the coherent component, within $\pm 10\,\%$. This serves as a first cross-validation of the CCC measurement.

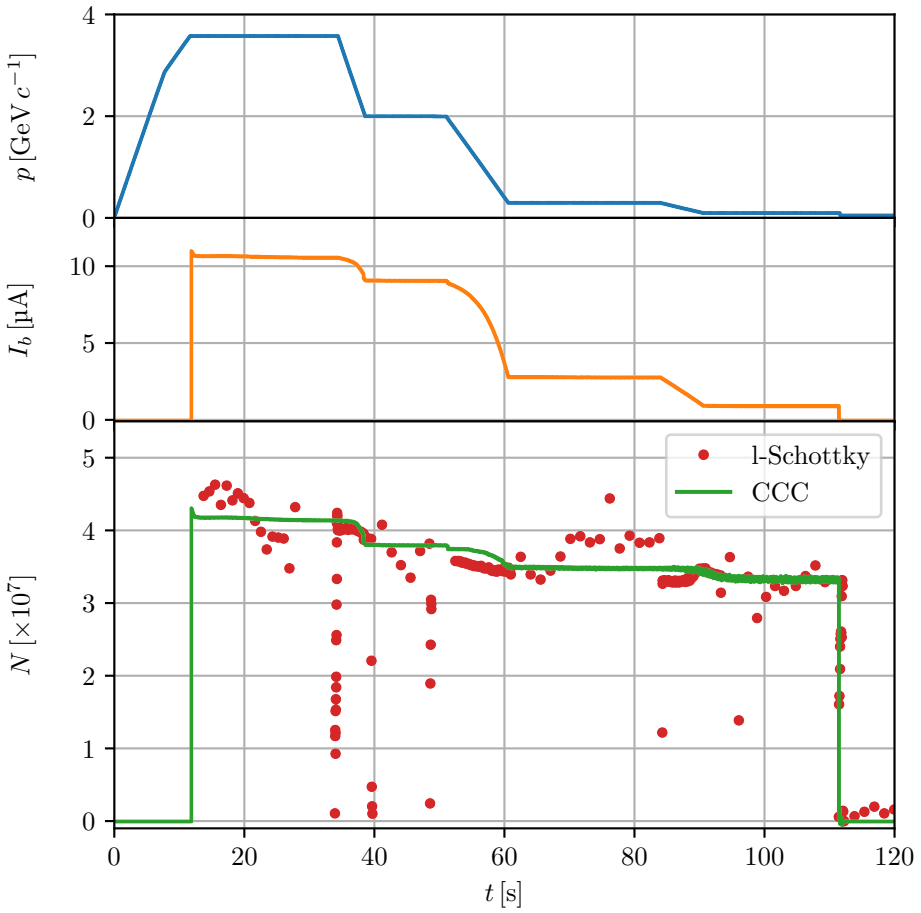

FIGURE 5.27: CCC beam intensity measurement and comparison with the l-Schottky monitor. Top plot: magnetic cycle; Middle plot: measured beam current; Bottom plot: beam intensity measurements obtained with the CCC (green trace) and with Schottky monitor (red dots).

Using the CCC as the reference one it is also possible to conclude that the Schottky measurement performance is much more sensitive to other factors that the beam intensity. When comparing the Schottky measurement during the first magnetic plateau for these two cycles, with comparable injected intensity, one observes that the measurement in Figure 5.28 is much more inaccurate than the one in Figure 5.27.

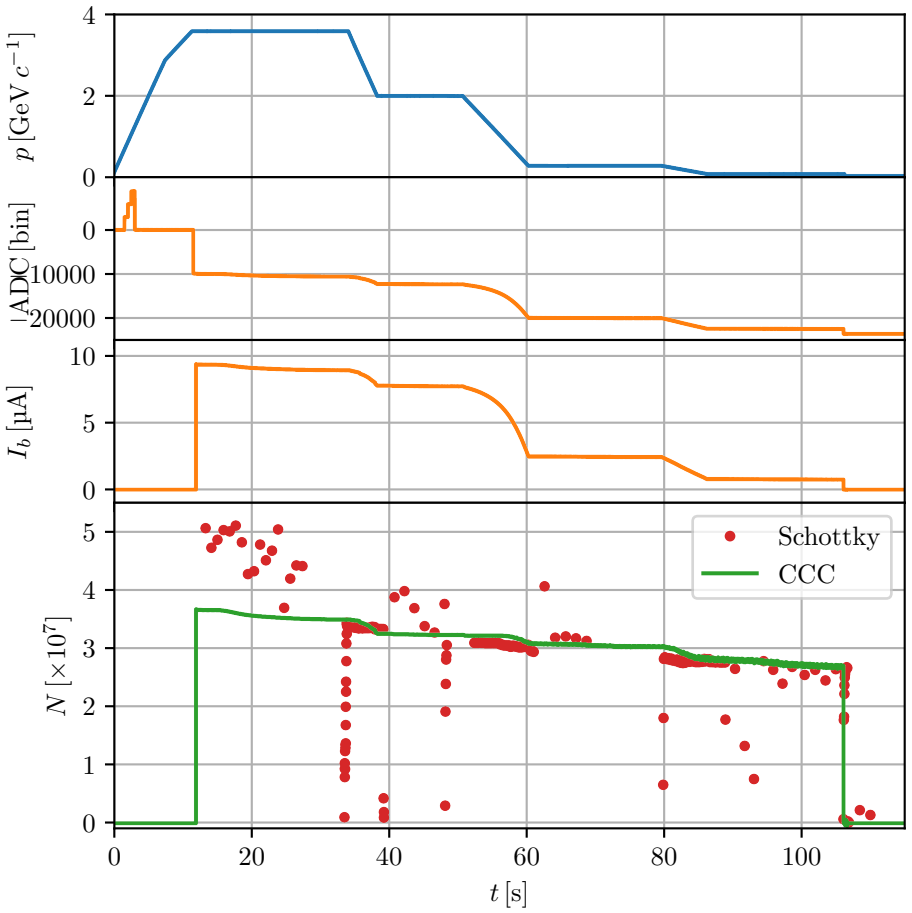

FIGURE 5.28: CCC beam intensity measurement and comparison with the l-Schottky monitor. Top plot: magnetic cycle; Middle plot: measured beam current; Bottom plot: beam intensity measurements obtained with the CCC (green trace) and with Schottky monitor (red dots).

5.3 Long-term performance analysis

With the acquisition system described in Section 3.5 it was possible to acquire and save in a consistent way the AD cycles during the first months of the 2017's run. This permitted to assess the monitor performance and stability over an extended period of time. Each saved cycle is represented in Figure 5.29 by a dot, where the injection intensity is plotted against the date and time of the cycle. A total of 24767 cycles were acquired, including many cycles where no beam was injected. Also, for about the first half of the acquired cycles the cryostat insulation vacuum was being pumped by a primary and a turbomolecular pump, and for the second half of acquired cycles these pumps were turned off. Different parameters were analysed for each cycle and its cumulative values represented by the histograms shown next.

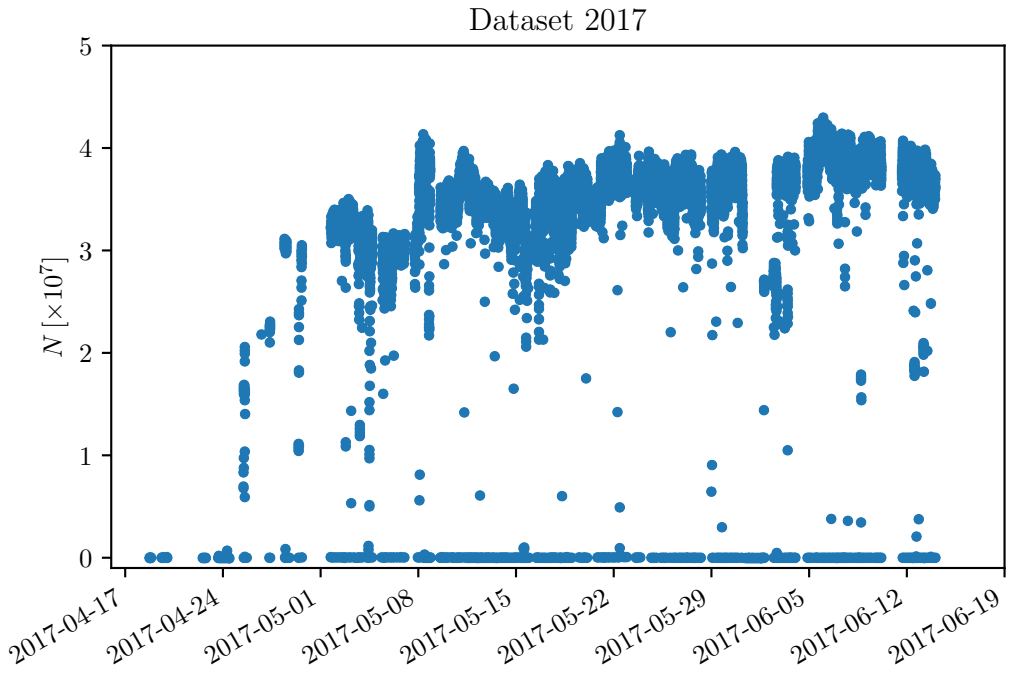

FIGURE 5.29: Acquired AD cycles used in the long-term performance analysis.

For each cycle the beam current resolution was measured immediately after the beam injection and before the beam ejection, including those where no beam was injected. The current resolution was estimated by computing the standard deviation of the acquired signal during a period of 1 s subtracted from its trend obtained using a polynomial fit. Figure 5.30 shows the histogram of the obtained values. The resolution $\sigma(I_b)$ is distributed around the value 2.6 nA, for the cycles when the vacuum pumps were turned off and around 5.4 nA when the pumps were on.

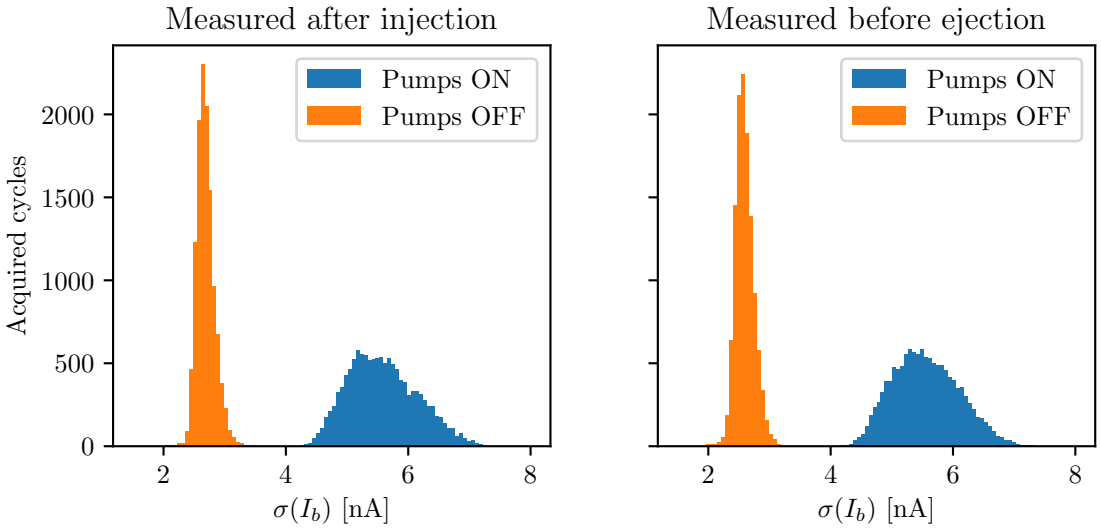

FIGURE 5.30: Distribution of the measured current resolution with the vacuum pumps turned on and off. Left: measurement after beam injection; Right: Measurement before beam ejection.

No observable difference exists between the measurement resolution after injection or before injection. Also no difference could be observed between the cycles with or without beam.

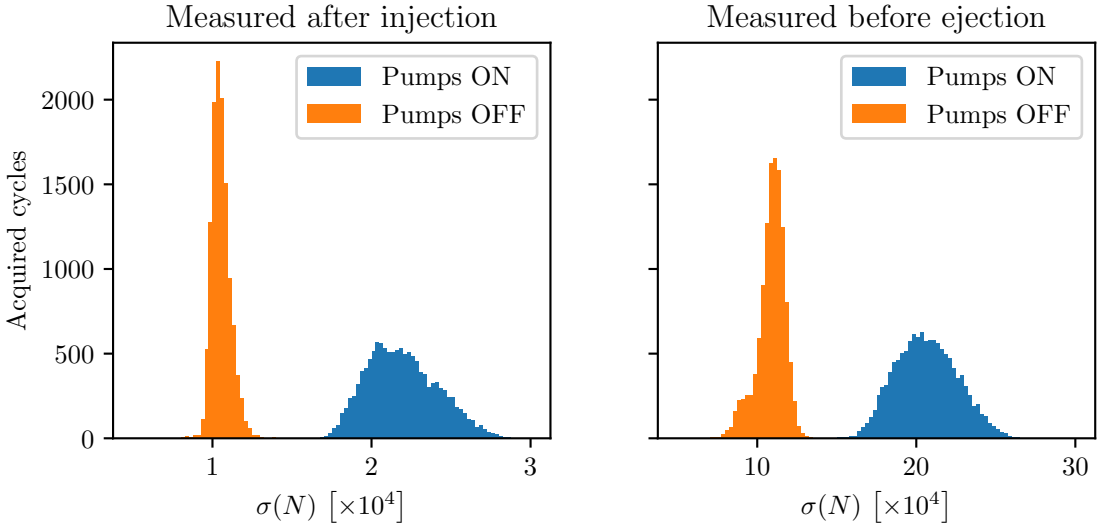

FIGURE 5.31: Histogram of the computed beam intensity resolution with the vacuum pumps turned on and off. Left: measured value right after injection; Right: measured value just before ejection.

Figure 5.31 shows the obtained distribution for the beam intensity measurement resolution. After injection, in the highest momentum plateau, the intensity resolution was centred around $1.0 \times 10^4\,\overline{p}$ and $2.1 \times 10^4\,\overline{p}$, when the pumps were off and on, respectively. Before ejection the intensity resolution was centred around $11.1 \times 10^4\,\overline{p}$ and

$20.4 \times 10^4\,\overline{p}$, when the pumps were off and on, respectively. This degradation of the intensity resolution is according to expectation due to the normalisation procedure, and resulting lower SNR.

The error introduced by the observed baseline variations was also analysed over the acquired cycles. First, the trend of the current measurement of all the cycles where no beam was injected was calculated by filtering the raw signal with a moving average filter (with a Blackman window[3] [139] of 100 ms duration), as shown in Figure 5.32, and the variation was calculated using

$$\Delta I_b^{\text{trend}} = \left|\max\left(I_b^{\text{trend}}\right) - \min\left(I_b^{\text{trend}}\right)\right|. \tag{5.10}$$

The histogram of this measurement is shown in Figure 5.32.

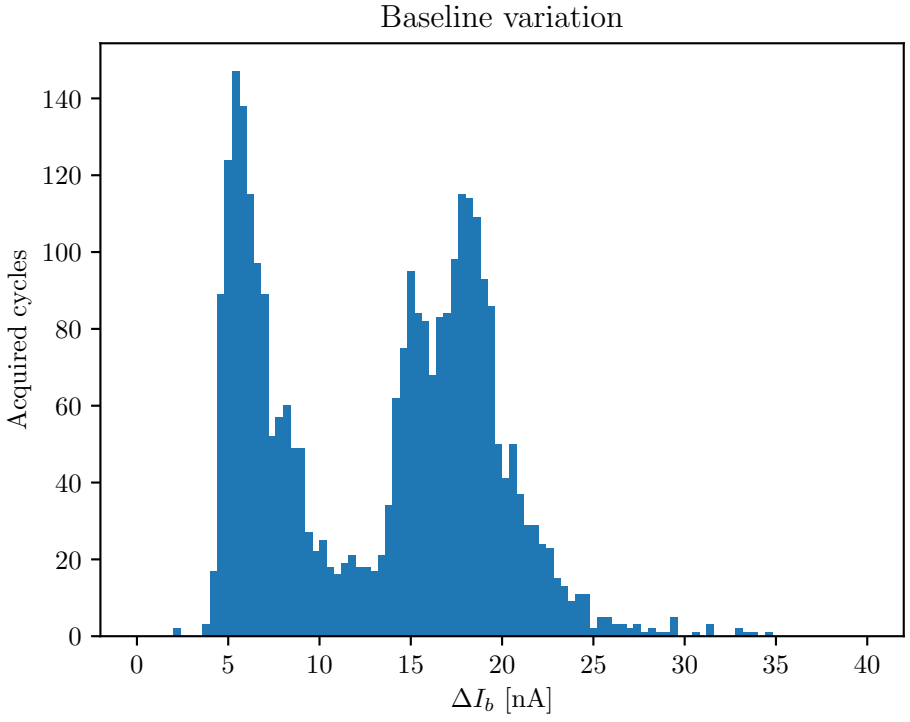

FIGURE 5.32: Histogram of the current measurement baseline variation.

The maximum observed value for the baseline variation was $\Delta I_b \approx 25\,\text{nA}$. The low distribution of values $<\approx 10\,\text{nA}$ was seen to correspond to cycles where the AD magnets were not being powered and hence are not representative of beam measurement conditions. For the remaining cycles the baseline variation was observed to vary

[3]The Blackman window is a type windowing signal usually used to truncate time-domain signals prior to the computation of the discrete Fourier transform in order to reduce the spectral leakage. The characteristics of this window are its very low spectral leakage combined with reasonable bandwidth and amplitude error.

between $10\,\text{nA} < \Delta I_b < 25\,\text{nA}$. This corresponds to an error in the intensity measurement between $4 \times 10^4\,\overline{p} < \Delta N < 10 \times 10^4\,\overline{p}$ in the first plateau, and an error between $1 \times 10^5\,\overline{p} < \Delta N < 3 \times 10^5\,\overline{p}$ in the last plateau.

5.3.1 Observed jump at injection

Figure 5.33 shows the measured jump for a typical injection occurring at $t = 0$, and this is compared with the signal that would be expected to be measured in the case of an injected beam with $N = 5 \times 10^7\,\overline{p}$ like shown in Figure 3.31. Before the beam is injected there is a slight increases in the measured signal, and when the beam is injected the output signal starts decreasing, unable to track the input beam current.

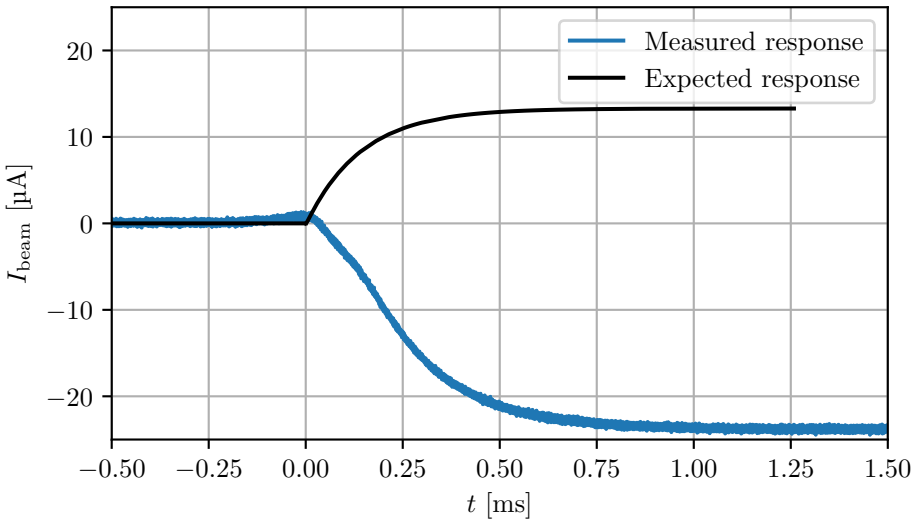

FIGURE 5.33: Measurement of the perturbation occurring at the moment of beam injection (blue trace), compared with the expected signal response for beam injection with $N = 5 \times 10^7\,\overline{p}$.

Different settings of the FLL loop parameters were tested but for all of them the observed flux jump at injection was present. Also different tests were performed by trying to identify whether this could be caused not by the beam itself but by the EMI interference of some other equipment triggered simultaneous with the beam injection. Many times the main sources of perturbations in an accelerator are the beam injection/extraction kicker magnets, which in AD are pulsed with much higher intensity during injection. By pulsing the injection kicker magnet only, with no beam, it was verified that this had no influence in the CCC measurement. The identified possible source were the RF-cavities used for beam rotation a few tens of micro-second after the beam is injected. By pulsing these cavities without no beam, it was observed that most of the times they did not cause any flux jump. However, on very few cases these indeed cause some flux jumps. These measurements should be repeated in a more consistent and systematic way, which until now was not possible to do.

Also, the measurement using a waveform generator signal to simulate beam at AD injection was repeated. This time the current was injected through the calibration loop, or port 3 in Figure 5.7, and the output was acquired over a much shorter time scale to really capture the transient of the output measurement every time the signal input was turned on. Different peak-to-peak voltages were used which correspond to the input average currents shown in Table 5.4, given that the resistance of the calibration loop is $\approx 3\,\Omega$. The measurement was subject to a strong 50 Hz interference from the electric network, most probably induced from an electrical ground loop between the waveform generator and the SQUID electronics, but it was still possible to stably lock the SQUID/FLL and measured the injected signal.

Figure 5.34 shows the acquired responses, which indicate that the SQUID/FLL is able to accurately track the input signals. These signals were fitted to the expected time response of a second order signal, given in Appendix B, and the obtained parameters for the poles frequencies are compatible with the expected first pole of the coupling circuit at 1.12 kHz and a second pole at 10 kHz from the output filter, shown in Figure 5.7.

Input Voltage		Input	Measured	Ratio		
Peak	Average	Current	Current	Errors	Pole 1	Pole 2
$[mV_{pp}]$	$[mV_{avg}]$	$[\mu A_{avg}]$	$[\mu A_{avg}]$		[kHz]	[kHz]
1	0.12	≈ 4	3.87	ref.	1.12	8.53
2	0.24	≈ 8	7.75	0.3 %	1.09	10.08
3	0.36	≈ 12	11.72	2.8 %	1.06	11.81
5	0.60	≈ 20	19.45	2.6 %	1.07	10.04

TABLE 5.4: Parameters of the AD injection current signal, injected through the CCC calibration loop, and the resulting measured average current, as well as the fitted pole parameters obtained from the measured time responses.

Also the measured current amplitudes are inline with the expected values, and the ratio errors which are below 3 % could be due the strong 50 Hz perturbation.

Also the measurement of cycles such as the one shown in Figure 5.35, where the injection beam current of $\approx 10\,\mu A$ is suddenly lost, and the CCC is able to track this current variation as verified by comparing with the Schottky measurement. However, this measurement was taken with much reduced sampling rate, making it impossible to verify how fast the beam losses really happens.

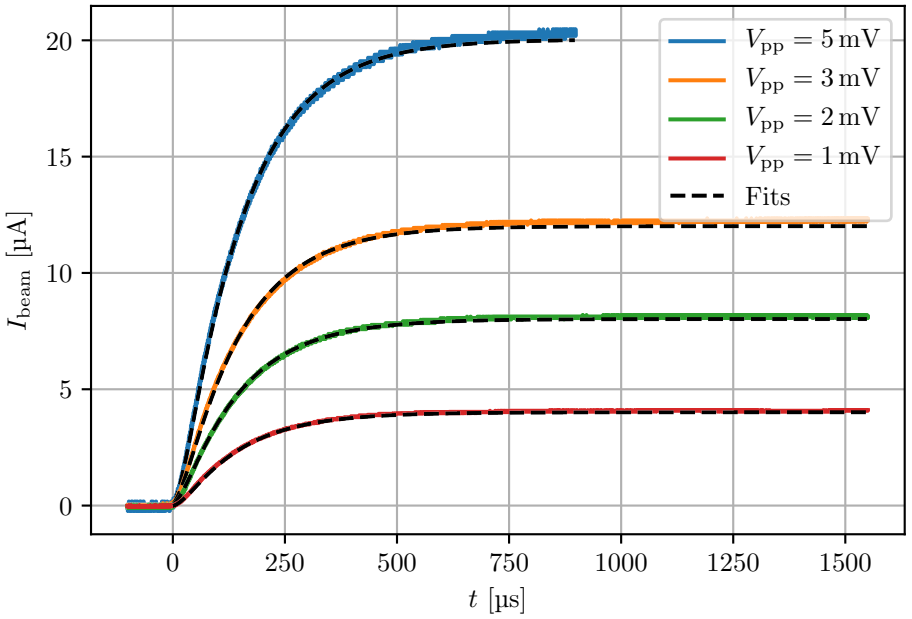

FIGURE 5.34: Measurement of the CCC response to current pulses similar to the AD injection bunched beam, using a signal generator coupled to the calibration loop. Response to different voltage amplitudes of injected pulses was measured. These were fitted to a double decaying exponential function.

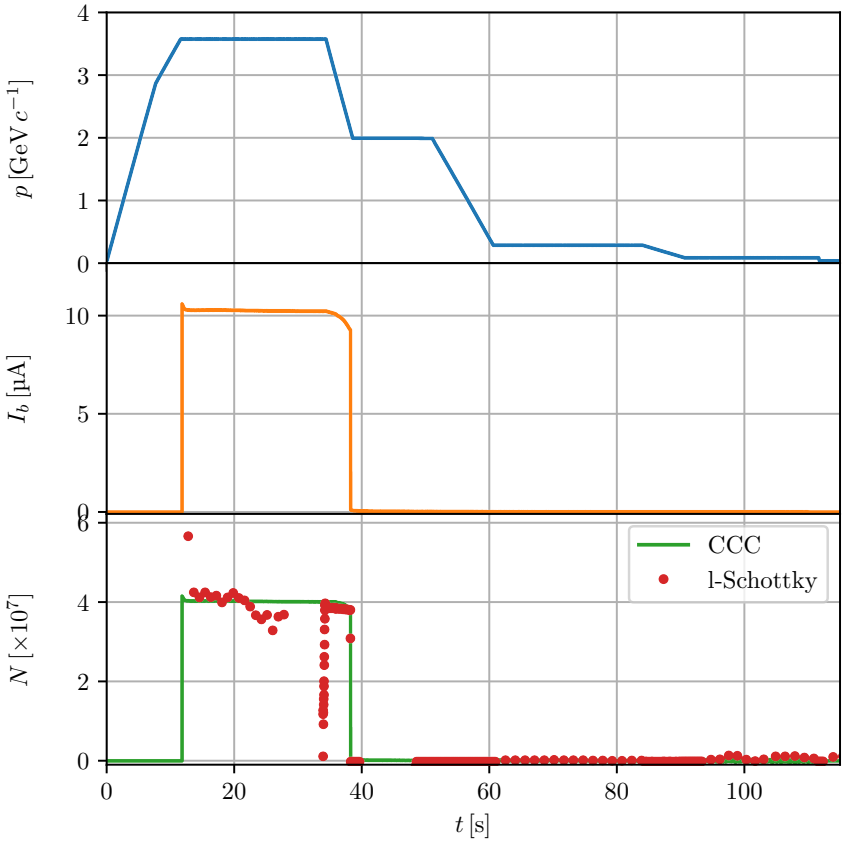

FIGURE 5.35: Top-plot: magnetic cycle of AD dipoles in arbitrary units; Middle-plot: SQUID/FLL raw signal of beam current (in green), and same signal filtered with a moving average (in orange); Bottom-plot: calibrated beam current measurement after filtering and baseline recovery (before beam injection and after beam extraction).

Further measurements and studies should be conducted to try to identify and if possible completely eliminate this jump at injection. For the moment it was only possible to verify that the CCC should be able to measure the injection beam current, but that probably the high SR imposed during the injection transient, combined with other sources of EMI perturbations are in the origin of the observed jump.

5.4 Conclusion

This chapter presented the measurements obtained with the CCC. Before installation in the AD the CCC monitor was characterised in laboratory and the results were compared with the theoretical expectations of the previous chapters. The first measurements of the CCC were performed in the University of Jena in a laboratory with low-level of mechanical and EMI interferences, before the CCC was installed in the new cryostat. The obtained values for the coupling sensitivity using a wire simulating the beam passing through the CCC was $S_{I_b} = 10.49\,\phi_0/\mu\text{A}$, which is inline with the expected value of $S_{I_b} = 10.7\,\phi_0/\mu\text{A}$. A difference of 0.6 % was observed when compared to the calibration obtained using the coil wound directly around the pickup core inside the CCC shield, which will be used for calibration in the AD. This difference could be due to the fact that the calibration loop passes through the SQUID cartridge, and some cross couplings may reduce the field that is coupled to the high-sensitivity pickup core. The noise spectral density was also measured, and it closely followed the theoretical curve of the noise induced by the resistor in the *RC* filter of the coupling circuit, which is the dominant source. Excess perturbations were measured at frequencies below 1 Hz, and between 10 Hz and 100 Hz. These are thought to be mostly due to mechanical perturbations. The current resolution was $\sigma(I_b) \approx 3\,\text{nA}$.

After installation in the cryostat the CCC was measured in the Cryolab at CERN, where the mechanical and EMI level of perturbations were much higher. Additionally, the RF-bypass installed in the ceramic gap was responsible for the noise due to stray currents flowing in the beam pipe that were then picked up by the monitor. This was also the case for the first beam measurements in the AD, where an excess of the perturbations at 50 Hz and harmonics limited the unfiltered current resolution to $\approx 250\,\text{nA}$. Removing the RF-bypass eliminated most these perturbations, and resulted in current resolutions of $\approx 2.5\,\text{nA}$ when the cryostat vacuum pumps were turned off, and in $\approx 5.8\,\text{nA}$ when these were on.

The stability of this resolution values was confirmed over many AD cycles. The analysis of the distribution of the baseline drift for the cycles where no beam was injected, but most of the other accelerator equipment were running, revealed that the drift of the baseline is the dominant factor limiting the overall absolute accuracy.

Tests performed to identify the source of the flux jump observed at the injection were inconclusive. Nevertheless, these seem to indicate that the combination of the high

SR transient induced by the beam injection current, together with perturbations from other sources, possibly from the bunch rotation RF-cavities, may be the culprit.

Chapter 6

Summary and outlook

The work performed within this PhD project led to the development and installation of an improved accelerator beam intensity diagnostic for the low-intensity beams of the AD. This project was developed as a collaboration between University of Liverpool, GSI Helmholtz Centre for Heavy Ion Research, the Friedrich-Schiller-University Jena and CERN.

The first chapter began with a description of the low-energy antiproton experimental program at CERN, which currently use the $\overline{p}$ beam supplied by the AD. The main aspects of the AD synchrotron decelerator are discussed with emphasis on the deceleration cycle and the beam parameters. The AD beam contains only $5 \times 10^7\,\overline{p}$ which are decelerated down to a momentum $100\,\mathrm{MeV}/c$, by going through different deceleration (when the beam is bunched) and beam cooling (when it is debunched) phases. The reduced number of particles and momentum result in beam currents as low as 100 nA. The non-intercepting measurement of these low intensities is very challenging for beam diagnostics, particularly during the debunched phases. However, this is a fundamental measurement for the accelerator operation, optimisation, but also for the experiments calibration.

The chapter proceeds with an overview of the more common non-intercepting beam intensity instrumentation, and how these diagnostics have until present been used to measure the AD beam, and its fundamental performance limitations. Then, the SQUID-based CCC devices are introduced and a review of other projects using CCCs for beam current measurements is presented. These projects have demonstrated the superior performance in terms of current resolution of these devices, but suffered from some limitations concerning the immunity to external perturbations, particularly mechanical vibrations, and where only able to measure slow debunched beams.

The CCC device relies on several aspects of superconducting technology, and devices using LTS and HTS technology have been proposed, with the LTS versions achieving the best current resolution performance of the order of nano-ampere. From this analysis it was decided to pursue the development of a LTS device for measuring the AD beam intensity.

Building on the work developed by other groups, the current project should aim at designing, fabricating and installing a CCC capable of measuring the high-dynamic range of the AD beam with a current resolution below 10 nA. This should be able to cope with both the debunched and bunched beam phases, present a strong immunity to external perturbations, as well as present an overall stability and availability to allow it to be used as an operational device.

In chapter 2 the theoretical basis required to understand the different aspects of the CCC devices functioning are introduced. It starts with a description of superconductivity, combining aspects of the classical theory of the London brothers with aspects of the macroscopic quantum wavefunction description. The basic principle of the CCC relies on the measurement of the magnetic field induced by a current of charged particles. It is the perfect diamagnetism of SCs in the Meissner state that allow the design of shielding geometries that allows a field distribution to be obtained that is solely dependent on the absolute magnitude of the currents being measured, and independent of the path followed by the particles. This shield geometry is also important to reject external perturbations perturbed by other sources of magnetic fields, e.g. the Earth's magnetic field.

The chapter continues with a description of the theory of Josephson junctions which are the building blocks of SQUID sensors used to measured the magnetic field induced by the beam in a CCC device, and proceeds by describing the theory of the DC-SQUID. It is explained how the periodic V-Φ transfer function appears as a consequence of the quantisation of the magnetic flux in superconducting loops, and how are this can be used as a magnetic field sensor. When used alone, despite presenting a very high sensitivity to magnetic fields, DC-SQUIDs have a very limited dynamic range due to their non-linear transfer function. This limitation is overcome by the FLL readout electronic scheme, which linearises the SQUID response to magnetic fields augmenting by many orders of magnitude its dynamic range limits.

The various design aspects of the CCC monitor were presented in chapter 3. This started by analysing the coupling circuit between the beam magnetic field pickup inductor and the SQUID input in the DC regime. To measure the average beam current throughout the entire AD cycle the magnetic field is transferred to the SQUID using a flux transformer which by the fact of being a superconducting loop is able to couple DC fields. It is shown that using a high-permeability ferromagnetic core increases the coupling sensitivity, although it also introduces thermal noise to the circuit. This is followed by a discussion of the behaviour of ferromagnetic materials at cryogenic temperatures, and how can the induced noise be theoretical estimated from the complex permeability. The performed measurements of the complex permeability of two sample materials at cryogenic temperatures are presented, putting in evidence the superior properties of nano-crystalline materials at these temperatures. The beam current sensitivity and resolution were then computed for different coupling circuits, with and without a

ferromagnetic core, and with and without an intermediate inductance matching transformer. Using a ferromagnetic core and a matching transformer increases the sensitivity by several orders of magnitude, but the gains in current resolution are not so significant. However, in the current project both were used and a theoretical sensitivity of $I_b = 10.7\,\mu\text{A}$ and resolution of $\sigma(I_b) = 0.15\,\text{nA}$ were estimated, when taking into account only the SQUID and core noise.

Next the analysis of the dynamic behaviour of the CCC when measuring the AD beam was presented in chapter 3. The mechanism of the flux jumps of the SQUID/FLL readout is described as well as its impact on the current measurements. An estimation of the maximum input signal slew rate and stability limits was performed using a simple theoretical model and a simulation model that used the measured SQUID V-Φ characteristic. If the AD injection signal was entirely coupled to the SQUID the magnetic flux slew rate would be 3 orders of magnitude above the stability limit. Hence, a modification of the coupling circuit was performed in order to low-pass filter the input signal before it reaches the SQUID, and hence reduce the flux slew rate. Two filter configurations were considered, one with a *RC*-parallel and another with an *RC*-series shunt in the coupling circuit. The design was done taking into account: the amount of filtering provided; noise introduced by the resistor; and the limited availability of component values suitable to work at cryogenic temperatures. The selected option was the *RC*-parallel which presented the best attenuation, and despite adding more noise to the measurement, $\sigma(I_b) = 0.92\,\text{nA}$, this was still under the resolution requirement. The performed dynamic simulations with this configuration resulted in a stable system as long as the FLL feedback loop bandwidth was set to $\approx 10\,\text{MHz}$, which is a reasonable value for the present day FLL direct read-out electronics. The expected noise level in the SQUID should also not be a problem to attain this bandwidth. Chapter 3 concludes with the description of the acquisition and control system that was installed in the AD to automatise all the data taking during the AD cycles. This system also controlled the SQUID electronics, as well as the calibration current source, which was used to perform a quick calibration before each measured cycle. This acquisition system was essential to make this CCC an operations ready device, and to allow the consistent data taking of many cycles required to perform the long-term performance and stability analysis.

The performed theoretical analysis of the CCC performance provided a fairly accurate picture of the observed characteristics and behaviour, and can be used for the future development of other devices.

Chapter 4 presented the different aspects concerning the installation and integration of the CCC monitor in the AD and the cryostat design. The aperture of the beam pipe in the section allocated in the AD ring for the CCC installation was too big to fit a cryostat housing the FAIR CCC shield. However, due to modifications of the machine optics that have occurred over the years, it was possible to reduce the diameter of the beam pipe to 100 mm as was verified by looking into the machine optics functions. An estimation of the stray magnetic fields expected in this section was performed, by simulating the

fields induced by the closest accelerator magnets. These were estimated to be smaller than the Earth's magnetic field. Real measurements performed afterwards revealed that these were higher, but still in order of magnitude of the Earth's magnetic field. Hence, CCC performance should not be strongly affected my magnetic perturbations during the AD cycle.

The CCC monitor with complete acquisition was installed in the AD. This has been able to consistently provide a beam current measurement with resolutions 2.5 nA. This performance was possible even with the cryocooler reliquefier running and supplying liquid-helium to the cryostat, what was only possible due to the careful design of the cryostat to suppress most mechanical vibrations. Also when vacuum pumps attached to the cryostat were running it was possible measure the beam with a current resolution of 5 nA. However, a flux jump was always occurring at the beam injection. Tests performed to identify the source of the flux jump observed at the injection were for the moment inconclusive. To compensate for this jump, the baseline offset is acquired at the end of the cycle, after beam extraction, allowing for providing the absolute measurement after each was terminated cycle.

Statistical analysis of the monitor performance reveals that the drift of the baseline is the dominant factor limiting the overall absolute accuracy. And future studies should be conducted to reduce the observed drifts. Also tests performed to identify the source of the flux jump observed at the injection were inconclusive. Nevertheless, these seem to indicate that the combination of the high SR transient induced by the beam injection current, together with perturbations from other sources, possibly from the bunch rotation RF-cavities, may be the culprit.

This is the first fully operational CCC system able to continuously measure both bunched and coasting beams in a synchrotron accelerator. The performed measurements demonstrated that the CCC can be an invaluable tool for reducing the beam commissioning time, reducing the accelerator troubleshooting times, and for increasing machine efficiency. During the current year, the measurements provided by this device have been routinely used by the AD operations team. Another particular improvement is the possibility of absolute calibration of the experiments receiving the particle beam using data from the CCC, as well as cross-calibration of other intensity monitors for which no simple calibration method is available.

Appendix A

Matlab simulation models

The following Matlab/Simulink simulation was used to solve the dynamic equations of the RCSJ-model of the Josephson equation and obtain the voltage curves shown in Figure 2.10.

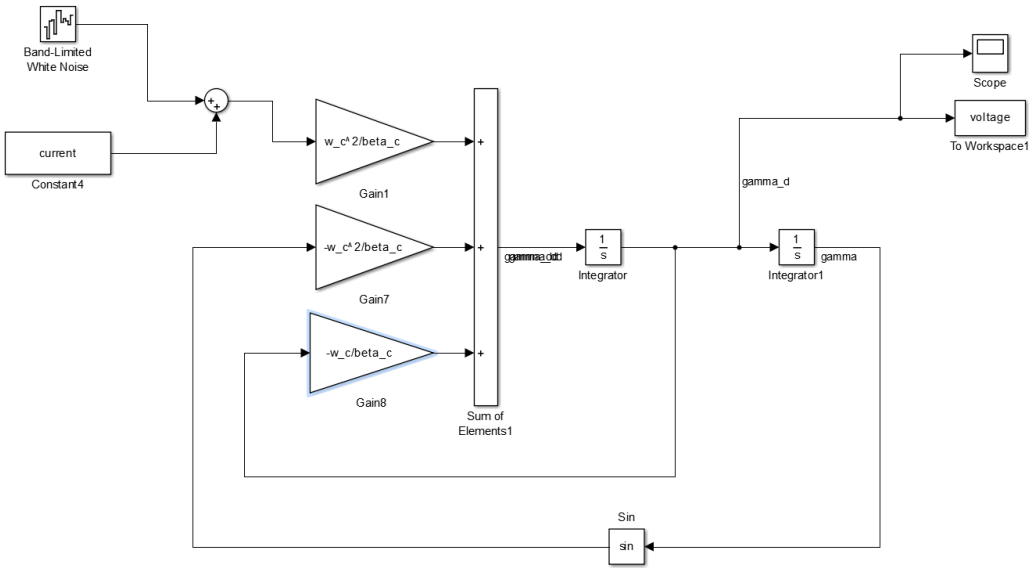

FIGURE A.1: Matlab/Simulink model used to solve the dynamics of the RCSJ dynamic model of the Josephson junction.

The following Matlab/Simulink model was used in the simulations of the dynamics of the SQUID/FLL system shown in Section 3.3. The SQUID block implements the measured V-Φ curve shown in Figure 3.5.

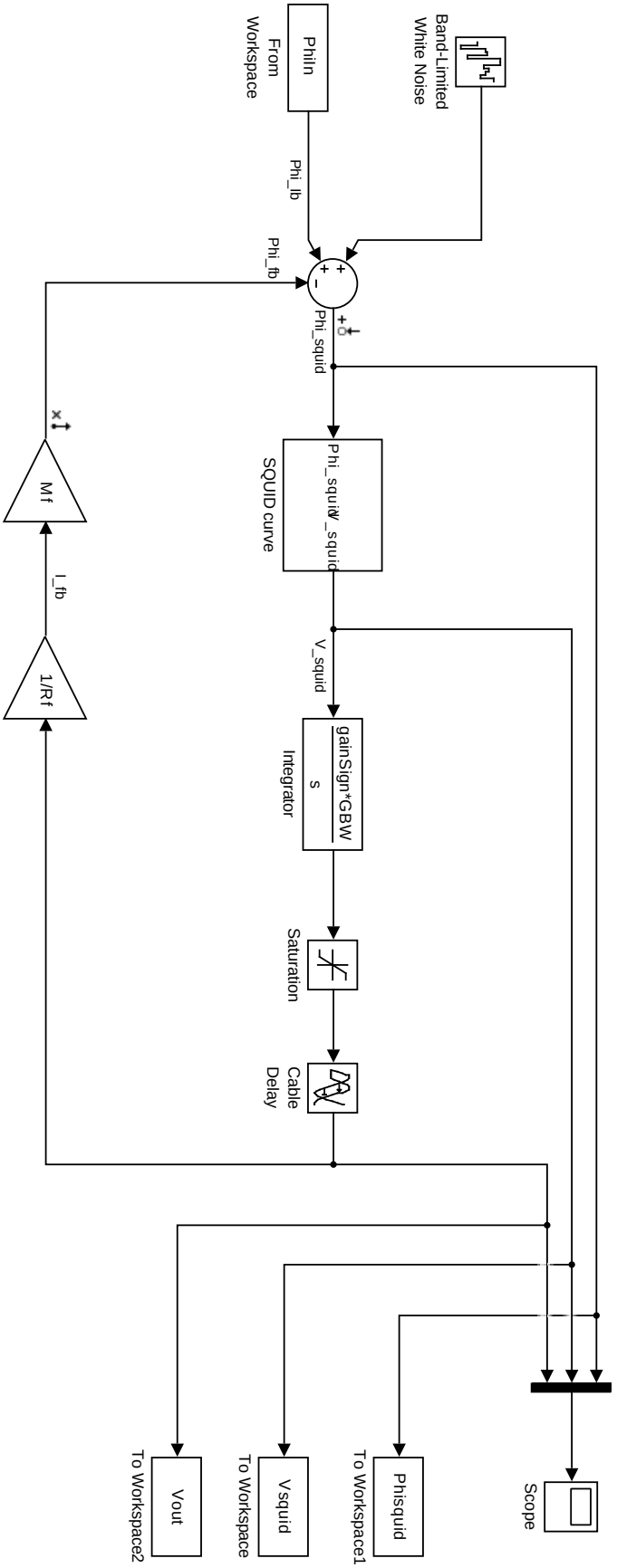

FIGURE A.2: Matlab/Simulink implementation of the SQUID/FLL system.

Appendix B

Second order linear systems

A linear time-invariant second order system can be represented by the following transfer function in the Laplace domain, where s is a complex frequency variable.

$$T(s) = \frac{\omega_n^2}{s^2 + 2\xi\omega_n s + \omega_n^2}. \tag{B.1}$$

The parameter ξ is the damping factor and ω_n is the natural frequency. The roots of the denominator are the poles, and their location in the complex plan determines the behaviour of the system. A second-order system has two poles and they are located at

$$p_{1,2} = -\omega_n \left(\xi \pm \sqrt{\xi^2 - 1}\right). \tag{B.2}$$

Three different types of behaviour are possible depending on the value of the ξ:

- Overdamped circuit ($\xi > 1$): The two poles are real and there is not resonance or oscillation in the frequency and time-domain;
- Critically damped ($\xi = 1$): The poles are real and equal;
- Underdamped circuit ($\xi < 1$): The poles are complex and system shows a resonance and damped oscillations with frequency ω_d;

The oscillation frequency in the underdamped case is given by,

In the underdamped case the expression of the time-response to an step input at t_0 is given by

$$y(t) = \left[1 - \frac{\exp(-\xi\omega_n t)}{\sqrt{q - \xi^2}} \sin\left(\sqrt{q - \xi^2}\omega_n t + \theta\right)\right] h(t). \tag{B.3}$$

which exhibits a decaying oscillation at frequency ω_d

$$\omega_d = \omega_n\sqrt{1 - \xi^2}. \tag{B.4}$$

In the overdamped case, where the poles are real, the step response is given by

$$y(t) = k\left(1 - \frac{p_2\, e^{-\frac{p_1}{2\pi}(t-t_0)} - p_1\, e^{-\frac{p_2}{2\pi}(t-t_0)}}{p_2 - p_1}\right). \tag{B.5}$$

Figure B.1 shows the time response to a step input for different values of the damping factor ξ. Figure B.2 shows the magnitude and phase of the frequency response for

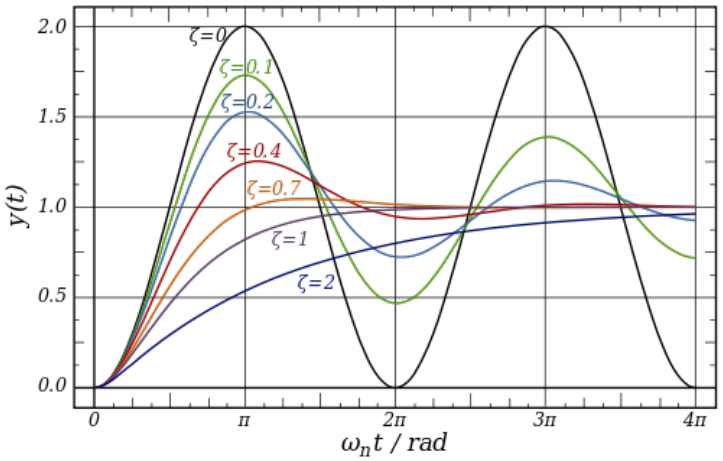

FIGURE B.1: Time response of a second-order linear system for different values of the damping factor.

different values of ξ

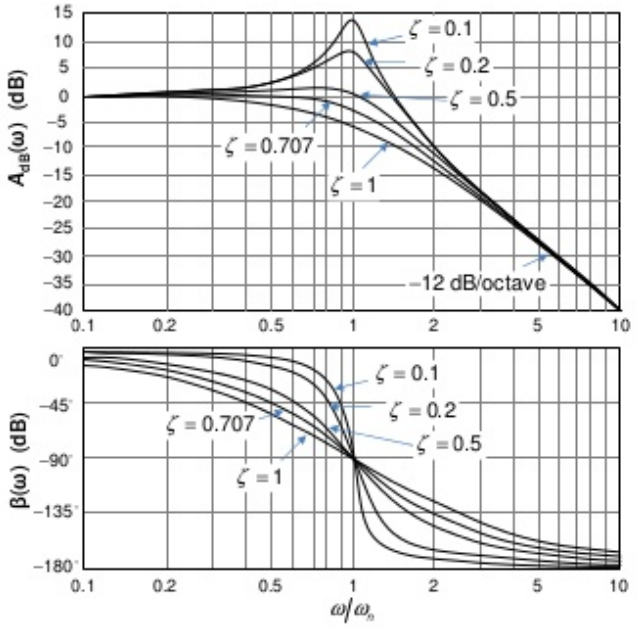

FIGURE B.2: Frequency response of a second-order system for different values of the damping factor.

Appendix C

Drawings

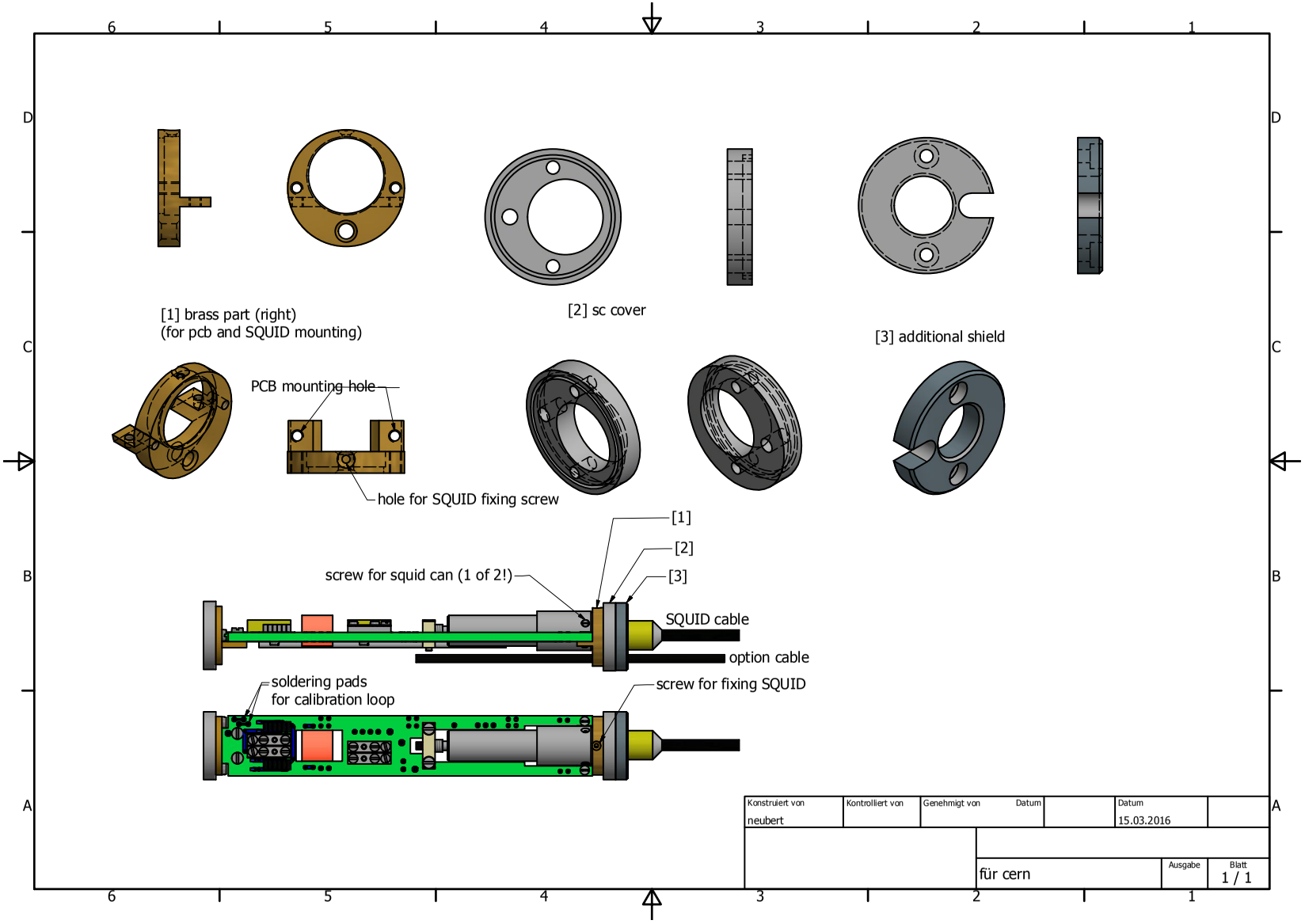

FIGURE C.1: Mechanical drawing of the SQUID cartridge fabricated to hold PCB containing the SQUID and the coupling circuit.

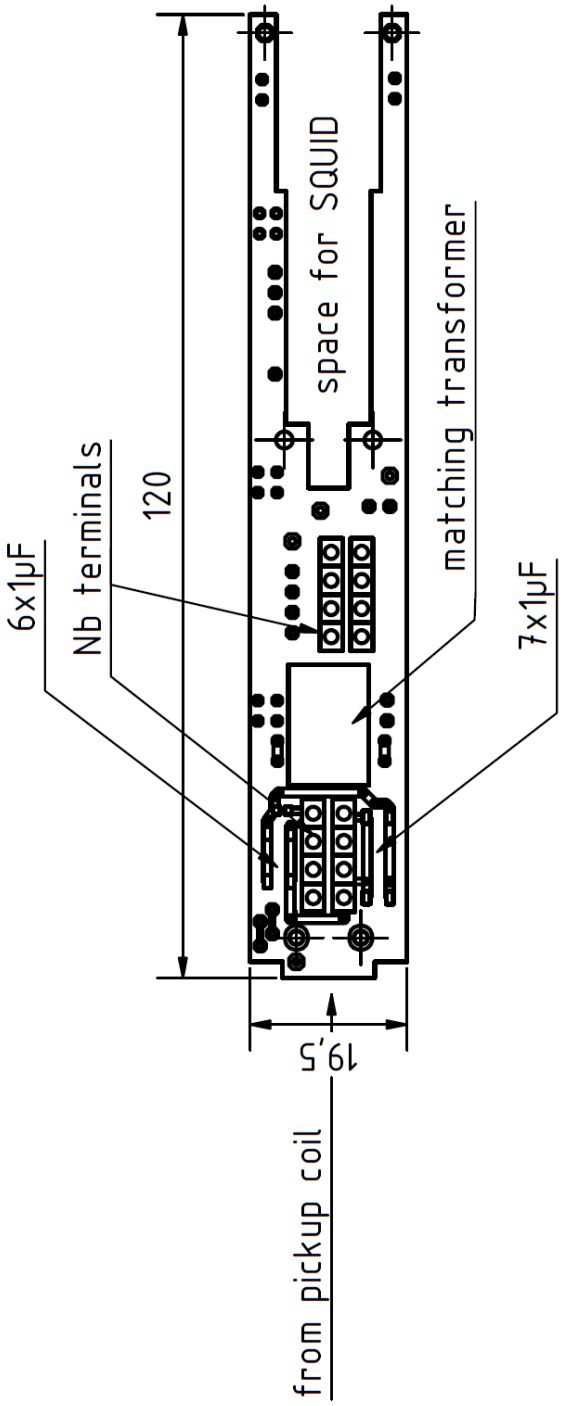

FIGURE C.2: Mechanical drawing of the coupling circuit PCB.

Appendix D

Calibration curve and error determination

The following procedure was used in the current calibration and position dependency estimations. A periodic wave function, such as a sine or square wave, was generated by the precision current source and used as input current with a known amplitude and frequency, I^{known}. The output of the CCC to this input signal was measured for a few periods, and a non-linear interactive least-squares fitting method was used to fit measured signal with the same shape as the one used at the input. The amplitude for this fitted curve was used as the measured current output. No error in the input currents I^{known} were considered.

In the case of a sinusoidal input, shown in Figure D.1, the measured output was fit to

$$y^{fit}(t) = V^{\text{obs}} \sin(\omega t + \theta_0) + k, \tag{D.1}$$

where ω is known from the input signal, and V^{obs}, k and θ_0 are free parameters to be fitted. From this fit the value of the measured amplitude V^{obs} was obtained and used in the second fit to estimate the calibration curve.

The error considered in the measurement for each current value $\sigma(V^{\text{obs}})$ was not the error resulting directly from the covariance matrix of the fit, which is normalised by the number of points of the signal acquisition in each curve. Instead, the standard deviation of the measured curves subtracted from the fitted curves, shown in Figure D.1, was used. In the shown example the estimated error was $\sigma(V_{\text{squid}}) = 2.7\,\text{mV}$ while the fit error would have been $\sigma(V_{\text{squid}}) = 86\,\mu\text{V}$. This underestimates the error of the measurements to be performed with the CCC since the desired measurement period is much shorter than the length of the current signals used for purpose of calibration.

The measured voltage was converted to an observed flux Φ^{obs} by using the SQUID/FLL gain G_{fll}, given in Equation 2.53. This was done without considering any error for this parameter. After obtaining the various pair of values Φ^{obs} and I^{known}

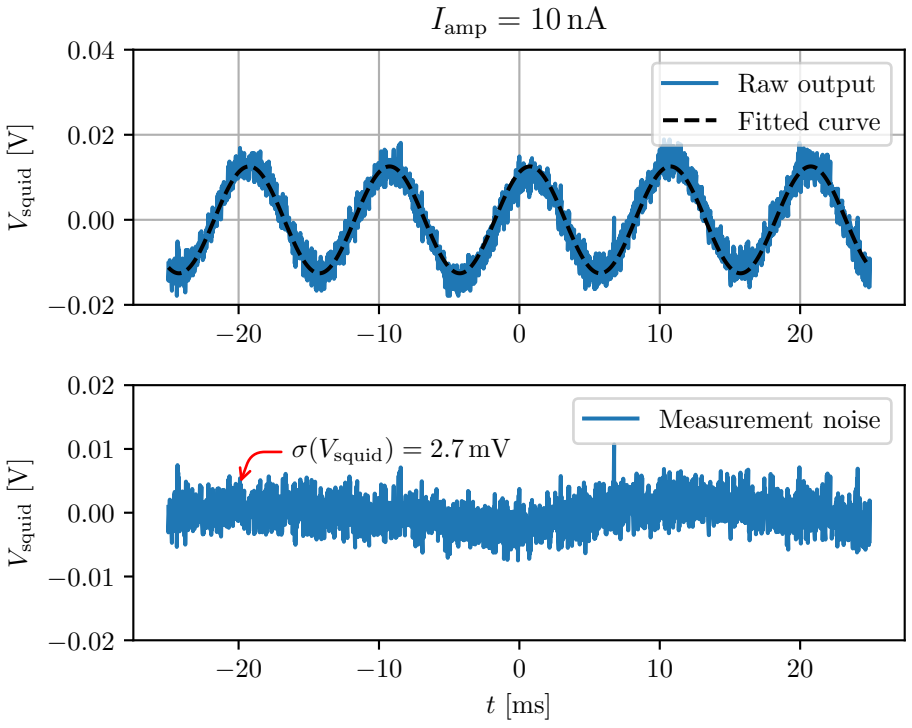

FIGURE D.1: Measurement and fit of calibration current signal.

The coupling sensitivity parameters could be obtained by fitting the following linear function [140].

$$I^{\text{obs}} = (S_{I_b})^{-1}\Phi^{\text{obs}} + I_{\text{offset}} \tag{D.2}$$

For this a linear least-squares method that took into account the error of the observed values was used. This was done by weighing each point by the observed error in the function to minimise by the fit,

$$\sum_i \left(\frac{I_i^{\text{known}} - I_i^{\text{obs}}}{\sigma_i^{\text{obs}}} \right)^2 . \tag{D.3}$$

Appendix E

Measured AD cycles

Next Figures show examples of measured AD cycles where the beam was lost in the machine before the complete deceleration could proceed. This are examples of situations where the intensity measurement obtained with the CCC provides valuable information to the operations team.

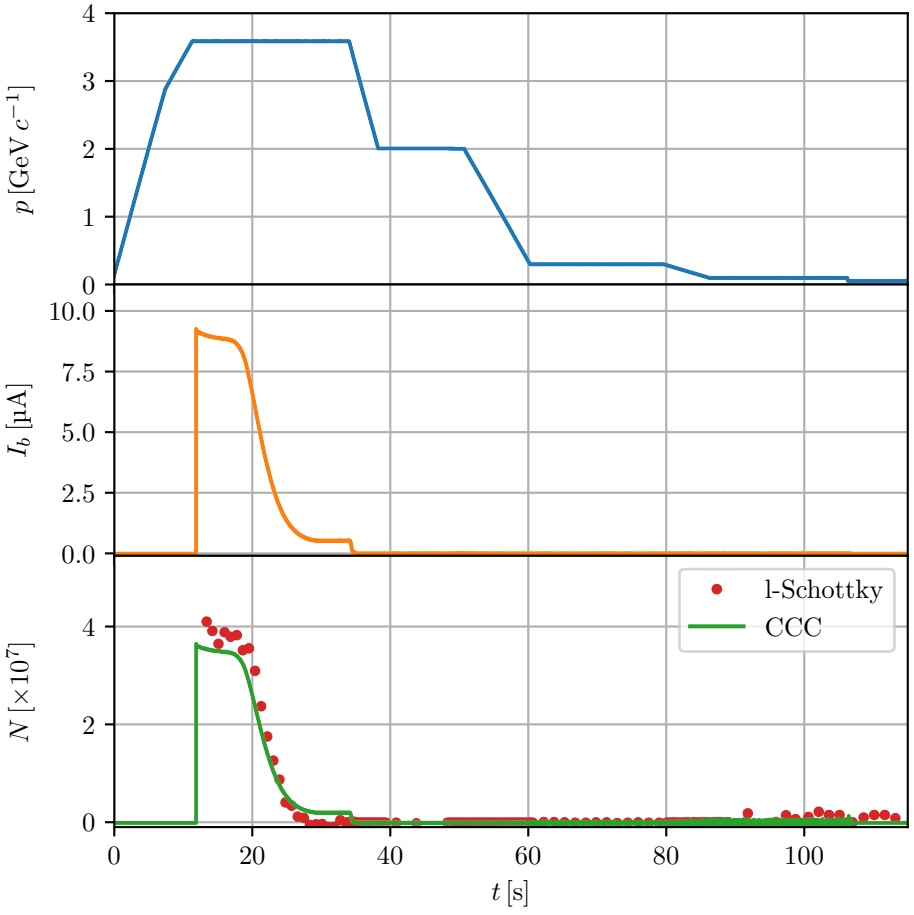

FIGURE E.1: Cycle where the beam is lost at the beginning of the first deceleration ramp.

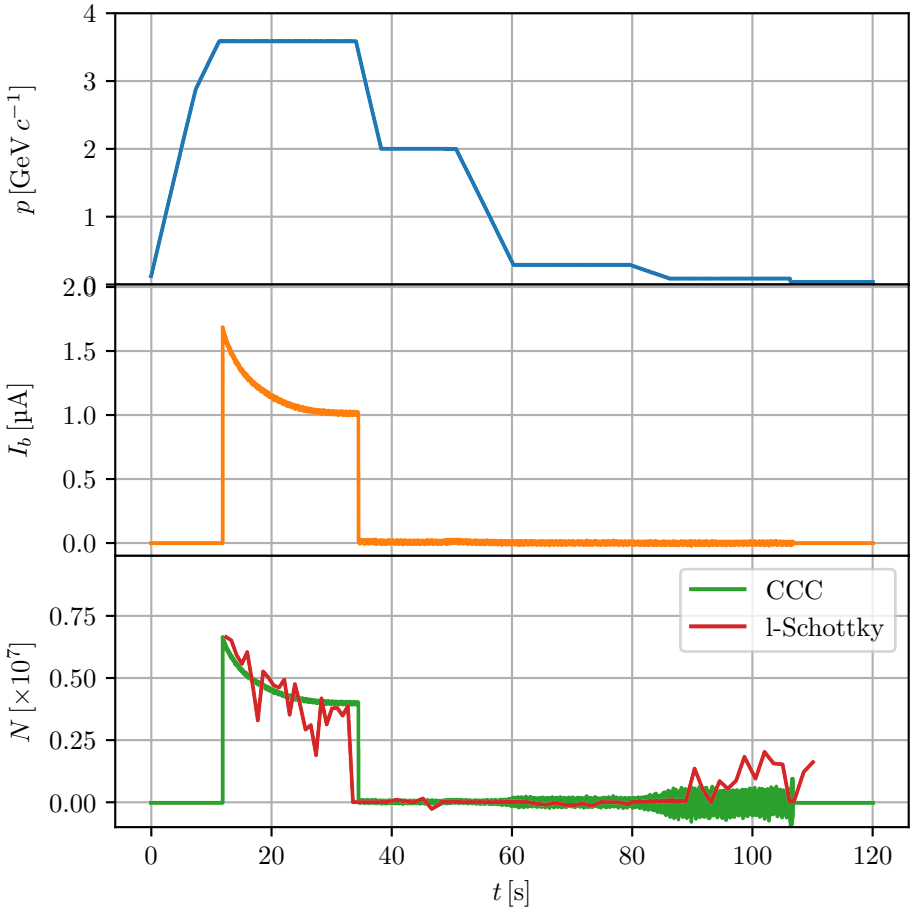

FIGURE E.2: Cycle where the beam is lost during first plateau.

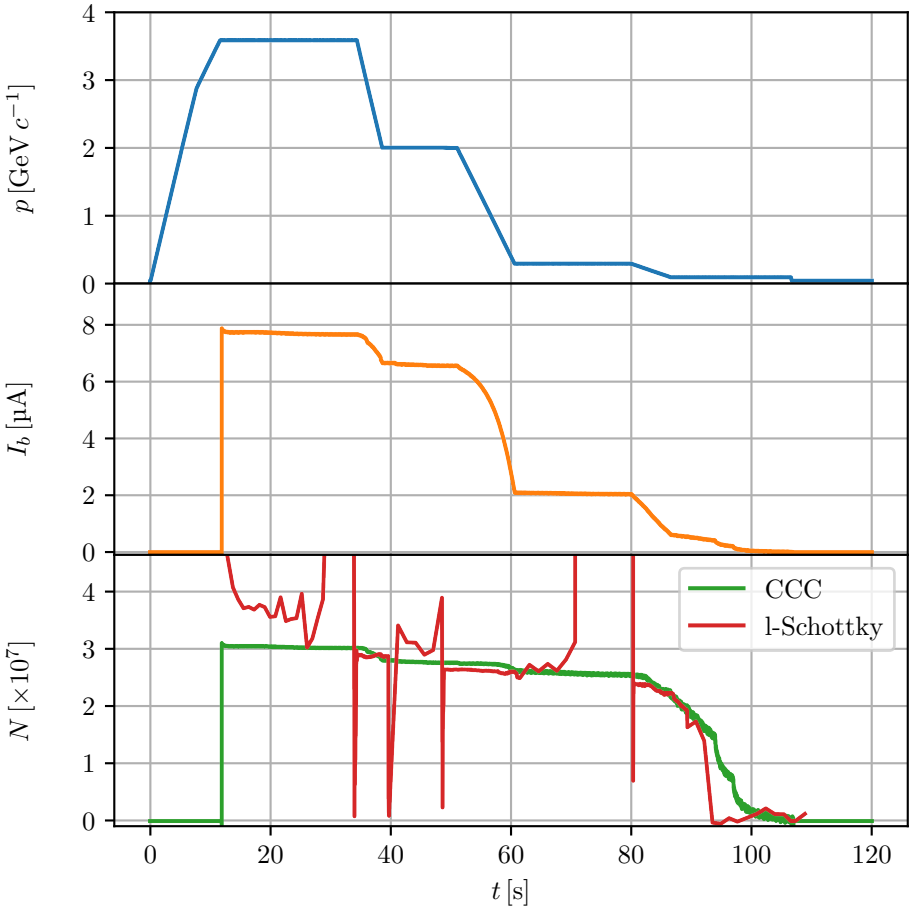

FIGURE E.3: Cycle where the beam becomes unstable during the last deceleration ramp.

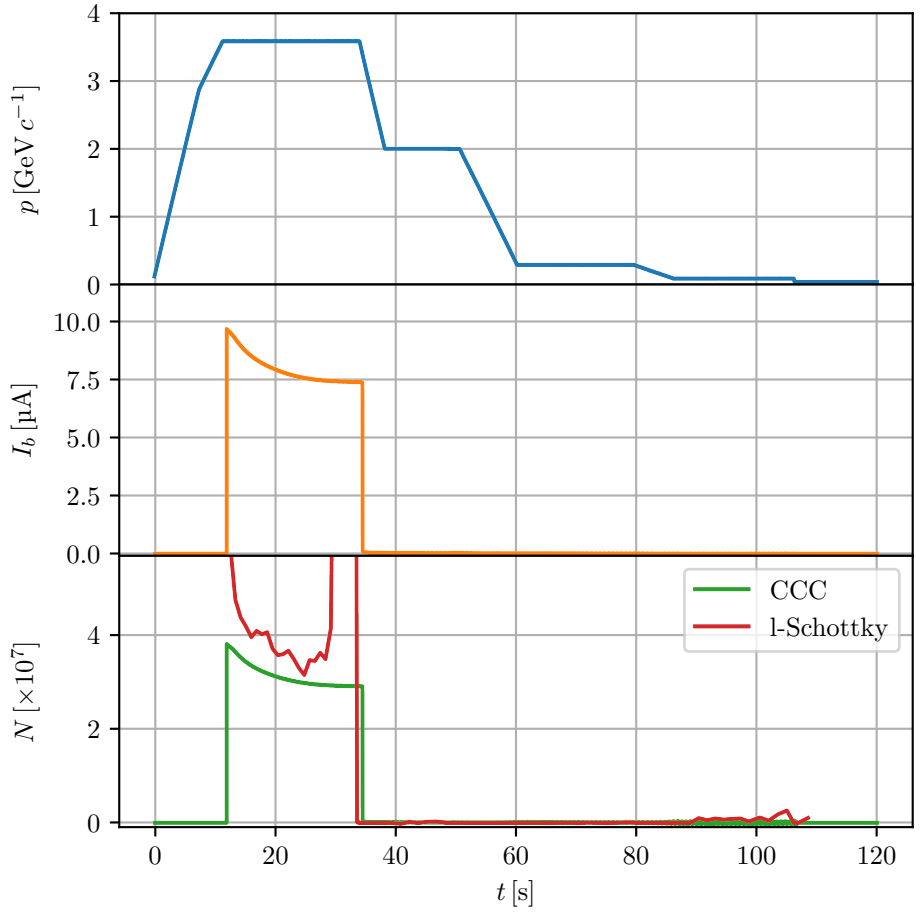

FIGURE E.4: Cycle where the beam is lost at beginning of first deceleration ramp.

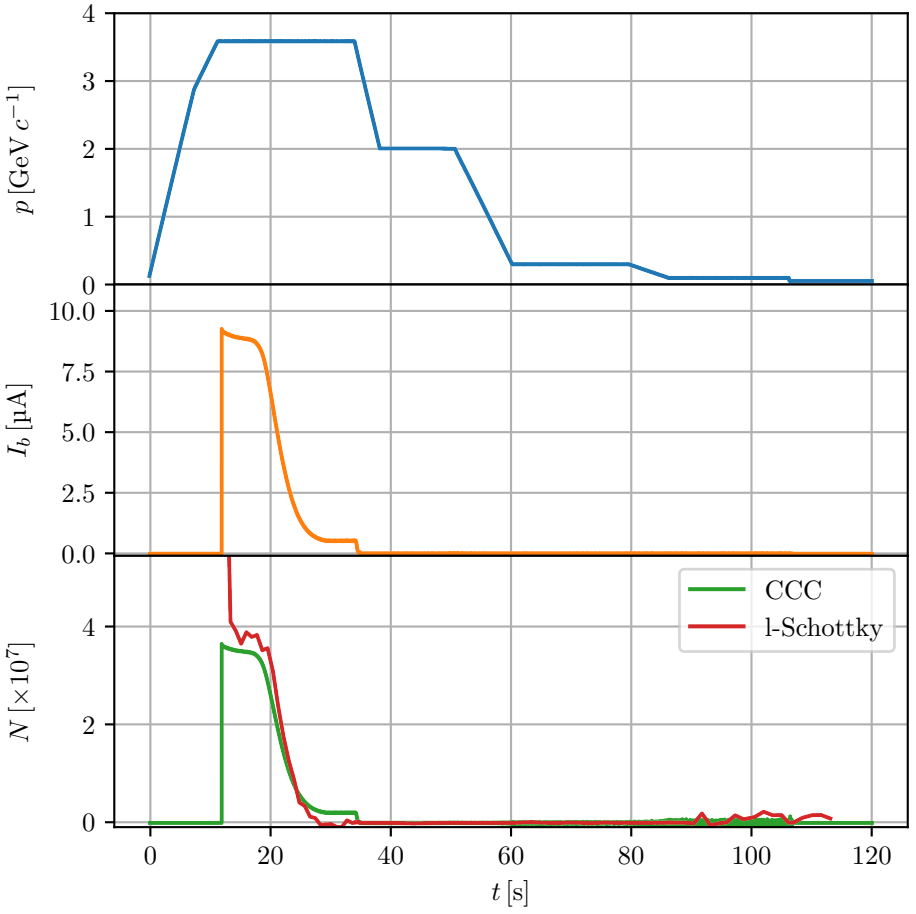

FIGURE E.5: Cycle where the beam is lost during the first stochastic cooling plateau.

Bibliography

[1] T. Nakada. European Strategy for Particle Physics. *Nuclear Physics News*, 25(2): 38–39, 2015. doi: 10.1080/10619127.2015.1035943. URL http://dx.doi.org/10.1080/10619127.2015.1035943.

[2] S.A. Baird, D. Berlin, J. Boillot, J. Bosser, M. Brouet, J. Buttkus, F. Caspers, V. Chohan, D. Dekkers, T. Eriksson, R. Garoby, R. Giannini, O. Gröbner, J. Gruber, J.Y. Hémery, H. Koziol, R. MacCaferri, S. Maury, C. Metzger, K.D. Metzmacher, D. Möhl, H. Mulder, M. Paoluzzi, F. Pedersen, J.P. Riunaud, C. Serre, D.J. Simon, G. Tranquille, J.W.N. Tuyn, and B. Williams. Design study of the antiproton decelerator: AD. Technical Report CERN-PS-96-043-AR, CERN, Nov 1996. URL https://cds.cern.ch/record/317704.

[3] S. Maury. The Antiproton Decelerator: AD. *Hyperfine Interactions*, 109(1):43–52, 1997. doi: 10.1023/A:1012632812327. URL http://dx.doi.org/10.1023/A:1012632812327.

[4] P. Belochitskii, T. Eriksson, and S. Maury. The CERN antiproton decelerator (AD) in 2002: status, progress and machine development results. *Nuclear Instruments and Methods in Physics Research Section B: Beam Interactions with Materials and Atoms*, 214:176 – 180, 2004. doi: http://dx.doi.org/10.1016/S0168-583X(03)01765-8. URL http://www.sciencedirect.com/science/article/pii/S0168583X03017658. Low Energy Antiproton Physics (LEAP'03).

[5] C. Smorra, K. Blaum, L. Bojtar, M. Borchert, K.A. Franke, T. Higuchi, N. Leefer, H. Nagahama, Y. Matsuda, A. Mooser, M. Niemann, C. Ospelkaus, W. Quint, G. Schneider, S. Sellner, T. Tanaka, S. Van Gorp, J. Walz, Y. Yamazaki, and S. Ulmer. BASE The Baryon Antibaryon Symmetry Experiment. *Eur. Phys. J. Special Topics*, 224(16):3055–3108, 2015. doi: 10.1140/epjst/e2015-02607-4. URL https://doi.org/10.1140/epjst/e2015-02607-4.

[6] M. Amoretti, C. Amsler, G. Bonomi, A. Bouchta, P. Bowe, C. Carraro, C. L. Cesar, M. Charlton, M. J. T. Collier, M. Doser, V. Filippini, K. S. Fine, A. Fontana, M. C. Fujiwara, R. Funakoshi, P. Genova, J. S. Hangst, R. S. Hayano, M. H. Holzscheiter, L. V. Jorgensen, V. Lagomarsino, R. Landua, D. Lindelof, E. Lodi Rizzini, M. Macri, N. Madsen, G. Manuzio, M. Marchesotti, P. Montagna, H. Pruys, C. Regenfus, P. Riedler, J. Rochet, A. Rotondi, G. Rouleau, G. Testera, A. Variola, T. L.

Watson, and D. P. van der Werf. Production and detection of cold antihydrogen atoms. *Nature*, 419(6906):456–459, Oct 2002. doi: 10.1038/nature01096. URL http://dx.doi.org/10.1038/nature01096.

[7] M. Hori and J. Walz. Physics at CERN's Antiproton Decelerator. *Progress in Particle and Nuclear Physics*, 72:206 – 253, 2013. doi: http://dx.doi.org/10.1016/j.ppnp.2013.02.004. URL http://www.sciencedirect.com/science/article/pii/S0146641013000069.

[8] J. Eschke. International Facility for Antiproton and Ion Research (FAIR) at GSI, Darmstadt. *Journal of Physics G: Nuclear and Particle Physics*, 31(6):S967, 2005. URL http://stacks.iop.org/0954-3899/31/i=6/a=041.

[9] C.P. Welsch and J. Ullrich. FLAIR – a facility for low-energy antiproton and ion research. *Hyperfine Interactions*, 172(1):71–80, 2006. doi: 10.1007/s10751-007-9534-3. URL http://dx.doi.org/10.1007/s10751-007-9534-3.

[10] Ute Linz, editor. *Ion Beam Therapy Fundamentals, Technology, Clinical Applications*. Springer-Verlag Berlin Heidelberg, 1 edition, 2012. ISBN 978-3-642-21413-4. doi: 10.1007/978-3-642-21414-1.

[11] E.C. Calvo, F.J. Santos, J.M. López-Gutiérrez, S. Padilla, M. García-León, J. Heinemeier, C. Schnabel, and G. Scognamiglio. Status report of the 1 MV AMS facility at the Centro Nacional de Aceleradores. *Nuclear Instruments and Methods in Physics Research Section B: Beam Interactions with Materials and Atoms*, 361:13 – 19, 2015. doi: http://dx.doi.org/10.1016/j.nimb.2015.02.022. URL http://www.sciencedirect.com/science/article/pii/S0168583X15001391. The Thirteenth Accelerator Mass Spectrometry Conference.

[12] J.F. Ziegler. *Ion Implantation Science and Technology - 2nd ed.* Academic Press, 1988. ISBN 9780127806211.

[13] M. Holzscheiter, J. Alsner, N. Bassler, H. Knudsen, S. Sellner, and B.S. Sørensen. Relative Biological Effectiveness of Antiprotons the AD-4/ACE Experiment. *JPS Conf. Proc.*, 18:011039, 2017. doi: 10.7566/JPSCP.18.011039.

[14] V. Chohan, C. Alanzeau, M.E. Angoletta, J. Baillie, D. Barna, W. Bartmann, P. Belochitskii, J. Borburgh, H. Breuker, F. Butin, M. Buzio, O. Capatina, C. Carli, E. Carlier, M. Cattin, T. Dobers, P. Chiggiato, L. Ducimetiere, T. Eriksson, S. Fedemann, T. Fowler, R. Froeschl, R. Gebel, N. Gilbert, S. Hancock, J. Harasimowicz, M. Hori, L.V. Jorgensen, R. Kersevan, D. Kuchler, J.M. Lacroix, G. LeGodec, P. Lelong, L. Lopez-Hernandez, S. Maury, J. Molendijk, B. Morand, A. Newborough, D. Nisbet, A. Nosych, W. Oelert, M. Paoluzzi, S. Pasinelli, F. Pedersen, D. Perini, B. Puccio, J. Sanchez-Quesada, D. Schoerling, L. Sermeus, L. Soby, M. Timmins, D. Tommasini, G. Tranquille, G. Vanbavinckhove,

A. Vorozhtsov, C.P. Welsch, and T. Zickler. *Extra Low ENergy Antiproton (ELENA) ring and its Transfer Lines: Design Report*. CERN, Geneva, 2014. URL `http://cds.cern.ch/record/1694484`.

[15] W. Oelert. The ELENA project at CERN. *Acta Phys. Polon.*, B46(1):181–189, 2015. doi: 10.5506/APhysPolB.46.181.

[16] S. Maury, W. Oelert, W. Bartmann, P. Belochitskii, H. Breuker, F. Butin, C. Carli, T. Eriksson, S. Pasinelli, and G. Tranquille. ELENA: the extra low energy anti-proton facility at CERN. *Hyperfine Interactions*, 229(1):105–115, 2014. doi: 10.1007/s10751-014-1067-y. URL `http://dx.doi.org/10.1007/s10751-014-1067-y`.

[17] E. Lopez Sola, D. Horvath, and M. Calviani. Preliminary AD-Horn Thermomechanical and Electrodynamic Simulations. Technical Report CERN-EN-2016-002. CERN-ACC-2016-0334, CERN, Geneva, Nov 2016. URL `https://cds.cern.ch/record/2154274`.

[18] T. Eriksson. The CERN Antiproton Decelerator AD: Performance, developments and future possibilities. *AIP Conf. Proc.*, 796:389–392, 2005. doi: 10.1063/1.2130200. [,389(2005)].

[19] G. Gabrielse. Comparing the antiproton and proton, and opening the way to cold antihydrogen. In B. Bederson and H. Walther, editors, *Advances In Atomic, Molecular, and Optical Physics*, volume 45 of *Advances In Atomic, Molecular, and Optical Physics*, pages 1 – 39. Academic Press, 2001. doi: http://dx.doi.org/10.1016/S1049-250X(01)80037-9. URL `http://www.sciencedirect.com/science/article/pii/S1049250X01800379`.

[20] N. Kuroda, H.A. Torii, Y. Nagata, M. Shibata, Y. Enomoto, H. Imao, Y. Kanai, M. Hori, H. Saitoh, H. Higaki, A. Mohri, K. Fujii, C.H. Kim, Y. Matsuda, K. Michishio, Y. Nagashima, M. Ohtsuka, K. Tanaka, and Y. Yamazaki. Development of a monoenergetic ultraslow antiproton beam source for high-precision investigation. *Phys. Rev. ST Accel. Beams*, 15:024702, Feb 2012. doi: 10.1103/PhysRevSTAB.15.024702. URL `http://link.aps.org/doi/10.1103/PhysRevSTAB.15.024702`.

[21] Y. Bylinsky, A.M. Lombardi, and W. Pirkl. RFQD: A 'Decelerating' radio frequency quadrupole for the CERN anti-proton facility. *eConf*, C000821:TUD05, 2000. [,554(2000)].

[22] R.C. Webber. A tutorial on non-intercepting electromagnetic monitors for charged particle beams. In *8th International Topical Meeting on Nuclear Applications and Ultilization of Accelerators (AccAPP'07) Pocatello, Idaho, July 30-August 2, 2007*, 2007. URL `http://lss.fnal.gov/cgi-bin/find_paper.pl?conf-07-394`.

[23] P. Strehl. *Beam Instrumentation and Diagnostics*. Particle Acceleration and Detection. Springer Berlin Heidelberg, 2006. ISBN 9783540264040. doi: 10.1007/3-540-26404-3. URL http://link.springer.com/book/10.1007%2F3-540-26404-3.

[24] P. Forck. *Lecture notes on beam instrumentation and diagnostics: Joint University Accelerator School, January - March 2013*. [s.n.], [S.l.], 2013. URL https://cds.cern.ch/record/2252577.

[25] D Möhl. Principle and technology of beam cooling. In *RCNP Kikuchi Summer School*, pages 251–295, Osaka, Japan, Nov 1986. URL https://cds.cern.ch/record/173312.

[26] J. Harasimowicz, C.P. Welsch, L. Cosentino, A. Pappalardo, and P. Finocchiaro. Beam diagnostics for low energy beams. *Phys. Rev. ST Accel. Beams*, 15:122801, Dec 2012. doi: 10.1103/PhysRevSTAB.15.122801. URL http://link.aps.org/doi/10.1103/PhysRevSTAB.15.122801.

[27] J.B. Sharp. The induction type beam monitor for the PS: Hereward transformer. Technical Report MPS-Int-CO-62-15. CERN-MPS-Int-CO-62-15, CERN, Geneva, Dec 1962. URL https://cds.cern.ch/record/1068123.

[28] A.W. Chao, K.H. Mess, M. Tigner, and F. Zimmermann. *Handbook of accelerator physics and engineering; 2nd ed.* World Scientific, Singapore, 2013. URL https://cds.cern.ch/record/1490001.

[29] K. Unser. Beam Current Transformer with D. C. to 200 MHz Range. *IEEE Transactions on Nuclear Science*, 16(3):934–938, June 1969. doi: 10.1109/TNS.1969.4325406.

[30] H.C. Appelo, M. Groenenboom, and J. Lisser. The Zero-Flux DC Current Transformer a High Precision Bipolar Wide-Band Measuring Device. *IEEE Transactions on Nuclear Science*, 24(3):1810–1811, June 1977. doi: 10.1109/TNS.1977.4329095.

[31] P. Odier, M. Ludwig, and S. Thoulet. The DCCT for the LHC Beam Intensity Measurement. Technical Report CERN-BE-2009-019, CERN, Geneva, May 2009. URL https://cds.cern.ch/record/1183400.

[32] Bergoz instrumentation.

[33] P. Odier. DCCT technology review. In *DC current transformers and beam-lifetime evaluations. Beam intensity measurements and lifetime calculations. Proceedings, Workshop, CARE-HHH-ABI networking, Lyon, France, December 1-2, 2004*, pages 3–5, 2004. URL http://care-hhh.web.cern.ch/CARE-HHH/ABI/CARE-Conf-2004-023-HHH.pdf.

[34] M.E. Angoletta, V. Chohan, M. Ludwig, O. Marqversen, P. Odier, F. Pedersen, U. Raich, L. Søby, G. Tranquille, and T. Spickermann. Beam Measurement Systems for the CERN Antiproton Decelerator (AD). In *Proc. of 19th IEEE Particle Accelerator Conference*, page 4 p, Chicago, IL, USA, Jul 2001. URL `https://cds.cern.ch/record/510663`. Revised version number 1 submitted on 2001-07-30 11:17:50.

[35] P. Odier. Personal communication, 2014.

[36] W. Schottky. Über spontane Stromschwankungen in verschiedenen Elektrizitätsleitern. *Ann. Phys.*, 362(23):541–567, 1918. doi: 10.1002/andp.19183622304. URL `http://doi.wiley.com/10.1002/andp.19183622304`.

[37] D. Boussard. Schottky noise and beam transfer function diagnostics. In *CAS - CERN Accelerator School: Advanced accelerator physics. 1.*, pages 416–452, Oxford, UK, May 1986. URL `http://cds.cern.ch/record/168143`.

[38] S. van der Meer. Diagnostics with Schottky noise. In *3rd Joint US-CERN School on Particle Accelerators: Frontiers of Particle Beams, Observation, Diagnosis and Correction Capri, Italy, October 20-26, 1988*, pages 423–433, Oct 1988. URL `https://cds.cern.ch/record/195311`.

[39] F. Caspers. Schottky signals for longitudinal and transverse bunched-beam diagnostics. In *CAS - CERN Accelerator School: Course on Beam Diagnostics*, Dourdan, France, 2009. doi: http://dx.doi.org/10.5170/CERN-2009-005.407. URL `https://cds.cern.ch/record/121328`.

[40] M.E. Angoletta, L. Bojtar, V. Chohan, A. Findlay, M. Ludwig, O. Marqversen, and F. Pedersen. Antiproton beam parameters measurement by a new digital-receiver-based system. Technical Report CERN-PS-2001-016-BD, CERN, Geneva, Apr 2002. URL `https://cds.cern.ch/record/546424`.

[41] M. Ludwig, L. Bojtar, M. Fernandes, M. Gasior, L. Soby, and G. Tranquille. CERN Antiproton Decelerator beam instrumentation for the ELENA era. In *IPAC2014: Proceedings of the 5th International Particle Accelerator Conference*, page 4 p, Dresden, Germany, Jun 2014. URL `https://cds.cern.ch/record/1742319`.

[42] M. Bregman, M. Calvetti, G. Carron, S. Cittolin, M. Hauer, H. Herr, H. Koziol, F. Krienen, P. Kristensen, G. Lebée, D. Möhl, G. Petrucci, C. Rubbia, D. Simon, G. Stefanini, L. Thorndahl, S. van der Meer, and T. Wikberg. Measurement of Antiproton Lifetime using the ICE Storage Ring. *Physics Letters B*, 78(1): 174 – 175, 1978. doi: http://dx.doi.org/10.1016/0370-2693(78)90376-3. URL `http://www.sciencedirect.com/science/article/pii/0370269378903763`.

[43] J.X. Wu, Y.D. Zang, F. Nolden, M.S. Sanjari, P. Hülsmann, F. Caspers, T.C. Zhao, M. Li, J.Z. Zhang, J. Li, Y. Zhang, G.Y. Zhu, S.H. Zhang, X.W. Ma,

H.S. Xu, J.C. Yang, J.W. Xia, R.S. Mao, and P. Petri. Performance of the resonant Schottky pickup at CSRe. *Nuclear Instruments and Methods in Physics Research Section B: Beam Interactions with Materials and Atoms*, 317, Part B: 623 – 628, 2013. doi: https://doi.org/10.1016/j.nimb.2013.08.017. URL `http://www.sciencedirect.com/science/article/pii/S0168583X13008653`. {XVIth} International Conference on ElectroMagnetic Isotope Separators and Techniques Related to their Applications, December 27, 2012 at Matsue, Japan.

[44] E.O. Göbel and U. Siegner. Superconductivity, Josephson Effect, and Flux Quanta. In *Quantum Metrology: Foundation of Units and Measurements*, pages 61–102. Wiley-VCH Verlag GmbH & Co. KGaA, 2015. ISBN 9783527680887. doi: 10.1002/9783527680887.ch4. URL `http://dx.doi.org/10.1002/9783527680887.ch4`.

[45] C.M. Caves. Quantum limits on noise in linear amplifiers. *Phys. Rev. D*, 26:1817–1839, Oct 1982. doi: 10.1103/PhysRevD.26.1817. URL `https://link.aps.org/doi/10.1103/PhysRevD.26.1817`.

[46] J. Clarke. Fundamental Limits on Squid Technology. In B. Deaver and J. Ruvalds, editors, *Advances in Superconductivity*, pages 13–50. Springer US, Boston, MA, 1983. ISBN 978-1-4613-9954-4. doi: 10.1007/978-1-4613-9954-4_2. URL `http://dx.doi.org/10.1007/978-1-4613-9954-4_2`.

[47] I. K. Harvey. A Precise Low Temperature DC Ratio Transformer. *Review of Scientific Instruments*, 43(11):1626–1629, 1972. doi: http://dx.doi.org/10.1063/1.1685508. URL `http://scitation.aip.org/content/aip/journal/rsi/43/11/10.1063/1.1685508`.

[48] Natural Physical Laboratory. Cryogenic Current Comparator, 2016. URL `http://www.npl.co.uk/electromagnetics/electrical-quantum-standards/products-and-services/cryogenic-current-comparator`.

[49] M. Kuchnir, J. McCarthy, and P. Rapidis. SQUID based beam current meter. *IEEE Trans. Magn.*, 21(2):997–999, mar 1985. doi: 10.1109/TMAG.1985.1063601. URL `http://ieeexplore.ieee.org/lpdocs/epic03/wrapper.htm?arnumber=1063601`.

[50] A. Peters and H. Reeg. Review of the Experimental Results with a Cryogenic Current Comparator. *Proc. ...*, 1996. URL `http://accelconf.web.cern.ch/AccelConf/e96/PAPERS/TUPL/TUP033L.PDF`.

[51] A. Peters, W. Vodel, H. Koch, R. Neubert, H. Reeg, and C.H. Schroeder. A Cryogenic Current Comparator for the Absolute Measurement of nA Beams. *AIP Conference Proceedings*, 451(1):163–180, 1998. doi: http://dx.doi.org/10.1063/1.56997. URL `http://scitation.aip.org/content/aip/proceeding/aipcp/10.1063/1.56997`.

[52] T. Tanabe, K. Chida, and K. Shinada. A cryogenic current-measuring device with nano-ampere resolution at the storage ring TARN II. *Nuclear Instruments and Methods in Physics Research Section A: Accelerators, Spectrometers, Detectors and Associated Equipment*, 427(3):455 – 464, 1999. doi: http://dx.doi.org/10.1016/S0168-9002(99)00058-3. URL `http://www.sciencedirect.com/science/article/pii/S0168900299000583`.

[53] R. Geithner, R. Neubert, W. Vodel, P. Seidel, K. Knaack, S. Vilcins, K. Wittenburg, O. Kugeler, and J. Knobloch. Dark current measurements on a superconducting cavity using a cryogenic current comparator. *Review of Scientific Instruments*, 82(1):013302, 2011. doi: 10.1063/1.3527063. URL `http://dx.doi.org/10.1063/1.3527063`.

[54] W. Vodel, R. Neubert, S. Nietzsche, K. Knaack, M. Wendt, K. Wittenburg, and A. Peters. Cryogenic current comparator for absolute measurements of the dark current of superconducting cavities for TESLA. *IEEE Transactions on Applied Superconductivity*, 13(2):743–746, June 2003. doi: 10.1109/TASC.2003.814026. URL `http://ieeexplore.ieee.org/xpl/articleDetails.jsp?arnumber=1211710`.

[55] W. Vodel, R. Neubert, S. Nietzsche, P. Seidel, K. Knaack, K. Wittenburg, and A. Peters. A new measurement tool for characterization of superconducting rf accelerator cavities using high-performance LTS SQUIDs. *Superconductor Science and Technology*, 20(11):S393, 2007. URL `http://stacks.iop.org/0953-2048/20/i=11/a=S18`.

[56] W. Vodel, R. Neubert, S. Nietzsche, K. Knaack, K. Wittenburg, and A. Peters. An LTS-SQUID Based Measurement Tool for Characterization of Superconductive RF Cavities. *IEEE Transactions on Applied Superconductivity*, 17(2):621–624, June 2007. doi: 10.1109/TASC.2007.898693.

[57] L Hao, J.C. Macfarlane, D.A. Peden, R.A.M. Lee, J.C. Gallop, and C. Carr. Design and performance of an HTS current comparator for charged-particle-beam measurements. *IEEE Trans. Applied Supercond.*, 11(1):635–638, mar 2001. doi: 10.1109/77.919424. URL `http://ieeexplore.ieee.org/lpdocs/epic03/wrapper.htm?arnumber=919424`.

[58] T. Watanabe, S. Watanabe, T. Ikeda, M. Kase, Y. Sasaki, T. Kawaguchi, and T. Katayama. A prototype of a highly sensitive cryogenic current comparator with a HTS SQUID and HTS magnetic shield. *Supercond. Sci. Technol.*, 17(5):S450–S455, may 2004. doi: 10.1088/0953-2048/17/5/073. URL `http://stacks.iop.org/0953-2048/17/i=5/a=073?key=crossref.ecaeb9fd4490f68f7792a4369bc4059f`.

[59] K. Grohmann, H.D. Hahlbohm, D. Hechtfischer, and H. Lübbig. Field attenuation as the underlying principle of cryo current comparators. *Cryogenics*, 16(7):423 –

429, 1976. doi: http://dx.doi.org/10.1016/0011-2275(76)90056-4. URL http://www.sciencedirect.com/science/article/pii/0011227576900564.

[60] K. Grohmann, H.D. Hahlbohm, D. Hechtfischer, and H. Lübbig. Field attenuation as the underlying principle of cryo-current comparators 2. Ring cavity elements. *Cryogenics*, 16(10):601 – 605, 1976. doi: http://dx.doi.org/10.1016/0011-2275(76)90192-2. URL http://www.sciencedirect.com/science/article/pii/0011227576901922.

[61] M. Fernandes, J. Tan, L. Soby, and C.P. Welsch. Cryogenic Current Comparator as Low Intensity Beam Current Monitor in the CERN Antiproton Decelerators. In *IBIC2013: Proceedings of the 2nd International Beam Instrumentation Conference*, page 4 p, Oxford, UK, Sep 2013. URL https://cds.cern.ch/record/1637990.

[62] T. Watanabe, N. Fukunishi, M. Kase, O. Kamigaito, S. Inamori, and K. Kon. Beam Current Monitor with a High-Tc Current Sensor and SQUID at the RIBF. *Journal of Superconductivity and Novel Magnetism*, 26(4):1297–1300, 2013. doi: 10.1007/s10948-012-1943-0. URL http://dx.doi.org/10.1007/s10948-012-1943-0.

[63] G. Gelato. Beam current and charge measurements. 1994.

[64] W. Buckel and R. Kleiner. *Superconductivity: Fundamentals and Applications, 2nd, Revised and Enlarged Edition*. Wiley-VCH, 2004. ISBN 978-3-527-40349-3.

[65] J. Clarke and A.I. Braginski. *The SQUID Handbook*. Wiley, Weinheim, 2006. URL https://cds.cern.ch/record/988225.

[66] T. Van Duzer and C.W. Turner. *Principles of superconductive devices and circuits*. Elsevier, 1981. ISBN 9780444004116. URL https://books.google.fr/books?id=rBpRAAAAMAAJ.

[67] R. Flükiger. Overview of Superconductivity and Challenges in Applications. *Rev. Accel. Sci. Technol.*, 05(April 2013):1–23, jan 2012. doi: 10.1142/S1793626812300010. URL http://www.worldscientific.com/doi/abs/10.1142/S1793626812300010.

[68] C. Buzea and K. Robbie. Assembling the puzzle of superconducting elements: a review. *Superconductor Science and Technology*, 18(1):R1, 2005. URL http://stacks.iop.org/0953-2048/18/i=1/a=R01.

[69] F. London and H. London. The Electromagnetic Equations of the Supraconductor. *Proceedings of the Royal Society of London A: Mathematical, Physical and Engineering Sciences*, 149(866):71–88, 1935. doi: 10.1098/rspa.1935.0048. URL http://rspa.royalsocietypublishing.org/content/149/866/71.

[70] V.L. Ginzburg and L.D. Landau. On the Theory of Superconductivity. *Zh. Eksp. Teor. Fiz.*, 20:1064–1082, 1950.

[71] H.K. Onnes. The resistance of pure mercury at helium temperatures. *Commun. Phys. Lab. Univ. Leiden*, 12:120+, 1911.

[72] D. Goodstein and J. Goodstein. Richard Feynman and the History of Superconductivity. *Physics in Perspective*, 2(1):30–47, 2000. doi: 10.1007/s000160050035. URL http://dx.doi.org/10.1007/s000160050035.

[73] D.J. Quinn and W.B. Ittner. Resistance in a Superconductor. *Journal of Applied Physics*, 33(2):748–749, 1962. doi: http://dx.doi.org/10.1063/1.1702504. URL http://scitation.aip.org/content/aip/journal/jap/33/2/10.1063/1.1702504.

[74] B. Fellmuth, H. Maas, and D. Elefant. Investigation of the Superconducting Transition Point of Niobium as a Reference Temperature. *Metrologia*, 21(4):169, 1985. URL http://stacks.iop.org/0026-1394/21/i=4/a=002.

[75] S.R. Foltyn, L. Civale, J.L. MacManus-Driscoll, Q.X. Jia, B. Maiorov, H. Wang, and M. Maley. Materials science challenges for high-temperature superconducting wire. *Nat. Mater.*, 6(9):631–642, Sep 2007. doi: 10.1038/nmat1989. URL http://www.nature.com/doifinder/10.1038/nmat1989.

[76] W. Meissner and R. Ochsenfeld. Ein neuer Effekt bei Eintritt der Supraleitfaehigkeit. *Naturwissenschaften*, 21(44):787–788, Nov 1933. doi: 10.1007/BF01504252. URL http://link.springer.com/10.1007/BF01504252.

[77] J. Bardeen, L.N. Cooper, and J.R. Schrieffer. Theory of Superconductivity. *Phys. Rev.*, 108:1175–1204, Dec 1957. doi: 10.1103/PhysRev.108.1175. URL http://link.aps.org/doi/10.1103/PhysRev.108.1175.

[78] H. Fröhlich. Theory of the Superconducting State. I. The Ground State at the Absolute Zero of Temperature. *Phys. Rev.*, 79:845–856, Sep 1950. doi: 10.1103/PhysRev.79.845. URL https://link.aps.org/doi/10.1103/PhysRev.79.845.

[79] J. Annett. *Superconductivity, superfluids, and condensates*. Oxford University Press, Oxford New York, 2004. ISBN 9780198507567.

[80] CODATA Value: magnetic flux quantum. http://physics.nist.gov/cgi-bin/cuu/Value?flxquhs2e, 2014. Accessed: 2017-02-15.

[81] B.D. Josephson. Possible new effects in superconductive tunnelling. *Physics Letters*, 1(7):251 – 253, 1962. doi: http://dx.doi.org/10.1016/0031-9163(62)91369-0. URL http://www.sciencedirect.com/science/article/pii/0031916362913690.

[82] W.C. Stewart. Current-Voltage Characteristics of Josephson Junctions. *Applied Physics Letters*, 12(8):277–280, 1968. doi: 10.1063/1.1651991. URL `http://dx.doi.org/10.1063/1.1651991`.

[83] D.E. McCumber. Effect of AD Impedance on DC Voltage-Current Characteristics of Superconductor Weak-Link Junctions. *Journal of Applied Physics*, 39(7): 3113–3118, 1968. doi: 10.1063/1.1656743. URL `http://dx.doi.org/10.1063/1.1656743`.

[84] R. L. Kautz and R. Monaco. Survey of chaos in the RF-biased Josephson junction. *Journal of Applied Physics*, 57(3):875–889, 1985. doi: http://dx.doi.org/10.1063/1.334687. URL `http://scitation.aip.org/content/aip/journal/jap/57/3/10.1063/1.334687`.

[85] B. Chesca, R. Kleiner, and D. Koelle. SQUID Theory. In *The SQUID Handbook: Fundamentals and Technology of SQUIDs and SQUID Systems, Volume I*, pages 29–92. Wiley-VCH Verlag GmbH & Co. KGaA, 2005. ISBN 9783527603640. doi: 10.1002/3527603646.ch2. URL `http://dx.doi.org/10.1002/3527603646.ch2`.

[86] D. Robbes. Highly sensitive magnetometersa review. *Sensors and Actuators A: Physical*, 129(12):86 – 93, 2006. doi: http://dx.doi.org/10.1016/j.sna.2005.11.023. URL `//www.sciencedirect.com/science/article/pii/S0924424705006643`.

[87] R.L. Fagaly. Superconducting Quantum Interference Device Instruments and Applications. *Review of Scientific Instruments*, 77(10):101101, 2006. doi: 10.1063/1.2354545. URL `http://dx.doi.org/10.1063/1.2354545`.

[88] D. Drung. High-Tc and low-Tc dc SQUID electronics. *Superconductor Science and Technology*, 16(12):1320, 2003. URL `http://stacks.iop.org/0953-2048/16/i=12/a=002`.

[89] D. Drung and M. Mück. SQUID Electronics. In *The SQUID Handbook: Fundamentals and Technology of SQUIDs and SQUID Systems, Volume I*, pages 127–170. Wiley-VCH Verlag GmbH & Co. KGaA, 2005. ISBN 9783527603640. doi: 10.1002/3527603646.ch4. URL `http://dx.doi.org/10.1002/3527603646.ch4`.

[90] D. Drung, H. Matz, and H. Koch. A 5-MHz bandwidth SQUID magnetometer with additional positive feedback. *Review of Scientific Instruments*, 66(4):3008–3015, 1995. doi: 10.1063/1.1145587. URL `http://dx.doi.org/10.1063/1.1145587`.

[91] D. Drung, S. Bechstein, K.P. Franke, M. Scheiner, and T. Schurig. Improved direct-coupled dc SQUID read-out electronics with automatic bias voltage tuning. *IEEE Transactions on Applied Superconductivity*, 11(1):880–883, Mar 2001. doi: 10.1109/77.919485.

[92] D. Drung. Advanced squid read-out electronics. In Harold Weinstock, editor, *SQUID Sensors: Fundamentals, Fabrication and Applications*, pages 63–116. Springer Netherlands, Dordrecht, 1996. ISBN 978-94-011-5674-5. doi: 10.1007/978-94-011-5674-5_2. URL https://doi.org/10.1007/978-94-011-5674-5_2.

[93] J. Gallop and F. Piquemal. SQUIDs for Standards and Metrology. In *The SQUID Handbook: Applications of SQUIDs and SQUID Systems, Volume II*, pages 95–137. Wiley-VCH Verlag GmbH & Co. KGaA, 2006. ISBN 9783527609956. doi: 10.1002/9783527609956.ch9. URL http://dx.doi.org/10.1002/9783527609956.ch9.

[94] K. Grohmann, H.D. Hahlbohm, H. Lubbig, and H. Ramin. Construction Principles and Properties of ironless DC and AC Current Comparators with Superconducting Shields. *PTB Mitteilungen*, 83:313, 1973.

[95] D.B. Sullivan and R.F. Dziuba. Low temperature direct current comparators. *Review of Scientific Instruments*, 45(4):517–519, 1974. doi: 10.1063/1.1686674. URL http://dx.doi.org/10.1063/1.1686674.

[96] K. Grohmann, H.D. Hahlbohm, H. Lubbig, and H. Ramin. Ironless Cryogenic Current Comparators for AC and DC Applications. *IEEE Transactions on Instrumentation and Measurement*, 23(4):261–263, Dec 1974. doi: 10.1109/TIM.1974.4314287.

[97] J. Sese, E. Bartolome, A. Camon, J. Flokstra, G. Rietveld, and C. Rillo. Simplified calculus for the design of a cryogenic current comparator. *IEEE Transactions on Instrumentation and Measurement*, 52(2):612–616, April 2003. doi: 10.1109/TIM.2003.811579.

[98] H. De Gersem, N. Marsic, W.F.O. Müller, F. Kurian, T. Sieber, and M. Schwickert. Finite-element simulation of the performance of a superconducting meander structure shielding for a cryogenic current comparator. *Nuclear Instruments and Methods in Physics Research Section A: Accelerators, Spectrometers, Detectors and Associated Equipment*, 840:77 – 86, 2016. doi: https://doi.org/10.1016/j.nima.2016.10.003. URL http://www.sciencedirect.com/science/article/pii/S016890021631021X.

[99] CST - Computer Simulation Technology. CST EM Studio, 2016. URL https://www.cst.com/products/cstems.

[100] F. Kurian and M. Schwickert. Field attenuation of the magnetic shield for a cryogenic current comparator. *Proc. BIW, Newport ...*, pages 2–4, 2012. URL http://accelconf.web.cern.ch/accelconf/BIW2012/papers/mopg001.pdf.

[101] A.I. Braginski and J. Clarke. Introduction. In *The SQUID Handbook: Fundamentals and Technology of SQUIDs and SQUID Systems, Volume I*, pages 1–28. Wiley-VCH Verlag GmbH & Co. KGaA, 2005. ISBN 9783527603640. doi: 10.1002/3527603646.ch1. URL http://dx.doi.org/10.1002/3527603646.ch1.

[102] Magnicon GmbH. SQUID Sensors, 2011. URL http://www.magnicon.com/fileadmin/download/datasheets/Magnicon_Squids.pdf. High-performance low-noise dc SQUID sensors.

[103] Magnicon GmbH. SQUID Electronics, 2011. URL http://www.magnicon.com/fileadmin/download/datasheets/Magnicon_XXF-1.pdf. XXF-1 - Ultra-high bandwidth dc SQUID electronics.

[104] Magnicon GmbH. SQUID Cryocablke, 2011. URL http://www.magnicon.com/fileadmin/download/datasheets/Magnicon_SQUIDPackage.pdf. SQUID Packaging and Wiring.

[105] D. Duret and P. Karp. Figure of merit and spatial resolution of superconducting flux transformers. *Journal of Applied Physics*, 56(6):1762–1768, 1984. doi: 10.1063/1.334182. URL http://dx.doi.org/10.1063/1.334182.

[106] J. Sese, A. Camon, C. Rillo, and G. Rietveld. Ultimate current resolution of a cryogenic current comparator. *IEEE Transactions on Instrumentation and Measurement*, 48(6):1306–1313, Dec 1999. doi: 10.1109/19.816153.

[107] C. Coillot, M. El Moussalim, E. Brun, A. Rhouni, R. Lebourgeois, G. Sou, and M. Mansour. Magnetic noise contribution of the ferromagnetic core of induction magnetometers. *J. Sensors Sens. Syst.*, 4(1):229–237, jun 2015. doi: 10.5194/jsss-4-229-2015. URL http://www.j-sens-sens-syst.net/4/229/2015/.

[108] S. Vitale, G.A. Prodi, and M. Cerdonio. Thermal magnetic noise in rf SQUIDS coupled to ferromagnetic cores. *Journal of Applied Physics*, 65(5):2130–2136, 1989. doi: http://dx.doi.org/10.1063/1.342862. URL http://scitation.aip.org/content/aip/journal/jap/65/5/10.1063/1.342862.

[109] S. Vitale, R. Tommasini, M. Cerdonio, M. Bonaldi, a. Cavalleri, and G. Durin. Magnetic viscosity, thermal relaxation, and thermal equilibrium noise in Co-based amorphous alloys at milliKelvin temperatures. *J. Appl. Phys.*, 72(10):4820, 1992. doi: 10.1063/1.352045. URL http://scitation.aip.org/content/aip/journal/jap/72/10/10.1063/1.352045.

[110] M. Pardavi-Horvath. Magnetic noise - barkhausen effect. In John G. Webster, editor, *Wiley Encyclopedia of Electrical and Electronics Engineering*. John Wiley & Sons, Inc., 1999. ISBN 9780471346081. doi: 10.1002/047134608X.W4514.pub2. URL http://dx.doi.org/10.1002/047134608X.W4514.pub2.

[111] N.R. Hutzler, K.I. Penanen, and T.C.P. Chui. Low temperature, high frequency permeability of Metglas 2714A and its potential for use as a core material for EMI filters. *Cryogenics*, 47(56):279 – 281, 2007. doi: http://dx.doi.org/10.1016/j.cryogenics.2007.03.004. URL http://www.sciencedirect.com/science/article/pii/S0011227507000483.

[112] Michael E McHenry, Matthew A Willard, and David E Laughlin. Amorphous and nanocrystalline materials for applications as soft magnets. *Progress in Materials Science*, 44(4):291 – 433, 1999. ISSN 0079-6425. doi: https://doi.org/10.1016/S0079-6425(99)00002-X. URL `http://www.sciencedirect.com/science/article/pii/S007964259900002X`.

[113] A. Steppke, R. Geithner, S. Hechler, R. Nawrodt, R. Neubert, W. Vodel, M. Schwickert, H. Reeg, and P. Seidel. Application of LTS-SQUIDs in Nuclear Measurement Techniques. *IEEE Transactions on Applied Superconductivity*, 19 (3):768–771, June 2009. doi: 10.1109/TASC.2009.2019542.

[114] R. Geithner, D. Heinert, R. Neubert, W. Vodel, and P. Seidel. Low temperature permeability and current noise of ferromagnetic pickup coils. *Cryogenics*, 54:16 – 19, 2013. doi: http://dx.doi.org/10.1016/j.cryogenics.2012.10.002. URL `http://www.sciencedirect.com/science/article/pii/S0011227512002007`.

[115] R. Geithner. Personal communicatio, 2014.

[116] N. Blaz, A. Maric, L. Radosavljevic, G.and Zivanov, G. Stojanovic, I. Atassi, and W. Smetana. Modeling and Charactetrization of Frequency and Temperature Variation of Complex Permeability of Ferrite LTCC material. *Prog. Electromagn. Res. B*, 23(July):131–146, 2010. doi: 10.2528/PIERB10061103. URL `http://www.jpier.org/PIERB/pier.php?paper=10061103`.

[117] J. Slama, P. Krivosik, and V. Jancarik. Modification of permeability components modelling. *J. Magn. Magn. Mater.*, 215:641–643, 2000. doi: 10.1016/S0304-8853(00)00249-3.

[118] G. Durin, P. Falferi, M. Cerdonio, G. A. Prodi, and S. Vitale. Low temperature properties of soft magnetic materials: Magnetic viscosity and 1/f thermal noise. *Journal of Applied Physics*, 73(10):5363–5365, 1993. doi: http://dx.doi.org/10.1063/1.353732. URL `http://scitation.aip.org/content/aip/journal/jap/73/10/10.1063/1.353732`.

[119] D. Drung, C. Abmann, J. Beyer, A. Kirste, M. Peters, F. Ruede, and T. Schurig. Highly Sensitive and Easy-to-Use SQUID Sensors. *IEEE Transactions on Applied Superconductivity*, 17(2):699–704, June 2007. doi: 10.1109/TASC.2007.897403.

[120] R.H. Koch. Maximum theoretical bandwidth and slewrate of a dc SQUID feedback system. *IEEE Transactions on Applied Superconductivity*, 7(2):3259–3262, June 1997. doi: 10.1109/77.622044.

[121] D. Drung, M. Götz, E. Pesel, J.H. Storm, C. Aßmann, M. Peters, and T. Schurig. Improving the stability of cryogenic current comparator setups. *Supercond. Sci. Technol.*, 22(11):114004, nov 2009. doi: 10.1088/0953-2048/22/

11/114004. URL http://stacks.iop.org/0953-2048/22/i=11/a=114004?key=crossref.aad287abe307ff5c6fbf05802c911e35.

[122] F. Teyssandier and D. Prêle. Commercially Available Capacitors at Cryogenic Temperatures. In *Ninth International Workshop on Low Temperature Electronics - WOLTE9*, Guaruja, Brazil, June 2010. URL https://hal.archives-ouvertes.fr/hal-00623399.

[123] D. Drung. Personal communication, 2014.

[124] Panasonic: Plastic Film Chip Capacitor - Product Specification. URL https://industrial.panasonic.com/content/data/CP/PDF/PUA1C_MA5_e.pdf.

[125] R.L. Patterson, A. Hammoud, and M. Elbuluk. Electronic Components for Use in Extreme Temperature Aerospace Applications. In *12th International Components for Military and Space Electronics Conference (CMSE 08)*, San Diego, California, February 2008. URL https://ntrs.nasa.gov/search.jsp?R=20090004677.

[126] INCAA Computers. ADC VD80, 2016. URL http://www.magnicon.com/fileadmin/download/datasheets/Magnicon_Squids.pdf. Datasheet: VME-VD80-15016.

[127] M. Fernandes, D. Alves, R. Geithner, T. Koettig, A. Lees, R. Neubert, E. Oponowicz, M. Schwickert, T. Stoehlker, J. Tan, and C.P. Welsch. Optimized Cryogenic Current Comparator for CERN's Low-Energy Antiproton Facilities. In *Proc. of International Beam Instrumentation Conference (IBIC'16), Barcelona, Spain, Sept. 13-18, 2016*, number 5 in International Beam Instrumentation Conference, pages 161–164, Geneva, Switzerland, Feb. 2017. JACoW. ISBN 978-3-95450-177-9. doi: doi:10.18429/JACoW-IBIC2016-MOPG48. URL http://jacow.org/ibic2016/papers/mopg48.pdf.

[128] A. Guerrero, J. J. Gras, J. L. Nougaret, M. Ludwig, M. Arruat, and S. Jackson. CERN front-end software architecture for accelerator controls. In *Proceedings, ICALEPCS 2003, the 9th International Conference on Accelerator and Large Experimental Physics Control Systems, October 13-17, 2003, Gyeongju, Korea*, pages 342–344, 2003. URL http://cdsweb.cern.ch/search.py?sysno=002418623CER.

[129] Inc. Keithley Instruments. *Model 6220 DC Current Source, Model 6221 AC and DC Current Source Reference Manual.* Keithley Instruments, Inc. URL http://www.tek.com/product-series/ultra-sensitive-current-sources-series-6200-manual-0.

[130] B.J. Holzer. Introduction to Transverse Beam Dynamics. In *Proceedings, CAS - CERN Accelerator School: Ion Sources: Senec, Slovakia, May 29-June 8, 2012*, pages 27–45, 2014. doi: 10.5170/CERN-2014-005.21,10.5170/CERN-2013-007.

27. URL https://inspirehep.net/record/1288538/files/arXiv:1404.0923.pdf. [,21(2014)].

[131] A. Holmes-Siedle, F. Ravotti, and M. Glaser. The Dosimetric Performance of RADFETs in Radiation Test Beams. In *2007 IEEE Radiation Effects Data Workshop*, volume 0, pages 42–57, July 2007. doi: 10.1109/REDW.2007.4342539.

[132] A. Lees, T. Koettig, M. Fernandes, and J. Tan. Design and optimisation of low heat load liquid helium cryostat to house cryogenic current comparator in antiproton decelerator at CERN. *IOP Conference Series: Materials Science and Engineering*, 171(1):012033, 2017. URL http://stacks.iop.org/1757-899X/171/i=1/a=012033.

[133] URL http://www.cryomech.com/.

[134] T. Koettig, F. Richter, C. Schwartz, R. Nawrodt, M. Thürk, and P. Seidel. Cold-Head Vibrations of a Coaxial Pulse Tube Refrigerator. In *Proceedings of the 15th International Cryocooler Conference (ICC'15), Long Beach, CA, June 20-25, 2012*, number 18 in International Cryocooler Conference, pages 687–693. ICC press, June 2015. ISBN 978-1934021040. URL http://cryocooler.org/proceedings/paper-flies/C15papers/083.pdf.

[135] M.F. Fernandes, R. Geithner, R. Neubert, M. Schwickert, T. Stöhlker, J. Tan, and C.P. Welsch. A Cryogenic Current Comparator for the Low-Energy Antiproton Facilities at CERN. In *Proc. of International Beam Instrumentation Conference (IBIC2015), Melbourne, Australia, 13-17 September 2015*, number 4 in International Beam Instrumentation Conference, pages 143–147, Geneva, Switzerland, Jan 2015. JACoW, JACoW. ISBN 978-3-95450-176-2. doi: 10.18429/JACoW-IBIC2015-MOPB043. URL http://accelconf.web.cern.ch/AccelConf/IBIC2015/papers/mopb043.pdf.

[136] P. Welch. The use of fast Fourier transform for the estimation of power spectra: A method based on time averaging over short, modified periodograms. *IEEE Transactions on Audio and Electroacoustics*, 15(2):70–73, Jun 1967. doi: 10.1109/TAU.1967.1161901.

[137] Stefan Scholl. Exact signal measurements using fft analysis, 2016. URL http://nbn-resolving.de/urn/resolver.pl?urn:nbn:de:hbz:386-kluedo-42930.

[138] M. Fernandes, R. Geithner, J. Golm, R. Neubert, M. Schwickert, T. Stoehlker, J. Tan, and C.P. Welsch. Non-perturbative measurement of low-intensity charged particle beams. *Superconductor Science and Technology*, 30(1):015001, 2017. URL http://stacks.iop.org/0953-2048/30/i=1/a=015001.

[139] G. Heinzel, A. Rüdiger, and R. Schilling. Spectrum and spectral density estimation by the Discrete Fourier transform (DFT), including a comprehensive list of

window functions and some new flat-top windows. Technical report, Max-Planck-Institut für Gravitationsphysik, Germany, 2002. URL `http://pubman.mpdl.mpg.de/pubman/item/escidoc:152164:1`.

[140] L. Lyons. *A Practical Guide to Data Analysis for Physical Science Students*. Cambridge Univ. Press, Cambridge, 1991. URL `https://cds.cern.ch/record/233280`.